Ultrafast Probing and Coherent Vibrational Control of a Surface Structural Phase Transition

DISSERTATION

zur Erlangung des mathematisch-naturwissenschaftlichen Doktorgrades

"Doctor rerum naturalium"

der Georg-August-Universität Göttingen

–

im Promotionsprogramm ProPhys

der Georg-August University School of Science (GAUSS)

vorgelegt von

Herrn Jan Gerrit Horstmann

aus Minden

Göttingen, 2021

Betreuungsausschuss

Prof. Dr. Claus Ropers, IV. Physikalisches Institut

Prof. Dr. Stefan Mathias, I. Physikalisches Institut

Mitglieder der Prüfungskommission

Referent:	Prof. Dr. Claus Ropers, IV. Physikalisches Institut
Korreferent:	Prof. Dr. Stefan Mathias, I. Physikalisches Institut
2. Korreferent:	Prof. Dr. Michael Horn-von Hoegen, Universität Duisburg-Essen

Weitere Mitglieder der Prüfungskommission

Prof. Dr. Fabian Heidrich-Meisner, Institut für Theoretische Physik

Prof. Dr. Tim Salditt, Institut für Röntgenphysik

Prof. Dr. Thomas Weitz, I. Physikalisches Institut

Prof. Dr. Alec M. Wodtke, Max-Planck-Institut für biophysikalische Chemie

Tag der mündlichen Prüfung: 2. Juni 2021

Every breath you take and every move you make
Every bond you break, every step you take, I'll be watching you.

Sting

Abstract

The present thesis explores the coherent control of surface structural phase transitions by all-optical manipulation of key vibrational modes. To this end, ultrafast low-energy electron diffraction (ULEED) in combination with femtosecond pulse sequences and optical pump-probe spectroscopy (OPP) is harnessed to probe and control the Peierls-like transition between the insulating (8×2) and the metastable, metallic (4×1) phase of atomic indium wires on the (111) surface of silicon.

Single-pulse optical excitation is used to drive the $(8 \times 2) \rightarrow (4 \times 1)$ transition well below the critical temperature of $T_c = 125$ K via the (de-)population of electronic states coupled to shear and rotational phonon modes connecting both phases. Whereas transient reflectivity measurements point to an acceleration of initial atomic motion at high excitation densities, ULEED underlines the impact of nanoscale heterogeneity on the transition and the subsequent recovery of the ground state for the case of a partially excited surface.

In a second set of ULEED experiments, a double-pulse optical excitation scheme is employed to exert coherent control over the transition close to its threshold. Here, pronounced oscillations in the delay-dependent switching efficiency evidence the decisive role of long-lived vibrational coherence in shear and rotation modes for governing the structural transformation. The corresponding lifetimes suggest that these modes act as a phonon bottleneck for energy relaxation between electronic and lattice subsystems. Based on the analysis of mode-specific frequency changes, initial phases and amplitudes, two possible coherent control mechanisms are discussed, involving the ballistic motion of the order parameter across the barrier and absorption modulation by Raman-active phonons, respectively. Multi-pulse experiments demonstrate the selective excitation of shear and rotation phonons and the applicability of 2D spectroscopy schemes for the investigation of possible mode couplings. Furthermore, the joint results of ULEED, OPP and density functional theory (DFT) suggest a description of the transition in terms of a two-dimensional potential energy surface (PES) with an off-diagonal transition state.

The outcome of this work shows that coherent atomic motion can be harnessed to affect the efficiencies and thresholds of structural phase transitions. Mode-selective coherent control of surfaces could open new routes to switching chemical and physical functionalities, enabled by metastable and nonequilibrium states.

Contents

List of Figures

Chapter 1

Introduction

Ultrafast science has changed our notion of how the interplay between electronic, lattice and spin degrees of freedom shapes the physical and chemical properties of solids in and out of equilibrium. Combining the rich toolbox of solid-state spectroscopy with recent advances in ultrafast optics makes it possible to track the motion of electrons, phonons and quasi-particles on nanosecond to attosecond[1] timescales, revealing the energy flow and couplings between individual subsystems. This way, complex and dynamic processes such as metal-insulator transitions [1, 2], superconductivity [3–5], charge density waves [6–12] and the underlying driving forces can be understood from a different perspective. To this end, ultrashort, intense pulses of light are harnessed to rapidly transfer energy to one or more degrees of freedom, while electronic [13–15], structural [16–23] or magnetic [24, 25] probes monitor the state of the system at varying time delays. Based on a sound understanding of the fundamental dynamics in condensed matter systems, the focus of this flourishing field of research is continuously shifting from the mere *observation* to the active, optical *control* of material properties far from equilibrium.

Generally, the last years saw remarkable progress in the field of materials synthesis, lately aided by, e.g. the combination of density functional theory (DFT) with computational approaches to identify promising candidates for high-temperature (high-T_c) [26] superconductivity and catalysis [27], or the development of sophisticated methods for the engineering of low-dimensional quantum materials, as recently exemplified by the case of magic-angle twisted bilayer graphene [28]. These approaches achieve new functionalities by changing chemical composition, combining different

[1] $1\,\mathrm{ns} = 10^{-9}\,\mathrm{s}$ (nano), $1\,\mathrm{ps} = 10^{-12}\,\mathrm{s}$ (pico), $1\,\mathrm{fs} = 10^{-15}\,\mathrm{s}$ (femto), $1\,\mathrm{as} = 10^{-18}\,\mathrm{s}$ (atto).

materials [29, 30] or applying external strain [31] to affect electronic and vibrational states. In this context, ultrafast science promises an alternative pathway to gain control over the properties of matter through the optical manipulation of decisive microscopic degrees of freedom in the time domain. In particular, the ability to guide the motion of electrons and atoms between different states of matter with intense electromagnetic fields holds the potential to create hybrid states governed by light-matter interaction [32] or to access thermodynamically forbidden, or "hidden" states [33]. Milestones on this path include all-optical magnetic switching [34, 35], light-induced metastable or exotic phases of solids [9, 32, 36, 37], and the coherent control of chemical reactions [38–41].

On their intrinsic timescales of a few femtoseconds to hundreds of picoseconds, the dynamics of optically excited electrons and phonons in solids can differ markedly from the undirected statistical motion in thermal equilibrium. Triggered by an external (impulsive) force [42], oscillations of carriers and lattice atoms around their equilibrium coordinates can occur *coherently*, i.e. with a fixed phase relation over a macroscopic spatial range. This allows for, e.g. the formation of electronic or vibrational wave packets and the interference of pathways between different states, for which the (vibrational) phase becomes a key parameter [38]. The lifetime of such effects is usually limited by rapid dephasing due to the coupling to other degrees of freedom, which renders ultrafast diffraction and spectroscopy ideal tools for probing and functionalising electronic and vibrational coherences.

The feasibility of this approach has been demonstrated by seminal experiments of A. H. Zewail (Nobel prize in 1999) and co-workers in what has become the field of femtochemistry [22, 39, 40]. Facilitated by the advent of fs-laser systems, this discipline entails the search for understanding and control of ultrafast reaction pathways. For this purpose, coherences in the electronic and vibrational states of reactants are used to affect transitions in a complex, generally multidimensional energy landscape [38, 43–45]. Archetypal femtochemistry experiments steer reactions by means of all-optical manipulation of phases between interfering pathways from educt to product states [46], or by sequences of precision-timed optical excitations to initiate and guide wave packet motion across the transition state [39, 47, 48].

However, while these central concepts of *coherent control* are established for small molecules, the possible transfer to extended systems and solids is complicated by, e.g. the high electronic and vibrational density of states, and by couplings to an

external heat bath. This typically results in short coherence times and a large number of relevant degrees of freedom to be controlled simultaneously. In this respect, low-dimensional materials represent a promising intermediate between bulk solids and molecules, with *phase transitions* assuming the role of a "reaction". Due to their reduced dimensionality and enhanced correlations between electrons and phonons, these systems often host phases with intriguing properties, linked by very few characteristic electronic transitions or the displacement of specific structural modes, respectively.

The prototypical case of such a transition is given by the Peierls instability, in which a *metal-to-insulator transition* is linked to *phonon softening* and the appearance of a static *periodic lattice distortion* (PLD). Coherent oscillations of the PLD, known as amplitude modes or amplitudons, are frequently observed in the optical pumping of such transitions, especially close to their thresholds. Here, the weak coupling of low-dimensional systems to the environment and the strong susceptibility of amplitudons to electronic excitation results in large vibrational amplitudes and enhanced coherence times. In analogy to the vibrational spectroscopy of reacting molecules [49], amplitudons can be used to track ultrafast changes in the lattice symmetry across a phase transition [7, 50–52]. However, it remains to be shown how coherent amplitude motion can be used to manipulate the outcome of a structural transition.

In this thesis, we demonstrate coherent control over a metal-insulator structural phase transition in a quasi-one-dimensional solid-state surface system [53]. Specifically, using ultrafast low-energy electron diffraction (ULEED) [17, 18, 53–55], we investigate the (8×2) → (4×1) transition of atomic indium wires on the (111) surface of silicon, a prominent Peierls system which recently attracted interest for its ultrafast dynamics [9–12, 56–58] (see artist's impression in Fig. 1.1). Harnessing the high temporal resolution and the ultimate surface sensitivity of ULEED, we track the ultrafast transition from the insulating (8×2) ground state to a metastable metallic (4×1) state after single-pulse optical excitation. A thorough analysis of the subsequent ns relaxation highlights the impact of surface heterogeneity on the recovery of the ground state. In a next step, motivated by control schemes of femtochemistry, we employ double-pulse optical excitation [39, 59–61] to switch the system from the broken-symmetry (8×2) to the high-symmetry (4×1) phase and monitor the corresponding structural changes by ULEED. The observation of delay-dependent

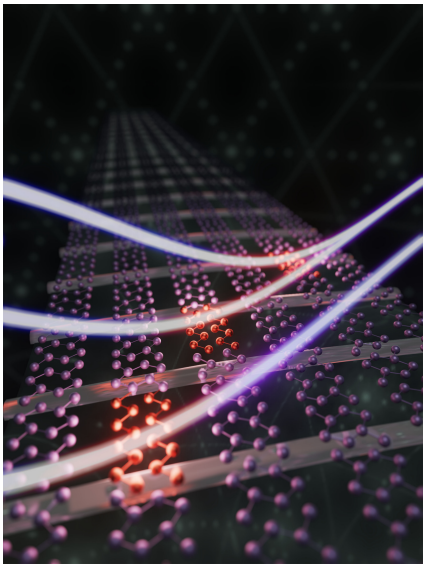

Figure 1.1: Artist's impression of the optically-induced structural phase transition in atomic indium wires on the (111) surface of silicon. Property of Murat Sivis.

oscillations in the double-pulse switching efficiency evidences the coherent control over the transition, which is found to be facilitated by vibrational coherence in shear and rotational phonon modes connecting both phases. Combining ULEED with first optical pump-pump measurements on the In/Si(111) surface and a two-dimensional spectroscopy scheme, we investigate the distinct roles of these modes in governing the transition. On this basis, we propose a two-dimensional potential energy surface for the transition characterised by an off-diagonal transition state and compare our model to recent DFT calculations.

This first investigation of a surface-specific structural phase transition with few-ps low-energy electron pulses in combination with sequential optical excitation marks another pivotal step towards establishing ULEED as a powerful tool for surface science.

1.1 Outline

The organisation of this thesis is as follows: In Sec. 2, the reader is introduced to theoretical concepts and methods of surface science relevant to this work. This includes, among others, an overview of Peierls physics and charge density waves in one dimension, followed by a brief discussion of ideas underlying the optical control over matter on ultrafast timescales. Moreover, this section covers the theoretical basics of LEED from surfaces, as well as ultrafast optical spectroscopy, facilitating

the analysis and interpretation of experimental data in Sec. 5 and Sec. 6.

In addition, Sec. 3 reviews the current status of ultrafast low-energy electron diffraction and recent technical advances enabling the investigation and control of the metal-insulator structural phase transition in atomic indium wires on silicon. This includes the generation of fs optical pulse trains, the combination of ULEED and optical pump-probe spectroscopy, and the preparation of metallic monolayers on semiconducting samples.

Particular emphasis is placed on the description of the material system, i.e. the Si(111)(8×2)-In surface. In this regard, Sec. 4 describes the progress made in the field from the discovery of indium-induced reconstructions of the Si(111) surface to the discovery of the Peierls-like transition at low-temperatures, and discusses recent insights provided by ultrafast electron diffraction, as well as time- and angle-resolved photoemission spectroscopy.

Building on the aforementioned theoretical and experimental foundations, the main results of this work are presented and discussed in Sec. 5 and 6. In a first step, the (8×2) → (4×1) phase transition and the subsequent relaxation to the ground state are studied in ULEED pump-probe experiments with few-ps electron pulses (Sec. 5). In Sec. 6, we report on the coherent control of the transition by harnessing vibrational coherence in key structural modes connecting both phases. Furthermore, in combination with multipulse excitation schemes and ultrafast optical spectroscopy, ULEED is used to identify the roles of these modes in the transition and the location of the transition state on the potential energy surface.

In Sec. 7, a brief summary of the major aspects and results of the thesis is given, followed by an outlook on further investigations of the In/Si(111) sample system, as well as future directions of ultrafast LEED and related techniques.

Chapter 2

Concepts and methods

2.1 Phase transitions in one-dimensional systems

At the heart of condensed matter physics lies the question as to how the properties of a solid *emerge* from the interactions of its fundamental building blocks. In this regard, the insight that matter consists of atoms, i.e. electrons and nuclei, is of paramount importance, or as Richard Feynman famously put it [62]:

"If, in some cataclysm, all of scientific knowledge were to be destroyed, and only one sentence passed on to the next generation of creatures, what statement would contain the most information in the fewest words? I believe it is the atomic hypothesis that *all things are made of atoms – little particles that move around in perpetual motion, attracting each other when they are a little distance apart, but repelling upon being squeezed into one another.* In that one sentence, you will see, there is an enormous amount of information about the world, if just a little imagination and thinking are applied."

At a second glance, Feynman's quote hints at another meaningful insight – that it is the interaction of electrons and nuclei among and with each other that endows solids with their unique properties. These include, among others, periodic structure, lattice symmetry, stiffness under shear, electrical as well as thermal conductivity, or magnetisation [63, 64]. Of particular interest are solid-state systems for which these quantities change as a function of one or more state variables, e.g. temperature or pressure, or due to external perturbations. Such processes are called *phase transitions*. Generally, the macroscopic changes during a phase transition can be attributed to microscopic dynamics of electrons and nuclei, which are reflected in

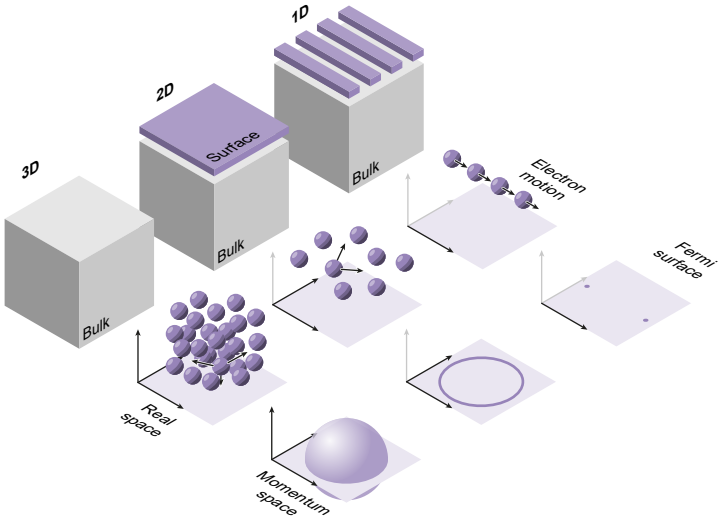

Figure 2.1: Electronic correlations in solids and the role of dimensionality. Electron motion and electronic states at the Fermi surface in 3D (front), 2D (middle) and 1D (back). Reducing the dimensionality of a system from 3D (bulk) to 2D (e.g. surface or atomic layer) to 1D (e.g. atomic wires) restricts electron motion in phase space, resulting in enhanced correlation effects. Specifically, in 1D electronic (or generally quasi-particle) excitations are collective. Dimensionality also affects electronic states or the band structure, thereby promoting, e.g. electron-electron or electron-hole interactions via phonons (electron-phonon coupling).

the electronic and lattice band structure. From a reductionist point of view, one may assume that any of these transitions could be explained at the level of individual, non-interacting electrons inside the electrostatic potential of the lattice atoms [65, 66].

However, the last century has seen the discovery of novel states of matter, which do not obey this principle. Here, the collective oscillations of the atomic lattice, i.e. *phonons*, mediate interactions between electrons. This in turn leads, e.g. to the formation and condensation of electron-electron or electron-hole pairs and ultimately to collective effects – prominent examples being conventional or BCS superconductivity [67, 68] or the formation of charge [69, 70] and spin density waves [71]. Many-body phenomena of this type are often termed *emergent* [65, 72] as the properties of the system as a whole cannot be explained by the properties of the individual particles. In other words, as P.W. Anderson put it in his seminal essay in *Science* in 1977 [65]: "More is different." For a large variety of materials, the underlying many-body problem can often be reduced to considering non-interacting (quasi-)particles, e.g.

electrons and phonons, with renormalised properties due to their mutual interactions – an ansatz commonly referred to as *mean-field* or *Fermi liquid theory* [73–75]. However, especially in the case of low-dimensional materials, Fermi liquid theory often fails to predict the emerging properties, marking the transition to the regime of *strongly-correlated phenomena*[1] [72, 76, 77]. Important examples from this flourishing field of research include, e.g. spin-charge separation [78] in Luttinger-liquids [79–81], (high-T_c) superconductivity [82–85], a number of spin (SDW) [71, 86] and charge density wave (CDW) systems [87], Mott insulators [88], or the fractional quantum Hall effect [89].

How is it that some physical systems host emergent phenomena and others do not? As already mentioned, in many cases, strong interactions or correlations, e.g. between electrons and phonons, play a decisive role. Above all, these are influenced by an essential property of any physical system: its *dimensionality*. This can be understood by considering the example of electron-electron interactions in phase space (see Fig. 2.1): Reducing the dimensionality of a system by confining electrons in one or two dimensions reduces the phase space volume available for scattering [77]. In this case, the movement of a single electron can no longer be considered independent but becomes a function of the positions and movements of all other electrons. As an example, take a one-dimensional chain of particles: to insert an additional particle, all others to the left (right) of it must shift by one-half of the average inter-particle distance along the wire. In this limit, the electron motion is highly correlated and excitations of the system are collective in nature [70, 77]. At the same time, dimensionality also affects electronic and vibrational states of materials. In low-dimensional systems, peculiar geometric features in the band structure facilitate the coupling between electrons and phonons and the formation of new ground states [70, 72, 76]. Perhaps remarkably, irrespective of their vastly different physical properties, all of these peculiar states of matter emerge from interactions between the same fundamental building blocks – if only you squeeze them a little harder.

[1] Note, however, that there seems to be no uniform definition of the term *strongly-correlated phenomena* in the literature. In this work, those systems are referred to as strongly correlated for which mean-field approaches break down.

2.1.1 Peierls instability and charge density waves

Arguably one of the most intriguing phenomena in low-dimensional materials is the Peierls instability and the associated formation of *charge density waves* (CDW). In the 1950s, R. Peierls [63] and H. Fröhlich [90] were the first to notice that at zero temperature, a one-dimensional (1D), equally-spaced atomic chain with one electron per ion is unstable to a periodic distortion of the lattice. Their theoretical model only received more attention when, in the 1970s, quasi-one-dimensional (quasi-1D) materials systems such as self-assembled polymer chains [91] came into focus, motivated by the search for high-T_c superconductors [92]. Instead of hosting a superconducting (SC) state, some of these systems with partially-filled bands underwent a *metal-insulator transition*[2] (MIT) below critical temperature T_c concomitant with pronounced changes of the chain structure. Transitions of this type were later termed *Peierls transitions*. Today, CDW materials are among the most frequently investigated solid-state systems, with examples in simple metals [93], transition-metal dichalcogenides [94, 95] or bronzes [96, 97], rare earth tellurides [98–100] as well as organic linear chain compounds [91] or metallic nanowires [101, 102]. Moreover, some of these materials are promising candidates for various technological applications, e.g. in ultrafast electronics or detectors [10].

From a theory perspective, a CDW is a broken-symmetry state of a low-dimensional metal formed due to the condensation of electron-hole pairs and mediated by electron-phonon interactions [69, 70]. Here, we will discuss CDW formation using the model system considered by Peierls. In the simplest case of a linear atomic chain with real-space lattice constant a (reciprocal lattice constant $b = 2\pi/a$), each atom shares a single electron, forming a quasi-free 1D electron gas. Since each electronic state can be filled with two electrons of opposite spin, this corresponds to a half-filled band (see Fig. 2.2a). Introducing a lattice distortion with periodicity $2a$ leads to degenerate states at $k = \pm k_F = \pm\pi/2a$.

For $T < T_c$, the coupling of electrons and holes (with opposite spins) removes this degeneracy via the formation of electronic band gaps around the Fermi energy E_F, i.e. a lowering (lifting) of (un-)occupied states [63, 69, 70, 88] (see Fig. 2.2a and Sec. 2.1.3). This reduces the electronic contribution to the total energy and

[2] In some cases, the transition is referred to as metal-semiconductor transition, depending on the size of the associated bandgap.

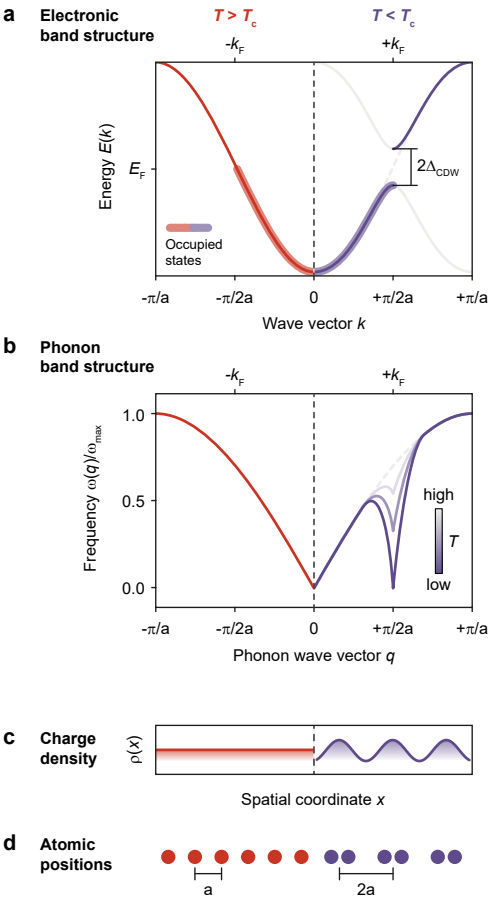

Figure 2.2: Signatures of the Peierls transition. **a**, Band structure of a 1D Peierls chain above (left) and below (right) T_c. For $T < T_c$ the Peierls instability leads to the formation of electronic band gaps at the $\overline{\text{X}}$ point ($\pm k_F$). **b**, Phonon band structure and temperature-dependent phonon softening (Kohn anomaly) at $q = 2k_F$ above (left) and below (right) T_c. Colour bar, temperature T. **c**, Constant (periodically modulated) charge density above (below) T_c along the 1D chain. Note that the total charge is conserved. **d**, Atomic equilibrium positions (left) and PLD below T_c (right).

thus stabilises the new phase. The opening of band gaps at the $\overline{\text{X}}$ point breaks the discrete translational symmetry of the system, which manifests itself in a periodic modulation of the charge density $\rho(r)$ with wavelength $\lambda_0 = \pi/k_F = 2a$ (Fig. 2.2c) and long-range order [69, 70]. Herein, the coupling of electrons and holes across the Brillouin zone is enabled by phonons with wave vector $q = 2k_F$ connecting opposite sections of the Fermi surface S_F.[3] This process is commonly referred to as *Fermi surface nesting* and will be discussed in more detail in Sec. 2.1.2. At the same time, the particular phonons soften in frequency because of the strong electron-phonon correlations (Fig. 2.2b, see also Sec. 2.1.3). As $\omega_q \to 0$, the mode becomes macroscopically occupied and a static periodic lattice distortion (PLD) with periodicity λ_0 is formed (Fig. 2.2d). However, this is at the expense of an increase

[3]Note that for $T > T_c$, valence-band electrons excited across the single particle gap screen the electron-phonon interactions and thus prevent the Peierls transition [103].

in total energy due to the Coulomb repulsion between the ionic cores. Hence, the Peierls transition is governed by the delicate balance between electronic and elastic energy (see Sec. 2.1.3).

The following sections provide a summary of the theoretical concepts used to describe characteristic properties of CDWs and PLDs in 1D, including Fermi surface nesting, the Kohn anomaly, electronic gap formation and collective excitations. In particular, it will become clear that CDWs and PLDs cannot be treated separately, but rather represent coupled entities. Finally, we will briefly address the question of how long-range order is established in quasi-1D CDW systems.

2.1.2 Fermi surface nesting

The Fermi surface S_F of a one-dimensional electron gas is remarkably simple: it consists of two points at $\pm k_\mathrm{F}$ [70, 77] (Fig. 2.3a). In reality, few physical systems are strictly one-dimensional, in the sense that they often represent 2D or 3D materials with highly anisotropic crystal and electronic structures, exhibiting quasi-1D character [66, 70]. Nonetheless, in many cases, the properties of such materials are well-described by one-dimensional models. As a prototypical example, an array of quasi-1D metallic chains on a 2D surface exhibits parabolic bands parallel to the chain direction (k_x-direction) and little to no dispersion in the perpendicular or k_y-direction (see Fig. 2.3d,e). Cuts through this 3D band structure in the k_x-direction resemble the electronic dispersion of a single linear chain of atoms. It is therefore justified to consider only the one-dimensional problem at this point. In order to understand charge density wave formations, we model the rearrangement of the charge density $\rho(r)$ in a 1D electron gas in response to an external perturbation given by the potential $\phi(r)$.[4] According to linear response theory [70, 104], the induced charge density $\rho^\mathrm{ind}(r)$ and the perturbation $\phi(r)$ are linked by

$$\rho^\mathrm{ind}(q) = \chi(q)\phi(q), \tag{2.1}$$

where $\rho^\mathrm{ind}(q)$ and $\phi(q)$ are the Fourier representations of $\rho^\mathrm{ind}(r)$ and $\phi(r)$ in momentum space and $\chi(q)$ is the one-dimensional *Lindhard response function*

[4] Herein, we consider a single half-filled metallic band, i.e. $k_\mathrm{F} = \pm\pi/2a$.

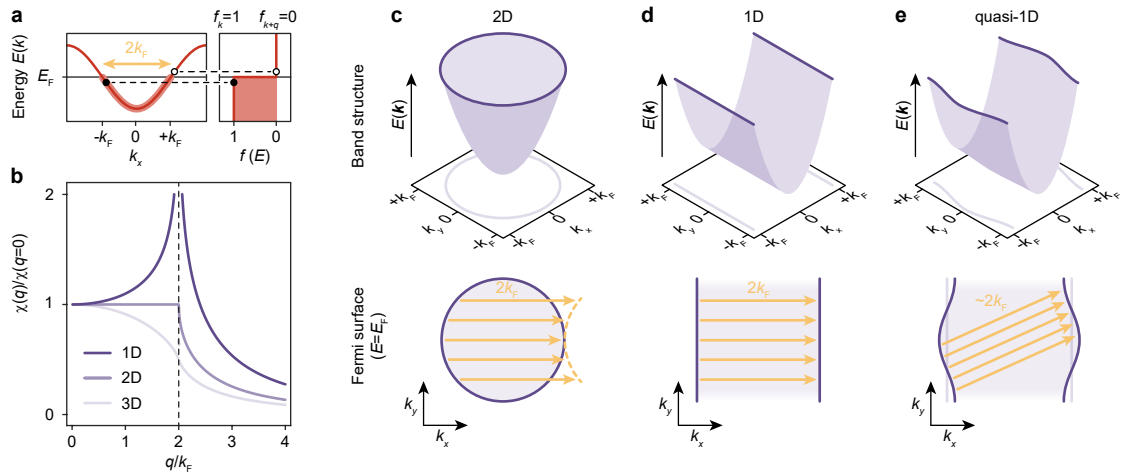

Figure 2.3: **a**, Fermi surface nesting for a 1D electron gas due to occupied and unoccupied states close to ϵ_F separated by $q = 2k_F$. **b**, Lindhard response function in 1D, 2D and 3D as a function of the normalized wave vector q/k_F. **c**-**e**, (Top) Band structures of (**c**) a 2D electron gas, (**d**) a 1D electron gas with vanishing dispersion perpendicular to the 1D chain and (**e**) a quasi-1D electron gas exhibiting weak dispersion in y-direction. (Bottom) Visualisation of corresponding nesting conditions: Improper nesting is expected for the 2D electron gas due to the topology of the Fermi surface. Note that in the quasi-1D case, nesting is still possible due to large parallel-running sections of ϵ_F. Adapted from Ref. [70].

$$\chi(q) = \int \frac{\mathrm{d}k}{2\pi} \frac{f_k - f_{k+q}}{\epsilon_k - \epsilon_{k+q}}. \tag{2.2}$$

Here, $f_k = f(\epsilon_k) = 1/(\exp(\epsilon_k/k_B T) + 1)$, is the Fermi distribution and $\epsilon_k = \epsilon(k)$ the dispersion relation for electrons evaluated at momentum k. From Eq. 2.2 it follows that the response of the electron gas diverges for wave vectors q connecting occupied and unoccupied states close to the Fermi energy, for which $\epsilon_k - \epsilon_{k+q} \to 0$ and $f_k - f_{k+q} > 0$ (see Fig. 2.3a). Assuming linear dispersion around $k = \pm k_F$, i.e. $\epsilon_k - \epsilon_F = \hbar v_F (k - k_F)$, Eq. 2.2 can be approximated by

$$\chi(q) = -e^2\, n(\epsilon_F) \ln \left| \frac{q + 2k_F}{q - 2k_F} \right|, \tag{2.3}$$

where $n(\epsilon_F)$ is the density of states at the Fermi level and e is the elementary charge. Clearly, $\chi(q)$ diverges at $q = 2k_F$ (see Fig. 2.3b), tantamount to a significant charge redistribution. It follows that at $T = 0$ K, any 1D electron gas is unstable against the formation of a periodic charge density modulation with wavelength $\lambda_0 = 2\pi/2k_F =$

π/k_F. Evaluating the numerator $f_k - f_{k-2k_\mathrm{F}}$ in Eq. 2.2 yields the temperature-dependence of the response function at $q = 2k_\mathrm{F}$ [70]:

$$\chi(q = 2k_\mathrm{F}, T) = -e^2\, n(\epsilon_\mathrm{F}) \ln\left(\frac{1.14\,\epsilon_\mathrm{F}}{k_\mathrm{b}T}\right). \tag{2.4}$$

Here, k_B is the Boltzmann constant. The divergence of $\chi(q)$ for low temperatures due to the pairs of electron and hole states separated by $q = 2k_\mathrm{F}$ is mainly determined by the topology of the Fermi surface and thus referred to as Fermi surface nesting. For a strictly one-dimensional model system with a half-filled band, i.e. an isolated metallic chain of atoms, the nesting condition is naturally fulfilled, because of the trivial Fermi surface (see Fig. 2.3a). Although such systems exist and have recently been studied, e.g. with regard to the role of fluctuations [105] (see Sec. 2.1.4), most CDW systems are either bulk, surface, or layered materials. This raises the question of which properties promote CDW formation in higher dimensions. In this regard, many 2D or 3D Peierls systems exhibit a strongly anisotropic or quasi-1D band (and lattice) structure with large parallel sections of $S_\mathrm{F}(k_x, k_y)$ (see Fig. 2.3c-e), prominent examples being organic linear chain compounds [91], transition-metal bronzes [96, 97] or atomic wire arrays on surfaces [101, 102]. Here, the coupling between neighbouring chains typically results in a non-zero band dispersion or buckling of the Fermi surface (perpendicular to the chains, see Fig. 2.3e) but leaves large parallel sections of the Fermi surface, thus enabling CDW formation via nesting for nearly all values of k_y. However, there are also many prominent Peierls systems which cannot be explained by Fermi-surface nesting alone [106], e.g. because strong interchain-couplings largely remove the one-dimensional character of the band structure. This points to the importance of other material properties for CDW formation, above all electron-phonon coupling, which will be discussed in Sec. 2.1.3.

2.1.3 Kohn anomaly and band gap opening

While the above considerations indicate the instability of a 1D electron gas to external perturbations as well as the role of electron-phonon coupling and Fermi surface topology therein, the question remains how these effects facilitate the observed structural changes and band gap opening. In this respect, a basic understanding of

the underlying physics requires a more thorough quantum mechanical treatment as found in Refs. [69, 70]. The following paragraphs essentially summarise the results of Ref. [70]. Generally, the dynamics of any non-relativistic quantum mechanical system are determined by the time-dependent Schrödinger equation

$$\mathrm{i}\hbar\frac{\partial}{\partial t}\left|\psi(t)\right\rangle = \mathcal{H}\left|\psi(t)\right\rangle. \tag{2.5}$$

Here, i is the imaginary unit, $\hbar = h/2\pi$ the reduced Planck constant, $|\psi\rangle$ the state vector in Hilbert space, and $\mathcal{H}$ the Hamiltonian corresponding to the total energy ϵ_{tot} of the system. In order to study CDW formation in a 1D electron gas, three contributions to ϵ_{tot} have to be considered, namely the energies of electronic and lattice subsystems as well as electron-phonon coupling. Accordingly, in the formalism of second quantisation, CDWs are described in terms of the Fröhlich Hamiltonian

$$\mathcal{H} = \sum_k \epsilon_k a_k^\dagger a_k + \sum_q \hbar\omega_q b_q^\dagger b_q + \sum_{k,q} g_q a_{k+q}^\dagger a_k (b_{-q}^\dagger + b_q), \tag{2.6}$$

where $a_k^\dagger$ and a_k are the creation and annihilation operators for electron states of momentum k and energy $\epsilon_k = \hbar v_{\mathrm{F}}(k - k_{\mathrm{F}})$,[5] and $b_q^\dagger$ and b_q are the corresponding operators for vibrational states or phonons of momentum q and energy $\hbar\omega_q$. The electron-phonon coupling constant g_q is the probability amplitude for scattering of an electron in momentum state k to a state $k' = k \pm q$ due to the absorption or emission of a phonon with momentum $\pm q$ [70]:

$$g_q = \mathrm{i}\sqrt{\frac{\hbar}{2NM\omega_{k'-k}}}\,(k'-k)V_{k'-k}. \tag{2.7}$$

Here, N is the number of lattice sites per unit length, M the ionic mass, $k' = k \pm q$, and $V_{k'-k}$ the Fourier transform of the single-atom potential $V(r)$.

Lattice subsystem

As mentioned in Sec. 2.1.1, the Peierls transition involves a structural phase transition, i.e. a static and periodic modulation of the atomic positions below critical

[5] For a 1D electron gas and k near k_{F}. Generally, the dispersion relation is given by $\epsilon_{\mathrm{k}} = \hbar^2 k^2/2m_{\mathrm{e}}$, with m_{e} being the electron mass.

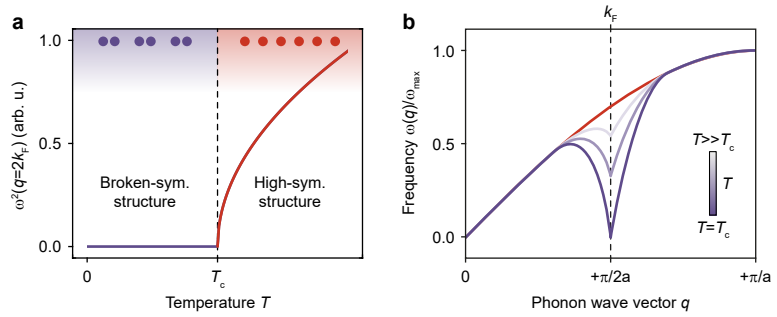

Figure 2.4: Kohn anomaly and phonon softening. **a**, Frequency square of the soft phonon mode at $q = 2k_\mathrm{F}$ driving structural transition as a function of temperature T. **b**, Phonon band structure and temperature-dependent phonon softening (Kohn anomaly) around $q = 2k_\mathrm{F}$. Band dispersion in the high-symmetry phase well above T_c, red. Colour bar, temperature. Subfigure **b** adapted from Ref. [70].

temperature T_c. In order to understand how this PLD follows from the electron-phonon coupling term in the Fröhlich Hamiltonian (Eq.2.6), the periodically varying lattice displacements have to be linked to the phonon creation and annihilation operators:

$$u(x) = \sum_q \sqrt{\frac{\hbar}{2NM\omega_q}}(b_q + b^\dagger_{-q})\ \exp(\mathrm{i}qx). \tag{2.8}$$

Here, $Q_q = (b_q + b^\dagger_{-q})$ is the normal coordinate of the ionic motion due to a phonon of wave vector q, ω_q the associated phonon frequency and x the spatial coordinate along the 1D chain of atoms. The above relation can be used to derive the equation of motion for the normal coordinate via $\hbar^2\ddot{Q}_q = -[[Q_q, \mathcal{H}], \mathcal{H}]$:

$$Q_q = -\left(\omega_q^2 + \frac{2g^2\omega_q}{M\hbar}\,\chi(q,T)\right) Q_q, \tag{2.9}$$

where it is assumed that the electron-phonon coupling constant $g_q = g$ is independent of q. Moreover, it is important to note that Eq. 2.9 represents a mean-field approach. Specifically, all interactions of electrons and phonons are modelled in terms of an effective force linear in g (see Ref. [70] for details). From this follows the renormalised phonon frequency

$$\omega^2_{\mathrm{ren},q} = \omega_q^2 + \frac{2g^2\omega_q}{\hbar}\,\chi(q,T), \tag{2.10}$$

which remarkably is a function of the q-dependent electronic susceptibility (Eq. 2.2) and the electron phonon coupling strength g. As a consequence, for phonons with $q \to 2k_\mathrm{F}$, the corresponding phonon frequency or energy, respectively, is significantly reduced[6], which is commonly referred to as *phonon softening* or *Kohn anomaly* (see also Fig. 2.4). Inserting Eq. 2.4 into Eq. 2.10 and setting $q = 2k_\mathrm{F}$ yields the temperature-dependent frequency of those phonon modes associated with Fermi surface nesting:

$$\omega^2_{\mathrm{ren},2k_\mathrm{F}} = \omega^2_{2k_\mathrm{F}} - \frac{2g^2 n(\epsilon_\mathrm{F})\omega_{2k_\mathrm{F}}}{\hbar} \ln\left(\frac{1.14\epsilon_0}{k_\mathrm{B}T}\right) = \omega^2_{2k_\mathrm{F}} \left(\frac{T - T_\mathrm{c}^\mathrm{MF}}{T_\mathrm{c}^\mathrm{MF}}\right)^{1/2}. \tag{2.11}$$

Here, it was used that $k_\mathrm{B}T_\mathrm{c}^\mathrm{MF} = 1.14\,\epsilon_0 \exp(-1/\lambda_g)$, with $\lambda_g = g^2 n(\epsilon_\mathrm{F})/\hbar\omega_{2k_\mathrm{F}}$ and T_c^MF being the mean-field transition temperature for which $\omega^2_{\mathrm{ren},2k_\mathrm{F}} = 0$. In other words, below T_c^MF, the corresponding phonon mode is frozen-in, representing a static periodic distortion of the crystal lattice, i.e. "a macroscopically occupied phonon mode with non-vanishing expectation values $\langle b_{2k_\mathrm{F}}\rangle = \langle b^\dagger_{-2k_\mathrm{F}}\rangle$" [70]. In analogy to superconductivity, this relation can be used to define a complex order parameter (see also Sec. 2.1.4)

$$\Delta = |\Delta| \exp(\mathrm{i}\phi) = g(\langle b_{2k_\mathrm{F}}\rangle + \langle b^\dagger_{-2k_\mathrm{F}}\rangle), \tag{2.12}$$

with amplitude $|\Delta|$ and phase ϕ. Accordingly, we have $\Delta = 1$ in the low-temperature symmetry-broken state, and $\Delta = 0$ in the high-temperature high-symmetry state. Finally, the average PLD along the atomic chain as a function of the order parameter is given by

$$\langle u(x)\rangle = \sqrt{\frac{\hbar}{2NM\omega_{2k_\mathrm{F}}}} \frac{2|\Delta|}{g} \cos(2k_\mathrm{F}x + \phi_0), \tag{2.13}$$

where ϕ_0 is the initial phase of the PLD. In summary, the structural phase transition underlying the Peierls transition can be understood in terms of atomic displacements induced by strong couplings of electrons and soft phonons with $q = 2k_\mathrm{F}$.

[6] Here, we have used that $\mathrm{sign}(g^2) \sim \mathrm{sign}(\mathrm{i}^2) = -1$.

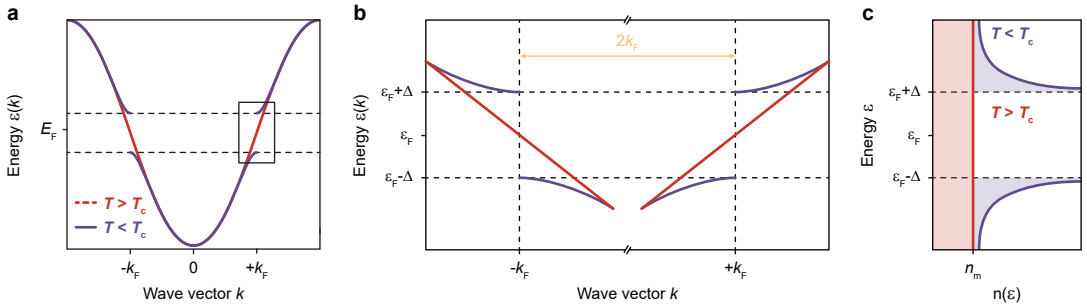

Figure 2.5: Electronic gap formation in the Peierls transition. **a**, Band structure of the 1D electron gas above and below T_c. **b**, selected regions of the band structure in **a** around $\pm k_F$, highlighting the opening of electronic band gaps around ϵ_F. **c**, Electronic density of states (DOS) in the metallic and CDW state as a function of energy. Adapted from Ref.[70].

Electronic subsystem

So far, only the effects of electron-phonon coupling on the lattice subsystem have been considered. In a next step, we will briefly discuss the changes in the electronic band structure during the Peierls transition. Given the above results, the electronic part of the Fröhlich Hamiltonian can be diagonalised for phonon modes with $q = 2k_F$ [70], leading to the energy eigenvalues

$$E_k = \epsilon_F + \mathrm{sign}(k - k_F)\sqrt{\hbar^2 v_F^2 (k - k_F)^2 + \Delta^2}. \tag{2.14}$$

As a result, for $T < T_c$ and in the vicinity of $\pm k_F$, the previously linear dispersion relation of the metallic state develops electronic gaps of width $\Delta E = 2\Delta$ (see Fig. 2.5). In this process, occupied (unoccupied) electronic states are lowered (lifted), resulting in a net reduction of electronic energy. Taking into account the additional elastic energy due to the PLD, the overall energy gain due to a Peierls transition from a high-symmetry metallic to a symmetry-broken CDW ground state is given in terms of the condensation energy

$$E_{con} = E_0 - E_{CDW} = \frac{n(\epsilon_F)}{2}\Delta^2, \tag{2.15}$$

with E_0 being the total energy of the metallic state. Generally, it is the delicate energy balance between lattice and electronic contributions to the total energy that

governs the Peierls transition. It is important to note that vibrational entropy may further (de-)stabilize the low-temperature phase [94, 107], as is the case for the In/Si system studied in this work (see Sec. 4)[7].

Stability of charge density waves

The above considerations demonstrate that the formation of a CDW costs Coulomb and elastic energy [94]. This is compensated by the lowering of occupied states in the electronic band structure. Accordingly, the necessary criterion for a Peierls transition can be formulated in the following way [94]:

$$\Delta E_{\text{latt.}} - \Delta E_{\text{el.}} < 0. \tag{2.16}$$

Here, $\Delta E_{\text{latt.}} = 1/2 M\omega_q^2 u_q^2$ and $\Delta E_{\text{el.}} = |V_q|^2 \chi(q)$ are the contributions of the lattice and electronic subsystems to the total energy, $V_q = g_q u_q \sqrt{2M\omega_q/\hbar}$ is the effective potential due to the static displacement of the phonon mode q, and g_q is the q-dependent electron-phonon coupling constant. In the transition, the characteristic pairing of electrons and holes is facilitated by a diverging electronic susceptibility and Fermi surface nesting, as is the case for Peierls systems with highly anisotropic (band) structures. At the same time, however, there are materials systems that do not meet these requirements but still host CDW phases [87, 106, 108, 109]. Thus, it is reasonable to ask what makes a good Peierls system. To identify the decisive parameters, we follow Ref. [94] and insert the explicit expressions for $\Delta E_{\text{latt.}}$ and $\Delta E_{\text{el.}}$ into Eq. 2.16. This results in

$$\frac{4g_{q^*}^2}{\hbar\omega_{q^*}} > \frac{1}{\chi_{q^*}}, \tag{2.17}$$

where q^* is the key phonon mode associated with the transition. Equation 2.17 provides an intuitive approach to the stability criterion for CDWs. First, we notice that a large electronic susceptibility at $q = q^*$ promotes the transition. However, the same applies to electron-phonon coupling. It is therefore expected that Peierls transitions in systems with insufficient nesting are enabled by electron-phonon coupling.

[7] Specifically, in a free energy picture, the lower electronic energy of the symmetry-broken phase is partially compensated by the lower vibrational entropy compared to the high-symmetry phase ($F = E - TS$) [107]. This in turn shifts the transition temperature T_c.

Commensurability

The original model of a linear Peierls chain with one electron per atom naturally exhibits half-filled bands with $k_\mathrm{F} = \pi/2a$ and a nesting vector $q = 2k_\mathrm{F}$. Consequently, the periodicity of the associated CDW or PLD is exactly doubled compared to the undistorted lattice of the high-symmetry phase[8]. However, it is certainly not *a priori* necessary for a lattice modulation to have a periodicity which is a rational multiple of a original unit cell [110]. Hence, a distinction is made between two scenarios:

- For band filling factors $n_\mathrm{e} = 1/p$ with $1/p \in \mathbb{Q}$ (*rational filling*), the reciprocal lattice vector $k_a = \pi/a$ can be represented as an integer multiple of k_F, i.e. $k_a = p \cdot k_\mathrm{F}$. The corresponding wavelength of the lattice distortion is given by $\lambda_\mathrm{PLD} = p \cdot a$. Therefore, the unit cell edges of the distorted and undistorted lattice coincide at certain positions [111]. Charge density wave systems of this type are classified as *commensurate*, with prominent examples given by the low-temperature phases of $1T$-TaS_2 ($T_\mathrm{CCDW} = 183 - 221$ K), $2H$-$TaSe_2$ ($T_\mathrm{CCDW} = 90$ K), $1T$-$TiSe_2$ ($T_\mathrm{CCDW} = 202$ K) [94], or atomic indium wires on silicon ($T_\mathrm{CCDW} = 125$ K) [102].

- For band filling factors $n_\mathrm{e} = 1/p$ with $1/p \notin \mathbb{Q}$ (*irrational filling*), the reciprocal lattice vector $k_a = \pi/a$ cannot be represented as an integer multiple of k_F. The corresponding wavelength of the lattice distortion is still given by $\lambda_\mathrm{PLD} = p \cdot a$. However, the unit cell edges of the distorted and undistorted lattice never coincide exactly. Systems of this type are classified as *incommensurate*. While various transition metal dichalcogenides host both commensurate and incommensurate CDW phases, the ICDW temperature temperature is typically higher ($1T$-TaS_2: $T_\mathrm{ICDW} = 543$ K; $2H$-$TaSe_2$: $T_\mathrm{ICDW} = 122$ K) [94][9].

This classification applies to all kinds of superstructures in one, two or three dimensions and will be discussed again in Sec. 2.3.3. In the case of CDWs, commensurability has important consequences. Specifically, a commensurate CDW is locked to the

[8] In real-space, this corresponds to a doubling of the unit cell size in the chain direction due to dimerisation.

[9] We further note the case of nearly commensurate CDW phases, for which the "CDW phase locally registers with the atomic lattice creating commensurate patches that are separated by discommensurations" [112]. Such a step-wise incommensurable CDW phase has been observed in $1T$-TaS_2 at room temperature [7, 8, 18, 94].

underlying lattice, i.e. the total energy of the system is minimised for certain phases of the order parameter (local ground states; see also Fig. 2.8a and b in Sec. 2.1.4). As a result, all excitations of a commensurate CDW exhibit gaps. Incommensurate CDWs, on the other hand, are not in registration with the underlying lattice. Here, the total energy is independent of the phase of the order parameter (Eq. 2.12) which allows for specific gapless excitations that realise a "frictionless" sliding of the CDW.

2.1.4 Landau theory and collective excitations

In modeling the changes in the electronic and lattice subsystems throughout the Peierls transition, we have harnessed the concept of a complex order parameter Δ (see Eq. 2.12), with $\Delta \neq 0$ for $T < T_c$, $\Delta = 0$ for $T > T_c$ and $\Delta = 1$ for $T = 0$. In particular, we saw that Δ connects the PLD amplitude (Eq. 2.13) and the electronic band gap (Eq. 2.14), highlighting the strong correlations between electrons and phonons. Furthermore, the order parameter links the quantum mechanical description of the Peierls transition to the phenomenological theory of phase transitions introduced by Lev Landau [113, 114]. Here, the momentary state of a system undergoing a symmetry-breaking transition is described by its order parameter in a 1D free energy landscape $F(\Delta, T)$, the shape of $F(\Delta, T)$ resulting from the total energy of the system as a function of the order parameter. This concept can be adapted to a variety of physical systems by associating Δ with, e.g. bond lengths or atomic displacements (structural transition), the electronic band gap (electronic transitions) or the magnetisation (magnetic transitions). For this reason the model is ideally suited to qualitatively describe Peierls transitions and associated phenomena such as collective modes [9, 70, 115, 116][10].

Symmetry-breaking transitions and metastability

Landau theory distinguishes between continuous and discontinuous phase transitions. These correspond to second- and first-order transitions in the Ehrenfest classification, which is still predominant in the relevant literature and therefore adopted here. Although most Peierls transitions are of second order, there are some CDW

[10] However, it is important to note that the phenomenological Landau models do not provide an atomic-scale picture of phase transitions, since the relevant thermodynamic potential is only defined for a statistical ensemble.

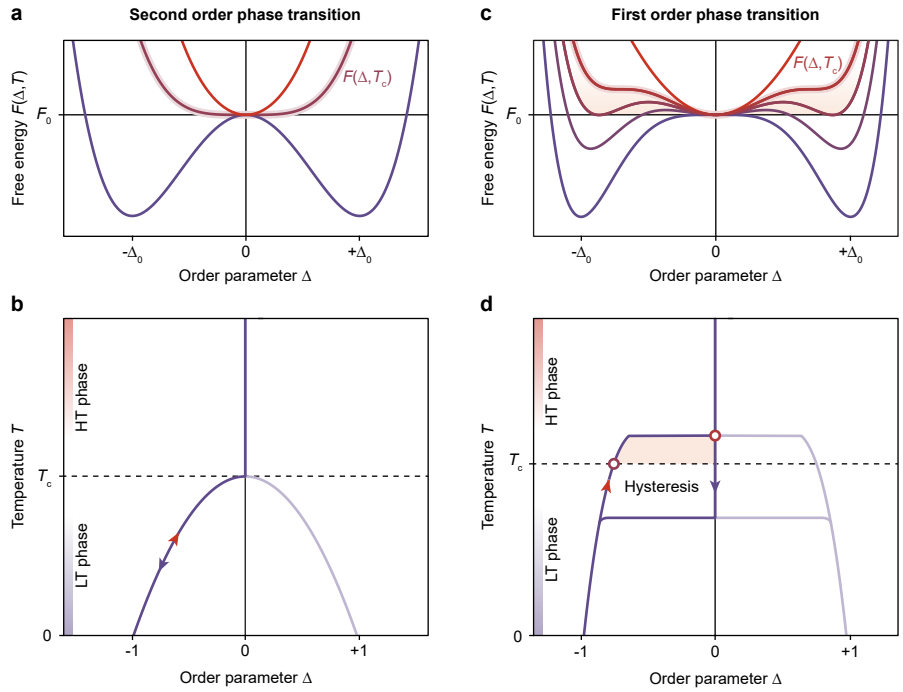

Figure 2.6: First and second order phase transitions in the Landau picture. **a**, Free energy landscape of a second order phase transition as a function of the order parameter Δ, drawn for different temperatures T. **b**, Order parameter Δ as a function of temperature T during cooling (violet arrow) and heating (red arrow). Light violet line, order parameter in the energetically degenerated ground state. T_c, Critical or transition temperature. **c**, Free energy landscape of a first order phase transition. Orange area, transition regime and metastable broken-symmetry state. **d**, $\Delta(T)$ during cooling (violet arrow) and heating (red arrow). Note the hysteresis behaviour and the distinct transition temperatures (circles) for cooling and heating due to the existence of a barrier between high- and broken symmetry states. Adapted from Ref. [116].

and SDW systems in which additional couplings and correlations, e.g. between neighbouring chains, lead to a first-order character of the symmetry-breaking transition[11] [117]. Therefore, we will use the Landau picture to discuss both possible scenarios. For a second-order phase transition, the order parameter is a continuous function of temperature across T_c (Fig. 2.6b). In the absence of external fields the free energy exhibits a mirror symmetry ($F(\Delta) = F(-\Delta)$), and $F(\Delta, T)$ can be expanded in even powers of $|\Delta|$ [70]. Accordingly, the free energy landscape of a

[11] This category also includes the material system of atomic indium wires on the (111) surface of silicon, which is investigated in this work (see Sec. 4 for a detailed introduction)

second-order transition is approximated by

$$F(\Delta, T) = F_0 + \frac{1}{2}a(T)|\Delta|^2 + \frac{1}{4}b(T)|\Delta|^4 + \mathcal{O}(|\Delta|^4), \tag{2.18}$$

where $a = a_0\,(T - T_\mathrm{c})/T_\mathrm{c}$ and $b \approx b(T_\mathrm{c}) = b_0$ are material-specific coefficients ($a_0, b_0 > 0$). Figure 2.6a shows $F(\Delta, T)$ for $T \ll T_\mathrm{c}$ (violet), $T \gg T_\mathrm{c}$ (red) and $T = T_\mathrm{c}$ (orange-shaded). Using that the thermodynamic equilibrium position of the system is defined by

$$\left.\frac{\partial F(\Delta, T)}{\partial \Delta}\right|_{\Delta_0} = 0, \text{ and } \left.\frac{\partial^2 F(\Delta, T)}{\partial \Delta^2}\right|_{\Delta_0} > 0, \tag{2.19}$$

we can also determine $\Delta(T)$ (see Fig. 2.6b). This polynomial model qualitatively describes the transition from the symmetry-broken ground state ($\Delta \neq 0$; violet potential in Fig. 2.6a) to the high-symmetry state ($\Delta = 0$; red) at $T = t_\mathrm{c}$, enabled by temperature-induced changes of the free energy curve. Note that although $F(\Delta)$ is often discussed as a direct function of temperature, it is rather the temperature-dependent occupation of electronic states that shapes the free energy landscape.

In the case of a first-order transition, the evolution of the order parameter as a function of temperature changes significantly (see Fig. 2.6c and d). In particular, the existence of a finite energy barrier separating high- and low-symmetry phases leads to a hysteresis and distinct transition temperatures for heating or cooling, respectively [113, 114, 117]. The associated the Landau free energy polynomial reads [70]

$$F(\Delta, T) = F_0 + \frac{1}{2}a(T)|\Delta|^2 + \frac{1}{4}b(T)|\Delta|^4 + \frac{1}{6}c(T)|\Delta|^6 + \mathcal{O}(|\Delta|^6), \tag{2.20}$$

with coefficients $a = a_0\,(T - T_\mathrm{c})/T_\mathrm{c}$, $b \approx b_0$, $c \approx c_0$ and $a_0, c_0 > 0$ as well as $b_0 < 0$. Remarkably, for a first order transition the high-symmetry (or high-temperature) state still exists as a local minimum on the free energy landscape even well below T_c, though it does no longer represent the ground state of the system. This implies that a quench, i.e. a rapid deformation of the Landau potential due to cooling below T_c, leaves the system in a *supercooled* or *metastable* state which is subsequently transformed into the symmetry-broken ground state, e.g. by means of thermal fluctuations above the barrier (Fig. 2.7) or heterogeneous (homogeneous) nucleation,

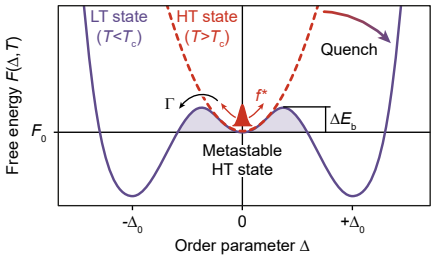

Figure 2.7: Metastability of the high-symmetry (high-temperature or HT) state below T_c. The transition into the symmetry-broken (low-temperature or LT) ground state is governed by temperature T and the barrier height ΔE_b. Γ, transition rate; f^*, effective oscillation frequency.

respectively[12]. According to the Arrhenius equation, the transition rate Γ to the ground state is determined by the temperature T and the barrier height ΔE_b [118]:

$$\Gamma = f^* \exp\left(\frac{\Delta E_b}{k_B T}\right). \tag{2.21}$$

Here, f^* is the effective oscillation frequency of the system in the metastable state, whose half-life can be determined via $t_{1/2} = \ln(2)/\Gamma$. For example, at a base temperature of $T = 60$ K – comparable to the transition temperatures of many CDWs – and an energy barrier of $\Delta E_b \sim 100$ meV, the corresponding half-life $t_{1/2} \sim 10^{-9}$ s of the metastable state is long compared to the atomic-scale dynamics of electrons and phonons underlying CDW formation but too short to be directly measured by conventional spectroscopy.

Collective excitations

Landau theory also provides an intuitive understanding insight of the elementary excitations of broken-symmetry or CDW states if the complex nature of the order parameter is considered (see Eq. 2.12). This approach is often referred to as Ginzburg-Landau theory and has originally been developed for the phenomenological description of conventional superconductors [119]. Besides, the theory has been successfully applied to other symmetry-breaking transitions and specifically CDWs [18, 115, 120]. Here, the free energy of a 1D chain of atoms is given in terms of the Ginzburg-Landau functional

$$F = F_0 + n(\epsilon_F) \int \mathrm{d}x \left[a|\Delta|^2 + b|\Delta|^4 + c|\Delta|^6 + d\left|\frac{\mathrm{d}\Delta}{\mathrm{d}x}\right|^2 + e\left|\frac{\mathrm{d}\Delta}{\mathrm{d}t}\right|^2 \right], \tag{2.22}$$

[12] We will later see that electronic excitations also influence the free energy landscape enabling a population of the metastable state below T_c (see Sec. 4.4).

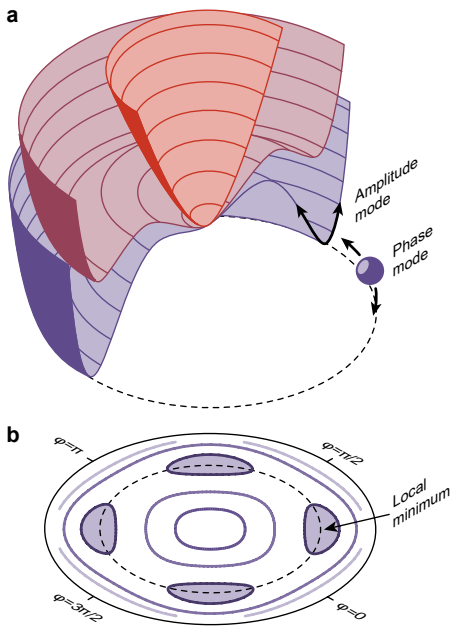

Figure 2.8: Collective excitations in CDWs. **a**, Cut through the free energy landscape of a first-order Peierls transition with complex order parameter above (red), close to (dark red), and below (violet) T_c. Order parameter motion due to amplitude mode (amplitudon) and phase mode (phason) in the CDW ground state are indicated by arrows. **b**, Contour plot of the ground state free energy landscape as a function of $|\Delta_0|$ and ϕ for a commensurate CDW.

where the term $|\mathrm{d}\Delta/\mathrm{d}x|^2$ is associated with spacial variations of the order parameter and $|\mathrm{d}\Delta/\mathrm{d}t|^2$ represents the kinetic energy due to temporal fluctuations of Δ. These spatial and temporal variations must be taken into account when defining the order parameter $\Delta = \Delta(x,t)$:

$$\Delta(x,t) = [|\Delta_0| + \delta(x,t)]\,\exp(\mathrm{i}(\phi_0 + \phi(x,t))). \tag{2.23}$$

In this, $\delta(x,t)$ and $\phi(x,t)$ describe spatio-temporal fluctuations of the amplitude and phase around the mean values $|\Delta_0|$ and $\phi_0 = 0$ of the order parameter. Both types of order parameter fluctuations can be visualised in a *champagne bottle bottom potential* $F(\Delta,\phi)$ (see Fig. 2.8a). In this picture, the previously considered 1D free energy landscape represents a cut through $F(\Delta,\phi)$ for a fixed phase ϕ. Inserting Eq. 2.23 into Eq. 2.22 and following the arguments of Ref. [70] yields two separate equations of motion for amplitude and phase fluctuations:

$$d\frac{\mathrm{d}^2\delta}{\mathrm{d}t^2} - c\frac{\mathrm{d}^2\delta}{\mathrm{d}x^2} + 2a\delta^2 = 0; \tag{2.24}$$

$$d\frac{\mathrm{d}^2\phi}{\mathrm{d}t^2} - c\frac{\mathrm{d}^2\phi}{\mathrm{d}x^2} = 0. \tag{2.25}$$

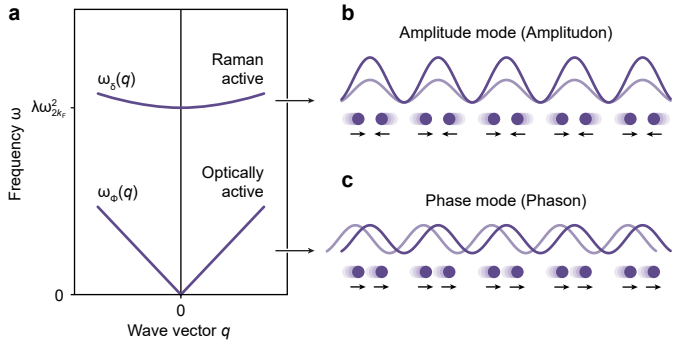

Figure 2.9: **a**, Dispersion relations of amplitude and phase modes. **b**,**c**, Effect of amplitude (**b**) and phase modes (**c**) on the charge density (violet lines) and the PLD. Arrows indicate the direction of atomic motion.

The solutions of Eqs. 2.24 and 2.25 are plane waves of the form $u_\delta = u_{\delta,0}\exp(\mathrm{i}\omega t - qx)$ or $u_\phi = u_{\phi,0}\exp(\mathrm{i}\omega t - qx)$, respectively, and are called *amplitude* or *phase modes*. The corresponding dispersion relations are

$$\omega_\delta(q) = \left(\lambda\omega_{2k_\mathrm{F}}^2 + \frac{1}{3}\frac{m}{m^*}v_\mathrm{F}^2 q^2\right)^{1/2} \tag{2.26}$$

$$\omega_\phi(q) = \left(\frac{m}{m^*}v_\mathrm{F}^2 q^2\right)^{1/2}, \tag{2.27}$$

with the effective mass $m^* = m_\mathrm{e}\,(1 + 4\Delta^2/\lambda_{\text{el-ph}}\hbar^2\omega_{2k_\mathrm{F}}^2)$ and the dimensionless electron-phonon coupling constant $\lambda_{\text{el-ph}}$ defined in Ref. [70].[13]. The amplitude mode or *amplitudon* (Eq. 2.26) [7, 51, 52, 70, 115, 122–124], is associated with amplitude modulations of the CDW and PLD (see Fig. 2.9a (top) and Fig. 2.9b) and directly affects the electronic band gap as well as the atomic displacements. Accordingly, for a first-order Peierls transition, excitation of this mode beyond a certain threshold may transform the broken-symmetry into the high-symmetry state (Fig. 2.8a) [10, 123]. In fact, as can be seen from Eq. 2.26, this mode exhibits a finite excitation gap ($\sim \lambda\omega_{2k_\mathrm{F}}^2$) and a large effective mass around $q = 0$. Therefore, it can be considered a Raman-active optical mode [70]. Furthermore, it has been demonstrated that amplitude motion can be induced and controlled by instantaneous changes of the free energy landscape [51, 52], which will be discussed in detail in Sec. 2.2.2 and 6. The phase mode or *phason* (Eq. 2.27), on the other hand, corresponds to a sliding of the CDW relative to the underlying lattice (Fig. 2.9b). For an incommensurate CDW and in the absence of pinning potentials, this mode is gapless and has no

[13] In deriving Eq. 2.26 and 2.27, the coefficients a, b, c and d have been determined on the basis of a microscopic theory and the Fröhlich picture introduced in Sec. 2.1.3. For a thorough derivation of the above relations, the reader is referred to Refs.[70] and [121].

preferred phase (see Fig. 2.8a and Fig. 2.9a (bottom)). In commensurable systems, however, there often exists a finite number of energetically degenerated CDW ground states [125] for which the free energy exhibits a local minimum as a function of ϕ (Fig. 2.8b), leading to a finite gap for phase excitations [70]. Besides, phase modes have a non-vanishing dipole moment and thus are optically active [70].

Fluctuations and long-range order

Many of the above considerations imply that CDW phases naturally exhibit long-range order and *a priori* ignore the role of fluctuations. In this simplified mean-field scenario, below the finite temperature $T_\mathrm{c}^\mathrm{MF} := T_\mathrm{c}$ (see Eq. 2.11), a system undergoing a Peierls transition to a symmetry-broken ground state forms a stable, long-range order CDW or PLD, respectively. However, low-lying and eventually gapless fluctuation modes, i.e. phasons, are likely to destroy any long-range correlations. In other words, long-wavelength distortions of the CDW order cost almost no energy, and the associated fluctuation modes are thermally occupied for $T > 0$ K. A mathematical argument is given in Ref.[70] based on a calculation of the spatial mean value of the order parameter

$$\langle \Delta(x) \rangle \approx |\Delta_0| \, \langle \exp(\mathrm{i}\phi(x)) \rangle \approx |\Delta_0| \exp\left(-\frac{1}{2} \langle \phi^2(x) \rangle \right). \tag{2.28}$$

Representing $\langle \phi^2(x) \rangle$ in terms of its Fourier components $\phi_{q'}$ and using the equipartition theorem[14] gives

$$\langle \phi^2(x) \rangle = \frac{k_\mathrm{B} T}{\hbar v_\mathrm{F} n(\epsilon_\mathrm{F})} \int_0^{\pi/a} \mathrm{d}q' \, \frac{\exp(\mathrm{i}q'x)}{(q')^2}, \tag{2.29}$$

where $q' = q - 2k_\mathrm{F}$. The integral diverges, and as a consequence, the order parameter has a vanishing expectation value for $T > 0$ K. Beyond this, it has been shown by Mermin and Wagner [126–128] that there is no phase with spontaneous breaking of a continuous symmetry for $T > 0$ K in $d \leq 2$ dimensions[15]. Yet, in reality, there are many materials with highly anisotropic electronic and lattice structures that exhibit Peierls transitions into long-range ordered ground states at finite temperatures. This

[14] That is $n(\epsilon_\mathrm{F})(\hbar v_\mathrm{F} q')^2 \langle \phi_{q'}^2 \rangle = k_\mathrm{B} T$

[15] However, caution is advised in applying the Mermin-Wagner theorem to systems with *discrete* (translational) symmetry, such as a 1D chain of atoms.

raises the question of what limits the influence of fluctuations. Here, once again dimensionality plays an essential role. Specifically, the weak coupling of a quasi-1D system to its environment, e.g. by means of van der Waals forces between neighbouring atomic chains or couplings to the bulk substrate via phonons, leads to a three-dimensional character of fluctuations [70]. In some cases, this *dimensional crossover* [66, 129, 130] maintains the 1D nature of particular excitations of the system and thus allows for CDW formation and other phenomena in low-dimensional materials.

2.2 Exerting optical control over matter on ultrafast timescales

The preceding chapters featured an introduction to phase transitions in low-dimensional materials and the prominent example of the Peierls instability. While these phenomena are interesting in themselves and have been investigated extensively, at this point the question arises as to how such phase transformations can be induced and finally controlled. Typically, phase transitions involve pronounced changes in the electronic or lattice subsystems, which are driven by band structure effects or the coupling of electrons and phonons. Therefore, steering a system, e.g. from an insulating broken-symmetry to a metallic high-symmetry state requires control over the motion of electrons and nuclei via the populations of k-dependent electronic or vibrational states. In thermodynamic equilibrium, adiabatically changing state variables such as temperature beyond a critical threshold can be used to induce certain phase transitions. For example, in a Peierls insulator heated above T_c, electrons thermally excited above the band gap screen the electron-phonon interactions necessary to maintain the insulating state and thus promote the transition into the metallic phase [70]. In other words: The sample is heated quasi-adiabatically to a point where the high-symmetry configuration remains the only (or the minimum-energy) thermodynamically stable phase (see Landau picture in Sec. 2.1.4). However, regarding the efficient control of atomic scale dynamics, this has several disadvantages: First, by the nature of the Fermi-distribution $f = f(T)$, populating states well above E_F requires high temperatures and the transfer of a large amount of energy into the system. Second, thermally-induced atomic motion is incoherent, i.e. there is no fixed phase relation between oscillating atoms from different unit cells, which limits the degree of control. Third, as recently demonstrated, there are thermodynamically forbidden (or hidden) [36] as well as transient [9, 37, 131] states[16], which cannot be accessed or investigated by means of heat transfer.

As a consequence, the last four decades have seen a considerable effort to directly address key electronic or vibrational states in phase change materials and guide the motion of electrons and nuclei on their natural timescales, promising efficient control of phase transitions and switching times of the order of femto- or picoseconds [38, 41, 46, 132, 133]. However, this necessitates a significantly higher degree of

[16] Such transient states are typically metastable (with short lifetime) or otherwise characterised by a nonequilibrium between electronic and lattice subsystems [55, 112].

control and a completely new set of experimental tools. In this regard, the advent and rapid advancement of ultrafast optics [134, 135] provided chemistry and physics with just such a powerful toolbox. Most importantly, direct interactions of electrons and phonons with light enable an efficient energy transfer to targeted degrees of freedom via optical excitation. Furthermore, the use of high-power ultrashort light pulses [134] facilitates time-resolved investigations of electron [13, 136] or lattice dynamics [1, 22], transitions to nonequilibrium states of matter [32, 36, 37, 131], and the excitation of collective atomic motion [3, 7, 131, 136–140], e.g. coherent phonons. Herein, the high degree of control over field strength, carrier-envelope phase, central wavelength and frequency bandwidth in combination with sophisticated detection schemes drastically enhances the selectivity and sensitivity of experiments.

The next sections will elucidate on how ultrashort light pulses can be harnessed to exert control over solids. In particular, it will be discussed how light can be coupled to specific, decisive degrees of freedom, i.e. electronic states and coherent lattice modes. For the case of molecular reactions in the gas phase the feasibility of this approach has already been demonstrated by femtochemistry. Central ideas of (femto-)chemistry, such as the concept of the potential energy surface, can be adapted for the description of solid-state systems and are introduced below. Moreover, different optical excitation mechanisms for phase transitions will be discussed, with a focus on the generation of coherent phonons and their possible role in controlling phase transitions.

2.2.1 Potential energy surfaces

Just like chemical reactions, phase transitions in solids between initial and final states[17] involve the motion and interaction of electrons and nuclei. In order to understand and finally control such transition sequences, a meaningful model of the underlying dynamics is essential. In a universal approach, the dynamics of electrons and nuclei can be described by the time-dependent Schrödinger equation (see Eq. 2.5

[17] For a chemical reaction, initial and final state structures correspond to, e.g. reactant and product states.

in Sec. 2.1.3) and the Hamiltonian

$$\begin{aligned}\mathcal{H} &= T_\mathrm{e} + T_\mathrm{a} + V_\text{e-e} + V_\text{a-a} + V_\text{e-a} \\ &= -\sum_i^{N_\mathrm{e}} \frac{\hbar^2}{2m_\mathrm{e}} \nabla_i^2 - \sum_j^{N_\mathrm{a}} \frac{\hbar^2}{2M_j} \nabla_j^2 - \sum_i^{N_\mathrm{e}} \sum_j^{N_\mathrm{a}} \frac{Z_i e^2}{|\boldsymbol{r}_i - \boldsymbol{R}_j|} + \sum_{i<k}^{N_\mathrm{e}} \frac{e^2}{|\boldsymbol{r}_i - \boldsymbol{r}_k|} + \sum_{j<l}^{N_\mathrm{a}} \frac{Z_j Z_l e^2}{|\boldsymbol{R}_j - \boldsymbol{R}_l|}\end{aligned} \tag{2.30}$$

of a system with N_i (N_j) electrons (nuclei) at positions $\boldsymbol{r}_i$ ($\boldsymbol{R}_j$), masses m_e (M_j) and charges e (Z_j), interacting via Coulomb forces (see, e.g. Ref. [66, 141])[18]. Here, T_e and T_a are the kinetic energies of the electrons or nuclei, respectively, and $V_\text{e-e}$, $V_\text{a-a}$ as well as $V_\text{e-a}$ represent electron-electron, atom-atom, and electron-atom interactions. Obviously, a complete description of a transition in terms of the time-dependent coordinates of all particles is challenging, if not impossible, depending on the size of the system and the strength of interactions between its constituents[19]. However, assuming that nuclear motion occurs on a significantly longer time scale compared to electrons[20], the Hamiltonian given by Eq. 2.30 can be separated into an electronic and a quasi-stationary nuclear or lattice part [142]. This has important implications: First, in solving the Schrödinger equation for the electronic subsystem, nuclear motion can be neglected ($T_\mathrm{a} \approx 0$). The nuclei act on the electrons solely via $V_\text{a-a}$ and $V_\text{e-a}$, and the resulting electronic eigenstates depend only parametrically on the nuclear coordinates [143]. Second, nuclear motion is almost unaffected by the instantaneous positions of the electrons. However, the nuclei interact with an effective electronic potential. As a consequence, changes in the electronic states of the system also change the interaction potential in which the atoms move. This ansatz, formally known as *Born-Oppenheimer approximation* [142], forms the basis for the discussion of reactions and phase transitions using the concept of the potential energy surface (PES) [143, 144].

To calculate the PES for a specific reaction, the Schrödinger equation with only

[18] Neglecting spin degrees of freedom and associated contributions like spin-orbit coupling.

[19] Among others, the fourth term of Eq. 2.30 introduces electron-electron interactions, which pose a particular problem and lead to emergent phenomena, as discussed in Sec. 2.1.

[20] It is important to note that for materials with strong electron-phonon coupling this assumption is not necessarily justified. While such systems are likely feature non-adiabatic dynamics, adiabatic models may still yield qualitatively correct insights as well as an intuitive understanding of specific aspects.

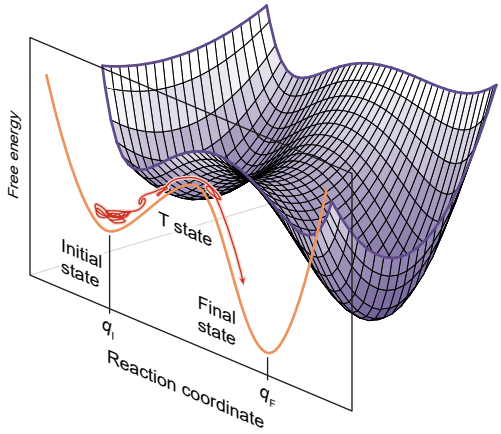

Figure 2.10: Exemplary scheme of the PES for a chemical reaction or phase transition and the path along the reaction (structural) coordinate. The initial (q_I) and the final state (q_F) of the transition are represented by local minima of the PES. The reaction coordinate corresponds to a slice through the PES along the lowest-energy path between q_I and q_F. "T state", Transition state; Red curve, exemplary trajectory of the system along q_i^*. From Ref. [147]. Adapted with permission from AAAS.

the electronic part of the Hamiltonian (Eq. 2.30) is solved for different nuclear configurations, e.g. by *ab initio* methods[21], yielding the electronic energy as a function of the relative atomic positions $\boldsymbol{q}_i$. Depending on the number of degrees of freedom, the result is a hyper-dimensional surface that relates the geometry of a molecule or solid-state system to its energy (typically the Gibbs G or Helmholtz free energy F is used). In many cases, the dimensionality of the PES can be reduced by considering only relevant degrees of freedom or by grouping different types of atomic motion. This way, the simplified PES often enables an intuitive understanding of reaction dynamics [43, 143, 145]. Due to its broad applicability, the PES model has become an essential concept of computational chemistry [143, 146].

Stationary points on the PES

A similar approach can be used to investigate phase transitions in solids. In fact, the Landau free energy landscape introduced in Sec. 2.1.4 represents the special case of a one-dimensional PES if the complex order parameter is associated with

[21] It should be noted that this statement does not do justice to the actual effort required to calculate PES of complex systems.

distortions of the atomic lattice or bond lengths. In analogy to chemical reactions, some transitions involve more than one independent order parameter or decisive degree of freedom, respectively. In such cases, a description of the transition in terms of a multidimensional PES often proves helpful. For this reason, we will shortly discuss central features of the concept, which provide insights into the dynamics of phase transitions. Given the PES, i.e. $F(\boldsymbol{q}_i)$, of a system undergoing a phase transition, stationary points reveal both initial and final state structures, as well as possible transition pathways. Specifically, points with

$$\frac{\partial F}{\partial \boldsymbol{q}_i} = 0 \qquad \text{and} \qquad \frac{\partial^2 F}{\partial \boldsymbol{q}_i^2} > 0 \;\; \forall\, \boldsymbol{q}_i, \tag{2.31}$$

correspond to (local) minima of the PES and indicate (meta-)stable structural configurations, whereas points for which

$$\frac{\partial F}{\partial \boldsymbol{q}_i} = 0; \qquad \text{and} \qquad \frac{\partial^2 F}{\partial \boldsymbol{q}_i^2} > 0 \;\; \forall\, \boldsymbol{q}_i \setminus \boldsymbol{q}_i^*, \tag{2.32}$$

are saddle points (with $\partial^2 E / \partial \boldsymbol{q}_i^{*2} < 0$). The coordinate $\boldsymbol{q}_i^*$ is called *reaction* or *structural coordinate* since it represents a slice through the PES along the lowest-energy path[22] between two minima [143]. The saddle point itself is commonly referred to as *transition state* or *transition structure* [43, 45, 145, 146, 148] and represents a maximum of F or *barrier* along the reaction coordinate. The rate of a reaction or transition across such a barrier is given by transition state theory [148, 149].

Vibrational motion and Polanyi rules

Up to this point the nuclei were assumed to be static. However, even at $T = 0\,\mathrm{K}$, zero-point energy leads to spatial fluctuations of the atoms around their equilibrium positions defined by the minimum of the PES (Eq. 2.31). With increasing temperature, incoherent atomic motion in this ground state potential influences thermodynamic properties and enables fluctuations between different states on the PES. Furthermore, ultrafast electronic excitation can induce coherent oscillations inside the ground state potential (see Sec. 2.2.2). To analyse structural dynamics within a PES model, movements of the system can be decomposed into normal modes

[22] Note that the lowest energy path is not necessarily a straight line.

associated with different degrees of freedom by diagonalisation of the Hessian

$$\boldsymbol{H} = \frac{\partial^2 F}{\partial \boldsymbol{q}_i \partial \boldsymbol{q}_j} = \begin{pmatrix} \frac{\partial^2 F}{\partial \boldsymbol{q}_1 \partial \boldsymbol{q}_1} & \frac{\partial^2 F}{\partial \boldsymbol{q}_1 \partial \boldsymbol{q}_2} & \cdots & \frac{\partial^2 F}{\partial \boldsymbol{q}_1 \partial \boldsymbol{q}_n} \\ \frac{\partial^2 F}{\partial \boldsymbol{q}_2 \partial \boldsymbol{q}_1} & \frac{\partial^2 F}{\partial \boldsymbol{q}_2 \partial \boldsymbol{q}_2} & \cdots & \frac{\partial^2 F}{\partial \boldsymbol{q}_2 \partial \boldsymbol{q}_n} \\ \vdots & \vdots & \ddots & \vdots \\ \frac{\partial^2 F}{\partial \boldsymbol{q}_n \partial \boldsymbol{q}_1} & \frac{\partial^2 F}{\partial \boldsymbol{q}_n \partial \boldsymbol{q}_2} & \cdots & \frac{\partial^2 F}{\partial \boldsymbol{q}_n \partial \boldsymbol{q}_n} \end{pmatrix} = \mathrm{Q} \begin{pmatrix} k_1 & 0 & \cdots & 0 \\ 0 & k_2 & \cdots & 0 \\ \vdots & \vdots & \ddots & 0 \\ 0 & 0 & \cdots & k_n \end{pmatrix} \mathrm{Q}^{-1}, \tag{2.33}$$

with $i, j = (1, ..., n)$, the mode-specific force-constants k_i and $\mathrm{Q} = \boldsymbol{q}_{ij}$ [143]. For small amplitudes, vibrational motion inside the ground state potential is accurately described by an harmonic ansatz with $F_{\mathrm{local}}(\boldsymbol{q}_i) \sim 1/2\, k_i q_i^2$. However, for larger amplitudes and especially for atomic displacements towards the transition state, the vanishing curvature[23] $\partial^2 F / \partial q_i^* \partial q_i^*$ results in a reduced force constant k_i^*. Consequently, the frequency $f = (1/2\pi c)\sqrt{k_i^*/M_{\mathrm{a}}}$ of the associated mode softens along the reaction coordinate. Perhaps remarkably, close to a transition the PES model thus qualitatively provides the same result as the exclusively quantum mechanical treatment of the Peierls transition in Sec. 2.1.3.

The question arises to what extent such atomic vibrations can influence transitions, e.g. regarding their efficiency. In chemistry, the role of vibrational motion in determining the outcome of chemical reactions has been identified by J.C. Polanyi and co-workers [43, 44, 145, 146] by studying a number of prototypical reactions of type $\mathrm{AB} + \mathrm{C} \rightarrow \mathrm{A} + \mathrm{BC}$. Summarising their main findings, the impact of atomic vibrations (i.e. time-dependent modulations of bond lengths, e.g. r_{AB}) depends on the location of the transition state relative to reactant and product states (see Fig. 2.11). Herein, a distinction is made between *early-barrier* and *late-barrier* reactions. For an early-barrier (Fig. 2.11a), the transition structure resembles the reactants. In this case, translational motion directly towards the transition state promotes the reaction, whereas vibrational motion in the initial state may hinders it, even for amplitudes considerably larger than the barrier height [43, 145, 146]. Such early-barrier reactions are typically exothermic [44]. For a late-barrier reaction (Fig. 2.11b), on the other hand, the roles of translational and vibrational motion are reversed. Moreover, the reaction rate becomes a function of the vibrational phase of the system (compare red and violet trajectories in Fig. 2.11b). Such reactions are usually endothermic [44]. Hence, atomic vibrations play a key role in

[23] Or in other words: the anharmonicity of the potential.

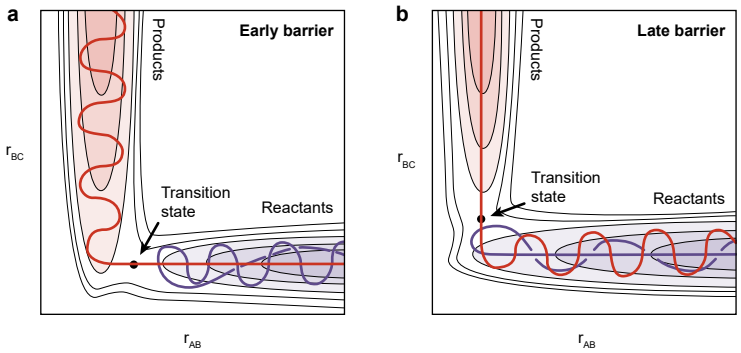

Figure 2.11: Role of vibrational motion in early and late-barrier reactions. **a**, For an early-barrier reaction of type $AB + C \rightarrow A + BC$ the transition state is "reactant-like". Translational motion of the AB-complex promotes the transition (red trajectory), whereas vibrational excitation hinders it (violet trajectory). **b**, For a late-barrier reaction, the transition state resembles the products and vibrational motion facilitates the reaction, depending on, e.g. the vibrational phase (compare red and violet trajectories). Adapted from Ref. [43].

chemical reactions, depending on the morphology of the PES. Furthermore, seminal works in femtochemistry have demonstrated that coherent vibrational motion can even be harnessed to exert control over specific reactions (see Sec. 2.2.3). Whether such concepts also remain valid for phase transitions in solids remains a largely open question that will be dealt with in this work.

2.2.2 Coupling of light to decisive degrees of freedom

The previous chapters have highlighted the role of vibrational motion for reactions and phase transitions in molecules or low-dimensional solids, respectively. Here, the amplitudes of lattice vibrations and the evolution of the order parameter in structural transitions were mainly linked to temperature. At the same time, it has already been indicated in Sec. 2.2 that optical excitation of electrons and phonons promises a significantly higher degree of control over matter. Hence, the following sections are concerned with the question of how light can be used to excite and manipulate structural degrees of freedom. Besides, although Landau theory and the concept of the PES enable a rather intuitive description of symmetry-breaking phase transitions and the structural changes therein, it is important to understand how these models are linked to the underlying microscopic dynamics in the electronic and lattice subsystems. This concerns in particular the impact of optically-excited

electronic states on the PES and ultimately on the atomic motion during phase transitions, which will be discussed in the following.

Interactions of light with electrons and phonons

The interactions of light with electrons and phonons offers various routes to control atomic motion on ultrafast timescales. Two fundamental types of coupling will be explained below.

First, light may directly interact with lattice modes via absorption (i.e. resonant coupling to certain vibrational states), or by means of *Rayleigh* and *Raman scattering* (see Fig. 2.12). Here, we briefly discuss each of these channels, highlighting the coupling conditions which are mainly determined by energy momentum conservation and symmetry. In the case of resonant coupling, the energy $\hbar\omega_\gamma$ of an incident photon matches the energy $\hbar\omega_p$ of a particular phonon. Absorption of the photon excites the system to a higher vibrational state. Since typical phonon energies range between $1 - 100$ meV, the corresponding optical frequencies are in the terahertz (THz), far infrared (FIR) or mid infrared (MIR) regime. Furthermore, as can be shown in a classical wave picture, this process restricts to modes with a non-vanishing dipole moment associated with the atomic displacement along the phonon coordinate [150]. Modes of this type are called *IR-active*. Because of energy-momentum conservation, resonant coupling occurs only for IR-active phonons with $\boldsymbol{q} \approx 0$, i.e. close to the Γ point [150].

Raman scattering, on the other hand, affects modes for which the polarisability $\boldsymbol{\alpha}$ changes as a function of the atomic displacement $\delta\boldsymbol{q}$ [151]. Using symmetry arguments, it can be shown that modes are typically either IR or Raman active [152]. Generally, the polarisability describes the response of a charge distribution to local electric field $\boldsymbol{E}$ in terms of the induced dipole moment

$$\boldsymbol{p} = \boldsymbol{\alpha} \cdot \boldsymbol{E}. \tag{2.34}$$

For small displacements, $\boldsymbol{p}$ can be expanded to first order in powers of $\delta\boldsymbol{q}$, yielding

$$\boldsymbol{p} \approx \boldsymbol{\alpha}_0 \boldsymbol{E} + \left(\frac{\partial \boldsymbol{\alpha}}{\partial(\delta \boldsymbol{q})} \right) \delta\boldsymbol{q} \cdot \boldsymbol{E} + ... \tag{2.35}$$

The term $(\partial\boldsymbol{\alpha}/\partial(\delta\boldsymbol{q}))$ is also known as the *Raman tensor* [151, 152]. Assuming the

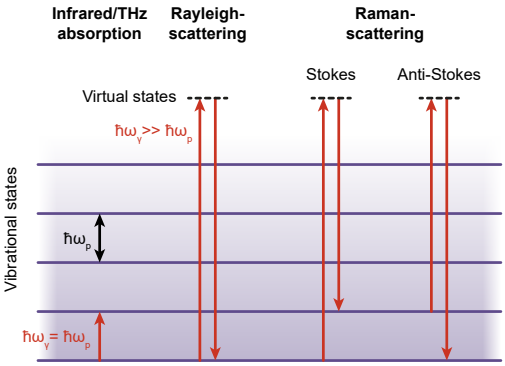

Figure 2.12: Some elementary mechanisms for the coupling of light and phonons, including resonant coupling (absorption), Rayleigh- as well as Raman scattering. Note that only first-order processes have been considered. Couplings of light with more than one phonon are thus omitted.

time-dependent displacement and electric field are given by $\delta\boldsymbol{q}(t) = \delta\boldsymbol{q}_0 \cos(\omega_\mathrm{p} t)$ or $\boldsymbol{E}(t) = \boldsymbol{E}_0 \cos(\omega_\gamma t)$, respectively, the above relation can be rewritten in terms of

$$\boldsymbol{p} \approx \boldsymbol{\alpha}_0 \boldsymbol{E} + \frac{\delta\boldsymbol{q}_0 \, \boldsymbol{E}_0}{2} \left(\frac{\partial \boldsymbol{\alpha}}{\partial(\delta\boldsymbol{q})} \right) \left[\cos((\omega_\gamma + \omega_\mathrm{p})t) + \cos((\omega_\gamma - \omega_\mathrm{p})t) \right] . \tag{2.36}$$

Thus, for $\partial\boldsymbol{\alpha}/\partial(\delta\boldsymbol{q}) \neq 0$, the light field generated by the oscillating dipole exhibits frequency sidebands at $\omega_\gamma \pm \omega_\mathrm{p}$ corresponding to Stokes- and anti-Stokes scattering (see also Fig. 2.12). Remarkably, $\boldsymbol{p}$ is a function of the derivative of $\boldsymbol{\alpha}$ with respect to the time-dependent atomic displacement $\delta\boldsymbol{q} = \delta\boldsymbol{q}(t)$. The consequences of this periodically modulated dipole strength for the optical properties of materials on ultrashort time scales will be discussed in Sec. 2.3.4. Moreover, it is important to note that Stokes- and anti-Stokes as well as Rayleigh scattering involve virtual excited states and therefore do not require energy matching between photons and phonons. As a consequence, both effects are observed over a broad frequency range including the visible part of the electromagnetic spectrum, and can be harnessed to investigate the vibrational modes of molecules as well as solids and their surfaces.

Second, an indirect interaction of light with the lattice is enabled by optical excitation of electronic states and a subsequent energy transfer to vibrational modes via electron-phonon coupling. Here, the absorption of photons induces vertical transitions, e.g. above a band gap[24], in the electronic band structure, creating excited carriers in the conduction band as well as holes in the valence band (see Fig. 2.13a and d). Relaxation of electrons (holes) then typically leads to the population of

[24]Note that also resonant ($\hbar\omega_\gamma = \Delta E_\mathrm{gap}$) or sub-bandgap ($\hbar\omega_\gamma < \Delta E_\mathrm{gap}$) optical excitation can be used to drive structural dynamics [58, 153].

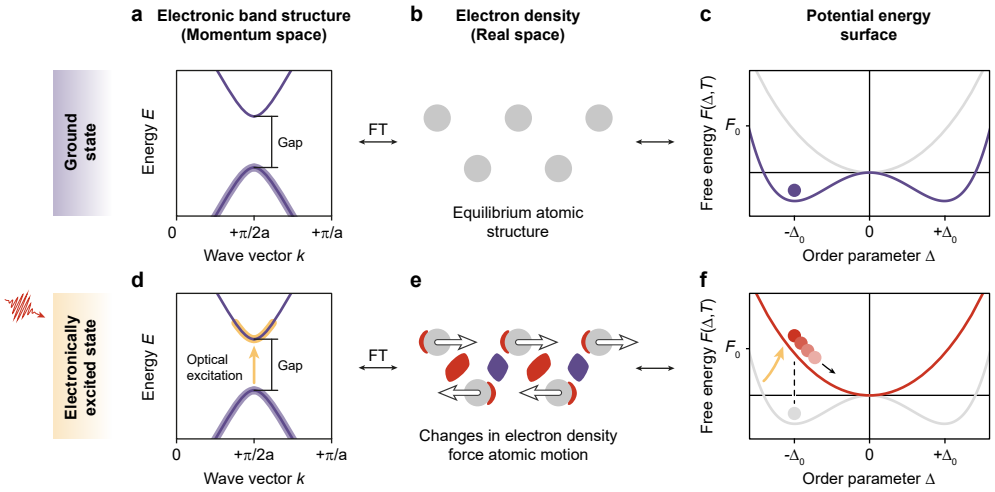

Figure 2.13: Connection of k-space electronic excitation and r-space structural dynamics. Electronic band structure scheme (**a**,**c**), atomic structure (**b**,**d**) and Landau potential energy surface (**c**,**f**) before (top row) and after (bottom row) electronic excitation. Electronic excitation, yellow arrows and states; relative changes in electron density (panel **e**), red (increase) and violet (decrease); white arrows indicate the resulting motion of atoms. FT, Fourier transform.

states located at the conduction (valence) band edge. But how exactly does the excitation of electrons affect atomic motion? To answer this question, we first have to understand how electronic transitions at specific positions in momentum space are reflected in the real-space distribution of charges. In this context, Puschnig *et al.* [154] have shown that atomic orbitals and the band structure of molecules and solids are related by

$$|\mathcal{F}\psi_{\mathrm{i}}(\boldsymbol{k})| \sim \frac{\sqrt{I_{\mathrm{i}}(\theta,\phi)}}{|\boldsymbol{A}\cdot\boldsymbol{k}|}, \tag{2.37}$$

with $\mathcal{F}\psi_{\mathrm{i}}(\boldsymbol{k})$ being the Fourier transform of the real-space electronic wave function, $I_{\mathrm{i}}(\theta,\phi)$ the photocurrent from a particular state i measured in photoelectron spectroscopy and $\boldsymbol{A}$ the vector potential of the light used for excitation. It follows that both inter-atomic bonds and the real-space electron density $n(\boldsymbol{r}) \sim |\psi(\boldsymbol{r})|^2$ can be reconstructed from the electronic band structure by a Fourier transform (and vice versa) [11, 154]. Hence, electronic excitations in momentum space correspond to a redistribution of charges in real-space, resulting in net forces on the positively charge nuclei and a shift of equilibrium coordinates (compare Fig. 2.13b and e). From a more chemical point of view, the generation of excited electrons or holes either weak-

ens or strengthens specific bonds. Furthermore, Zeiger *et al.* [42] have demonstrated that the effect of optically-induced electronic excitation on symmetry-breaking phase transitions can be described in a Landau free energy model by including an additional quadratic potential that depends linearly on the density n of excited carriers:

$$F(\Delta, T, n) = F_0 + \frac{1}{2}a(T)|\Delta|^2 + \frac{1}{4}b(T)|\Delta|^4 + (c_1 + c_2|\Delta|^2)n + \mathcal{O}(|\Delta|^4). \quad (2.38)$$

Here, the term $c_1 n$ corresponds to electrons transferred across the band gap and $c_2|\Delta|^2 n$ to the modulation of that gap by the displacement $|\Delta|$ [42]. In this picture, electronic excitation reshapes the free energy landscape analogous to an increase in temperature (Fig. 2.13c and f). Today, *ab initio* methods enable the calculation of multidimensional PES for arbitrary electronic excitations in a given band structure, providing insights into vibrational modes of excited states and trajectories on the PES after optical excitation [10, 155].

Generation of coherent phonons

Atomic vibrations can be used to steer chemical reactions on ultrashort timescales [38] and are therefore also likely to play a key role in controlling solid-state phase transitions. However, in contrast to reactions of single molecules, macroscopic phase transitions in solids require the synchronised motion of atoms across hundreds and thousands of unit cells. Therefore, we now turn to the question of how direct and indirect interactions of light and lattice can be used to excite collective atomic motion in solids, i.e. coherent phonons. In thermodynamic equilibrium, there is no fixed phase relation between atomic oscillations in different unit cells and the population of phonon modes is determined by the *Bose-Einstein distribution* [64, 156]. In contrast, a coherent phonon represents a nonequilibrium state of the lattice that is not described by classical thermodynamics. Here, atoms of distinct unit cells oscillate in-phase along a specific structural coordinate and the associated phonon mode is macroscopically occupied [150]. Two important approaches to generating coherent phonons are presented below.

Impulsive stimulated Raman scattering The direct coupling of light to Raman-active phonon modes forms the basis of impulsive stimulated Raman scattering (ISRS) [157]. Whereas Raman scattering of a single ("pump") photon with energy $\hbar\omega_{\gamma,\mathrm{p}}$ occurs spontaneously, the presence of a second ("Stokes") photon of energy

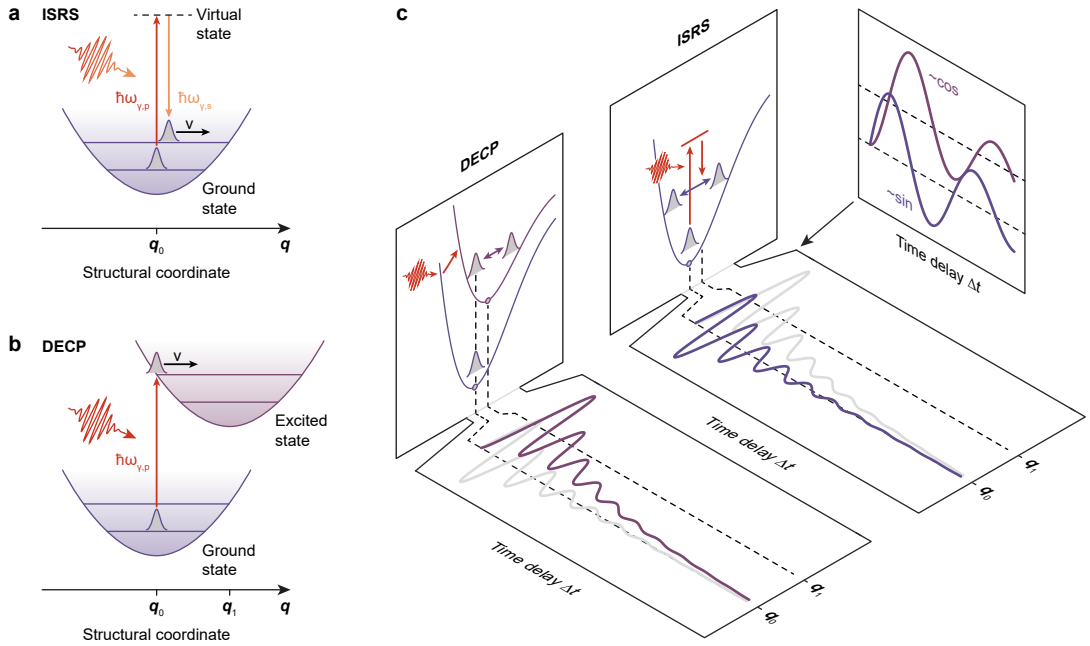

Figure 2.14: Impulsive stimulated Raman scattering (ISRS) and displacive excitation of coherent phonons (DECP). **a**,**b**, Schematic of ISRS (**a**) and DECP (**b**) mechanisms. v, velocity of the wave packet motion. **c**, Comparison of coherent oscillations induced by both mechanisms. Notice the distinct initial phases and the shift of the equilibrium coordinate in the case of DECP. The latter results from the relaxation of the PES on a fs-ps time scale linked to the decay of electronic excitations. Panels **a** and **b** adopted from Ref. [159].

$\hbar\omega_{\gamma,\mathrm{s}}$ significantly enhances the probability for Raman scattering, if $\hbar\omega_{\gamma,\mathrm{p}} - \hbar\omega_{\gamma,\mathrm{s}} = \hbar\omega_p$, the energy of a phonon (stimulated Raman scattering or SRS). ISRS is facilitated by ultrashort laser pulses with pulse durations short compared with the phonon oscillation period. The spectral bandwidth of the pulse then exceeds the vibrational frequency [157, 158] and thus comprises both pump and Stokes frequency components. The resulting quasi-instantaneous transfer of momentum to the lattice forces a sine-like oscillation of atoms within the ground state potential and along the mode coordinates (see Fig. 2.14a and c). Due to the high spatial and temporal coherence of the laser light used for excitation, the induced atomic motion is also coherent, i.e. all atoms within the illuminated volume oscillate collectively with the same initial phase.

Displacive excitation of coherent phonons As discussed above, the population of electronic states determines the shape of the PES. This principle can

be used to excite coherent phonons by means of indirect interactions. Specifically, photo-excitation of electrons and holes by ultrashort optical pulses induces transient changes of the PES on timescales short compared with lattice motion[25] [10, 42, 140]. Thus, the atoms are displaced with respect to the new quasi-equilibrium coordinate of the PES and start to oscillate inside the excited state potential (see Fig. 2.14b and c). In a real-space picture, ultrafast charge redistribution forces atomic motion via the Coulomb interactions. This generation mechanism is commonly referred to as displacive excitation of coherent phonons (DECP). As opposed to ISRS, the initial vibrational phase of DECP-driven phonons is cosine-like (see inset in Fig. 2.14c). Furthermore, DECP affects the PES, which is not the case for ISRS (neglecting optical absorption of pump and Stokes pulses). As a consequence, for high excitation densities, the ground states in phase change materials may be transformed into the high-symmetry state, which prohibits the observation of phonons of the symmetry-broken structure.

In the case of DECP, coherent atomic motion is governed by the timescales of electronic relaxation and phonon coherence: Whereas the population decay in the excited electronic states causes a continuous shift of the quasi-equilibrium coordinate, anharmonic coupling and the energy transfer to other phonon modes leads to a damping of the oscillation amplitude[26]. For ISRS, on the other hand, only the latter effect has to be considered (compare time-dependent amplitudes in Fig. 2.14c). Both mechanisms enable the control over vibrational amplitudes, e.g. by means of optical excitation with synthesized light fields and/or timed pulse sequences, as demonstrated by a number of seminal works, which are discussed in the following section.

2.2.3 Coherent and mode-selective control schemes

Exploiting the optical excitation mechanisms introduced above, a variety of techniques have been developed to exert control over atomic-scale dynamics in molecules and solids on their intrinsic timescales. As a general principle, these approaches harness optical manipulation of electronic or vibrational coherences to steer a system from its initial to one or more final states. The first proof-of-principle studies for

[25] Note that in contrast to ISRS, the DECP process requires the absorption of the pump pulse.
[26] In principle, it is possible that phonon coherences outlast electronic excitation.

some of these concepts were conceived in the early 1980s by A.H. Zewail and co-workers in femtochemistry [38, 40, 132]. The following paragraph provides a brief overview of the vast research field of coherent control. For further information, the reader is referred to Refs. [38, 41, 46, 132, 137].

Perhaps surprisingly, there seems to be no uniform definition of the term "coherent control" in the relevant literature. However, a basic distinction is made between at least three different approaches: First, in the *Brumer-Shapiro scheme*, coherent control means "coherently driving a state with phase coherence through multiple, coherent, indistinguishable, optical excitation routes to the same final state, [which] allows for the possibility of control" [46]. Here, constructive or destructive quantum interference of coherent excitation pathways between initial and final states are harnessed to influence the outcome of reactions (Fig. 2.15b). This ansatz exerts control in the frequency-domain and exploits the dependence of different pathways on the phase of the optical excitation field. A model example is given by the work of Zhu *et al.* [160], who exploited the interference of one- and three-photon absorption pathways to control the product distribution in the photo-dissociation of hydrogen iodide.

Second, the complementary *Tannor-Rice* or *pump-dump scheme* is based on the propagation of localised wave packets. In this scenario, a first optical pulse transfers a wave packet from the reactant or educt state of the initial PES to an excited PES, where it evolves until a properly timed second pulse causes stimulated emission back to a product state of the original PES (see (Fig. 2.15a and, e.g. Ref. [47, 48, 133, 161]). Herein, the mutual time delay between the two pulses controls the product state population. Consequently, this approach is commonly referred to as control in the time-domain [46].

Third, mode-selective excitation is based on the idea of matching the frequency of optical excitation(s) to the frequencies of targeted degrees of freedom, resulting in the breaking of associated bonds[27]. Thus, for this type of excitation "molecules react as if [a] particular degree of freedom was at a very high temperature whereas the rest of the molecular degrees of freedom are cold" [162]. Mode-selectivity is realised either by resonant excitation with THz or MIR driving fields [3, 131, 139, 163], or by

[27] In fact, this concept goes back to the very beginnings of femtochemistry, but was abandoned in favour of Brumer-Shapiro and Tannor-Rice approaches after doubts arose about its feasibility [133]

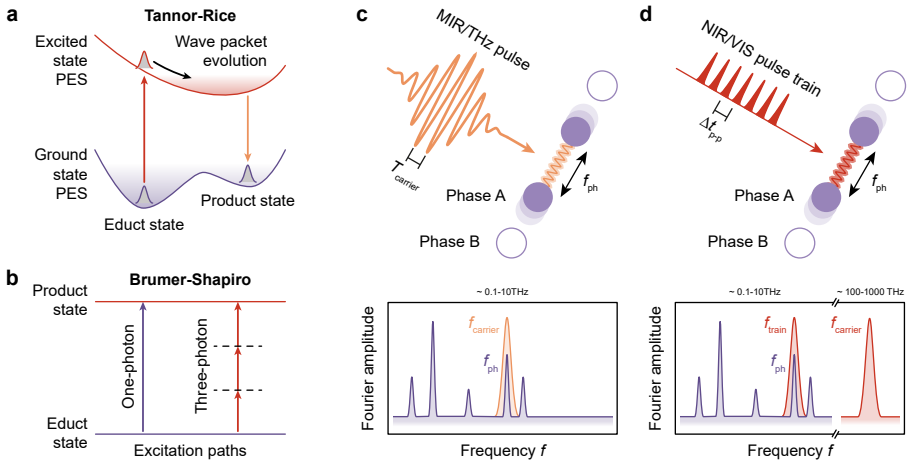

Figure 2.15: Coherent control schemes. **a**, Tannor-Rice (time-domain) control scheme based on wavepacket evolution on an excited state PES. Optical excitations, red and orange arrows. **b**, Brumer-Shapiro (frequency-domain) control scheme based on quantum interference between distinct excitation pathways. Virtual intermediate states, dashed black lines. **c**, Control via mode-selective excitation using resonant absorption. The carrier frequency of light is tuned to the frequency of decisive modes. **d**, Mode-selective excitation with pulse sequences. Here, the inter-pulse delay is matched to the desired mode.

optical pulse sequences (Fig. 2.15c and d) [61, 164, 165]. Although mode-selective excitation is not regarded by some as coherent control in the strict sense [46], it is often referred to as such, e.g. in the context of coherent phonon amplitudes controlled by pulse sequences [164]. Selective excitation has proven a powerful tool to control the amplitude of vibrational modes [3, 51, 52, 131, 139, 163, 164], chemical reactions [39] as well as many intriguing condensed matter phenomena, such as electronic phase transitions [139] or high-T_c superconductivity [3–5]. However, a major obstacle to mode-selective excitation and coherent control in general is the rapid redistribution of locally deposited energy to other degrees of freedom, especially for complex systems beyond simple molecules [133]. Whether intrinsic coherences in such systems can be used to influence the outcome of, e.g. phase transitions in low-dimensional systems, has still to be investigated experimentally in more detail. Generally, the application of the above control schemes to structural phase transitions requires not only sophisticated optical excitation but also ultrafast structure-sensitive probes – in our case low-energy electrons. Therefore, the next section will discuss aspects of structural analysis and the possible signatures of ultrafast structural changes.

2.3 Structural analysis and spectroscopy of surfaces

The reduced dimensionality and broken symmetry of a surface often leads to significant changes in the electronic, magnetic or lattice structure within the first atomic layers, and thus to the emergence of novel physical and chemical properties compared with the bulk. In fact, in many cases it is the surface that determines the functionality of materials, as exemplified by heterogeneous catalysis [166], topological insulators [167] or low-dimensional systems [101]. Therefore, detailed knowledge about the structure of solid-state surfaces is highly desirable, both concerning long-range order and atomic-scale inhomogeneities. In this context, real-space imaging techniques such as scanning tunneling microscopy (STM) [168] or atomic force microscopy (AFM) [169] are perfectly suited to study the local electronic, spin, or lattice[28] structure of surfaces with sub-nm resolution (see Fig. 2.16). Surface-sensitive diffraction techniques, on the other hand, are particularly useful to investigate the symmetry, as well as the periodic structure and long-range order of materials, since for single crystals the coherent superposition of waves scattered from hundreds or thousands of unit cells results in sharp diffraction spots and a nonlinear signal gain [111]. Photoemission [170] and optical spectroscopy [171–173] provide complementary insights into the band structure and the corresponding optical properties of solids and their surfaces. While each of these techniques has made important contributions to the understanding of surface phenomena, it is often only a combination of several complementary methods that makes it possible to draw a comprehensive picture of processes on surfaces. Figure 2.16 gives an overview of a number of relevant techniques for the investigation of surfaces employing electrons as probes to study electronic and lattice subsystems.

With the advent of ultrafast lasers [134, 173] and the subsequent realisation of time-resolved imaging [22], diffraction [9, 17, 18, 174, 175] and spectroscopy [134, 176], nonequilibrium dynamics, e.g. surface-specific structural phase transitions, have become accessible. Observing and finally controlling such lattice transformations on ultrafast timescales requires both high sensitivity to surface structure, and fs-ps temporal resolution. For this purpose, our group has recently developed

[28] Note that STM measures the local density of states (LDOS) which often reflects the atomic positions within the unit cell. However, a reliable determination of the lattice structure is only possible if the image is not distorted by particular electronic states [111].

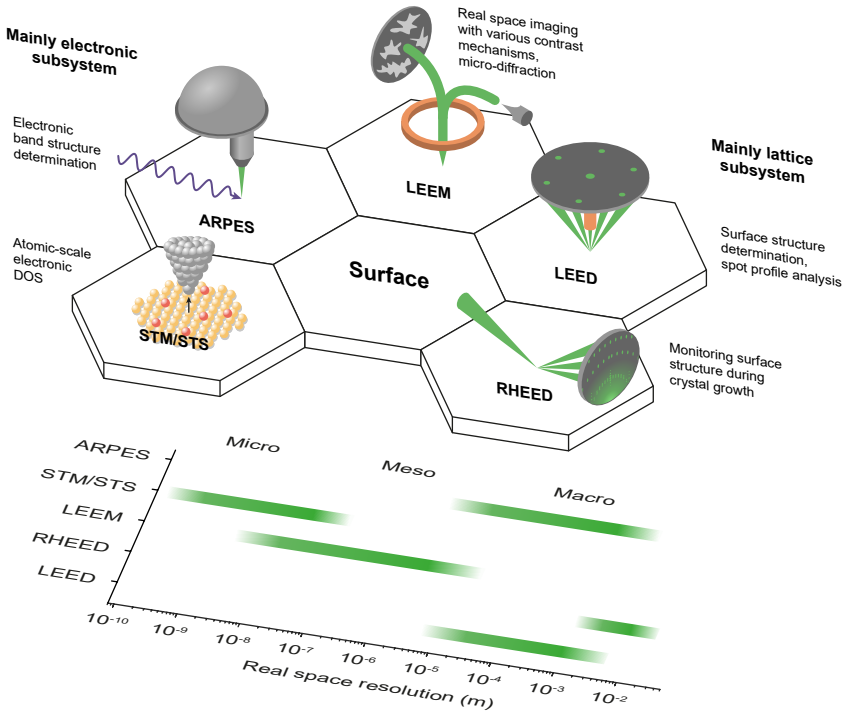

Figure 2.16: Surface structure probed by electrons. Overview of surface-sensitive experimental methods using electrons as probes of electronic and lattice structure in real and k-space. Note that although STM or ARPES (LEEM, LEED, RHEED) are primarily sensitive to the electronic (lattice) structure, information about the other subsystem can often be derived indirectly due to the couplings of electrons and nuclei. DOS, density of states; STS, scanning tunneling spectrosopy; LEEM, low-energy microscopy; RHEED, reflection high-energy electron diffraction.

ultrafast low-energy electron diffraction (ULEED) in transmission [17] and reflection [18, 112] geometry, which will be introduced in detail in Sec. 3. Within this work, ULEED has been harnessed to study the metal-insulator structural phase transition in quasi-1D atomic indium wires on the Si(111) surface. In order to extract information about the ultrafast structural changes during such a transition from the ULEED data, a solid understanding of the standard LEED technique and the underlying scattering theory is required. The following sections therefore introduce the reader to basic concepts of LEED and explain the contributions of different structural changes and dynamical effects to the diffraction patterns. Furthermore, optical pump-probe spectroscopy (OPP) has been used as a complementary probe to investigate the ultrafast optical response of the In/Si(111) surface [101, 177]. The basics of this method are therefore also briefly discussed.

2.3.1 Low-energy electron diffraction

Diffraction is a powerful tool for investigating atomic-scale structure, prominent examples being serial femtosecond crystallography [178], X-ray or LEED structure determination [179–181]. As a principle, the interaction of the probe (either light or matter waves) with the electronic, structural or spin degrees of freedom of the sample leads to a characteristic spatial distribution of scattered intensity via energy or momentum exchange (see Sec. 2.3.2). The resulting diffraction pattern can be used to identify, e.g. the lattice symmetry or the atomic coordinates within the unit cell. In the case of bulk solids, structure determination has been successfully carried out for more than a century (1913) [182]. However, solid-state surfaces remained largely inaccessible until the 1970s [111], when improvements in vacuum technology, dynamical scattering theory [180] and computational methods facilitated the use of low-energy electrons as structural probes. Today, low-energy electron diffraction (LEED) is a standard technique for qualitative and quantitative surface analysis and many other disciplines, including surface chemistry and materials science [111, 179, 183–185]. In LEED, the diffraction pattern of low-energy electrons back-scattered from a sample is analysed to gain insight into its surface structure (see Fig. 2.17a and Sec. 2.3.1). Therefore, we now turn to the question of why slow electrons are suitable for studying surfaces.

The wave nature of matter is at the heart of many diffraction techniques using either electrons [111, 179, 186], neutrons [187], Hydrogen [188], Helium [189–191] or nobles gas atoms [192] as probes. In particular, the de Broglie wavelength $\lambda_\mathrm{d} = h/p$ of a probing particle has to be smaller or comparable to the lattice constant of a crystal in order to resolve its structure in a diffraction experiment [111, 156, 180]. Here, h is the Planck constant, and p is the particle's momentum. In the case of electrons, $\lambda_\mathrm{d} = \sqrt{150.4/E_\mathrm{kin}[\mathrm{eV}]}$ Å, where E_kin is the kinetic energy due to acceleration in an electrostatic potential U. Hence, for an electron with kinetic energy $E_\mathrm{kin} = 100$ eV, the de Broglie wavelength is as small as 3.87 Å, which is of the same order of magnitude as most lattice constants in solids and thus allows for diffraction. As a consequence, scattering occurs at large angles, improving the momentum resolution in diffraction experiments.

Penetrating into the solid, electrons can be scattered either elastically ($\Delta E_\mathrm{kin} = 0$) or inelastically ($\Delta E_\mathrm{kin} \neq 0$). A schematic kinetic energy spectrum of electrons back-

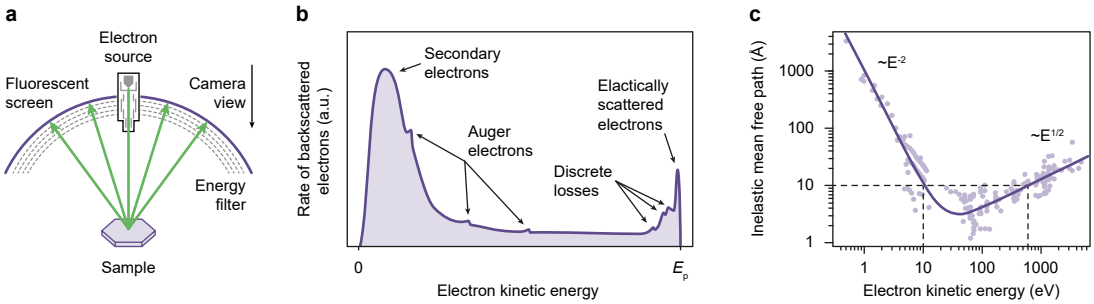

Figure 2.17: Basic principles of low-energy electron diffration. **a**, Schematic of a standard LEED apparatus. The electrons are emitted from a tip-shaped cathode. A Wehnelt cylinder is used to control the electron beam intensity while and electronstatic einzel lens is used for collimation. The electrons hit the sample surface and are back-scattered towards the fluorescent screen (detection). Retarding grids can be used to filter out inelastically scattered electrons. The resulting LEED pattern on the phosphor screen is recorded by a camera. The whole LEED setup is operated under ultrahigh vacuum (UHV) conditions. **b**, Prototypical electron kinetic energy spectrum of back-scattered electrons highlighting the contributions of elastic and discrete inelastic scattering, auger electrons, as well as secondary electrons. Adapted from Ref. [111]. **c**, Inelastic mean free path (IMFP) as a function of the electron kinetic energy. The universal curve exhibits a minimum between 10 and 100 eV. Adapted from Ref. [111].

scattered from a sample surface is shown in Fig. 2.17b. For elastic scattering, there exists a well-defined phase relation between incident and outgoing electrons. Since the scattering potential formed by the lattice atoms determines the relative phase, elastic contributions to the diffraction pattern, i.e the sharp diffraction peaks, contain information about the symmetry and atomic structure (see Sec. 2.3.2). Inelastically scattered electrons, on the other hand, transfer part of their initial energy to, e.g. structural degrees of freedom, such that there is no clear phase relation. These electrons mostly contribute to the diffuse background of the diffraction pattern (see Sec. 2.3.3), providing insights into the population of lattice modes and other energy relaxation pathways.

The high surface-sensitivity of low-energy electrons stems from their large scattering cross section, leading to typical inelastic mean free paths (IMFP)[29] of less than a few ångstroms. Consequently, only electrons back-scattered within the first few atomic layers contribute significantly to the diffraction signal. The energy-

[29]That is, the distance after which the $1/e^{th}$ fraction of the electrons still exhibits the initial energy $E_{kin,i}$ [193]

dependent IMFP is largely independent of the atomic number of the target and can thus be described in terms of a *universal curve*, which exhibits a global minimum between 10 and 100 eV (see Fig. 2.17c)[30]. We note that within this energy range, electrons simultaneously exhibit the optimum wavelength for diffraction and highest surface sensitivity. While the large scattering cross section of electrons in this energy range facilitates surface-sensitive measurements, it also enhances the probability of multiple scattering events, which complicates precise structure determination (see Refs. [180] and [111] and Sec. 2.3.2 for details). However, in many cases, important properties of the surface layer, e.g. its symmetry, can be readily extracted from the LEED pattern itself.

Another advantage of harnessing electrons as probes is that they can be easily generated, accelerated, deflected or collimated via electrostatic fields. For comparison, in the case of X-ray radiation the production of suitable optics is still challenging, whereas Helium or neutron sources are technically much more complex than most electron guns. On the other hand, slow electrons in particular are susceptible to stray electric or magnetic fields, so that precautions must be taken on the experimental side, e.g. by using non-magnetic materials. Overall, LEED has demonstrated to be capable of studying surface phenomena, such as reconstructions, molecular adsorbates or defect densities with high precision [111, 179, 183, 184]. In the following, we will take a closer look at how the diffraction pattern forms in LEED and what information can be extracted from it. With regard to the ULEED system presented in Sec. 3, these theoretical insights will enable the analysis of nonequilibrium phenomena, such as photoinduced structural phase transtions.

2.3.2 Scattering theory

Within the framework of scattering theory, the interactions of quantum mechanical particles such as photons or electrons with matter are generally described by the Schrödinger equation or equivalent representations, e.g. the Lippmann-Schwinger equation [194]. A main objective of scattering theory is to calculate the *scattering*

[30] For lowest energies, inelastic scattering of electrons is dominated by the generation of electron hole pairs [111]. Specifically, the probability for pair formation is proportional to the product of the available energy range of occupied ($\sim E$) and unoccupied states ($\sim E$), causing an increase of the IMFP $\sim E^2$. For energies higher than 100 eV, the IMFP is proportional to $\sqrt{E}$ due to plasmon excitations [111].

amplitude $|f_s(\boldsymbol{k}_0, \boldsymbol{k})|^2$, that is, the probability amplitude for a particle with initial momentum $\boldsymbol{k}_0$ to exhibit the final momentum $\boldsymbol{k}$ after interaction with a scattering potential $V_{\text{int}}(\boldsymbol{x})$.[31] If a particle interacts only weakly with the target, its final state after scattering can be expanded to first order in the powers of $V_{\text{int}}(\boldsymbol{x})$. This corresponds to first-order perturbation theory and gives the *Born approximation* for the scattering amplitude [194]

$$f_s(\boldsymbol{k}_0, \boldsymbol{k}) \sim -\frac{m}{2\pi} \int \mathrm{d}^3x \; \mathrm{e}^{-\mathrm{i}(\boldsymbol{k}_0 - \boldsymbol{k})\cdot\boldsymbol{x}} \; V(\boldsymbol{x}). \tag{2.39}$$

From a physics point of view, Eq. 2.39 considers only single (kinematic) scattering, which holds true, e.g. for surface X-ray diffraction (SXRD) [111, 181]. In this particular case, the scattering amplitude $f_s(\boldsymbol{k}_0, \boldsymbol{k})$ is given by the Fourier transform of the scattering potential, and the crystal structure can be directly determined from a single diffraction pattern. For low-energy electrons, however, the Born approximation is no longer justified since LEED is dominated by multiple (dynamic) scattering (see Sec. 2.3.1). Therefore, the full Lippmann-Schwinger equation has to be solved in order to extract the precise positions of the basis atoms.[32] At the same time, if only lattice symmetry is of interest, a single-scattering approach describes the formation of LEED patterns with sufficient accuracy. For this reason, the following theoretical description of low-energy electron diffraction from surfaces will mainly deal with kinematic scattering theory.[33]

The structure of a solid is defined by the symmetry of the underlying *Bravais lattice* and the atomic basis representing the smallest repeating unit having the full symmetry of the crystal [64, 111, 156]. The aim of LEED crystallography is to identify both the symmetry and the atomic coordinates within the surface unit cell by measuring diffraction patterns of electrons scattered from solids. It is important to note that LEED is specifically sensitive to atomic structure since the typical electron kinetic energies (20-500 eV) lie significantly above E_F. As a consequence, electrons are expected to scatter mainly due to interactions with the inner atomic shells or the nucleus, the corresponding scattering potentials being spherically symmetric

[31] It can be shown that $|f(\boldsymbol{k}_0, \boldsymbol{k})|^2 \sim \frac{\mathrm{d}\sigma}{\mathrm{d}\Omega}$, i.e. the differential cross section.

[32] This is the main reason why structure determination by LEED was not feasible until the 1970s, when computing power finally overcame a critical threshold.

[33] For more information about dynamical LEED theory the reader is referred to Refs. [180] and [111].

(*muffin-tin potential*, see Fig 2.18a).

Assuming single elastic scattering, kinematic scattering theory establishes a straightforward connection between the main observable in diffraction experiments, i.e. the position-dependent scattering intensity, and the microscopic structure of solids.[34] In this, incident electrons are treated as plane waves with initial wave vector $\boldsymbol{k}_0$ and wavelength $\lambda_\mathrm{d} = \hbar\boldsymbol{k}_0$. While multiple scattering is neglected, the short IMFP (see Sec. 2.3.1) is taken into account by considering only interactions of the electron waves with the first atomic layer. In a simple example, we study the scattering of an incident wave $A(\boldsymbol{r}_i) = A_0 \exp(\mathrm{i}\boldsymbol{k}_0 \cdot \boldsymbol{r}_i)$ with amplitude A_0 by individual atoms at positions $\boldsymbol{r}_i$, arranged in a two-dimensional lattice with non-trivial basis (see Fig. 2.18b)[35]. After scattering, the amplitude $A_i(\boldsymbol{r}_i) = A_0\, f_i(\boldsymbol{r}_i) \exp(\mathrm{i}\boldsymbol{k}_0 \cdot \boldsymbol{r}_i)$ is modified by an atom-specific scattering factor f_i (*atomic form factor*) and the contribution of the wave scattered at atom i to the amplitude at the detector is given by

$$\frac{A_i}{A_0} = \frac{f_i}{|\boldsymbol{R}_0 - \boldsymbol{r}_i|}\, \mathrm{e}^{\mathrm{i}\boldsymbol{k}_0\cdot\boldsymbol{r}_i}\, \mathrm{e}^{\mathrm{i}\boldsymbol{k}(\boldsymbol{R}_0-\boldsymbol{r}_i)} \approx \frac{1}{|\boldsymbol{R}_0|}\, \mathrm{e}^{\mathrm{i}\boldsymbol{k}\cdot\boldsymbol{R}_0}\, f_i\, \mathrm{e}^{-\mathrm{i}\Delta\boldsymbol{k}\cdot\boldsymbol{r}_i}. \tag{2.40}$$

Here, $\boldsymbol{R}_0$ is the distance to the detector, $\boldsymbol{k}$ the wave vector after scattering and $\Delta\boldsymbol{k} = \boldsymbol{k} - \boldsymbol{k}_0$ the momentum transfer or scattering vector, respectively. In this, we have assumed that after scattering, the electrons propagate as spherical waves originating from the scattering centers and that $|\boldsymbol{r}_i|$ is negligibly small compared to $|\boldsymbol{R}_0|$. The total amplitude $A = \sum_i A_i$ at the detector can now be calculated by adding up the contributions of the individual atoms. Furthermore, to separately analyse the contributions of the crystal lattice and the atomic basis to the diffraction pattern, we split the position vector $\boldsymbol{r}_i = \boldsymbol{R}_{mn} + \rho_j$ into a vector $\boldsymbol{R}_{mn}$ indicating the position of the mn^{th} unit cell (m and n denoting coordinates on the two-dimensional lattice grid) and a vector ρ_j pointing to the position of the j^{th} atom within that cell (see top right inset in Fig. 2.18b). Under these assumptions, the normalized intensity I/I_0 at the detector is given by

[34] In deriving the main theoretical results, we will mostly follow Ref. [111]. Alternative approaches may be found in Refs. [156] and [64].

[35] Here, we neglect the temporal evolution of the phase given by the standard phase factor $\mathrm{e}^{\mathrm{i}\omega_0 t}$.

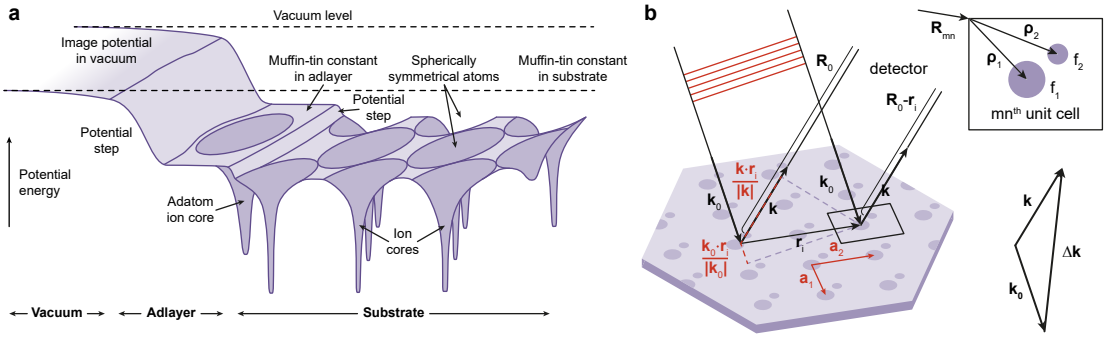

Figure 2.18: Surface scattering of low-energy electrons. **a**, Muffin-tin model of the scattering potential in LEED. Due to electron kinetic energies $E_{\mathrm{kin}} \gg E_{\mathrm{F}}$, scattering occurs at inner electron shells and ionic cores, leading to spherically symmetric and non-overlapping atomic potentials. Adlayers can introduce additional potential steps. Adapted from Ref. [179]. **b**, Auxiliary sketch showing the diffraction of an incident plane wave with wave vector $\boldsymbol{k}_0$ on a two-dimensional lattice with a polyatomic basis. $\boldsymbol{a}_1$, $\boldsymbol{a}_2$, basis vectors of the crystal lattice. (Top right) Surface unit cell with two basis atoms (see black rectangle in main panel). (Bottom right) Momentum transfer upon scattering. $\Delta\boldsymbol{k}$, scattering vector.

$$\frac{I}{I_0} = \left|\frac{A}{A_0}\right|^2 = \frac{1}{|\boldsymbol{R}_0|^2} \underbrace{\left|\sum_{m,n} \mathrm{e}^{-\mathrm{i}\Delta\boldsymbol{k}\cdot\boldsymbol{R}_{mn}}\right|^2}_{|G|^2} \underbrace{\left|\sum_j f_j\, \mathrm{e}^{-\mathrm{i}\Delta\boldsymbol{k}\rho_j}\right|^2}_{|F|^2}, \tag{2.41}$$

with the *lattice factor* G and the *structure factor* F determining the independent contributions of the Bravais lattice or the atomic basis, respectively. We will now separately discuss the roles of G and F in determining the final diffraction pattern. Concerning the lattice factor, we have defined the two-dimensional surface lattice in terms of

$$\boldsymbol{R}_{mn} = m\boldsymbol{a}_1 + n\boldsymbol{a}_2, \tag{2.42}$$

with $\boldsymbol{a}_1$ and $\boldsymbol{a}_2$ being the linearly independent base vectors of the crystal lattice in real-space (see Fig. 2.18b). The sum in Eq. 2.41 can therefore be factorised, yielding

$$|G|^2 = \left|\sum_{m=-\infty}^{m=+\infty} \left(\mathrm{e}^{-\mathrm{i}\Delta\boldsymbol{k}\cdot\boldsymbol{a}_1}\right)^m\right|^2 \cdot \left|\sum_{n=-\infty}^{n=+\infty} \left(\mathrm{e}^{-\mathrm{i}\Delta\boldsymbol{k}\cdot\boldsymbol{a}_2}\right)^n\right|^2, \tag{2.43}$$

where we have assumed an infinite, perfectly periodic crystal. Importantly, the two factors in Eq. 2.43 are non-zero only if $\exp(-\mathrm{i}\Delta\boldsymbol{k}\cdot\boldsymbol{a}_i) = 1$, which is equivalent to

$\Delta\boldsymbol{k}_\parallel \cdot \boldsymbol{a}_i = 2\pi q\,(q \in \mathbb{Z})$.[36] In this particular case, $|G|^2 = 1$, irrespective of the atomic basis or the magnitude of m and n. We thus look for a set of vectors that comply with the above relation. This motivates the definition of the two-dimensional *reciprocal lattice*

$$\boldsymbol{G}_{hk} = h\boldsymbol{b}_1 + k\boldsymbol{b}_2, \tag{2.44}$$

with $h, k \in \mathbb{Z}$ and vectors $\boldsymbol{b}_i$ fulfilling $\boldsymbol{b}_i \cdot \boldsymbol{a}_j = \delta_{ij}$ $(i, j = 1, 2)$. In two dimensions, the basis vectors $\boldsymbol{b}_i$ or the reciprocal lattice can be constructed from the real-space basis $\{\boldsymbol{a}_1, \boldsymbol{a}_1\} = \{(a_{1x}, a_{1y}), (a_{2x}, a_{2y})\}$ in the following way:

$$\boldsymbol{b}_1 = 2\pi \frac{\boldsymbol{a}_2 \times \boldsymbol{n}}{\boldsymbol{n} \cdot (\boldsymbol{a}_1 \times \boldsymbol{a}_2)} = \frac{2\pi}{A_{\text{real}}}(a_{2y},\, -a_{2x}), \tag{2.45}$$

$$\boldsymbol{b}_2 = 2\pi \frac{\boldsymbol{n} \times \boldsymbol{a}_1}{\boldsymbol{a}_1 \cdot (\boldsymbol{a}_2 \times \boldsymbol{n})} = \frac{2\pi}{A_{\text{real}}}(-a_{1y},\, a_{1x}). \tag{2.46}$$

Here, $\boldsymbol{n}$ is the surface normal vector and $|A_{\text{real}}| = |a_{1x}a_{2y} - a_{2x}a_{1y}|$ the area of the real-space unit cell (see Fig. 2.19a). For the LEED pattern, it follows that reflexes appear only in directions for which the in-plane component of the scattering vector $\Delta\boldsymbol{k}$ coincides with a reciprocal lattice vector:

$$\Delta\boldsymbol{k}_\parallel = \boldsymbol{k}_\parallel - \boldsymbol{k}_{0,\parallel} = \boldsymbol{G}_{hk}. \tag{2.47}$$

This is commonly referred to as the *Laue condition* for scattering from a two-dimensional sample. In the direction perpendicular to the surface layer, due to the lack of translational symmetry, momentum transfer is not restricted to discrete values. Consequently, the three-dimensional reciprocal lattice of the surface consists of *crystal truncation rods* (see Fig. 2.19a). To predict the LEED pattern from a surface with known symmetry, we can use the *Ewald construction* [64, 111, 156], that is, the graphical representation of Eq. 2.47 (see Fig. 2.19b). For this, we use that

$$|\boldsymbol{k}| = |\boldsymbol{k}_0|, \tag{2.48}$$

since only elastic scattering processes are considered. The incident electron wave is represented by its wave vector $\boldsymbol{k}_0$ pointing to the origin of reciprocal space, i.e. the

[36] Here, we only consider scattering from the two-dimensional first layer and therefore choose $\boldsymbol{k} = \boldsymbol{k}_\parallel$.

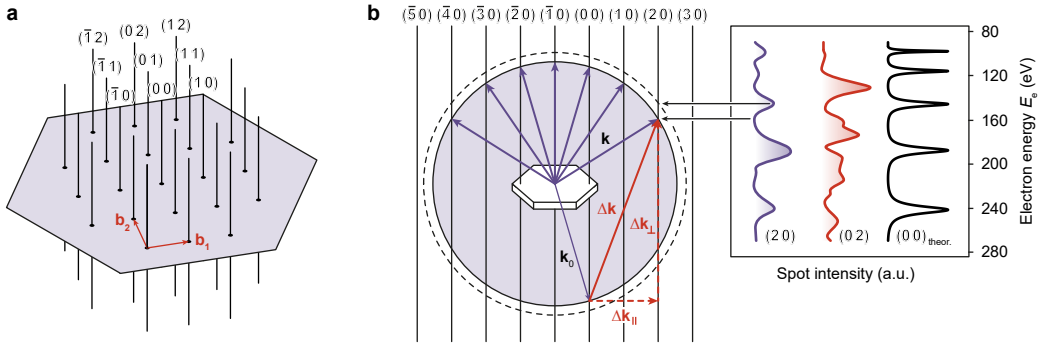

Figure 2.19: Reciprocal lattice and Ewald construction in LEED. **a**, Central section of the reciprocal space of a two-dimensional rectangular lattice around the (0 0) spot. $\boldsymbol{b}_1$, $\boldsymbol{b}_2$, basis vectors of the reciprocal lattice. Adopted from Ref. [156]. **b**, (Left) Construction of the Ewald sphere in LEED geometry. Adopted from Refs. [112, 156]. (Right) In real experiments, the finite electron penetration depth and sub-surface multiple scattering of electrons lead to characteristic intensity oscillations as a function of electron energy. LEED data (violet and read lines) taken from Ref. [195]. Black line, schematic intensity dependence of (0 0) spot for $|f_j(E)|^2 = |f(E)|^2 = 1$, according to Ref. [111]. Partially adapted from Refs. [156] and [55].

(0 0) rod. The Ewald sphere is now defined by the set of wave vectors $\boldsymbol{k}$ for which momentum conservation is satisfied (sphere with radius $|\boldsymbol{k}_0|$ centered at the origin of $\boldsymbol{k}_0$ in Fig. 2.19b). For intersection points of the Ewald sphere and the crystal truncation rods, both Eq. 2.48 (momentum conservation) and Eq. 2.47 (Laue criterion) are fulfilled, and diffraction reflexes can be observed[37]. So far, for simplicity we have only considered a perfectly two-dimensional lattice. However, depending on kinetic energy, electrons may penetrate several monolayers deep into the solid before being scattered. This leads to an additional weak Laue condition for scattering perpendicular to the surface and thereby to a periodic modulation of the rod intensity, as evidenced by energy-dependent LEED measurements (see Fig. 2.19b).

Whereas the lattice factor G can be used to identify the symmetry of the Bravais lattice, it does not contain any information about the atomic positions within the real-space unit cell. The latter are encoded in the structure factor F determining the intensity of diffraction reflexes given by G. Accordingly, a precise analysis of the intensity of individual diffraction spots provides information about the arrangement

[37] Due to the existence of rods perpendicular to the surface, the reciprocal lattice always intersects the Ewald sphere. Thus, in contrast to bulk-sensitive scattering methods, there are always reflexes observed in the LEED pattern.

of the basis atoms. However, in most cases, kinematic theory fails to predict the correct spot intensities, the reason being that multiple scattering can no longer be neglected [111, 180]. For a single atom at position ρ_i not only scattering of the incident plane electron wave has to be considered, but also the contribution of waves scattered from neighbouring atoms towards ρ_i and vice versa. In this scenario, the total wave amplitude scattered by a single atom depends on its own scattering factor f_i. As a consequence, modelling the effect of multiple scattering on the structure factor necessitates a self-consistent treatment of f_i [111] (which is replaced by a dynamic scattering factor f_i^{D}) that reproduces the drastic changes of the energy-dependent spot intensities and enables LEED structure determination (see Fig. 2.19b and Ref. [111, 180]).

Regardless of the additional complications introduced by dynamic scattering, G and F remain independent quantities. This allows us to harness LEED in combination with kinematic theory to identify the lattice symmetry by means of G, even if multiple scattering prevents us from determining exact atomic positions via F. This is particularly important in view of the objective of this work, namely the investigation of a symmetry-breaking phase transition of an adsorbate-induced surface reconstruction. In such transitions, the atomic structure changes significantly, and the new symmetry of the surface is reflected in the LEED pattern. At the same time, temperature effects, inelastic scattering or the excitation of lattice vibrations may additionally influence the diffraction signal via F. In order to disentangle the different contributions of these effects to $I(\Delta\boldsymbol{k})$, we will now study their characteristic signatures in LEED.

2.3.3 Surface structures and dynamic effects in LEED

Low-energy electrons are versatile structural probes. Interacting with a solid surface, they scatter either elastically or inelastically, coherently or incoherently, exchanging energy and momentum. As a matter of fact, the LEED pattern represents a superposition of these distinct scattering channels, each of them carrying information about specific observables, e.g. lattice symmetry, atomic structure, as well as long-range order or collective and dynamic phenomena. Whereas a comprehensive discussion of all these aspects is beyond the scope of this work, the following sections provide a very brief overview of relevant effects. These include, among others, temperature-

induced Debye-Waller-type spot suppressions, inelastic diffuse scattering, or periodic lattice distortions. Observing the impact of these effects on diffraction spot profiles with ps temporal resolution in ULEED allows to draw a picture of the surface on the time scales of atomic motion. First and foremost, however, it is important to understand surface structure itself, with superstructures and reconstructions being two of the most basic features.

Superstructures

As already mentioned in Sec. 2.3, the broken symmetry of a surface leads to changes in the electronic and atomic structure, giving rise to various surface-specific phenomena [184, 185, 196–198]. However, the question remains why the surface structure differs from the bulk. On the atomic level, to cleave a bulk crystal means to break inter-atomic bonds between two neighbouring crystal planes, which leaves the surface in a nonequilibrium state characterized by unsatisfied or *dangling* bonds [111] (see Fig. 2.20a). Under ultrahigh vacuum (UHV) conditions, minimising total energy, atoms of the first atomic layers subsequently rearrange, accompanied by the making and breaking of bonds (Fig. 2.20b)). While this applies to various classes of materials, the effects are particularly strong in semiconductors, as they are formed by covalent bonds with directional character [111]. Depending on the impact of structural rearrangements on the lateral symmetry of the first layers, a distinction is made between surface *relaxations* (identical symmetry of initial and final structure) and *reconstructions* (distinct symmetries of initial and final structure). In the latter case, the surface atoms form a periodic *superstructure* with modified lattice symmetry and a new, typically larger surface unit cell. Interestingly, for some materials, the newly formed surface is trapped in a metastable configuration, that is, a transition to a lower-energy (super-)structure is prevented by an energetically unfavored intermediate state. Only at elevated temperature, the enhanced thermal motion of the surface atoms overcomes the corresponding energy barrier. A prominent example of this is the (111) surface of silicon.

While cleaving a crystal in UHV leads to an intrinsic reorganisation at the surface, similar structural changes can also be caused by the adsorption of additional atoms[38]. Here too, energy minimisation due to the saturation of dangling bonds is

[38]Note that even under UHV conditions with pressures reaching down to 10^{-10} mbar, significant

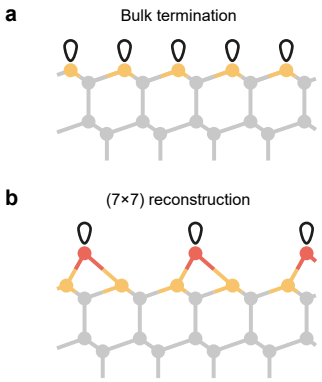

Figure 2.20: Energy minimisation by surface reconstruction for the Si(111) surface. **a**, Bulk-like terminated Si(111) surface. Silicon atoms, grey, red and yellow; dangling bonds, black/ white. **b**, (7×7) surface reconstruction of Si(111). Additional Si atoms (red) saturate the dangling bonds of the unreconstructed surface, reducing the total number of unsaturated bonds and minimising the total energy of the surface. Adapted from Ref. [199].

the main driving force. Adsorbate-induced surface reconstructions are of particular importance for a large number of research fields, including surface chemistry and catalysis [166, 179, 183], as well as the physics of low-dimensional systems [101]. Depending on the adatom species the surface can be endowed with completely new properties affecting chemical reactivity or surface conductivity. Figure 2.21a shows typical adsorption sites on a surface with hexagonal symmetry. Whereas physisorbed atoms only weakly influence substrate structure, in the case of chemisorption, the formation of strong bonds between adatoms and substrate often results in a more pronounced reconstruction of the surface.

The commonly used mathematical descriptions of superlattices have been established by Park and Madden [200], or Wood [201], respectively. In this work, mainly Wood's notation is used to refer to different surface reconstructions in the form of

$$\mathrm{X}(hkl)\,(m \times n)\,\mathrm{R}\theta - \mathrm{Ad}. \tag{2.49}$$

Here, X(hkl) refers to the substrate and the relevant crystal face (e.g. "Si(111)"), whereas $(m \times n)$ gives the unit cell dimensions of the superlattice in units of the substrate base vectors in real-space (e.g. "(4×1)"). The term Rθ is used to describe the orientation of the superlattice relative to a high-symmetry axis of the bulk structure[39], while the adsorbate species (Ad) is given at the end. Figures 2.21b-e show different surface reconstructions and the resulting diffraction patterns in LEED. Although Wood's notation is commonly used in literature, some non-trivial surface lattices require the matrix formalism developed by Park and Madden [200].

adsorbate coverages are observed after some time due to residual gas atoms.

[39] Note that for $\phi = 0$, this term is typically omitted.

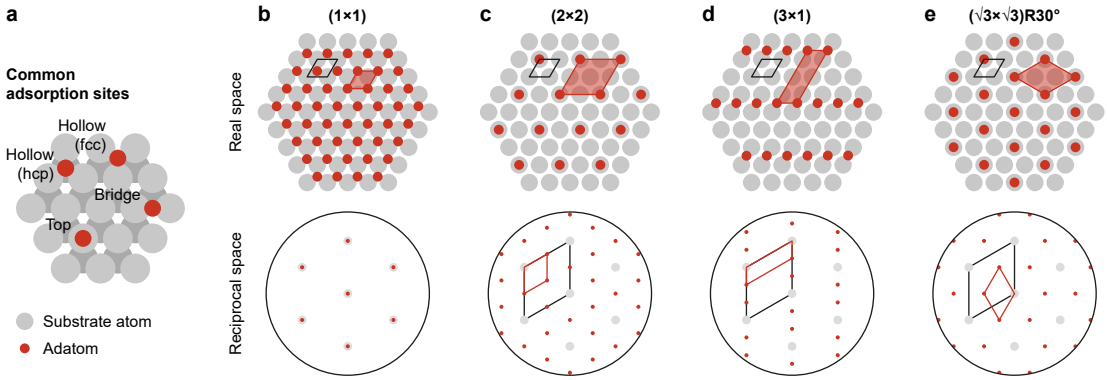

Figure 2.21: Overview of adsorbate-induced surface reconstructions. **a**, Common adsorption sites of adatoms on substrates with hexagonal symmetry, e.g. the (111) surface for cubic, bcc, fcc or diamond lattices. Note that the formation of strong bonds between adatoms or substrates can significantly change surface structure, making it difficult to assign adatoms to the specific adsorption sites described above. **b-e**, Frequently occurring surface reconstructions on substrates with hexagonal symmetry (top) and corresponding reciprocal lattice structures (bottom). Superstructure reflexes, red; substrate reflexes, grey; real/reciprocal surface unit cell of superstructure (substrate), red (black). Surface reconstructions either occur intrinsically by rearrangement of substrate atoms or due to absorption of additional atoms.

Here, the base vectors $\{\boldsymbol{a}_1^{\mathrm{s}}, \boldsymbol{a}_2^{\mathrm{s}}\}$ of the *superlattice* are given by a linear combination of the real-space base vectors $\{\boldsymbol{a}_1, \boldsymbol{a}_2\}$ of the bulk-terminated (unreconstructed) lattice:

$$\begin{pmatrix} \boldsymbol{a}_1^{\mathrm{s}} \\ \boldsymbol{a}_2^{\mathrm{s}} \end{pmatrix} = \begin{pmatrix} s_{11} & s_{12} \\ s_{21} & s_{22} \end{pmatrix} \cdot \begin{pmatrix} \boldsymbol{a}_1 \\ \boldsymbol{a}_2 \end{pmatrix} = \hat{\boldsymbol{S}} \cdot \begin{pmatrix} \boldsymbol{a}_1 \\ \boldsymbol{a}_2 \end{pmatrix}. \tag{2.50}$$

In this, the matrix $\hat{\boldsymbol{S}}$ relates the two basis sets via coefficients s_{ij}. However, surface-sensitive diffraction methods access structural information in reciprocal space. Here, the base vectors $\{\boldsymbol{b}_1^{\mathrm{s}}, \boldsymbol{b}_2^{\mathrm{s}}\}$ of the superlattice are related to the basis vectors $\{\boldsymbol{b}_1, \boldsymbol{b}_2\}$ of the bulk lattice by

$$\begin{pmatrix} \boldsymbol{b}_1^{\mathrm{s}} \\ \boldsymbol{b}_2^{\mathrm{s}} \end{pmatrix} = \hat{\boldsymbol{S}}^{-1} \cdot \begin{pmatrix} \boldsymbol{b}_1^{\mathrm{s}} \\ \boldsymbol{b}_2^{\mathrm{s}} \end{pmatrix} = \frac{1}{s_{11}s_{22} - s_{21}s_{12}} \begin{pmatrix} s_{22} & -s_{21} \\ -s_{12} & s_{11} \end{pmatrix} \cdot \begin{pmatrix} \boldsymbol{b}_1^{\mathrm{s}} \\ \boldsymbol{b}_2^{\mathrm{s}} \end{pmatrix}, \tag{2.51}$$

where we have used that $\hat{\boldsymbol{S}}^{-1} = \det(\hat{\boldsymbol{S}})^{-1} \operatorname{adj}(\hat{\boldsymbol{S}})$. For reconstructed surfaces the real-space unit cell is typically larger than the unit cell of the substrate. In this case, Eq. 2.51 predicts a smaller reciprocal unit cell of the superlattice and additional

reflexes in between substrate-related diffraction spots (see Fig. 2.21b-e (bottom)). In analysing LEED patterns, it is important to account for the coexistence of multiple symmetry-equivalent domains on the same surface. This typically happens if the superlattice is of lower symmetry compared with the substrate.

Static and dynamic effects on the diffraction spot profile

We now address the question of how static or dynamic changes to the lattice structure are mirrored in the LEED pattern. This will enable us to disentangle and identify the roles of different processes underlying the ultrafast structural dynamics observed by ULEED. Figure 2.22 gives an overview of a number of relevant effects to be considered in the analysis of LEED images, some of which are briefly discussed below. Generally, the k-dependent intensity distribution of the diffraction pattern is determined by the product $|G|^2 \cdot |F|^2$ and the *instrumental response function* $T(\Delta\boldsymbol{k})$ (IRF). For a perfect, rigid and infinite crystal and a perfect instrument, the LEED image would feature infinitely sharp peaks [179]. However, surface imperfections and the distortion of the diffraction pattern by the measurement device lead to a finite spot width σ_{spot}. In this regard, the IRF describes the contribution of the LEED apparatus to the observed broadening. Among other things, the finite spatial extension and energy width of the electron beam, the emission properties of the electron source, aberrations of the electron optics, and the finite spatial resolution of the detector have a significant influence on σ_{spot}. Accordingly, the measured LEED intensity function $I(\Delta\boldsymbol{k})$ is given by a convolution of the "ideal" intensity distribution $I^*(\Delta\boldsymbol{k})$ and the IRF [179]:

$$I(\Delta\boldsymbol{k}) = I^*(\Delta\boldsymbol{k}) * T(\Delta\boldsymbol{k}) = \int_{-\infty}^{+\infty} \mathrm{d}(\Delta\boldsymbol{k})\, T(\Delta\boldsymbol{k}) \cdot I^*(\Delta\boldsymbol{k} - \Delta\boldsymbol{k}'). \tag{2.52}$$

Information about the surface structure can be extracted from the Fourier transform of $I(\Delta\boldsymbol{k})$:

$$\mathcal{F}\{I(\Delta\boldsymbol{k})\}(\boldsymbol{r}) = \mathcal{F}\{I(\Delta\boldsymbol{k}) * T(\Delta\boldsymbol{k})\} = \Phi(\boldsymbol{r}) \cdot t(\boldsymbol{r}). \tag{2.53}$$

Here, $\Phi(\boldsymbol{r})$ is the autocorrelation function, which is a measure of lattice order for a given vector $\boldsymbol{r}$. The Fourier transform of the IRF gives the *transfer function* $t(\boldsymbol{r})$, the FWHM of $t(\boldsymbol{r})$ commonly being referred to as *transfer width* w_{t}. Since the autocorrelation function is modulated by $t(\boldsymbol{r})$, the corresponding transfer width can

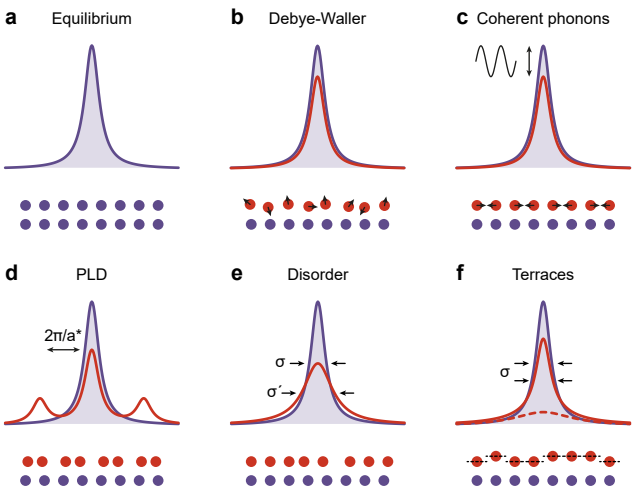

Figure 2.22: Impact of static and dynamic effects on the diffraction spot profile. Blue circles, equilibrium atomic positions within the surface layer; red circles and black arrows, (time-dependent) atomic displacements. Blue (red) line, original (modified) spot profile. Dashed red line in (**f**), diffuse background contribution.

be interpreted as the maximum distance for which spatial correlations between two scatterers can be observed. In experiments, the IRF can be approximated by the intensity profile of a suitable diffraction spot, assuming that the ideal spot width $\sigma_{\text{spot}}^{\text{ideal}}$ is negligibly small compared with $T(\Delta\boldsymbol{k})$. Provided a sufficiently high transfer width, LEED is sensitive to a variety of surface lattice phenomena, as exemplified by Fig. 2.22b-f:

- At elevated temperature, the incoherent thermal motion of atoms results in a reduction of the structure factor F and a diffuse background signal (b). While this *Debye-Waller effect* [202, 203] impacts the diffraction spot intensity, the spot width remains unaffected (see detailed discussion in App. A).

- The in-phase motion of atoms at the surface, i.e. *coherent surface phonons*, periodically changes the atomic coordinates within each unit cell, and thus affects the structure factor F [140]. The oscillations of atoms around their equilibrium positions cause modulations of the spot intensity at the frequencies according to the involved phonon modes (c). This contribution to the spot profile can only be investigated by ultrafast diffraction techniques with sufficiently high temporal resolution[40].

- The formation of a *periodic lattice distortion* (PLD, see Sec. 2.1.1 and 2.1.3) manifest itself in the diffraction pattern by the appearance of satellite peaks.

[40] In experiments with insufficient temporal resolution $\Delta\tau$ the effect of coherent phonons on F is averaged out over one oscillation period T_{phon}. Thus, ideally $\Delta\tau < T_{\text{phon}}/2$.

This can be understood by interpreting the PLD in terms of a sinusoidal phase modulation of the structure factor and calculating the resulting scattering amplitude using the Jacobi-Anger relation (for details of the calculation see Eq. 3-10 in Ref. [204]). The periodicity a^* of the real-space modulation can be determined from the distance between satellite and corresponding Bragg peaks in k-space via the relation $\Delta k = 2\pi/a^*$ (d).

- *Disorder* in the periodic lattice structure introduced, e.g. by atomic-scale defects result in a broadening of the diffraction spot profile (e). Consequently, the analysis of spot widths allows conclusions to be drawn about the correlation length of the lattice [18, 120, 205].

- The presence of *terraces* or the coexistence of two long-range ordered structural phases in the form of microscopic domains causes a diffuse Lorentzian background contribution to the spot profile (f). Whereas the width of the coherent contribution remains untouched by this effect, the width of the background signal can be used to infer the mean terrace or domain width [116, 205].

Many of the above effects are discussed in the light of the experimental results presented in Sec. 5 and 6. In addition, the effect of temperature on the diffraction spot intensity is treated to some extend in Appendix A. Insights into the associated Debye-Waller-type spot suppressions will be used in Sec. 5.3 to rule out a major contribution of lattice temperature to the ultrafast $(8\times2) \rightarrow (4\times1)$ transition and thus prove the electronic nature of the excitation mechanism. Other effects are explained in more detail where it seems necessary and in direct connection with the measurement results.

2.3.4 Ultrafast optical response of surface monolayers

Structure-sensitive probes such as LEED are capable of investigating the atomic lattice of a surface, and to some extend this also allows to draw conclusions about electronic properties, given a sufficiently strong coupling between electron and lattice subsystems and additional input from theory. Recently developed ultrafast electron diffraction schemes like ULEED [17, 18, 55] or trRHEED [9, 10] further allow to resolve the evolution of surface structure after optical excitation. However, in the case of materials with complex correlations between electronic and lattice structure

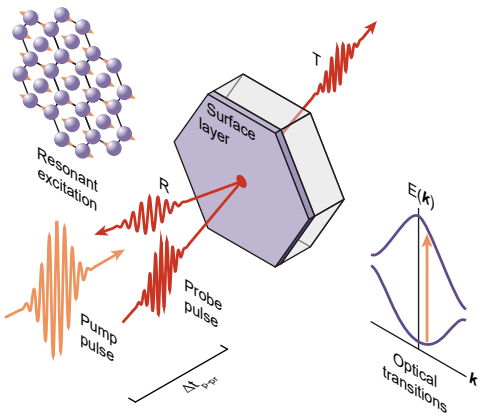

Figure 2.23: Ultrafast optical pump-probe spectroscopy. An intense ultrashort pump pulse excites electronic and/or structural dynamics by means of interband transitions in the band structure or direct (resonant) interaction with the lattice. A weaker pulse probes the optical properties, such as reflectivity R or transmission T, as a function of the pump-probe delay $\Delta t_{\text{p-pr}}$. This provides insights into nonequilibrium dynamics in electronic states and lattice degrees of freedom.

the combination of experiments with different observables often provides a more comprehensive picture of the physics. Therefore, when studying nonequilibrium surface dynamics with ULEED, a complementary method that also accesses the electronic properties of surfaces and atomic layers on ultrafast time scales is highly desirable.

While trARPES directly measures the population and evolution of the electronic band structure with both high surface sensitivity and fs temporal resolution, the technical requirements for this experimental approach are very high. A less demanding alternative is given by optical spectroscopy which measures the optical properties of solids and their surfaces. This offers a powerful way to access the population of electronic states and central features of the band structure, since these ultimately determine the macroscopic response of the surface layer to electromagnetic fields. Using ultrashort light pulses for excitation and probing in a stroboscopic scheme (see Fig. 2.23 and Sec. 3) enables to monitor changes in reflectivity R, transmission T and absorption A, e.g. due to electronic excitation, electronic or structural phase transitions, as well as the coherent motion of atoms. Within the scope of this work, it is not possible to give even a rudimentary overview of this still flourishing field of research. Instead, we focus on a few aspects of (ultrafast) optical spectroscopy which are relevant to the experiments described in Sec. 3 and 6.

In a first step, we define the relevant optical constants and relate them to macroscopic observables. In this, we mainly follow Ref. [206]. Furthermore, on the basis of Ref. [207], it will we shown how the corresponding equations can be adapted to describe reflection, transmission and absorption of thin optical layers. Last, we will

study how ultrafast changes in the electronic and lattice structure affect these quantities. This will enable the analysis and interpretation of the optical pump-probe (OPP) experiments on the transition in atomic indium wires presented in Sec. 6.

Optical constants

In the following, we analyse how the microscopic electronic or lattice structure is connected to macroscopic optical constants, i.e. the complex dielectric function $\hat{\varepsilon}$, the complex optical conductivity $\hat{\sigma}$ or the electric susceptibility, and proceed by linking these parameters to measurable properties such as the reflectivity R. In a microscopic real-space picture, the structure of a surface is defined by the periodic charge distribution formed by negatively charged electrons and the positively charged nuclei. Within the framework of classical electrodynamics, the interaction of charged particles with a local time-dependent electromagnetic field is treated in terms of driven oscillators. As mentioned in Sec. 2.2.1, electrons respond significantly faster to external perturbations than the atomic lattice, for which resonance frequencies typically lie in the MIR or THz regime. As a consequence, only electrons can interact resonantly with electromagnetic waves in the visible range[41]. However, lattice modes can couple indirectly to light via Raman-scattering (second order effect, see also Sec. 2.2.2).

The interaction of light and matter on macroscopic length scales is described by Maxwell's equations and the constitutive relations between the occurring fields and currents [206]. On this basis, the electric field $\boldsymbol{E}$ of light propagating inside the material obeys the wave equation

$$\nabla^2 \boldsymbol{E} = \frac{\varepsilon\mu}{c^2}\frac{\partial^2 \boldsymbol{E}}{\partial t^2} + \frac{4\pi\sigma\mu}{c^2}\frac{\partial \boldsymbol{E}}{\partial t}. \tag{2.54}$$

Here, ε is the dielectric constant, σ the optical conductivity, μ the magnetic permeability, and c the speed of light. Since we are dealing with non-magnetic materials, $\mu = 1$. Solutions to Eq. 2.54 are plane waves $\boldsymbol{E}(\hat{k}, t) = \boldsymbol{E}_0 \exp(\mathrm{i}(\hat{k} \cdot \boldsymbol{r} - \omega t))$ with frequency ω and the complex propagation constant $\hat{k}$. Whereas the real part of $\hat{k}$ is associated with the wave vector, the imaginary part describes the attenuation of

[41] As a remark, resonant excitation of lattice modes with intense MIR or THz light fields (pulses) is a promising concept to all-optically control atomic structure and steer exotic properties of solids, such as superconductivity [3] or ferroelectricity [131].

electric field inside the solid. Inserting this solution into the wave equations for $\boldsymbol{E}$ and $\boldsymbol{H}$ (see Ref. [206]), yields the dispersion relation of light in matter

$$\begin{aligned} -\hat{k}^2 &= \frac{\varepsilon\mu\omega^2}{c^2} - \frac{4\pi\mathrm{i}\sigma\omega}{c^2} \\ \hat{k} &= \frac{\omega}{c}\sqrt{\hat{\varepsilon}}, \end{aligned} \tag{2.55}$$

with the complex dielectric function $\hat{\varepsilon}$ describing the macroscopic polarisability of the material[42]. Moreover, $\hat{\varepsilon}$ and the complex conductivity $\hat{\sigma}$ are mutually connected by the following relations:

$$\hat{\varepsilon} = \varepsilon + \frac{4\pi\mathrm{i}\sigma}{\omega} := \varepsilon_1 + \mathrm{i}\varepsilon_2; \tag{2.56}$$

$$\hat{\sigma} = \sigma + \frac{\varepsilon\omega}{4\pi\mathrm{i}} := \sigma_1 + \mathrm{i}\sigma_2. \tag{2.57}$$

While both $\hat{\varepsilon}$ and $\hat{\sigma}$ are macroscopic quantities, they originate from the microscopic or atomic polarisability α (see Eq.2.34), which describes dipole formation in response to a local electric field on the level of a single unit cell. Microscopic and macroscopic pictures are linked by the Clausius-Mossotti relation

$$\frac{\hat{\varepsilon}/\varepsilon_0 - 1}{\hat{\varepsilon}/\varepsilon_0 + 2} = \sum_i \frac{N_i\alpha_i}{3\varepsilon_0}, \tag{2.58}$$

with N_i the number density of atoms of species i and α_i the corresponding polarisability. Furthermore, in many cases, the complex refractive index $\hat{n}$ is used to describe the refraction and absorption of light in materials:

$$\hat{n} = \sqrt{\hat{\varepsilon}} = \tilde{n}(\omega) + \mathrm{i}\tilde{k}(\omega). \tag{2.59}$$

From this, we yield the absorption coefficient $\alpha_{\mathrm{abs}} = 2\omega\tilde{k}(\omega)/c$[43]. The question remains as to how these optical constants are related to observables like the reflectivity, transmission or absorption (see Fig. 2.24a). To express R or the reflection coefficient r in terms of the complex refractive index, we define the reflectivity as

[42] Alternatively, the electric susceptibility $\hat{\chi} = (\hat{\varepsilon}/\varepsilon_0 - 1)$ can be used to describe the response of a material to external fields.

[43] Note that whereas the polarisability α relates to the optical field, the absorption coefficient refers to the light intensity.

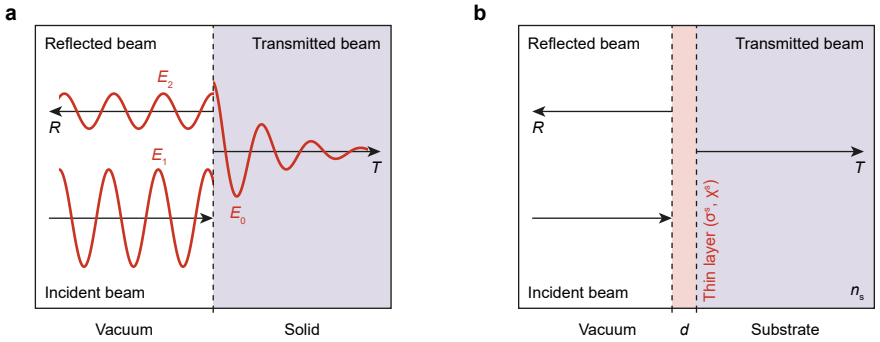

Figure 2.24: Auxiliary sketches for the definition of the optical properties of bulk solids and thin layers. **a**, Schematic of incoming, transmitted and reflected electric fields at the solid-vacuum interface, adapted from Ref. [206]. **b**, Sketch of a thin layer on a substrate with refractive index n_s. Adapted from Ref. [207].

the ratio between the amplitudes of reflected ($\boldsymbol{E}_2$) and incident ($\boldsymbol{E}_2$) waves, i.e. $R = |E_2/E_1|^2$ or $r = E_2/E_1$, respectively. Using the continuity conditions for $\boldsymbol{E}$ and $\boldsymbol{H}$ at the surface, the amplitudes of the incident, transmitted and reflected are connected to $\hat{n}$ by $E_2 = \frac{1}{2}E_0(1-\hat{n})$, $E_1 = \frac{1}{2}E_0(1+\hat{n})$ (for details, see Ref. [206]). Using these relations, we finally yield the macroscopic reflectivity

$$R = \left|\frac{1-\hat{n}}{1+\hat{n}}\right|^2 = \frac{(1-\tilde{n})^2+\tilde{k}^2}{(1+\tilde{n})^2+\tilde{k}^2}. \tag{2.60}$$

Optical properties of thin layers

Since this work is concerned with electronic and structural dynamics in indium monolayers on the Si(111) surface, we now deal with the question as to how the above relations for the optical properties translate to thin layers on dielectric substrates. First, we note that for the case of an indium layer on silicon and for pump (probe) wavelengths around 800 nm, the refraction of the substrate is essentially real ($\hat{n}_\mathrm{s} = 3.67 + 0.005\mathrm{i}$ at 800 nm). Accordingly, only the real part of the substrate refractive index is considered below ($\hat{n}_\mathrm{s} \to n_\mathrm{s}$). Following the arguments of Li and Heinz [207], the optical properties of a thin sheet on a substrate with vanishing imaginary part of $\hat{n}$ are accurately described by a two-dimensional model. In this, the coefficients for reflection and transmission of the layer can be expressed in terms of the sheet's

optical conductivity σ^{s} [207]:

$$r = \frac{1 - n_{\mathrm{s}} - Z_0\sigma^{\mathrm{s}}}{1 + n_{\mathrm{s}} + Z_0\sigma^{\mathrm{s}}}; \tag{2.61}$$

$$t = \frac{2}{1 + n_{\mathrm{s}} + Z_0\sigma^{\mathrm{s}}}. \tag{2.62}$$

Here, $\sigma^{\mathrm{s}} = -\mathrm{i}\chi\varepsilon_0\omega$, and $Z_0 = 1/\varepsilon_0 c$ is the vacuum impedance. Asserting that the thin sheet can be treated as a perturbation, r and t vary linearly with the sheet response $Z_0\sigma^{\mathrm{s}}$ of the thin layer [207]. In this case, Eq. 2.61 and 2.62 can be linearised with respect to $Z_0\sigma^{\mathrm{s}}$, yielding

$$r = r_0\left(1 - \frac{2}{1 - n_{\mathrm{s}}^2}Z_0\sigma^{\mathrm{s}}\right); \tag{2.63}$$

$$t = t_0\left(1 - \frac{1}{1 + n_{\mathrm{s}}}Z_0\sigma^{\mathrm{s}}\right), \tag{2.64}$$

with r_0 and t_0 being the standard expressions for the reflectivity and transmission coefficients derived above:

$$r_0 = \frac{(1 - n_{\mathrm{s}})}{(1 + n_{\mathrm{s}})}; \qquad t_0 = \frac{2}{(n_{\mathrm{s}} + 1)}. \tag{2.65}$$

On this basis, we can calculate the changes ΔR and ΔT in reflectivity R or transmission T, respectively, of the surface due to the presence of the thin layer, as well as the absorption A of the layer in terms of $A = 1 - R - T$:

$$\Delta R = |r_0|^2\left(\frac{4}{n_{\mathrm{s}}^2 - 1}\right)\mathrm{Re}(Z_0\sigma^{\mathrm{s}}) = -\frac{4(1 - n_{\mathrm{s}})}{(1 + n_{\mathrm{s}})^3}\,\mathrm{Re}(Z_0\sigma^{\mathrm{s}}), \tag{2.66}$$

$$\Delta T = -\mathrm{Re}(n_{\mathrm{s}})\,|t_0|^2\left(\frac{2}{1 + n_{\mathrm{s}}}\right)\mathrm{Re}(Z_0\sigma^{\mathrm{s}}) = -\mathrm{Re}(n_{\mathrm{s}})\frac{8}{(1 + n_{\mathrm{s}})^3}\,\mathrm{Re}(Z_0\sigma^{\mathrm{s}}), \tag{2.67}$$

$$A = \frac{4}{|1 + n_{\mathrm{s}}|^2}\,\mathrm{Re}(Z_0\sigma^{\mathrm{s}}). \tag{2.68}$$

As a main result, for a thin layer or atomic monolayer on a substrate with real refractive index, the changes in reflectivity and transmission are proportional to the monolayer absorption. Therefore, measurements of ΔR also provide information about the absorption of monolayers on the surface, provided a sufficiently strong contribution of the layer to the overall signal and a high signal-to-noise ratio.

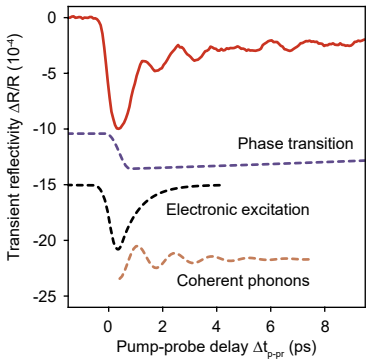

Figure 2.25: Contributions to the transient reflectivity signal measured by optical pump-probe spectroscopy (see also Sec. 6.3). Red line, Relative changes $\Delta R/R$ in reflectivity as a function of the pump-probe delay $\Delta t_{\text{p-pr}}$. Dashed lines schematically indicate the individual contributions of changes in the electronic band structure, e.g. due to a insulator-metal phase transition (violet), electronic excitations in the band structure affecting the rate of optical transitions for final states close to E_{F} (black), or coherent Raman- or IR- active phonons.

Ultrafast optical pump-probe spectroscopy

In a last step, we explore how ultrafast measurements of optical properties can be used to follow electronic and structural dynamics. In this context, essential questions concern the connection between the observables of optical spectroscopy, such as reflectivity R or absorption A, and the dynamics of electrons and phonons. Here, we focus on three possible contributions to transient reflectivity traces, i.e. electronic excitation, coherent phonons and phase transitions (see Fig. 2.25).

First of all, the pump pulse photo-excites electrons, which changes the occupation of states close to the Fermi energy [208]. This can influence the rate of allowed optical transitions into these states[44] for the probe pulse and, consequently, the imaginary part of the complex dielectric function. Changes of $\hat{\varepsilon}$ in turn affect the reflectivity via Eq. 2.59 and 2.60. Therefore, the exponential decay of the excited state population is mirrored in the pump-probe trace (see dashed black line in Fig. 2.25). Second, coherent Raman-active phonons excited by the pump pulse periodically change the polarisability α, which is connected to the macroscopic dielectric function through Eq. 2.58. As a consequence, for the probe pulse, the sample reflectivity and absorption become functions of the pump-probe delay $\Delta t_{\text{p-pr}}$:

$$\Delta R(\Delta t_{\text{p-pr}}) \sim \boldsymbol{E}_2 \cdot \left(\frac{\partial \boldsymbol{\alpha}}{\partial(\delta \boldsymbol{q})} \right) \delta q(\Delta t_{\text{p-pr}}) \cdot \boldsymbol{E}_1 \tag{2.69}$$

[44] More specifically, the probability $P_{\text{i}\to\text{f}}$ or rate $\Gamma_{\text{i}\to\text{f}}$, respectively, of interband transitions, i.e. transitions between occupied states of the valence band and unoccupied states of the conduction band, can be calculated by first order perturbation theory, i.e. Fermi's golden rule. Here, $\Gamma_{\text{i}\to\text{f}}$ depends on transition matrix element, describing the coupling between initial and final states by the light field, and the joint valence-conduction density of states.

Furthermore, for particular materials, the initial excitation of electrons or lattice vibrations can induce a phase transition, e.g. from an insulator to a metal. Such transitions typically involve pronounced changes in the orbital or electronic band structure, respectively. Here, it is not only the change in the occupation of electronic states that affects $\hat{\varepsilon}$, but the change of the band or lattice structure itself. For this reason, the associated effects on the transient reflectivity can last significantly longer, depending on the lifetime of the new electronic or structural phase.

In summary, the above considerations provide a basis for the interpretation of transient reflectivity data from atomic layers on optically-transparent substrates. Given a sufficiently strong change in reflectivity induced by the monolayer, surface-specific electronic and structural dynamics can be distinguished from bulk contributions due to the excitation of the substrate. Moreover, with regard to the sample system studied in this work, the proportionality between ΔR and A allows to monitor and finally control the energy absorption of the In/Si surface.

Chapter 3

Experimental details

The control of structural dynamics at surfaces requires the combination of ultrafast surface-sensitive probes with femtosecond optical excitation schemes. In this context, our group has recently developed ultrafast low-energy electron diffraction (ULEED) in transmission [17] and back-scattering [18, 54, 55, 112, 120] as a versatile tool to study optically-induced phase transitions and phase ordering processes with a temporal resolution of down to 1 ps. Consequently, a major objective of this work has been to further expand the capabilities of ULEED in order to enable not only the probing but also the all-optical control of nonequilibrium processes. The following sections present the technical advances in ULEED and the resulting experimental setup for the demonstration of coherent vibrational control over the Peierls-like transition in indium nanowires on Si(111).

The three main features of the experiment are discussed in Sec. 3.1-3.3: The femtosecond laser system, the ultrafast LEED and optical pump-probe (OPP) setups, as well as the preparation of samples under ultra-high vacuum (UHV) conditions. One of the tasks undertaken as part of this work was the maintenance of the ultrafast laser system and the extension of the optics setup to facilitate both multipulse optical excitation of surfaces (together with Hannes Böckmann-Clemens) and optical pump-probe spectroscopy (together with Felix Kurtz and Neele Kozák). Moreover, the work featured the development of procedures for the preparation of atomic wire arrays on single-crystal semiconductor surfaces, including the design of a direct-current heater (DCH) chamber and different sample holders, as well as the calibration of an electron beam evaporator (EBE).

In addition, Sec. 3.1.3 is intended to give an overview of the capabilities of ULEED,

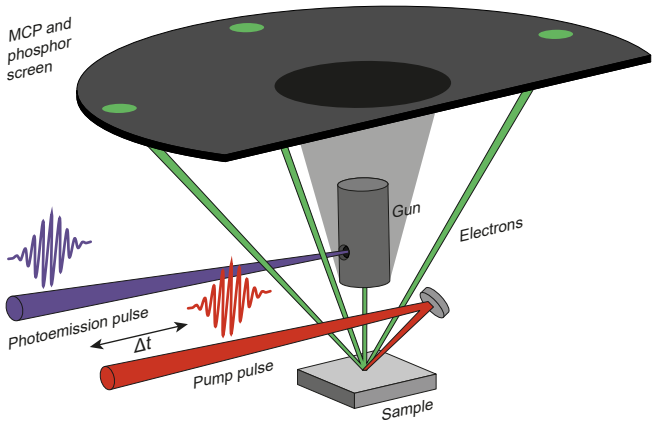

Figure 3.1: Basic concept of ULEED. Low-energy electron pulses from a laser-driven electron gun probe the state of the surface as a function of the delay time Δt with respect to optical excitation. Back-scattered electrons are detected on a microchannel plate (MCP).

featuring recent data from two types of miniaturised, ultrafast electron guns. These customised electron sources are at the heart of the ULEED apparatus, and will be briefly presented in Sec. 3.1.2. For a more detailed description of the different electron gun concepts for ULEED, the reader is referred to Refs. [54, 112, 120].

3.1 Ultrafast low-energy electron diffraction

LEED is a powerful tool for surface analysis (see also Sec. 2.3), providing access to the symmetry, atomic-scale structure and long-range order of the uppermost layers of solids. In this context, recent works from our group [17, 18, 54] have demonstrated how ultrafast photoemission of electrons from metallic nanotips [209, 210] can be harnessed to transfer the concept of LEED to the time-domain. Instead of a continuous electron beam, ULEED employs a beam of electron pulses to probe the state of a sample before/after timed optical excitation (see Fig. 3.1). Recording the LEED pattern as a function of the *pump-probe delay* Δt enables insights into the evolution of the surface structure on timescales determined by the optical and electron pulse durations. This *stroboscopic* approach is central to the experiment and requires control over as well as synchronisation of electron emission and propagation with sample excitation. A major challenge in realising ULEED is the dispersion-induced spatio-temporal broadening of electron pulses during propagation. One possibility to reduce this effect is to reduce the distance between the electron source and the sample harnessing miniaturised electron sources (hereafter referred to as "mm-sized gun" and "μm-sized gun" or "microgun"; see Sec. 3.1.2). The following paragraphs provide a description of the essential techniques and developments facilitating ULEED.

3.1.1 Laser system and optical setup

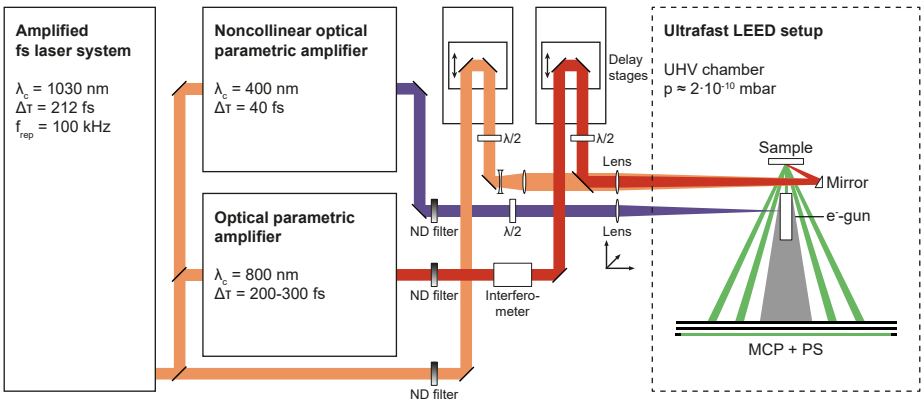

Figure 3.2: Optical setup for ultrafast low-energy electron diffraction (ULEED) setup used in this work. 1030 nm beam (P_1), orange; 800 nm beam (P_2), red; 400 nm beam, violet. Detailed layouts of the interferometer setups are shown in Fig. 3.3.

Various optical setups have been used throughout this work, allowing for the investigation of complementary observables such as the atomic structure (ULEED) or optical reflectivity (OPP) of sample surfaces. Moreover, different types of interferometers were harnessed to generate pulse sequences and exert control over phase transition efficiencies on ultrashort timescales.

The basic optics layout of the ULEED experiment is shown in Fig. 3.2: An Yb:YAG laser amplifier system (Light Conversion "Pharos", central wavelength $\lambda_c = 1030$ nm, $\hbar\omega = 1.20$ eV, pulse duration $\Delta\tau = 212$ fs, output power $P_{out} = 15\,\mathrm{W}$, repetition rate $f_{rep} = 100$ kHz[1], pulse energy $E_p = 150\,\mu\mathrm{J}$) pumps an optical parametric amplifier (OPA, Light Conversion "Orpheus", signal (idler) wavelength tunable between $\lambda = 630 - 1030\,(1030 - 2600)$ nm, $\hbar\omega = 1.96 - 1.20\,(1.20 - 0.47)$ eV, $\Delta\tau = 200 - 300$ fs) and a noncollinear optical parametric amplifier (NOPA, Light Conversion "Orpheus-N-2H"[2], signal wavelength tunable between $\lambda = 650 - 900$ nm

[1]For some measurements, the repetition rate was reduced to $f_{rep} = 25$ kHz to avoid cumulative heating of the samples.

[2]For the first experiments, the NOPA was used in its original 3H configuration. Here, the the nonlinear crystals are pumped by the third harmonic of the fundamental, that is, at 343 nm. The system was later modified to the 2H configuration ($\lambda_{pump} = 515$ nm) for technical reasons. However, the changes to the laser system did not have an influence on the outcome of the ULEED experiments.

($\hbar\omega = 1.91 - 1.38$ eV), or $\lambda = 325 - 450$ nm ($\hbar\omega = 3.81 - 2.76$ eV) after second harmonic generation (SHG) stage, pulse duration $\Delta\tau = 15 - 50$ fs).

The second harmonic NOPA output ($\lambda = 400$ nm, $\hbar\omega = 3.1$ eV, $E_{\mathrm{p,\,max}} = 500\,\mathrm{nJ}$, violet in Fig. 3.2) passes a set of neutral density (ND) filters for attenuation and a $\lambda/2$-plate to align the polarisation parallel to the nanotip inside the electron guns (see Sec. 3.1.2 for details on photoemission from nanoscale needle emitters and miniaturised electron sources). For experiments with the mm-sized electron gun, the UV pulses are focused through the main window of the UHV chamber (sapphire, CF160) onto the tip by a anti-reflex-coated fused silica lens (plano-concave) with focal length $l = 300$ mm. The significantly smaller entrance aperture of the μm-sized gun requires the use of an aspheric lens (focal length $l = 22$ mm) mounted on a xyz-piezo stage ("attocube") inside the UHV chamber (see Fig. B.3 in Appendix B).

A fraction of the amplifier output ($\lambda = 1030$ nm, $\hbar\omega = 1.20$ eV, 1.5 W at $f_{\mathrm{rep}} = 100\,\mathrm{kHz}$, $E_{\mathrm{p}} = 15\,\mu\mathrm{J}$, orange in Fig. 3.2) is coupled out by a beam splitter, attenuated and guided onto an optical delay stage to be used for timed optical excitation of the sample (P_1). The same happens with the OPA signal output P_2 ($\lambda = 800\,\mathrm{nm}$, $\hbar\omega = 1.55\,\mathrm{eV}$, $E_{\mathrm{p,\,max}} = 7\,\mu\mathrm{J}$, red in Fig. 3.2). Both P_1 and P_2 can be used in pump-probe experiments (single-pulse excitation). For measurements with two-pulse optical excitation, both NIR beams are combined collinearly via a dielectric mirror (highly-reflective at 800 nm) and focused onto the sample by a single anti-reflex-coated plano-concave lens (focal length $l = 400$ mm). To independently adjust the relative focus positions of the two beams along the optical axis[3], the divergence of the 1030 nm beam is controlled by a galilean telescope. Furthermore, to achieve the best possible temporal resolution in pump-probe experiments with the μm-sized gun, the signal output of the NOPA ($\lambda = 800$ nm, $\hbar\omega = 1.55$ eV, $E_{\mathrm{p,\,max}} = 2\,\mu\mathrm{J}$, see Fig. B.3 in Appendix B) was utilised for pumping.

To explore the effects of mode-selective excitation on the phase transition in atomic indium wires (see Sec. 6) and to identify the roles of different structural modes in the transition, two types of interferometers have been built (see Fig. 3.3a,b), which deliver either two (a) or four (b) identical pulses [59]. The mutual delays between excitations can be controlled by motorised linear delay stages (see Fig. 3.2 for location in the P_2 beam path). Scanning the frequency of the resulting 800 nm pulse

[3] The initial offset is due to chromatic aberration.

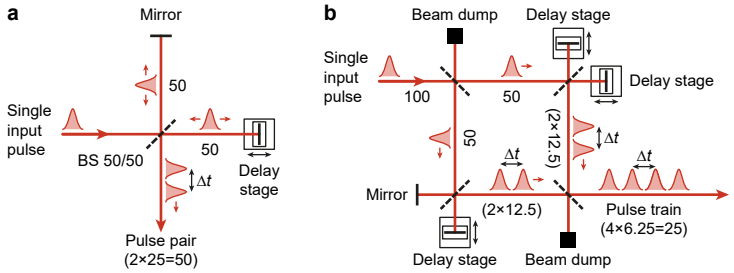

Figure 3.3: Optical interferometer setups for pulse pair (train) generation. **a**, Michelson interferometer setup providing pulse pairs at adjustable mutual delay. Numbers denote the fraction of the initial pulse energy in the different arms of the interferometer in percent. BS, beam splitter. **b**, Extended Michelson interferometer based on the scheme devised by Hase *et al.* [59].

trains across the frequencies of specific modes of the sample system and subsequently probing the state of the surface with ULEED enables experiments in analogy to two-dimensional optical spectroscopy (see, e.g. Ref. [211] and references therein), as will be discussed in Sec. 6.5.

All of the above experiments require a characterisation of the optical excitation, with results summarised below. In order to determine the temporal resolution $\Delta\tau_{\text{p-p}}$ in double-pump (multi-pump) experiments and to locate the temporal overlap (*time-zero*) between the different pump pulses, the P_1 and P_2 beams are collinearly focused onto a two-photon photodiode (GaAsP) for cross-correlation measurements (a typical data set is shown in Fig. 3.4a). For this, $\Delta\tau_{\text{p-p}}$ and the time-zero position $x_0 = x(\Delta t_{p-p} = 0)$ on the delay stage are extracted from the cross-correlation data by fitting a Gaussian model of the form

$$A(x) = \exp\left(-\frac{(x - x_0)^2}{2\sigma_x^2}\right) \tag{3.1}$$

to the normalised cross-correlation signal. Here, Δt_{p-p} is the mutual delay between two pulses, x the position of the optical delay stage[4] and $\sigma_x = (2\sqrt{2\ln(2)})^{-1}\,\sigma_{x,\text{FWHM}}$ the width of the cross-correlation peak. For the temporal resolution, it follows that

$$\Delta\tau_{\text{p-p}} = \sigma_{t,\text{FWHM}} = \frac{2\sigma_{x,\text{FWHM}}}{c} = \frac{4\sqrt{2\ln(2)}\,\sigma_x}{c}, \tag{3.2}$$

[4]One of the delay stages is fixed during the scan.

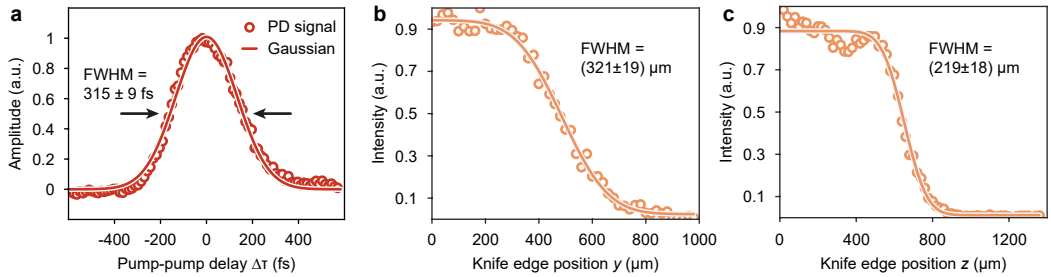

Figure 3.4: Spatio-temporal characterisation of optical excitation pulses. **a**, Cross-correlation of P_1 ($\lambda = 1030$ nm) and P_2 ($\lambda = 800$ nm) using a nonlinear photodiode. **b**, Intensity profile of the P_1 spot at the sample position along the y-direction, recorded in a knife-edge measurement. **c**, Intensity profile in z-direction. Intensity fluctuations for small z values are likely due to light scattering from a rough spot on the knife edge.

with c being the velocity of light. The corresponding error of $\Delta\tau_{\text{p-p}}$ is estimated in terms of the 95 % confidence interval (CI) of the fit. The spatial profile of the optical excitation is determined by a series of knife-edge measurements in the sample plane (yz-plane) inside the ULEED chamber (see exemplary data in Fig. 3.4b,c). Specifically, intensity profiles $I(y)$ (or $I(z)$) were recorded in y- and z-direction and for both 800 nm and 1030 nm beams, using a CCD camera placed outside the UHV chamber. The corresponding spot widths can be determined by means of a Gauss error function model fitted to each of the data sets:

$$I(z) = -I_0 \,\text{erf}\left(\frac{z - z_0}{\sqrt{2}\,\sigma_z}\right) + I_{\text{bg}}. \tag{3.3}$$

Here, I_0 is the maximum intensity of the laser spot, σ_z the spot width in z direction, and I_{bg} the constant background signal in the integrated images. Several consecutive measurements were combined to obtain the weighted mean values $\overline{\sigma}_y$ and $\overline{\sigma}_z$ and the corresponding errors. With this, the pump spot size $A_{\text{spot}} = 4\pi\overline{\sigma}_y\overline{\sigma}_z$ at the sample position and the excitation fluence F can be calculated via

$$F = \frac{P_{\text{cw}}}{f_{\text{rep}}\, A_{\text{spot}}}, \tag{3.4}$$

where P_{cw} is the continuous wave or average power of the pump laser and f_{rep} the repetition rate. This particular definition of F was chosen to be consistent with the definition used in the works of Frigge *et al.* [10, 56, 116] and thus allows for

a direct comparison of ULEED [53] and trRHEED [10, 56] measurements. Having characterised the optical excitation ("pump") we now turn to the heart of the ULEED setup, i.e. the miniaturised laser-triggered guns generating ultrashort electron pulses ("probe").

3.1.2 Miniaturized electron sources

Resolving details in the atomic structure and long-range order of surfaces requires diffraction experiments with both high sensitivity and k-space resolution. Furthermore, in the case of heterogeneous systems, μm to nm spatial resolution is desirable in order to extract diffraction information from small sample areas. However, following the *evolution* of the crystal lattice in real time additionally demands high temporal resolution, with structural changes in laser-excited materials occurring on a picosecond timescale. While conventional LEED – and SPA-LEED in particular – offer superior momentum resolution and very good signal-to-noise ratio, these methods lack temporal resolution. This has motivated the recent development and application of ultrafast LEED in our group [17, 18, 55], a key element being miniaturised electron guns driven by means of two-photon photoemission from tungsten needle emitters. The following paragraphs will focus on some technical aspects of these electron sources, including general remarks on ultrafast electron pulses, photoemission from metal nanotips and the two present gun designs. Again, for a more detailed review, the reader is referred to Refs. [112, 120].

The main challenge in ULEED is to prepare low-energy electron pulses with ps duration at the sample surface, while maintaining the coherence properties of the electron beam characteristic of conventional LEED. Like most time-resolved electron diffraction and microscopy schemes, the electron sources for ULEED are based on ultrafast photoemission [16, 19, 20, 22, 212–214]. Here, fs light pulses are focused onto a photocathode to generate electrons by means of the (nonlinear) photoelectric effect. Typically, cathode materials are chosen to select and harness specific emission channels (e.g. single-photon (1PPE), two-photon (2PPE) or multi-photon (MPPE), strong-field or thermally assisted photoemission) and/or to minimise the energy bandwidth of electron pulses by matching the photon energy $\hbar\omega$ to the work function ϕ (or vice versa). Frequently used materials include simple metals, such as gold, silver or tungsten, as well as refractory ceramics, with LaB_6 being a prominent

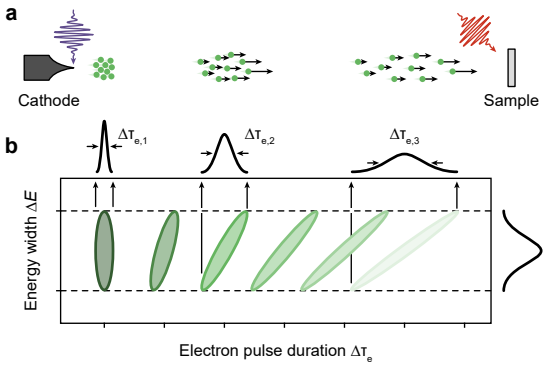

Figure 3.5: Dispersion induced broadening of electron pulses. **a**, Simple particle picture in real space: For a given energy distribution, photo-emitted electrons move towards the sample at different velocities. **b**, Phase space picture. Propagation corresponds to a shearing of the phase space density, which transforms the initial energy (momentum) distribution of the electrons into a temporal (spatial) distribution.

example. Due to the nature of the photoemission process (recall Fermi's golden rule [170]) the initial duration $\Delta\tau_e$ of the emitted electron bunch is of the order of the optical pulse duration $\Delta\tau$, or shorter.

At the same time, for a fixed propagation distance between source and sample, the final electron pulse duration is limited by several factors: First, from the above it is evident that $\Delta\tau$ determines the initial electron pulse duration. However, considering that commercial laser systems nowadays provide intense laser pulses with pulse durations short compared to the timescale of lattice dynamics, optical excitation is no longer a major obstacle for ultrafast electron diffraction and microscopy. Second, as the number of electrons in a bunch increases, Coulomb repulsion between the negatively charged particles leads to a broadening of the pulse in space and consequently in time[5] [212]. The effects of space-charged-induced broadening and the stochastic processes can be minimised by shortening the propagation time between source and sample, rapidly accelerating electrons to their final velocity, or reducing the number of electrons per pulse[6]. Third, depending on the emission geometry and the applied electrostatic potentials, electrons emitted at the same time but at different angles (positions) may follow trajectories of different lengths and thus arrive at the sample with a mutual delay. Most importantly for ULEED, however, the finite energy width ΔE of the electron kinetic energy spectrum strongly affects the final pulse duration. In photoemission, ΔE is given by the mismatch between the photon energy ($n \cdot \hbar\omega$ with $n \in \mathbb{N}$ for n-PPE) and the work function ϕ of the cathode ma-

[5]It should be noted that space-charge interactions also affect the kinetic energy distribution of the electrons [212].

[6]Over the last two decades, the development of ultrafast laser amplifier systems with repetition rates $f_{rep} > 100$ kHz has enabled experiments with less than one electron per pulse at sufficiently high signal levels.

terial. In a phase-space picture, due to the non-zero vacuum dispersion of electrons ($E = p^2/2m_e$), propagation of the electron bunch corresponds to a shearing of the associated phase space density and thus transforms the initial energy (momentum) distribution into a temporal (spatial) distribution (Fig. 3.5).

As will be shown below, ultrafast photoemission from metal nanotips [209, 210] (see Fig. 3.6) overcomes many of the above limitations and facilitates imaging and diffraction with high temporal resolution as well as excellent electron beam quality. In fact, whereas many time-resolved electron diffraction techniques, such as tr-RHEED [9, 10], ultrafast electron crystallography [215] or MeV diffraction [37, 214] employ planar photocathodes, e.g. nm-thick metal films on optically transparent substrates, electron sources for ULEED are based on needle emitters. This emitter geometry has significant advantages, among others, a very small source size and a rapid acceleration of the electrons. More specifically, in nonlinear photoemission from nanotips, electron emission is confined to the apex region of the tip due to the local enhancement of external optical fields (Fig. 3.6f, "lightning rod effect") [209, 210, 216]: For an n^{th} order emission process the photocurrent J is proportional to the n^{th} power of the light intensity I, which is highest at the apex (Fig. 3.6e). This way the effective source size A_s is reduced to the order of nm^2 (Fig. 3.6b), leading to a high transverse coherence of the electron beam[7] (for further discussion, see Sec. 3.1.3). Furthermore, the emission site can be controlled by means of electrostatic potentials. To this end, the negatively-biased tip is placed between a suppressor electrode and an extractor anode ($V_{\text{sup}} < V_{\text{tip}} < V_{\text{ext}}$, Fig. 3.6d). For a properly chosen voltage setting the electric field lines point away from the emitter only in the vicinity of the apex (Fig. 3.6c), allowing photoemitted electrons to leave the tip. Conversely, shaft and tip electrons emitted left of the cutoff-point (black line) are forced back to the tip surface and are thus suppressed.

The local field enhancement also has positive effects on the electron pulse duration: In the vicinity of the apex, the electric field of the negatively-biased tip resembles the field of a point charge[8], leading to a rapid acceleration of photoemitted electrons almost to their final energies within the first few nm of propagation [217]. This is in

[7] In contrast, for planar photocathodes A_s is roughly given by the the laser spot size on the cathode ($\sim \mu$m^2).

[8] In this case, the accelerating force $F(r) \sim E(r) \sim \frac{1}{r^2}$, with r being the radial distance from the apex.

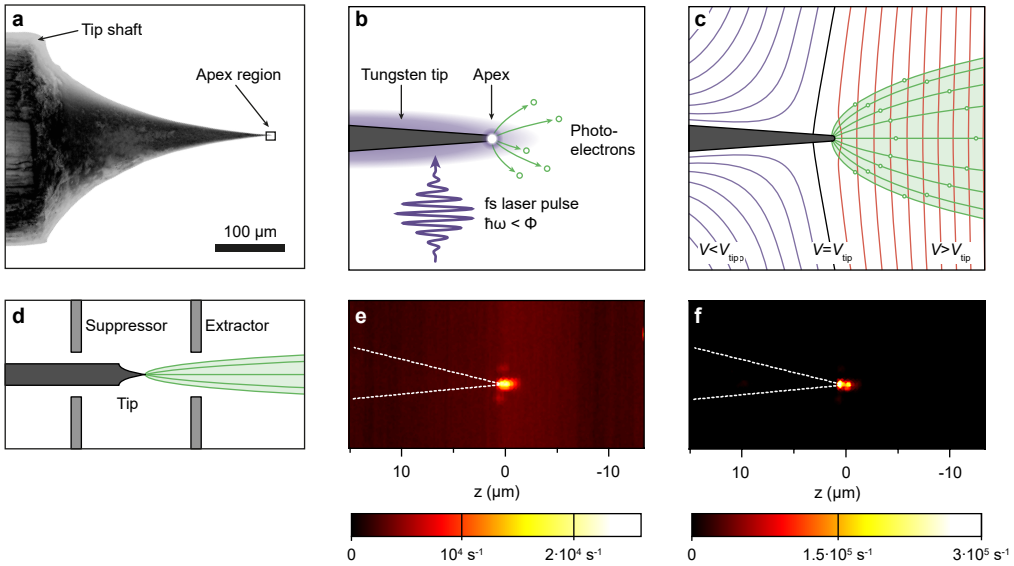

Figure 3.6: Principles of ultrafast nanotip photoemission. **a**, Scanning electron micrograph of a tungsten needle emitter, showing the shaft (typically around 250 μm in diameter) and the tip region tapering towards the apex. **b**, Schematic of the apex region and confinement of photoemission by nonlinear optical excitation. **c**, Typical electrostatic potential for the emitter setup shown in **d**. Red/violet lines, equipotential lines; green lines, electron trajectories; green points, electron positions on different trajectories for identical propagation times; black line, equipotential line with $V = V_{\mathrm{tip}}$. The intersection of the black equipotential line with the tip surface marks the cutoff point. **e**,**f**, Nonlinear light generation (**e**) and simultaneous electron emission (**f**) localized at the very end of an Au nanotip irradiated with 800 nm light pulses. Panels **e** and **f** adapted with permission from Ref. [210]. © 2007 by the American Physical Society.

stark contrast to planar photocathodes, where electrons are accelerated in a homogeneous electric field over significantly larger distances. Since space-charge as well as dispersion-induced broadening effects are particularly strong for slow electrons, and thus greatly affect the achievable temporal resolution in ULEED, the feasibility of the experiment heavily relies on localized photoemission from nanotips. In this context, analytical calculations by Refs. [217, 218] show that for a fixed distance from the electron source, acceleration in the spatially inhomogeneous field of a needle emitter results in significantly shorter electron pulse durations ($50 - 100$ times shorter) compared to a planar emitter geometry.

The advantages of nanotips as electron sources has been harnessed by a variety of fascinating experiments, including ultrafast low-energy electron diffraction in transmission [17] and reflection [18, 55, 219], ultrafast point-projection microscopy

[220–222], ultrafast TEM [23, 223, 224], or as sources for novel types of electron accelerators [225]. They are typically prepared by electrochemical etching of poly- or single-crystalline wires [226, 227] or focused ion beam milling [112]. For ULEED, tips are fabricated from a polycrystalline tungsten (W) wire measuring 250 μm in diameter, and the resulting apex radii range from 10 to 50 nm (Fig. 3.6a). Although the effect of field enhancement is more pronounced in materials with strong plasmonic resonances around the laser frequency, such as gold [228], tungsten was chosen for its high melting temperature, mechanical strength, good thermal conductivity and low vapor pressure [226]. With regard to photoemission, different crystal faces exhibit different work functions (4.47 eV for W(111), 4.63 eV for W(100) to 5.25 eV for W(110) [120]). Hence, for a 2PPE process with 400 nm pulses ($\hbar\omega = 3.1$ eV) – as used in this work – the maximum excess energy of photoelectrons is expected between $\Delta E_{\mathrm{max}} = 0.95 - 1.73$ eV [120].

As mentioned further above, in ultrafast experiments with few-electron pulses, the temporal resolution is mainly limited by dispersion-induced broadening. This poses a challenge for ULEED, as slowly propagating electrons are particularly susceptible to this effect. For example, after 15 mm propagation an electron pulse ($E_{\mathrm{kin}} =$ 100 eV) of fs initial duration and energy bandwidth $\Delta E = 1.5$ eV is stretched to approximately 20 ps (see also Fig. 3.7c). In this context, a number of different technical approaches have been pursued lately in order to minimise the effect of dispersion on the electron pulse duration: For studies of bulk materials[9], a variety of experiments employ high-energy electrons to reduce the electron time-of-flight with typical energies ranging from several tens of keV [16, 20] to the MeV [213] regime. Furthermore, the last years saw the successful development and application of radio-frequency (rf) or terahertz (THz) pulse compression schemes for electron pulses in this energy range [21, 229, 230].

While the applicability of such concepts to low-energy electron pulses is currently examined in our group, the most straightforward solution to reduce the effect of dispersion-induced pulse broadening in ULEED is to reduce the distance between electron source and sample. However, in LEED, electrons are recorded in back-scattering, and for decreasing distances between gun and sample distances,

[9] The case of trRHEED [9, 10, 16, 116] is a notable exception, since in RHEED surface sensitivity is achieved not by the energy-dependent mean-free path of the electrons but by the grazing incidence of the probe beam on the sample surface ($\sim 1°$).

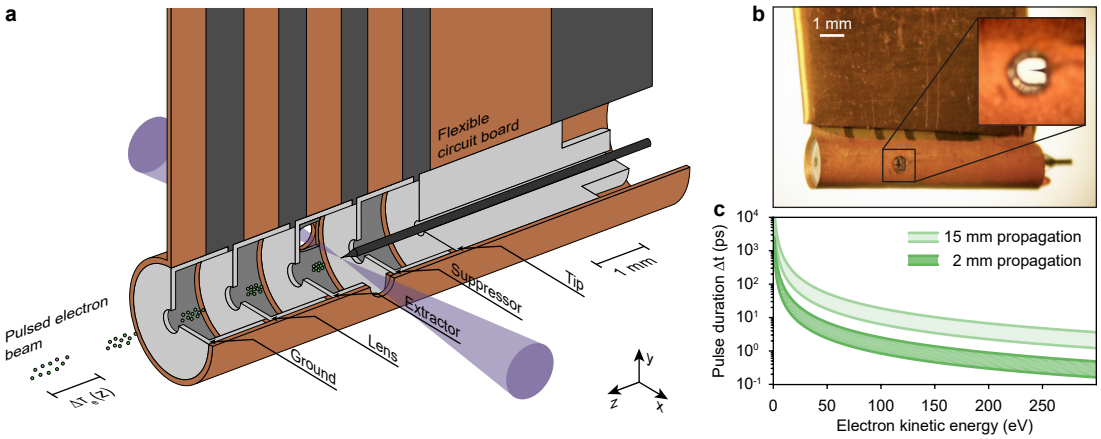

Figure 3.7: Details of the mm-sized electron gun. **a**, Schematic cross-section of the gun, showing the tungsten tip and the stainless steel apertures functioning as suppressor, extractor and an electrostatic einzel lens. Violet cone, fs UV laser focused onto the tip for optical excitation. **b**, Microscope image of the gun. Inset, magnified image of the tip inside the gun assembly. **c**, Electron pulse duration as a function of the electron kinetic energy for gun-sample distances of 2 mm and 15 mm. Upper and lower bounds correspond to kinetic energy spreads $\Delta E = 1.5$ eV and 0.5 eV, respectively. Figures **b** and **c** adapted from Ref. [120].

an increasing fraction of the LEED pattern is shadowed (see again Fig. 3.1 and Figs. 3.8d,e). This renders miniaturisation of laser-driven LEED guns inevitable. Considering that a conventional LEED gun consists not only of the emitter unit, but also of electron optics for beam collimation, this has been and still is a challenging task. In answer, over the last couple of years, Gero Storeck and co-workers from our group have developed two types of miniaturised laser-triggered electron guns. These electron sources are central to this work and will therefore be briefly introduced below. Details on the manufacturing can be found in Refs. [54, 112, 120].

The mm-sized gun (Fig. 3.7a,b) measures about 2 mm in diameter and allows for ULEED experiments with a temporal resolution of tens of picoseconds under realistic conditions (for detailed information on the pulse duration and momentum resolution see Sec. 3.1.3). The inner works of the gun consist of four cup-like metallic electrodes, which function as suppressor, extractor and an electrostatic einzel lens, and are insulated by thin polyimide (Kapton) rings (Fig. 3.7a). Electrons are generated by 2PPE from a tungsten tip (apex radius $r < 50$ nm) in a Schottky geometry (see Fig.3.6d) and pass the four metal apertures (hole diameter $d \approx 200\,\mu$m) to be collimated and accelerated towards the sample. The photoemission laser beam

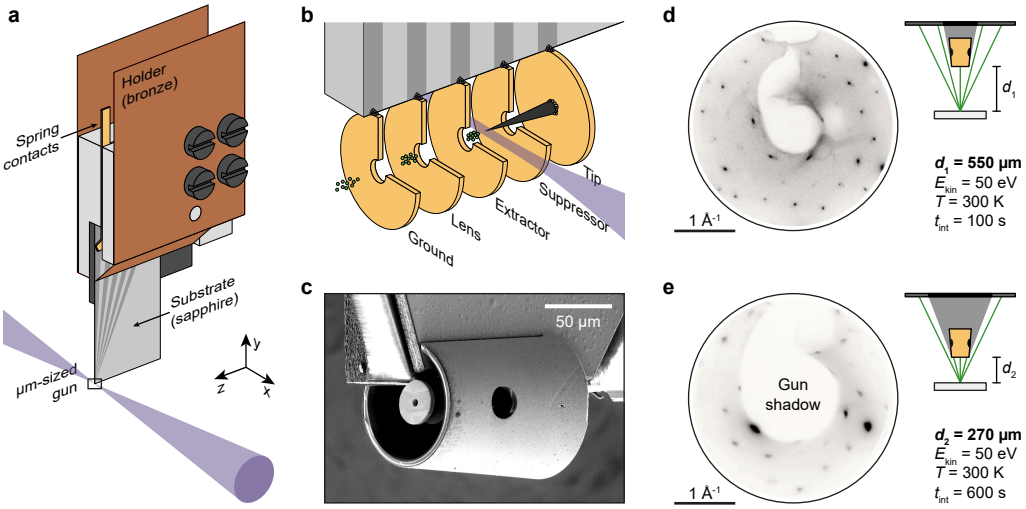

Figure 3.8: Details of the μm-sized electron gun. **a**, Schematic drawing of the microgun assembly including holder, substrate with metallic tracks as well as the gun itself (not visible, for position see small box). **b**, Enlarged section from (**a**, box) showing the tungsten needle emitter and Au apertures used for electron beam manipulation. **c**, Scanning electron micrograph of the μm-sized gun used in this work. **d**,**e**, Microgun diffraction images of the nearly commensurate phase of $1T$-TaS_2 recorded by Gero Storeck at gun-sample distances of 550 μm (**d**) and 270 μm (**e**). Figures **d** and **e** adapted from Ref. [54].

enters and leaves the gun through two aperture holes on the left and right (inset in Fig. 3.7b). The electrodes are held in position and contacted by a flexible printed circuit board wrapped around the gun assembly and covered with a thin copper layer for electric shielding. The mm-sized gun is typically operated at distances between 5 and 10 mm for electron energies between 20 and 160 eV, depending on the desired temporal resolution and the number of visible diffraction spots required for analysis.

To enable ULEED measurements on the intrinsic time scale of atomic motion, i.e. few picoseconds and below, Gero Storeck has miniaturised the concept of the mm-sized gun by another order of magnitude, resulting the the development of the μm-sized or "microgun" (Fig. 3.8a,b)[10]. In analogy to the mm-sized gun, the design is based on a tungsten needle emitter in a Schottky geometry combined with an electrostatic einzel lens. The four metallic electrodes are etched from a gold wire (diameter $d = 30\,\mu$m) using a focused ion beam device (FIB) and assembled on the

[10]The microgun used in this work was built by Felix Kurtz with assistance from Gero Storeck and Murat Sivis.

edge of a thin glass slide by platinum deposition (Fig. 3.8b). The platinum further contacts the electrodes to their respective contact lines, which are prepared on the surface of the glass slide in a photolithographic process. The nanotip is either cut from an existing tungsten tip or produced from a μm-thick tungsten wire by FIB milling. A metal-coated glass capillary surrounds the gun apertures to shield stray fields from the gun apertures (Fig. 3.8c, for further details on the gun architecture and further shielding steps see Ref. [54]). The laser is focused onto the tip through a 20 μm hole, which requires the focusing lens to sit inside the UHV chamber (see also Sec. 3.1.1). In summary, the microgun can be operated at sample distances well below 1 mm (see Fig. 3.8d,e) for electron energies between 20 and 105 eV.

3.1.3 Capabilities of the ultrafast LEED setup

The following chapter gives an overview of the capabilities of ULEED. From proof-of-principle experiments [217] to the observation and control of surface-specific structural dynamics [53], the technique has demonstrated its potential in various fields of surface science, including polymer and molecular dynamics at surfaces [217, 219], surface reconstructions on the μm scale [231], as well as ultrafast structural transitions and phase ordering kinetics in CDW systems [18, 53, 55]. Of crucial importance for all these experiments is the high temporal and momentum resolution of the two ultrafast electron guns, which will be reviewed first for this reason.

To demonstrate and compare the characteristics of the mm-sized and μm-sized guns, it is instructive to analyse ULEED diffraction images and time traces of 1T-TaS_2, an extensively studied CDW model system [6–8, 18, 55, 94]. Figures 3.9a and b display high-quality diffraction patterns of the nearly-commensurate (NC) CDW phase of 1T-TaS_2 at room temperature, formed by 100 eV electron pulses from the mm-sized gun (a) and the microgun (b). By analysing the spot profiles in both LEED patterns, the momentum resolution of the corresponding setup can be determined[11]. Specifically, for each image the cross-section through the sharpest

[11] Note that the diffraction patterns shown in Figs. 3.9a and b were taken of distinct TaS_2 samples and are therefore likely to feature different intrinsic spot widths. In this context, future measurements using a single sample will enable an even more thorough comparison.

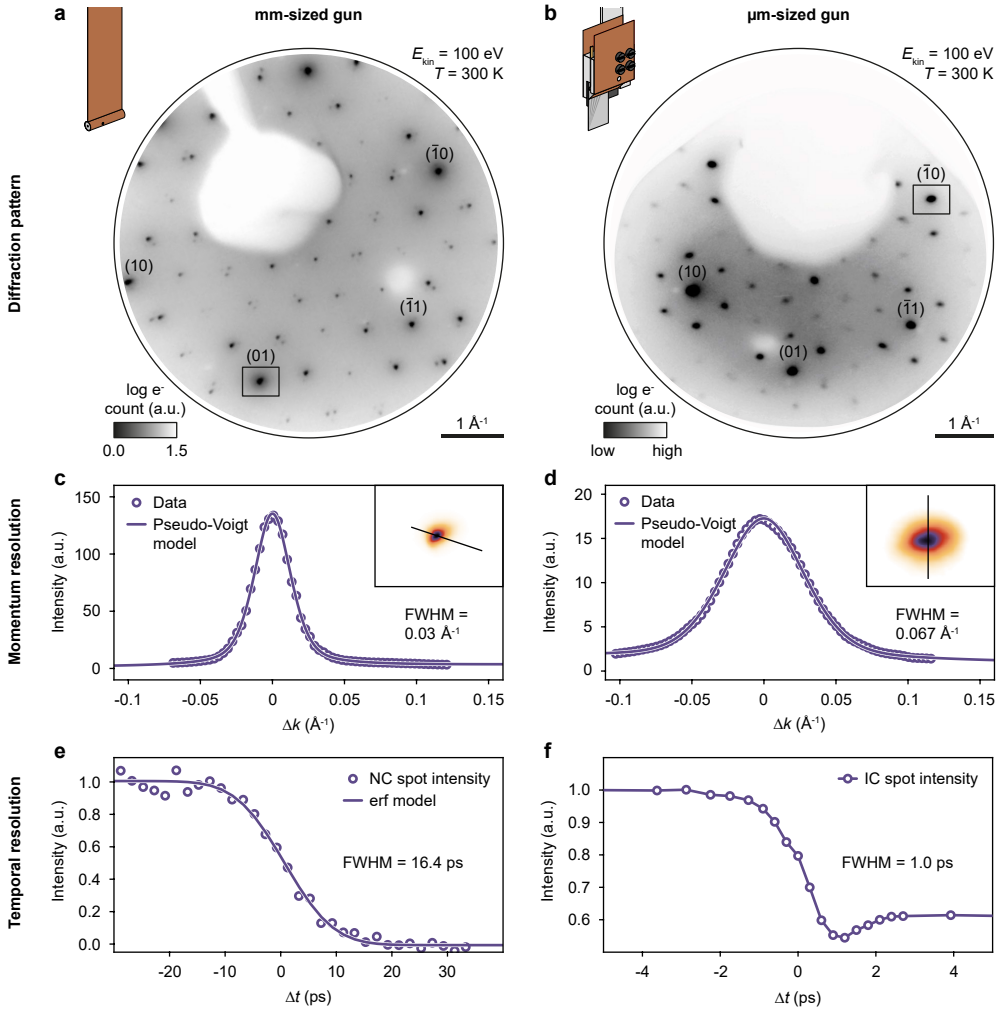

Figure 3.9: Momentum and temporal resolution of mm- and μm-sized electron guns. **a**,**b**, Diffraction images from the nearly-commensurate phase of 1T-TaS_2 taken by a mm-sized (**a**, integration time $t_{\mathrm{int}} = 180$ s) and a μm-sized (**b**, $t_{\mathrm{int}} = 90$ s) electron gun. **c**,**d**, Estimated transfer widths w_{t} achievable with (**a**) the mm- and (**b**) the μm-sized gun. **e**,**f**, Temporal resolution of both guns, determined from the time-dependent spot intensities after optical excitation of the TaS_2 surface. Figures **a**, **c** and **e** adapted from Ref. [18]; Figures **b** and **f** adapted from Ref. [112].

Bragg spot is fitted by the pseudo-Voigt model

$$I(x) = I_0 \left(\eta \left[\frac{1}{1 + \frac{4(x-x_0)^2}{\sigma_k^2}} \right] + (1-\eta) \left[\exp\left(-4\ln(2) \frac{(x-x_0)^2}{\sigma_k^2} \right) \right] \right) + bx + c, \quad (3.5)$$

with x being the coordinate along the cross-section, I_0 the spot intensity, $0 < \eta < 1$ a dimensionless parameter determining the line shape (Gaussian for $\eta = 0$; Lorentzian for $\eta = 1$), and σ_k the FWHM of the pseudo-Voigt line profile. For the mm-sized gun $\sigma_k^{\mathrm{mm}} = (3.0 \pm 0.4) \cdot 10^{-2}\,\text{Å}^{-1}$, and the corresponding transfer width in real space is given by $w_{\mathrm{t}}^{\mathrm{mm}} = 2\pi/\sigma_k^{\mathrm{mm}} = (21 \pm 3)$ nm (see Eq. 2.53 in Sec. 2.3.3). An analogous calculation yields a value of $\sigma_k^{\mu\mathrm{m}} = (6.7 \pm 0.1) \cdot 10^{-2}\,\text{Å}^{-1}$ in the case of the microgun, and a transfer width $w_{\mathrm{t}}^{\mu\mathrm{m}} = (9.3 \pm 0.2)$ nm. Hence, the k-space resolution of both ULEED experiments is at least comparable to state-of-the-art LEED systems, which typically achieve transfer widths between 10 and 30 nm [120, 232]. In this context, the high momentum resolution of ULEED has recently been harnessed to investigate phase-ordering dynamics in the nascent incommensurate (IC) CDW phase of 1T-TaS_2 via time-resolved spot-profile analysis [18].

In a next step, the structural response of the 1T-TaS_2 surface following optical excitation can be used to determine the temporal resolution in both types of ULEED experiments (Fig. 3.9e,f). Specifically, for laser pump fluences $F > 2.5\,\mathrm{mJ\,cm^{-2}}$, the material undergoes a temperature-induced transition between the room temperature NC and the IC phase, which is stable above 353 K. The underlying structural changes are mirrored by the suppression and enhancement of subsets of diffraction spots, each of which can be associated with one of the two phases. Moreover, femtosecond electron diffraction in transmission [8] has found an upper limit of 350 fs for the time constant of the NC-IC transition. With this knowledge, given the electron energy and the distance between electron gun and sample, the temporal resolution in ULEED can be estimated by fitting an error function model[12] to the delay-dependent NC spot intensity (see Fig. 3.9e). This results in values of $\Delta\tau^{\mathrm{mm}} \approx 17\,\mathrm{ps}$ for the mm-sized gun[13] and $\Delta\tau^{\mu\mathrm{m}} \approx 1$ ps for the microgun. Hence, whereas the mm-sized gun allows for the investigation of metastable states, phase ordering processes or energy relaxation on a ps-ns time scale, the superior temporal resolution of the microgun makes it an ideal tool to directly track the (coherent) atomic motion underlying structural transitions.

[12] In the case of the mm-sized gun, the temporal resolution is large compared to the intrinsic time constant of the structural transition. The latter can therefore be neglected. As for the microgun, the model for fitting is given by the convolution of an error function and a Gaussian (FWHM= 350 fs) to account for the finite time constant of the phase transition.

[13] In order to capture as many diffraction spots as possible the mm-sized gun is usually operated at larger distances from the sample ($\sim 5 - 8$ mm) and a temporal resolution of 40-45 ps.

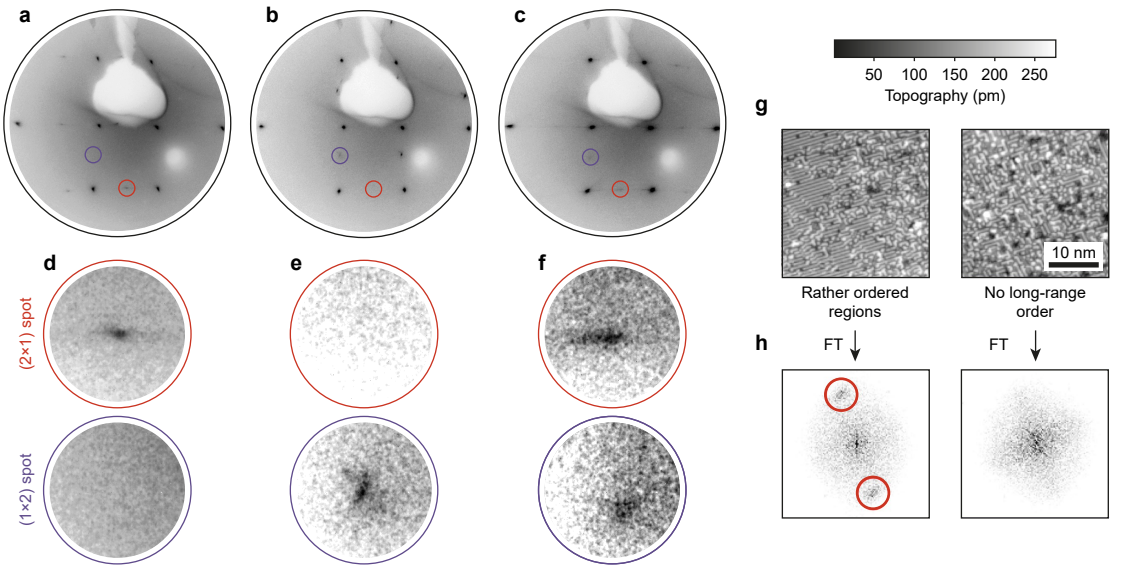

Figure 3.10: Micro-diffraction capabilities of the ULEED setup. **a-c**, LEED patterns recorded with the mm-sized electron gun at different positions of a freshly cleaved $LaB_6(001)$ surface exhibiting two distinct surface reconstructions ($(2 \times 1)/(1 \times 2)$) in μm-sized areas. **d-f**, Selected regions of the diffraction images in (**a**)-(**c**), showing only the (2×1) reconstruction (**a**,**d**), only the (1×2) reconstruction (**b**,**e**), and a superposition of signals from both superstructures (**c**,**f**). Note that the superstructure spots are not observable in conventional LEED because of the typically larger spot diameter. **g**, STM topography of the surface, showing areas with (left) and without (right) a rather long-range ordered reconstruction. **h**, 2D Fourier transform of the STM topography. Adapted with permission from Ref. [231]. © 2019 by the American Physical Society.

In addition to the high temporal and momentum resolution, a major advantage of ULEED is the small electron spot size on the sample, which is a direct consequence of gun miniaturisation and the use of needle emitters as high-brightness electron sources. This endows ULEED experiments with μm spatial resolution and enables the investigation of particularly heterogeneous surfaces. The electron spot size in ULEED is inferred from knife-edge measurements of the collimated beam in the sample plane (mm-sized gun) or transmission through TEM grids with predefined aperture dimensions (microgun). Whereas the mm-sized gun offers an electron spot size smaller than 80 μm in diameter, the microgun spot is significantly smaller at 5-10 μm, mainly depending on aperture dimensions. Considering that many materials can often only be synthesised in the form of sub-mm single crystals, the small spot diameters of the miniaturised electron guns offer a decisive advantage over standard

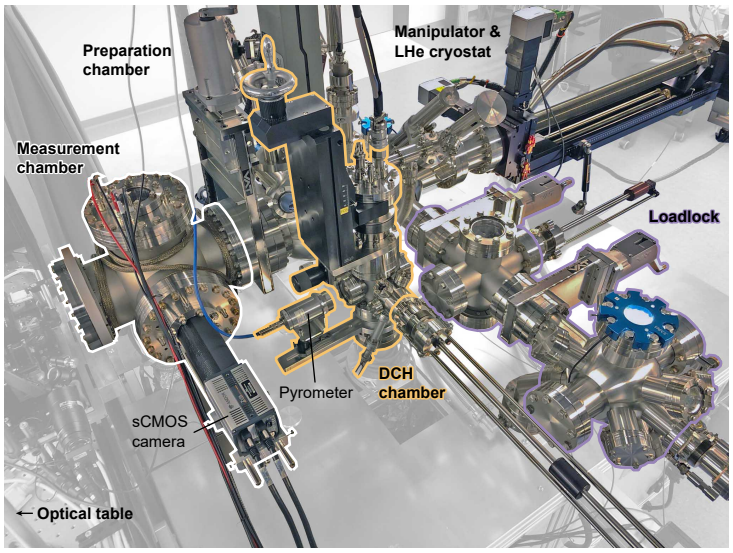

Figure 3.11: UHV setup for ULEED, including the load lock chamber (violet) enabling high sample throughput as well as sample storage, and the preparation section (back, middle) equipped with an Ar sputter gun, an EBE, a gas inlet, and a mass spectrometer. Semiconducting samples are prepared in a side chamber (yellow) where the DCH is installed. The samples are transferred by a motorised manipulator with integrated continuous-flow LHe/LN_2 cryostat (back, left). The electron guns and MCPs are mounted in the measurement chamber (white) next to the optical table.

LEED setups. Furthermore, even single crystals cleaved *in-situ* potentially exhibit surface inhomogeneities on a μm length scale, as exemplified by the case of the (001) surface of LaB_6 [231] (see Fig. 3.10). As evident from STM measurements (Fig. 3.10g, left), this particular surface forms rather long-range-ordered (2×1) or (1×2) superstructures in sample areas smaller than $100 \times 100\,\mu m^2$. For conventional LEED systems with electron spot sizes of several mm in diameter, such local reconstructions are not observable since the diffraction pattern is spatially averaged over large parts of the crystal surface. In contrast, the μm electron spot in ULEED allows to individually study areas with either dominant contributions of either (2×1) or (1×2) domains (see Fig. 3.10a-f). In summary, by combining the advantages of ultrafast nonlinear photoemission from nanotips with miniaturised electron optics, ULEED allows for insights into structural dynamics in a variety of different surface systems, combining high angular, temporal and spatial resolution.

At the same time, the constant expansion of sample preparation capabilities further broadens the range of examinable materials: Over the course of this work, the

ULEED chamber has been extended by a direct current heater (DCH) section (see yellow part in Fig. 3.11 and Sec. 3.3) and an optical pump-probe setup (see Sec. 3.2). In addition, various preparation techniques have been established, including several cleaving procedures, argon sputtering and subsequent annealing of surfaces via electron beam heating (EBH), deposition of metals using electron beam evaporation (EBE), evaporation and temperature-programmed desorption (TPD) of molecules as well as flash-annealing of semiconducting samples. The complete UHV chamber in its current state is shown in Fig. 3.11, including a load lock for high sample throughput (violet), the preparation chamber (background) equipped with a motorised cryo-manipulator, EBE, EBH, gas inlet, sputter gun and mass spectrometer, the DCH section (yellow) and the measurement chamber (white) equipped with the electron guns, two MCPs and a sapphire window for optical excitation.

3.2 Optical pump-probe spectroscopy

While ULEED provides detailed insights into atomic motion at the surface, information about the electronic response after ultrafast optical excitation can at best be obtained indirectly from diffraction images. Especially in the case of materials with strong couplings and correlations between electrons and phonons, it proves difficult to unambiguously assign specific observations, e.g. changes in diffraction spot intensity in LEED, to either of the two subsystems. A more comprehensive picture of the dynamics in such systems can often be obtained by a series of complementary experiments observing either the electronic or phonon subsystem. This approach is exemplified by various studies on complex materials, such as $1T$-TaS_2 [6–8, 18, 55, 94] or VO_2 [1, 2, 50].

In this respect, the Si(111)(8×2)-In surface is by no means an exception, as will be discussed in Sec. 4. Therefore, to investigate not only the structural evolution, but also the optical properties of the indium monolayer following optical excitation, the ULEED experiment has been supplemented by an optical pump-probe spectroscopy (OPP) setup (Fig. 3.12). This way it is possible to measure the transient reflectivity R of the In/Si(111) surface and relate its optical response to the transient structure of the sample observed in ULEED.

In OPP, a pump pulse ($\lambda_c = 1030$ nm, $f_{rep} = 100$ kHz, $\Delta\tau = 212$ fs) excites the sample surface, e.g. by inducing optical transitions in the electronic band structure

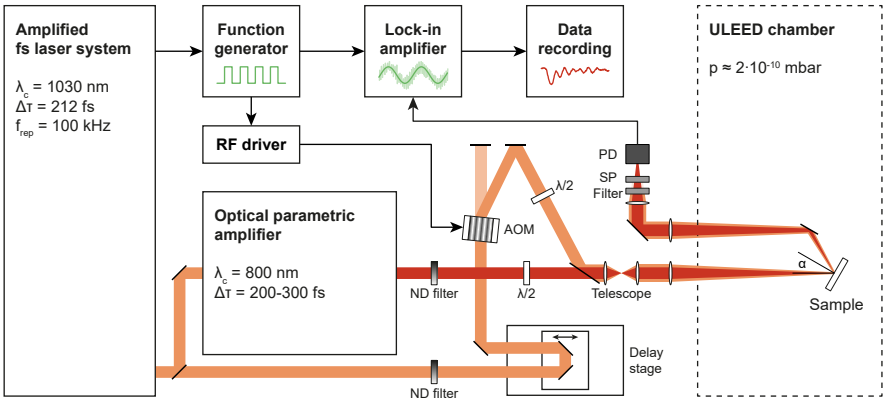

Figure 3.12: Experimental setup for optical pump-probe spectroscopy. 1030 nm beam (P_1), orange; 800 nm beam (P_2), red; SP filter, short-pass filter; PD, photodiode.

$E(\boldsymbol{k})$. Because of the direct relation between $E(\boldsymbol{k})$ and the complex dielectric function $\epsilon(\omega)$, excitations of the electronic subsystem also influence the optical properties of a solid, i.e. its reflectivity, absorption A and transmittance T (see also Sec. 2.3.4). Moreover, ultrafast optical excitation may induce phase transitions and/or generate coherent phonons by means of ISRS or DECP (see Sec. 2.2.2). In case of Raman-active phonons, this leads to periodic modulations of R, A and T (see Sec. 2.3.4). In transient reflectivity measurements, changes ΔR are monitored as a function of the time-delay $\Delta t_{\text{p-pr}}$ by an optical probe pulse ($\lambda_c = 800\,\text{nm}$, f_{rep}=100 kHz, $\Delta\tau = 230\,\text{fs}$) reflected from the sample surface. Hence, the temporal resolution of the experiment is given by the cross-correlation of the 1030 nm and 800 nm pulses (see Fig. 3.4a in Sec. 3.1.1).

In this work, pump and probe pulses from the Yb:YAG amplifier and OPA are collinearly focused onto the sample at an incident angle $\alpha = 31°$. The two beams are polarised perpendicular in order to avoid nonlinear interactions (e.g. electro-optic Kerr effect) of pump and probe pulses inside the optics. These typically cause additional features in pump-probe traces, which are, however, not related to electronic or structural dynamics at the sample surface. The reflected beam is guided through two short-pass filters (2× OD4 for $\lambda > 900$ nm) to attenuate the pump light, and subsequently focused onto a silicon photodiode. As in the case of ULEED, the mutual time delay between the pump and probe pulses is controlled by an optical delay stage.

Furthermore, a lock-in detection scheme is harnessed to enhance the signal-to-noise ratio of the reflectivity measurement. For this, the pump intensity is modulated at a frequency $f_{\mathrm{mod}} = 25$ kHz by an acousto-optic modulator (AOM) synchronized to the laser system via a function generator. The photodiode and reference signals are processed in a lock-in amplifier (Stanford Research Systems SR830). Multiplying and integrating both inputs over time, the amplifier yields a DC signal that is extremely sensitive to changes at the reference frequency, due to the orthogonality of sinusoidal functions. Since the pump beam is modulated at f_{mod}, the sensitivity to pump-induced changes (and consequently the signal-to-noise ratio) increases by orders of magnitude. Employing a two-phase lock-in amplifier, amplitude and phase of the measured signal can be analysed independently. The additional phase information is used to determine the sign of ΔR. Overall, the setup enables the observation of small changes in R associated with electronic or structural dynamics of the indium monolayer on Si(111).

To ensure the comparability of OPP and ULEED data sets, the condition of the Si(111)(8×2)-In surface is examined by ULEED (pump-probe experiments) before and after OPP measurements. Moreover, in analogy to Fig. 3.4b,c, pump and probe spot sizes are determined for the OPP excitation geometry by means of knife-edge measurements in the sample plane. Finally, regarding sample temperature, the same integrated continuous helium cryostat is used for both ULEED and OPP experiments (see also Sec. 3.3).

3.3 Sample preparation

Whereas the development of ULEED and OPP enable the investigation of surface dynamics with high temporal resolution, preparing surfaces with reproducible high quality is a challenge in itself. Adsorption of atoms or molecules as well as surface reactions may alter the physical and chemical properties of a surface and pin particular phases in phase change materials. In this regard, the sample system investigated in this work, i.e. of indium nanowires on the (111) surface of silicon [102], is no exception (for details, see Sec. 4.5). As a consequence, all steps of the sample preparation had to be carried out under ultra-high vacuum conditions (typical base pressure $p < 2 \cdot 10^{-10}$ mbar) in order to minimize surface defects from adsorption, which were found to have a significant influence on the phase transition dynamics

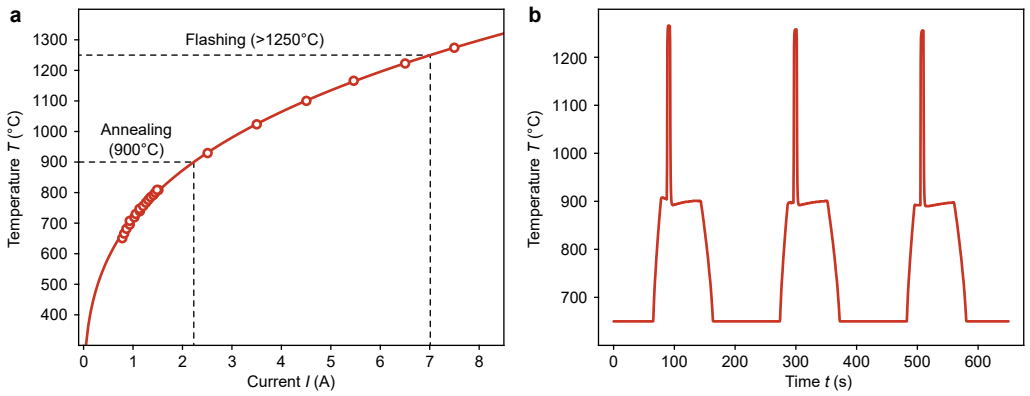

Figure 3.13: Calibration of the direct current heating and sample preparation. **a**, Surface temperature T measured by the pyrometer as a function of the current I through the sample. Dashed lines indicate the typical temperatures (currents) used for flash- or post-annealing, respectively. To obtain the calibration curve (solid red line), a model function of the form $T(I) = a \cdot I^b$ is fitted to the data (see also Ref. [116]). **b**, Typical flash-annealing cycles prior to indium evaporation.

in this system [9, 117, 233, 234].

The samples were prepared by flash-annealing Si(111) wafers (3×11 mm, phosphorous doped, resistivity $R = 0.6 - 2$ Ωcm) at $T_{\text{max}} > 1250$ °C via direct current heating (DCH). In order to be able to control the temperature T during the preparation process, a pyrometer (Optris CTvideo 1MH) was used to measure the surface temperature of the wafer as a function of the current I (see Fig. 3.13a). Based on this calibration, a clean Si(111)(7×7) reconstruction was prepared by pre-annealing the surface at 900 °C, flashing for 5 seconds at temperatures $T_{\text{max}} > 1250$ °C and subsequent post-annealing at 900 °C (typically three cycles, see Fig. 3.13b). The maximum pressure during flashing was kept below $p_{\text{max}} = 2 \cdot 10^{-9}$ mbar.

The indium nanowires array was grown by evaporating 1.2 monolayers (ML) of indium at a rate of about $8 \cdot 10^{-3}$ ML/s onto the Si(111)(7×7) surface reconstruction at room temperature. Subsequent annealing at $T = 500\,°\text{C}$ for 300 s via DCH resulted in a high-quality (4×1) phase (see Fig. 4.2 in Sec. 4.2.1), as verified in the ULEED setup. After inspection of the (4×1) phase, the samples were immediately cooled down to a base temperature of $T < 60$ K using an integrated continuous flow helium cryostat. The phase transition between the high-temperature (4×1) and the low-temperature (8×2) phase was observed at 125 K, which indicates a relatively

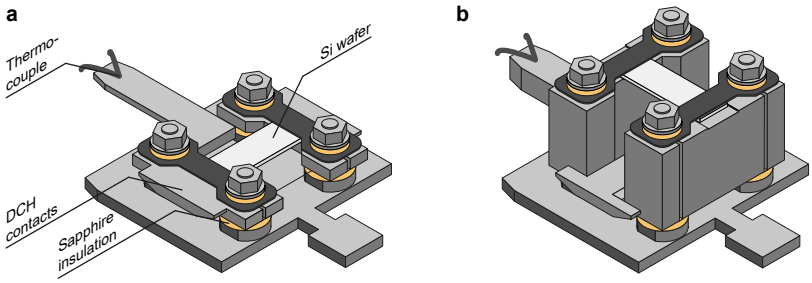

Figure 3.14: **a**, Sample holder design used for measurements with the mm-sized electron gun. **b**, For experiments with the microgun the holder design had to be adapted to enable sample excitation and probing at small working distances of less than 1 mm.

low initial density of adsorbate on the pristine Si(111)(4×1)-In surface [233].

The two types of miniaturised electron guns (mm- and μm-sized) required different sample holder designs (see Fig. 3.14a,b). In case of the μm-sized electron source, the corresponding holder (Fig. 3.14b) enables measurements at gun-sample distances well below 1 mm without clipping the UV beam that triggers pulsed electron emission from the tip. The holders have been designed to be both compatible with the DCH manipulator and suitable for use at cryogenic temperatures, and are made from molybdenum (conducting parts) and sapphire (insulating parts). To minimise outgassing during the flashing procedure, new sample holders were heated to 300 °C for several hours using an electron beam heater (EBH).

Chapter 4

Atomic indium wires on Si(111)

To steer nonequilibrium transitions between different states of matter requires simultaneous optical control over the decisive electronic, lattice or spin degrees of freedom. With increasing complexity of a physical system, the coherent control of its atomic-scale dynamics becomes more challenging, mainly due to the growing number of degrees of freedom [41]. This leads to three main complications: First, complex transitions between initial and final states typically involve many relevant degrees of freedom, e.g. different vibrations connected to a transition, which must be controlled simultaneously by tailored optical excitation. Second, because of the resulting high electronic or vibrational density of states, the excitation of relevant electronic states or structural modes must be highly selective in order to be effective. Third, after excitation, the coupling between different degrees of freedom and subsystems typically results in a fast energy redistribution away from key states or vibrational modes, and thus to a damping or dephasing of coherences.

While the synthesis of optical light fields has greatly expanded the toolbox of femtochemisty in the gaseous [38, 39] and the condensed phase [41], it is the complexity inherent to chemical or physical systems that restricts coherent control to relatively simple systems, e.g. molecular reactions. Therefore, regarding the transfer of concepts from femtochemistry to structural phase transitions in solids, the complexity of candidate materials plays a major role. A model system should exhibit very few decisive degrees of freedom, i.e. phonon modes, governing the transformation between two distinct structures. On the one hand, these modes should couple strongly to specific electronic states to facilitate direct optical excitation. On the other hand, to maintain coherences, they should couple only weakly to other modes and finally

the external heat bath. Such a model system would evolve from an initial to a final state on a transient Born-Oppenheimer potential energy surface shaped by precise electronic excitation [66]. In other words, we are looking for solid-state systems, simple enough to exhibit structural phase transitions that strongly resemble elementary molecular reactions.

As discussed in Sec. 2.1, the most obvious manifestation of complexity is dimensionality. Reducing the dimensionality of a system generally reduces the phase space volume, that is, the number of electronic and vibrational degrees of freedom [70]. In this respect, strongly-correlated quasi-one-dimensional solid-state systems are promising intermediates between molecules and bulk solids, and often exhibit intriguing phenomena, such as superconductivity [81], spin ordering [86] or Peierls transitions [102, 235, 236] (see also Sec. 2.1.1, or Ref. [70]).

One of the most intensively studied classes of quasi-one-dimensional materials are metallic nanowires on semiconducting substrates, which show a variety of phenomena including dimensional crossovers [129], charge density waves [102] or non-Fermi-liquid behaviour [80]. Of particular interest for this work is the system of atomic indium wires on the (111) surface of silicon [102, 177], which undergoes a metal-insulator structural phase transition from a (4×1) to a (8×2) surface reconstruction below the critical temperature $T_c = 125$ K. A multi-band Peierls instability [237] and an exothermic reaction [238], both linked to shear and a rotation phonon modes of the indium layer [107, 239, 240], have been proposed as possible driving mechanisms for the transition. Moreover, it has recently been shown that the (8×2) → (4×1) transition can be driven well below T_c by means of ultrafast electronic excitation and the generation of localized photo-holes at specific points of the Brillouin zone [10, 11, 241]. In this case, density functional theory (DFT) predicts a strong coupling of excited electronic states to shear and rotation phonons realising the structural transition. At the same time, the weak coupling of these modes to lower-lying optical or acoustic phonons of the indium wires and the substrate found in recent trARPES [57] promises long-lived vibrational coherence in decisive degrees of freedom. Altogether, this renders indium on Si(111) and ideal system to test the applicability of coherent control schemes to low-dimensional solids.

The following chapter gives an introduction to the materials system of indium on Si(111) and an overview of the research work carried out to date. Special attention is paid to the mechanism underlying the phase transition, the interactions between

electronic structure and lattice as well as the role of shear and rotational modes.

4.1 Adsorbate-induced surface reconstructions of silicon

Single-crystalline silicon (Si) is the cornerstone of semiconductor electronics. It crystallises in a diamond cubic crystal structure with a lattice constant $a = 5.43$ Å (see Fig. 4.1a) and exhibits an indirect band gap of $\Delta E_g = 1.17$ eV (at $T = 0$ K)[1]. Its (111) surface is one of the most extensively studied solid-state surface systems. It gained special attention in 1985, when Binnig *et al.* [242], in one of the first ever STM experiments, spatially resolved the (7×7) reconstruction of the surface and thus settled the long-standing debate over its ground state structure. In this work, the Si(111)(7 × 7) surface has been used as a substrate for the growth of quasi-one-dimensional atomic indium wires.

While the (7×7) structure represents the energetically most favorable state, freshly cleaved silicon crystals typically exhibit a (2 × 1) reconstruction. The (7×7) and (2 × 1) configurations are separated by an energy barrier. To overcome the barrier to the (7×7) structure, the surface has to be annealed at temperatures $T > 850\,^{\circ}$C. Figure 4.1b shows the LEED pattern of a Si(111)(7×7) surface recorded with 130 eV electron pulses at room temperature, directly after flash-annealing (see Sec. 3.3 for details of the preparation process). For the (111) surface, the effective lattice constant $a_{(111)}$ and the distance between adjacent diffraction planes $d_{(111)}$ are given by $a_{(111)} = a/\sqrt{2} = 3.84$ Å or $d_{(111)} = \sqrt{3}/2 \cdot a_{(111)} = 3.33$ Å, respectively. The length of the associated base vectors of the reciprocal lattice in LEED is $|\mathbf{g}_1| = |\mathbf{g}_2| = 2\pi/d_{(111)} = 1.89\ \text{Å}^{-1}$.[2]

Besides its intrinsic properties, the Si(111)(7×7) surface is of special interest for another reason: it exhibits a multitude of surface reconstructions induced by chemisorption of metal atoms, e.g. aluminium (Al) [177], lead (Pb) [243], gold (Au) [244, 245] or indium (In) [177]. Figure 4.1c depicts the exemplary case of indium adsorbed on the Si(111) surface for different submonolayer coverages and substrate temperatures. Similar reconstruction effects can be observed on several

[1] Note that ΔE_g changes only slightly as a function of temperature T. At room temperature, $\Delta E_g = 1.12$ eV. However, the band structure can be significantly altered by doping, which also impacts the optical, thermal and electronic properties of Si.

[2] Concerning the electronic band structure measured by ARPES, the dimension of the first Brillouin zone is given by $2\pi/a_{(111)} = 1.63\ \text{Å}^{-1}$.

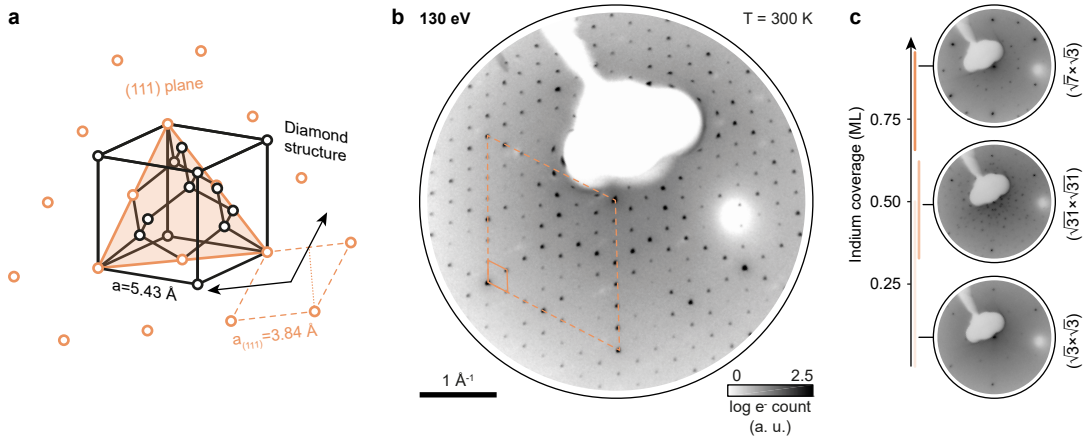

Figure 4.1: Properties of the (111) surface of silicon. **a**, Unit cell of bulk silicon (black). Silicon crystallises in a diamond cubic crystal structure. The (111) plane and in-plane silicon atoms are highlighted in orange. Dashed rhombus, hexagonal surface unit cell of Si(111); dotted line, lattice plane distance $d_{(111)}$. **b**, LEED pattern of the (7×7) structure recorded at room temperature with 130 eV electron pulses. Dashed orange line, reciprocal unit cell (RUC) of the unreconstructed Si(111) surface; solid orange line, RUC of the (7×7) reconstructed surface. **c**, LEED patterns of the $(\sqrt{3} \times \sqrt{3})$R30°, $(\sqrt{31} \times \sqrt{31})$R9° and $(\sqrt{7} \times \sqrt{3})$R9° structures recorded at room temperature with 130 eV electron pulses. The scale on the left indicates the indium coverage for each of the three phases.

other surfaces of silicon [129, 244–248] and various semiconductors, e.g. germanium (Ge) [249]. Generally, the formation of bonds between the semiconducting substrate and adatoms results in drastic changes of the electronic [246, 250, 251], structural [101, 177] or spin properties [248] of the reconstructed surface. Arguably the most fascinating phenomenon observed in this class of materials is the formation of quasi-one-dimensional atomic wires, as observed for Pb on Si(557) [246], Ag on Si(557) [247], Sn on Si(557) [252], Au on Ge(111) [249], Au on Si(111) [244, 245], or Au on Si(553) [129, 248]. However, it is In on Si(111) [102, 177] that has received the most attention.

Indium-induced reconstructions of the Si(111) surface were systematically studied for the first time by Lander and Morrison in 1964 using LEED [177]. Kawaji *et al.* [253] and Baba *et al.* [254] later refined the phase diagram, taking advantage of reflection high-energy electron diffraction (RHEED) to capture diffraction images of the In/Si surface during the growth of the indium layer. At the same time, Kraft *et al.* [255] used STM to record first real-space topographies. Altogether,

these studies identified four main superstructures at base or annealing temperatures between 400 °C and 550 °C: a $(\sqrt{3} \times \sqrt{3})$R30° structure for coverages $c < 0.5\,\mathrm{ML}$, a $(\sqrt{31} \times \sqrt{31})$R9° structure for $0.4\,\mathrm{ML} < c < 0.7\,\mathrm{ML}$, a (4×1) structure for $0.5\,\mathrm{ML} < c < 1\,\mathrm{ML}$, and a $(\sqrt{7} \times \sqrt{3})$R9° structure for $c > 0.8\,\mathrm{ML}$ [177, 253–255] (see also Fig. 4.1c). Despite the intriguing properties of the other reconstructions, we will now focus on the most frequently investigated phase of In on Si(111), namely the Si(111)(4×1)-In phase.

4.2 The (4×1) metallic zigzag phase

Within the last 30 years the Si(111)(4×1)-In surface has become a model system to study electronic and thermal transport [256], phase transitions [102, 107, 117, 237] as well as atomic scale defects [234] and fluctuations [257, 258] in low-dimensional materials. Since its discovery, the (4×1) phase has been examined by a large number of different experimental methods, including LEED [117, 259], I(V)-LEED [195], RHEED [116, 260, 261], reflective high-energy positron diffraction (RHEPD) [262], X-ray diffraction (XRD) [263], angle-resolved photoemission spectroscopy (ARPES) [12, 153, 250], Core-level PES [264], Auger-electron spectroscopy (AES) [260], electron energy loss spectroscopy (EELS) [265, 266], reflectance anisotropy spectroscopy (RAS) [267–270], Raman spectroscopy [240, 269, 271], electrical transport measurements [261, 272], and STM [125, 234, 255, 273–275]. From a theory perspective, the system has been investigated by density functional theory (DFT) [276, 277] and other approaches [237]. It is a prime example of how the development and improvement of new techniques in theoretical and experimental physics can contribute to a better understanding of processes in complex materials. Even today, the system serves as a benchmark for cutting edge time-resolved techniques such as time-resolved ARPES (trARPES) [11, 12, 57, 58] or ultrafast electron diffraction (UED) [10, 56], revealing fascinating nonequilibrium dynamics (see Sec. 4.4).

4.2.1 Atomic structure of the (4×1) phase

In the 1990s, Cornelison *et al.* [279], Nakamura *et al.* [260], Saranin *et al.* [280, 281], Pedreschi *et al.* [267] and Bunk *et al.* [263] were the first to recognise the quasi-one-dimensional nature of the (4×1) structure. Based on these early findings, a

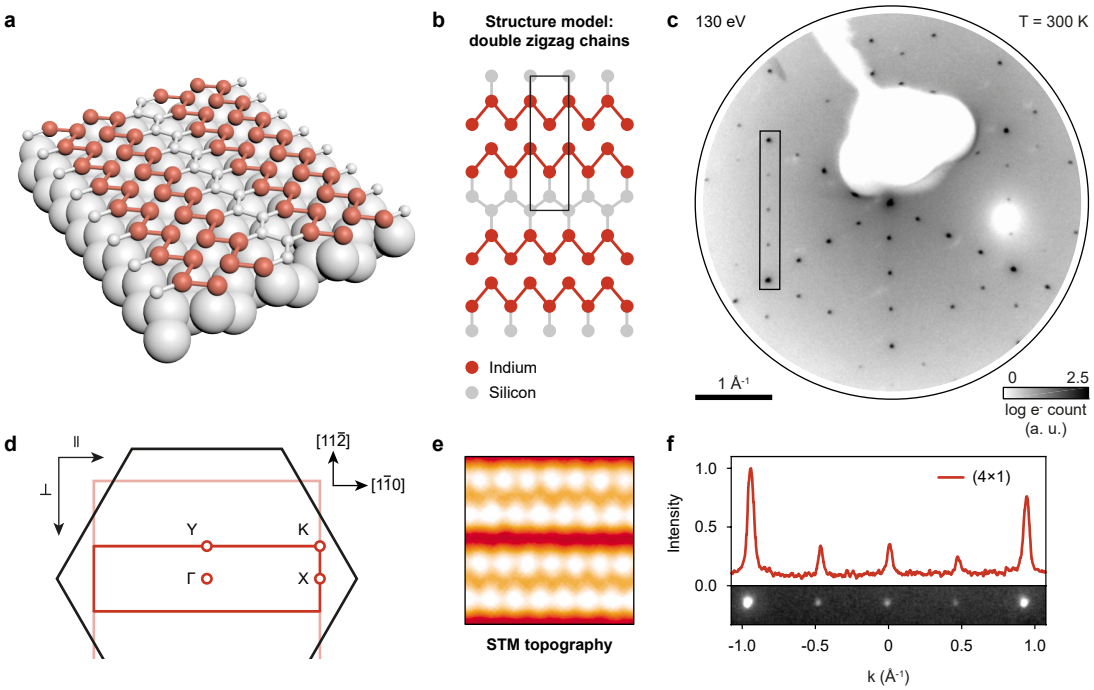

Figure 4.2: Atomic structure of the (4×1) phase of indium on Si(111). **a**, Three-dimensional model of the In-induced (4×1) surface reconstruction. The In atoms arrange in pairs of parallel zigzag chains separated by single rows of Si atoms. Red, indium; grey, silicon. **b**, Structure model of the (4×1) phase. Black rectangle, unit cell. **c**, LEED pattern of the (4×1) structure recorded at room temperature with 130 eV electron pulses. **d**, Surface Brillouin zone (SBZ) of the (4×1) phase. Arrows on the left indicate orientation relative to the atomic chains. Hexagonal SBZ of the Si substrate shown in black. **e**, STM topography recorded at $U_{\text{bias}} = -0.15$ V and $I = 20$ pA; $T = 135$ K. Adapted with permission from Ref. [278]. © 2004 by the American Physical Society. **f**, Selected regions and line-out from the LEED pattern (see black rectangle in **c**).

widely accepted structure model has been developed, featuring double zigzag chains of In atoms that run along the $[1\,\bar{1}\,0]$, $[0\,1\,\bar{1}]$ and $[\bar{1}\,0\,1]$ directions of the substrate, and are separated by single zigzag rows of Si atoms[3] (Fig. 4.2a,d). The underlying layers of the substrate remain largely unreconstructed [256], but may act as a charge reservoir[4]. Containing four In and two Si atoms, the (4×1) unit cell exhibits a two-

[3]It should be noted here that although the (4×1) structure is commonly described in terms of two parallel zigzag chains and the corresponding In–In bonds connecting inner and outer rows, the bonds between neighbouring zigzag chains are of comparable strength [237, 241]. Recent theoretical [237, 241] and experimental [11] studies have taken this into account (see also Sec. 4.3.3).

[4]In fact, a number of studies on the coexistence of the (4×1) and (8×2) phases below T_c found that the doping-dependent carrier concentration heavily influences the phase transition [237, 282–284] (see Sec. 4.5).

fold rotation, a mirror as well as a glide plane, thus belonging to the "pmg" 2D space group [240] (see also Fig. 4.2b). This structure model is consistent with STM [102, 255, 278] and DFT results [276] (see Fig. 4.2e).

In LEED, the formation of the Si(111)(4×1)-In phase leads to characteristic modifications of the original diffraction pattern (Fig. 4.2c,f). Specifically, the quadrupling of the unit cell perpendicular to the chain direction is signified by the appearance of three additional spots between the Bragg spots of the Si substrate along the $[1\,1\,\overline{2}]$, $[1\,2\,1]$ and $[\overline{2}\,1\,1]$ directions. The majority of the LEED patterns shown in this work were recorded using precision-oriented Si(111) substrates and thus feature contributions from domains of chains oriented along these three crystallographic directions[5] (mutual rotation of 120°). This causes the threefold symmetry of the LEED pattern seen in Fig. 4.2c. In this context, Stevens *et al.* [273] and Pedreschi *et al.* [267] investigated the growth of the (4×1) phase on vicinal surfaces, misaligned by up to 4° along, e.g. the $[1\,1\,\overline{2}]$ direction. Here, the surface exhibits a high density of parallel-running atomic terraces that facilitate the growth of single-domain In nanowires along the $[1\,\overline{1}\,0]$ direction. Within the scope of this work, samples of this kind were used in particular for measurements with the microgun (see Sec. 5.4).

4.2.2 Electronic structure of the (4×1) phase

The quasi-one-dimensional character of the (4×1) phase is also reflected in the highly anisotropic electronic band structure of the surface layer (see Fig. 4.3a-c). In this respect, ARPES has proven an ideal experimental tool to study the electronic properties of the system in and out of equilibrium (see, e.g. [66, 153, 250, 285–288]). Summarizing previous results, the band structure of the (4×1) phase hosts three metallic bands m_1, m_2 and m_3 with nearly free-electron-like dispersion along the chain direction ($\overline{\Gamma} - \overline{\mathrm{X}}$ or $k_\parallel$, see Fig. 4.3a,c) and little to no dispersion perpendicular to the chains [250, 285, 287, 288] ($\overline{\Gamma} - \overline{\mathrm{Y}}$ or $k_\perp$, see Fig. 4.3a,b). Transport measurements reveal that this anisotropy at the atomic level has a significant influence on the macroscopic surface conductance parallel or perpendicular to the chain direction[6] [289]. Furthermore, the (4×1) band structure shows strong similarities with the theoretical model introduced in Sec. 2.1.2, which again illustrates why In on

[5] Note that the area of the electron probe spot on the sample is orders of magnitude larger than the average domain size in this system and that the LEED pattern represents a superposition of

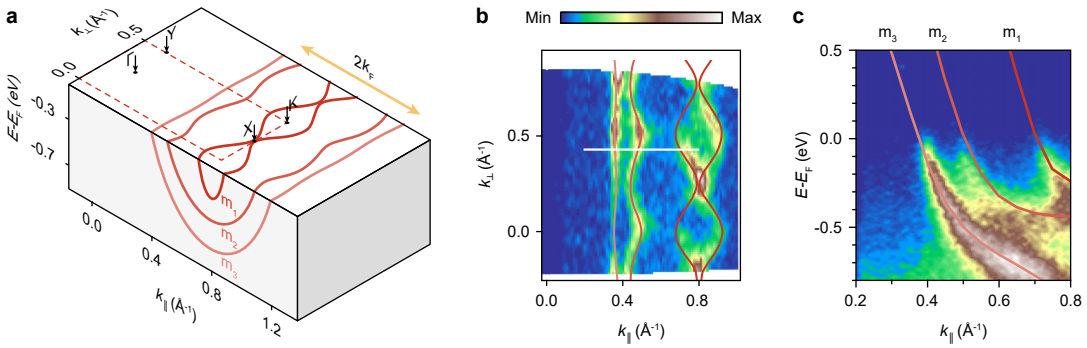

Figure 4.3: Electronic Band structure of the (4×1) phase of indium on Si(111). **a**, Schematic of the three-dimensional band structure exhibiting three prominent parabolic bands. Around E_F, the parallelism of the bands indicates the quasi-one-dimensional character of the system. Note that above T_c only m_3 fulfills the nesting condition. Dashed area, (4×1) unit cell. **b**, Fermi surface recorded by ARPES at $T = 150$ K. **c**, Band dispersion along the chain direction obtained at $k_y = 0.43$ Å^{-1}. Figures **b** and **c** adapted with permission from Ref. [57]. © 2019 by the American Physical Society.

Si(111) is a model system to investigate the properties of quasi-one-dimensional systems. As for the individual bands, m_1 exhibits a filling factor of $\eta = 0.11$ and crosses the Fermi energy E_F at $k_\parallel = 0.75$ Å^{-1}, forming a small electron pocket around the $\overline{\text{K}}$ point [287, 288] (Fig. 4.3b,c). The m_2 band ($\eta = 0.38$) crosses E_F at $k_\parallel = 0.54$ Å^{-1} and shows a somewhat weaker dispersion in $\overline{\Gamma} - \overline{\text{Y}}$ direction. Remarkably, the m_3 band is exactly half-filled ($\eta = 0.50$) and crosses E_F at $k_\parallel = k_F = 0.41$ Å^{-1}. In addition, this band exhibits no significant dispersion along $\overline{\Gamma} - \overline{\text{Y}}$, and therefore fulfills the two necessary conditions for Fermi-surface nesting, i.e. (1) half-filled bands with (2) large parallel sections of the Fermi surface (see Sec. 2.1.2).

4.3 Transition to the (8×2) insulating hexagon phase

The findings from the previous Sec. 4.2 suggest that the (4×1) structure is unstable to a Peierls-like distortion and a spontaneous transition into a symmetry-broken ground state. Therefore, at this point, it may not seem surprising that in 1999 Yeom *et al.* [102] reported a reversible metal-insulator structural phase transition of

signals from all domains within the probed area.

[6] Kanagawa *et al.* [289] found $\sigma_\parallel = (7.2 \pm 0.6) \cdot 10^{-4}$ S mm^{-2} parallel and $\sigma_\perp = (1.2 \pm 0.1) \cdot 10^{-5}$ S mm^{-2} perpendicular to the chain direction, corresponding to a 60 times higher conductance along the wires.

the Si(111)(4×1)-In surface to a (4 × "2") or (8×2) phase for temperatures below $T_c = 125\,\mathrm{K}$. Nevertheless, it took more than ten years to develop not only a robust structure model for the low-temperature phase, but also a more comprehensive understanding of the phase transition mechanism, which goes well beyond a simple Peierls scenario. The following subsections are therefore intended to give the reader a brief introduction to the developments in the field relevant for this work[7].

Understanding a phase transition requires detailed knowledge of both the atomic and electronic structure of the high- and low-temperature phases, as well as possible transient states. However, due to the strong coupling of electrons and phonons in this particular system, it is not possible to consider the electronic and lattice subsystems as being independent of each other. As a consequence, the difficulty in correctly modelling the phase transition is to simultaneously reproduce both the atomic configuration and the electronic band structure of the low-temperature phase, and to consistently describe how these properties emerge in the transition. This is only possible by combining a variety of complementary experimental and theoretical methods, as will be seen below. For reasons of clarity, the first part of this section will focus on the structural properties of the low-temperature phase, followed by a description of the corresponding electronic band structure in the second part. On this basis, the mechanism underlying the phase transition will then be discussed.

4.3.1 Atomic structure of the (8×2) phase

Yeom *et al.* [102] were the first to discover and investigate the low-temperature phase of the Si(111)(4×1)-In surface by means of STM, RHEED and ARPES. While STM and RHEED evidenced a doubling of the (4×1) unit cell size $a_{(4\times1)} = 3.84\,\text{Å}$ along the In chains below 125 K, ARPES revealed the semiconducting nature of the resulting (4 × "2") ground state[8] "without any electronic states crossing the Fermi level" [102]. Both the wavelength $\lambda = 2a_0$ of the periodic charge density modulation and the perfect nesting of the m_3 band ($2k_F = \pi/a_{(4\times1)}$, see Sec. 4.2) supported their interpretation in terms of a Peierls transition and the formation of a

[7] For a more comprehensive description of the subject – in particular the theoretical background – the reader is referred to Refs. [256], [101] or [290]

[8] Yeom *et al.* inferred the doubling of the (4×1) unit cell from the formation of two-fold streaks in RHEED, indicating a lattice distortion of periodicity $\lambda = 2a_{(4\times1)}$, poorly correlated between adjacent In wires [102]. The unconventional notation was chosen to distinguish this phase from a well-ordered (4 × 2) reconstruction.

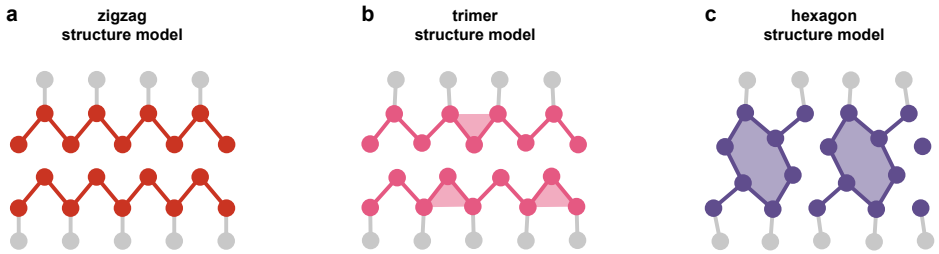

Figure 4.4: Structure models for the (4×1) and (8×2) phases. In atoms, coloured; Si atoms, grey. **a**, Double zigzag chain structure model of the (4×1) phase. **b**, Trimer model of the (8×2) phase, featuring a dimerisation of the two outer In rows. **c**, Hexagon model of the (8×2) phase, characterized by the weakening/strengthening of bonds within/in between adjacent In zigzag chains. Note that in **b** and **c**, only a (4 × 2) sub-cell is depicted. Adapted from Ref. [256].

commensurate one-dimensional CDW. Interestingly, the authors speculated that the true ground state of the system might feature an (8×2) reconstruction corresponding to a stable anti-phase arrangement of (4 × 2) sub cells of neighbouring wires, which they frequently observed in STM.

The first structure determination of the low-temperature phase was carried out by Kumpf *et al.* [291] using X-ray surface diffraction. The results confirmed a unit cell twice the size of the room temperature (4×1) structure along the chains, and strong chain to chain correlations in the perpendicular direction, suggesting an (8 × 2)-reconstructed ground state. However, with the two-fold streaks along the $[1\,1\,\overline{2}]$ direction persisting for low temperatures, Kumpf *et al.* argued against a simple Peierls mechanism, claiming that "the (8×2) superstructure is not fully developed and that the CDW fluctuations have not condensed" [291] even at 20 K. Based on their findings, Kumpf *et al.* proposed a structure model featuring a dimerization of the outer indium chains leading to the formation of indium trimers ("trimer model", see Fig. 4.4b). DFT calculations by Cho *et al.* [276] corroborated this model, finding that the trimer structure is more stable by 8 meV per (4×1) unit cell than the (4×1) structure itself. Anti-phase arrangement of the (4 × 2) subcells additionally lowers the total energy by 0.9 meV[9].

While the results of Cho *et al.* supported the interpretations of Kumpf *et al.* in

[9]Note that this difference in energy is very small and of the same order of magnitude as the computational errors [256, 276]. Furthermore, due to the large unit cell of the system, more advanced DFT techniques like simulated annealing were not feasible at that point. Therefore, the results may not be taken as unambiguous evidence for the (8×2) trimer structure.

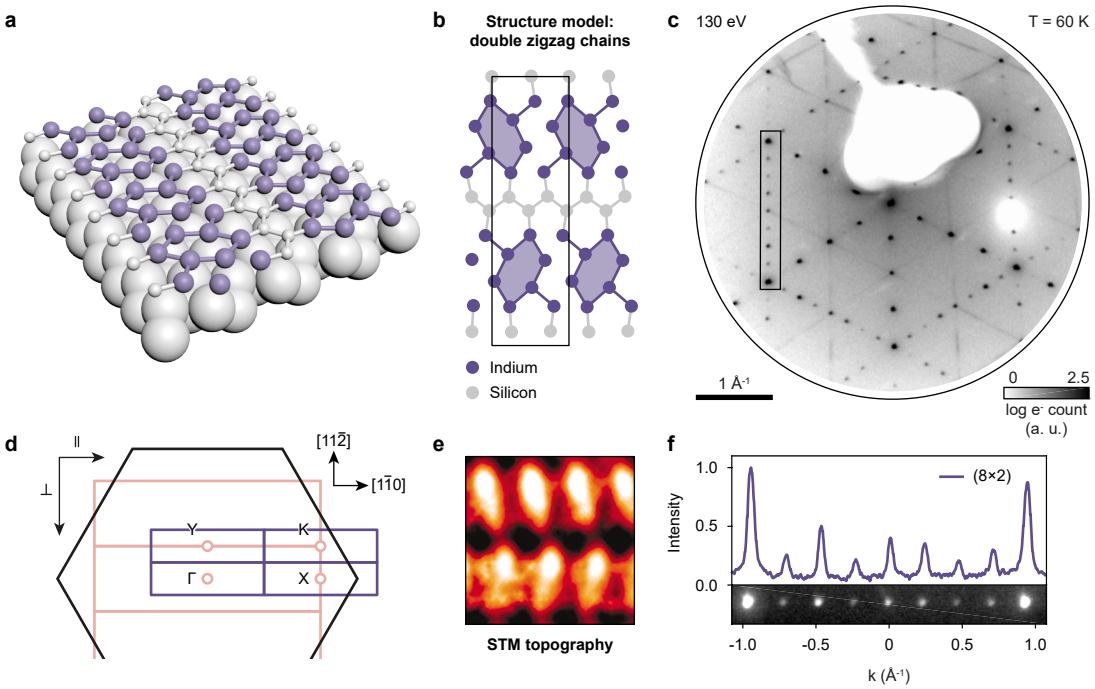

Figure 4.5: Atomic structure of the (8×2) phase of indium on Si(111). **a**, Three-dimensional model of the In-induced (8×2) surface reconstruction. The In atoms arrange in hexagons separated by single rows of Si atoms. Violet, indium; grey, silicon. **b**, Structure model of the (8×2) phase. Black rectangle, unit cell. **c**, LEED pattern of the (8×2) structure recorded at $T = 60$ K with 130 eV electron pulses. **d**, Surface Brillouin zone (SBZ) of the (8×2) phase (violett) and the (4 × 1) phase (light red). Arrows on the left indicate orientation relative to the atomic chains. Hexagonal SBZ of the Si substrate shown in black. **e**, STM topography recorded at $U_{\mathrm{bias}} = -0.15$ V and $I = 20$ pA; $T = 78$ K [278]. **f**, Selected regions and line-out from the LEED pattern in **c** (see black rectangle).

terms of the trimer model, they were not consistent with temperature-dependent resistivity measurements [272] and ARPES studies on the (8×2) phase [285–288], which clearly showed a metal-insulator transition (see also Sec. 4.3.2). In contrast, the calculated band structure of the trimer model still exhibited one band crossing E_{F}. This discrepancy was resolved by Gonzalez *et al.* [239] who harnessed DFT in combination with simulated annealing [292] to explore larger parts of configuration space, and discovered an alternative structure, more stable than the trimer state by 72 meV. This "hexagon model" (Fig. 4.4c) features an additional shear distortion between adjacent In zigzag chains of the (4×1) structure and leaves no electronic states at the Fermi energy below critical temperature T_{c}.

These results were later confirmed by additional first-principles calculations made

by Stekolnikov *et al.* [33], who found that the hexagon model is semiconducting in both the (4×2) in-phase and the (8×2) out-of phase configuration, with only the latter being energetically favourable over the high-temperature (4×1) structure[10]. Experimental confirmation of the (8×2) hexagon structure model was finally achieved by Chandola *et al.* [293] using infrared spectroscopic ellipsometry (IRSE) and reflection anisotropy measurements (RAS). To this end, the authors compared the optically anisotropic response of the Si(111)(8×2)-In surface to *ab initio* calculations [294], which predicted stark differences between hexagon and trimer models in the mid-infrared regime. Altogether, the results of XRD [291], RHEPD [262], DFT [33, 239, 256, 276, 294], ARPES [285, 287, 288], SPA-LEED [117, 233], and RAS [270, 270, 293] at this point strongly indicate a (8×2) hexagon ground-state structure.

Figures 4.5a and b show the (8×2) hexagon structure model for the low-temperature phase of In on Si(111). Based on the strength of the bonds between the individual indium atoms, their arrangement is typically described in terms of In hexagons separated by single zigzag rows of Si atoms. The hexagon model is consistent with the characteristic signature of the (8×2) phase in STM topography measurements (see Fig. 4.5e). In LEED, the formation of the Si(111)(8×2)-In phase leads to seven additional spots between the Bragg peaks, reflecting the strong chain-to-chain correlation in the direction perpendicular to the chains in agreement with X-ray diffraction [291] and RHEED [9, 10, 102, 116, 261] (see Fig. 4.5). Moreover, the two-fold streaks, first noted by Yeom *et al.* [102] are clearly visible. These streaks in the LEED pattern result from differently strong correlations between neighbouring (8×2) chains along or perpendicular to the chain direction, respectively [117, 263, 295]: First, we note that the (4×1) and (8×2) reconstructions are both commensurate to the Si substrate. Hence, for the (8×2) structure, there exist two possible mutual arrangements of neighbouring rows, i.e. in-phase and out-of-phase. Within a single (8×2) chain, the correlation of the (×2) surface elementary cells along the chains is strong, causing sharp (×2) features along the corresponding direction in LEED (i.e. horizontal in Fig. 4.5c). For adjacent (8×2) chains,

[10]The authors though mention that one has to be careful when discussing the question of whether the (8×2) trimer or the (8×2) hexagon is the correct ground state, on the basis of calculated energies alone. They further argue that the results of their calculations depend on the methodology used to describe electron-electron interactions [33].

however, the two possible relative phases between the (×2) elementary cells significantly reduce the correlation perpendicular to the chains[11], which in turn leads to the smearing of the (8×) LEED spots in the corresponding direction (i.e. vertical in Fig. 4.5c) and thus to the formation of streaks. In contrast, the sharp (8×) first-order spots indicate very strong chain-to-chain correlations perpendicular to the chain direction, that is, a well developed (8×) superstructure [116, 117, 278, 291]. Containing 16 In and eight Si atoms, the (4×1) unit cell exhibits only a glide plane, and is therefore classified as a "pg" 2D space group [240] (see also Fig. 4.5b).

As mentioned above, a comprehensive model of the In/Si(111) system has to describe not only the atomic structure of the low-temperature phase, but also its electronic structure as well as the transition itself. Therefore, the following section will elucidate the electronic band structure of the (8×2) phase.

4.3.2 Electronic structure of the (8×2) phase

Similar to the lattice, the electronic band structure of the Si(111)(4×1)-In surface shows drastic changes around T_c (see Fig. 4.6b,c). Most importantly, the system undergoes a metal-insulator transition[12], that is, the three metallic bands of the (4×1) phase no longer cross the Fermi level at any point of the Brillouin zone. Based on the interpretation of the transition in terms of a simple Peierls transition, this is not expected, since ARPES studies of the (4×1) phase [102, 250, 287] show that only the m_3 band meets the conditions for Fermi-surface nesting (see also Fig. 4.3 in Sec. 4.2.2). In fact, the evolution of the individual metallic bands across the phase transition reveals dynamics beyond a single-band Peierls transition, finally leading to the insulating nature of the (8×2) phase [288].

Below T_c, the m_1 band at the $\overline{\Gamma}$ point is lifted above E_F and thus depopulated, while m_2 shifts towards the $\overline{X}$ point. Subsequently, m_2 and m_3 form a gap around the $\overline{X}$ point ($\Delta E_g \sim 100-300$ meV)[13]. To explain this, Gallus *et al.* [285], Ahn *et al.* [287] and Sun *et al.* [288] proposed a charge transfer between m_1 and m_2. In this scenario, the depopulation of m_1 (band filling factor $\eta = 0.11$) and a subsequent transfer of

[11] Assuming that in-phase and out-of-phase configurations are energetically degenerate and randomly distributed.

[12] In the literature, the (8×2) phase is referred to either as an "insulating" or a "semiconducting" phase. The second designation takes into account the relatively small band gap of $\Delta E_g < 300$ meV.

[13] Below T_c, the m_2 and m_3 bands are often termed m_2' or m_3', respectively.

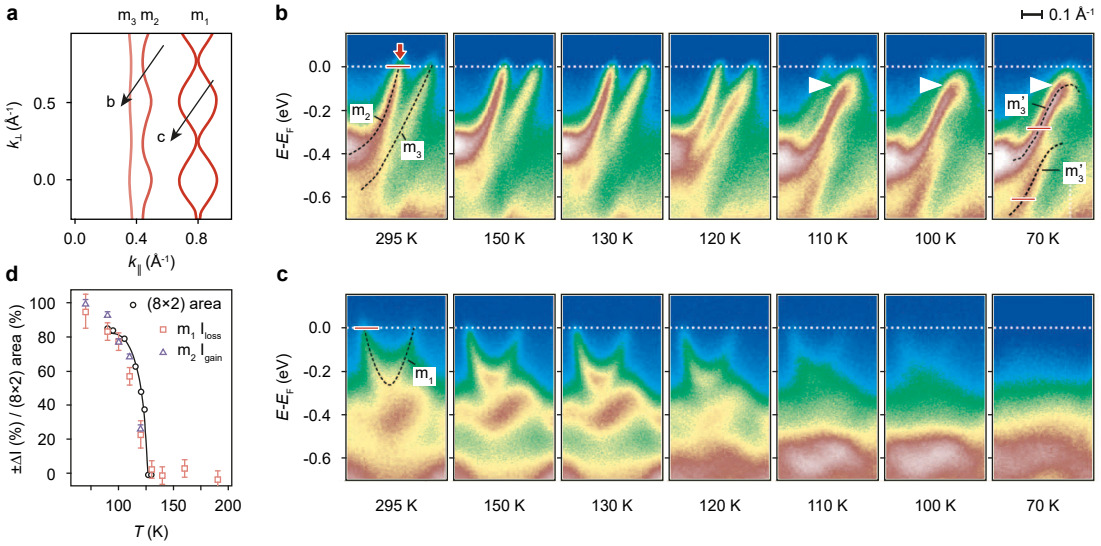

Figure 4.6: Changes in the electronic band structure during the (4×1) → (8×2) transition. **a**, Fermi surface contours of m_1, m_2 and m_3 bands. Black arrows indicate the cuts through the surface Brillouin zone along which the datasets in **b** and **c** have been measured. **b,c**, Changes of the m_2, m_3 (**b**) and m_1 (**c**) bands in the equilibrium phase transition. **d**, Intensity loss (gain) of the m_1 (m_2) band in ARPES compared to the (8×2) coverage of the surface observed by STM. Adapted with permission from Ref. [288]. © 2008 by the American Physical Society.

charge to m_2 ($\eta = 0.38$) leaves this band half-filled with $k(E_F) \approx k_F$. In analogy to the reconstruction of the atomic lattice, the periodicity of the low-temperature band structure is doubled both along and perpendicular to the chain direction ($\overline{\Gamma} - \overline{X}$, or $\overline{\Gamma} - \overline{Y}$ direction, respectively), as evident from Fermi contour measurements [287, 288]. While the opening of the band gap at k_F might be interpreted as a multi-band Peierls transition, the necessary inter-band charge transfer can not be explained in this picture and thus points to an additional, supporting mechanism. Hence, the question remains how the interaction of structural and electronic degrees of freedom enables both the charge transfer around $\overline{\Gamma}$ and the gap opening at $\overline{X}$, i.e. the metal-insulator transition.

4.3.3 Mechanism and driving force of the transition

It is clear from Sec. 4.3.1 and 4.3.2 that both specific distortions of the initial (4×1) structure and changes in electronic band structure play an essential role in the (4×1) → (8×2) phase transition. With regard to the typically strong coupling of

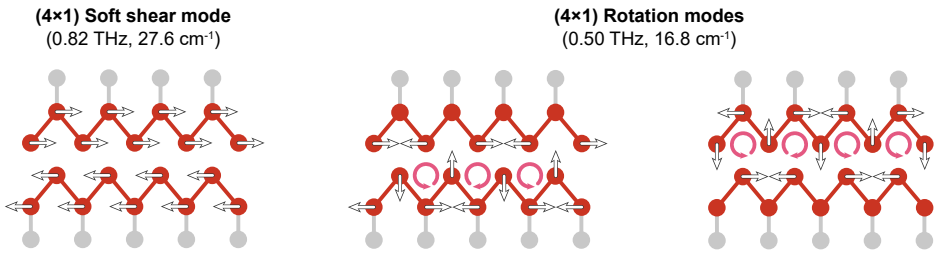

Figure 4.7: Structural modes of the (4×1) phase driving the phase transition. Grey, silicon atoms; red, indium atoms. White arrows indicate the normalized eigenvectors of the phonon modes, that is, the direction of motion for each of the In atoms. Pink circular arrows emphasise the rotational character of atomic motion (middle and right). Adapted from [240].

electrons and phonons in quasi-one-dimensional systems, this suggests that both subsystems strongly influence each other. Indeed, a number of theoretical and experimental studies on the lattice [102, 291] and electronic structure [102, 285, 287, 288] across the (4×1) → (8×2) phase transition have identified underlying cooperative mechanisms.

As for the lattice subsystem, distortions of the (4×1) structure associated with the transition into the (8×2) phase can be represented in terms of phonons. An unambiguous assignment of these *key* or *decisive* phonons requires detailed knowledge about the surface vibrational modes of the In monolayer. Using high-resolution Raman spectrosocpy in combination with frozen phonon calculations in DFT, Fleischer *et al.* [271] and Speiser *et al.* [240] explored the vibrational properties of the (4×1) zigzag and (8×2) hexagon phases and identified a large number of modes between frequencies of $10-90\,\mathrm{cm}^{-1}$ ($\hbar\omega_{\mathrm{ph}} \sim 1-11\,\mathrm{meV}$), which is the relevant energy range for phonon modes related to the displacement of In atoms. It is important to note that almost all modes within this range are thermally occupied at T_{c} and may therefore contribute to the phase transition, since their energy is smaller than $\mathrm{k_B}T_{\mathrm{c}} = 10.7\,\mathrm{meV}$.

On this basis, DFT can also be used to identify modes which are closely related to the transition. Specifically, by decomposing the hexagon structure into phonon eigenvectors of the (4×1) phase, Wippermann *et al.* [107, 256] demonstrated that a combination of a soft shear and two degenerate rotation modes transforms the (4×1) into the (8×2) structure within an accuracy of 0.01 Å average displacement

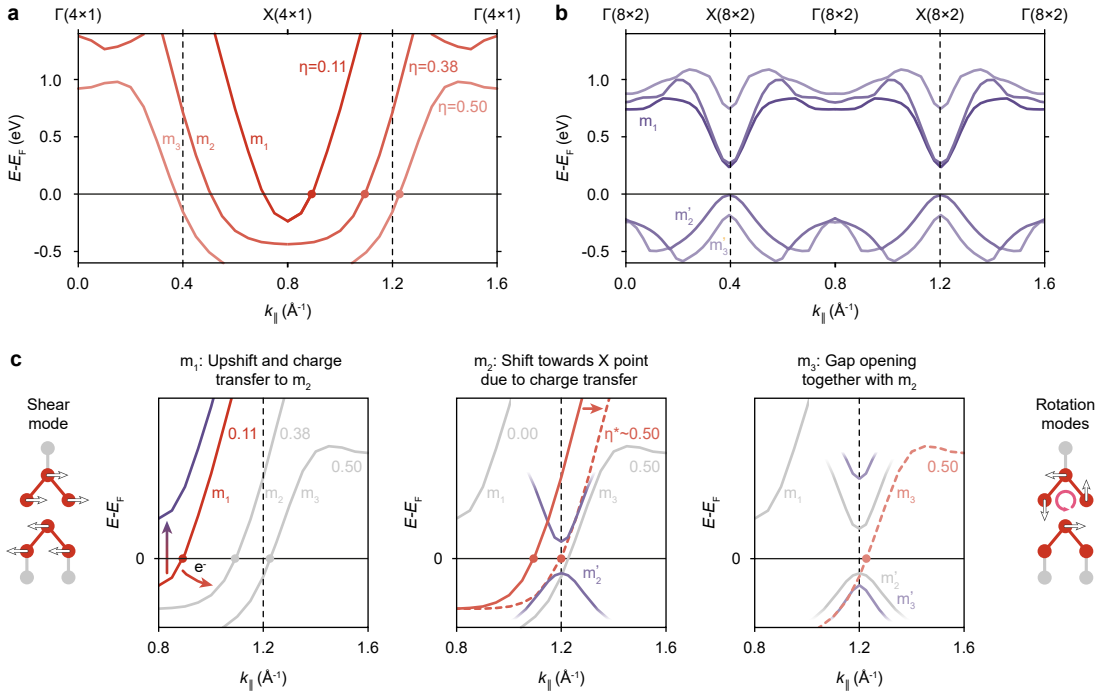

Figure 4.8: Connection between phonon modes and band structure dynamics during the transition. **a,b**, Electronic band structure of the (4×1) (**a**) and (8×2) (**b**) phase. Dots mark the Fermi momenta of the corresponding bands. η, band filling factor. **c**, Band structure dynamics during the (4×1) → (8×2) transition. The upshift of m_1 (at $\overline{\Gamma}_{(8\times2)}$) is closely connected to the excitation of the soft shear mode of the (4×1) phase, while the gap opening at $\overline{\mathrm{X}}_{(8\times2)}$ corresponds to the excitation of two degenerate rotation modes.

per atom[14]. The eigenvectors of the three relevant modes are shown in Fig. 4.7. Remarkably, this observation is in close agreement with Gonzalez *et al.* [239, 296, 297], who found that the transition into the hexagon structure involves a soft shear distortion of the (4×1) structure, that is, an opposite movement of upper and lower zigzag chains. At the same time, the two degenerate rotation modes dimerize the outer In chains, which is characteristic of the trimer model [291]. Thus, roughly speaking, rotation motion transforms the (4×1) into the trimer structure, whereas an additional shearing of the trimer structure leads to hexagon formation[15].

[14] In detail, Wippermann *et al.* [107, 256] arrived at the (4×2) structure by adding the eigenvectors $\mathbf{u}_{i,m}^{(4\times1)}$ of the (4×1) structure to the ideal atomic positions $x_i^{(4\times1)}$: $x = \sum_{i,m} x_i^{(4\times1)} + a_m \mathbf{u}_{i,m}^{(4\times1)}$. Here, i and m are the atomic and mode numbers, respectively, and a_m the mode-specific expansion coefficients used to determine the contribution of individual modes to the transition.

[15] Note that the complete transition involves not only these three characteristic in-plane modes, but also out-of-plain modes at higher frequencies [256]. Although LEED should in principle be

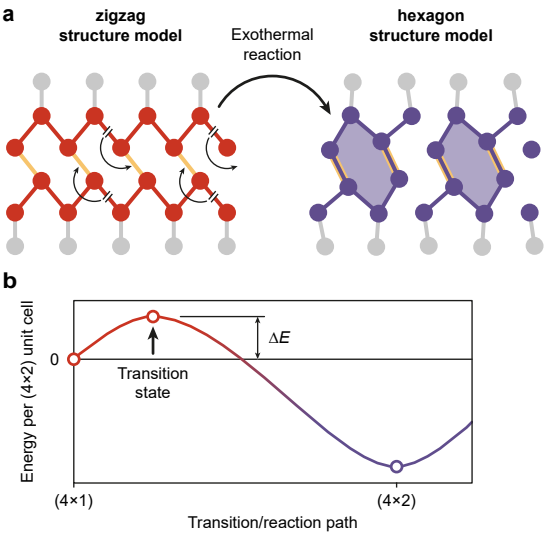

Figure 4.9: Interpretation of the (4×1) → (8×2) in terms of an exothermic reaction. **a**, (4×1) and (4 × 2) structure models of the high- and low-temperature phase of In on Si(111). Kim and Cho [238] propose a phase transition driven by the making and breaking of inter- or intra-chain bonds, respectively, similar to a chemical reaction. Yellow lines, newly formed covalent bonds between indium atoms; black double strokes, broken bonds. **b**, DFT calculations show the exothermic character of the (4×1) → (8×2) "reaction" (see activation energy ΔE), corresponding to a first-order solid-state phase transition. Adapted from Ref. [238].

We now come to the question of how these modes are connected to the electronic structure of the (4×1) phase. From a free-electron perspective, distortions of the atomic structure, represented by phonons, can change the periodicity of the lattice and affect the symmetry of a system. In general, these changes are reflected in the electronic band structure $E(\mathbf{k})$, since both electronic and lattice subsystems must have the same symmetry. In other words, modifications of the lattice periodicity alter the effective potential for the quasi-free electrons, and thereby also $E(\mathbf{k})$. In an alternative tight-binding picture, changes in the inter-nuclei distances result in the weakening/strengthening or even making/breaking of specific bonds between atoms, which affects the hybridisation of orbitals and consequently the electronic band structure. As mentioned in Sec. 2.1.3, the effect of this interplay between lattice and electronic subsystems on the properties of a particular material is determined by the nature of electron-phonon coupling.

In the case of the (4×1) → (8×2) transition, the connection between shear and rotation modes on the one hand and the electronic band structure on the other has been investigated both in theory [107, 239, 296, 297] and experiment [288]. The main findings are summarized in Fig. 4.8. A comparison of the high- and low-temperature band structures (Fig. 4.8a,b) reveals significant changes (see also

particularly sensitive to out-of-plane distortions, no signature of these modes has been found in the experiments described in Sec. 5 and 6. This is most likely due to the limited temporal resolution of the pump-probe and double-pulse excitation experiments.

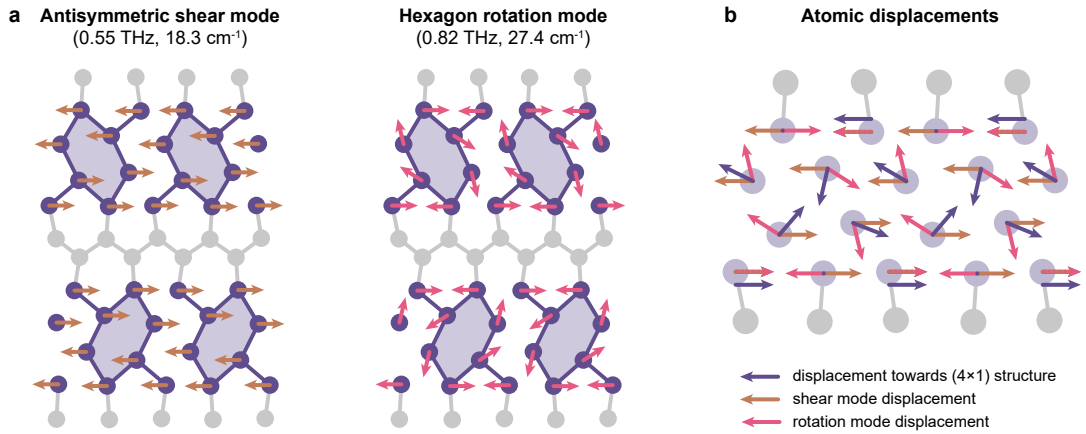

Figure 4.10: Structural modes of the (8×2) phase driving the (8×2) → (4×1) phase transition. **a**, Brown and pink arrows indicate the normalized eigenvectors of the antisymmetric shear and hexagon rotation phonon modes, respectively. Grey, silicon atoms; violet, indium atoms. **b**, Atomic displacements due to antisymmetric shear (brown arrows) and rotation modes (pink arrows) compared to the normalized displacement vectors pointing towards the ideal (4×1) structure (violet arrows). Expansion of the (4×1) structure in the eigenvectors of the (8×2) modes yields the largest coefficients for shear and rotation modes.

Fig. 4.6 in Sec. 4.3.2), in particular close to the $\overline{\Gamma}_{(8\times2)}$ and the $\overline{\mathrm{X}}_{(8\times2)}$ points. In this regard, DFT predicts that shear and rotation modes are intricately linked to electronic states in these regions of the Brillouin zone: A shear distortion of the In chains according to the displacement pattern in Fig. 4.7 (left) lifts the m_1 band at $\overline{\Gamma}_{(8\times2)}$ above the Fermi level and initiates the charge transfer to m_2 [57, 107, 288, 297]. Rotation motion, on the other hand, causes the dimerisation of the outer chain, and enables the gap opening at $\overline{\mathrm{X}}_{(8\times2)}$ [10, 107]. While the coupling of specific vibrational modes to electronic band gaps and the half-filling of m_3 (m_2) are indeed typical of Peierls-type transitions, alternative models [238] also predict the dominant role played by shear and rotation modes.

In a real-space picture, the electronic states at $\overline{\Gamma}_{(8\times2)}$ and $\overline{\mathrm{X}}_{(8\times2)}$ correspond to interchain or intrachain bonds, respectively [11, 155, 238, 241] (see Fig. 4.9a). In this scenario, the shearing of neighbouring zigzag chains leads to the making of covalent bonds between the inner In atoms (yellow) and thereby to hexagon formation. This alternative interpretation of the transition in terms of an exothermic reaction involving both bond breakage and new bond formation has been brought up recently

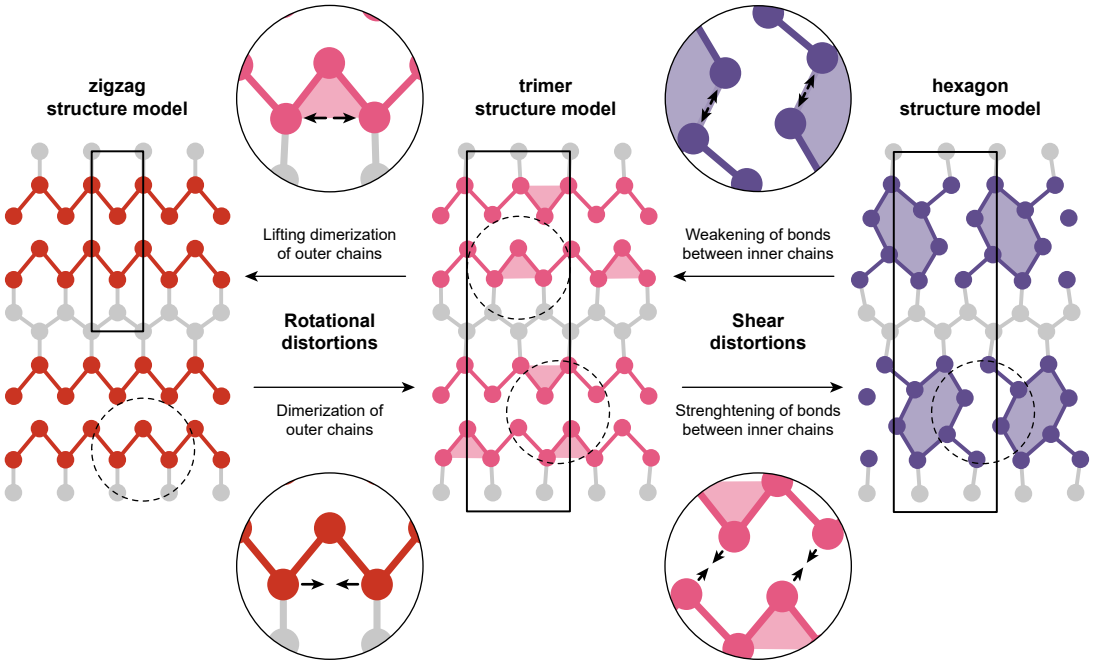

Figure 4.11: Role of shear and rotational distortions in the phase transition. Black arrows indicate the direction of atomic motion corresponding to shear or rotation distortions. Note that while rotation and shear modes comprise the motion of almost all atoms within the unit cell, only particular motions of the In lattice have been highlighted.

by Kim and Cho [238]. A discussion of the two main conceptual approaches to the origin of the (4×1) → (8×2) transition can be found further below.

So far, we have discussed the transition from the (4×1) into the (8×2) phase, which takes place upon cooling the surface below T_c. Now, we consider the opposite case, that is, the (8×2) → (4×1) transition upon heating the low-temperature phase. Here too, in analogy to the (4×1) → (8×2) transition, vibrational modes play a crucial role in realising the structural transition. However, high- and low-temperature phases have different symmetries (see Sec. 4.3.1) and therefore exhibit distinct sets of structural modes, as can be seen from temperature-dependent Raman measurements from Fleischer *et al.* [271]. The pronounced changes between Raman spectra of the (4×1) and (8×2) phases result both from the backfolding of edge modes of the (4×1) SBZ to the Γ point of the (8×2) SBZ and from changes of the phonon frequencies due to modifications of the atomic structure [240]. Furthermore, the doubling of the surface elementary unit cell along and perpendicular to the In chains results in an increase of the number of modes [240]. As a consequence, a representation of the

ideal (4×1) structure by the eigenvectors of the (8×2) vibrational modes yields two new key modes for the (8×2) → (4×1) transition: an antisymmetric shear mode at $f = 0.55$ THz (18.3 cm^{-1}, Fig. 4.10a) and a hexagon rotation mode at $f = 0.82$ THz (27.4 cm^{-1}, Fig. 4.10b) [107, 240, 256].

In the (8×2) → (4×1) transition, a displacement of the antisymmetric shear mode connected to electronic states around the $\overline{\Gamma}_{(8\times2)}$ point shifts the m_1 band below E_F. In real space, this corresponds a weakening of bonds between the inner In atoms. On the other hand, a displacement of the rotation mode closes the gap (m_2, m_3) at $\overline{X}_{(8\times2)}$, and thus lifts the dimerisation of the outer In chains. An overview of the role of shear and rotation distortions in the (4×1) → (8×2) and (8×2) → (4×1) transitions is given in Fig. 4.11. It has to be mentioned that DFT does not predict a sequential pathway for the transition under equilibrium conditions. In fact, the energy barrier for such a consecutive scenario involving an intermediate trimer state is rather large compared to the direct (4×1) → (8×2) transition.

In addition to the microscopic mechanisms underlying the phase transition and the coupling of electron and phonons therein, the question of whether the transition is of first or second order has been discussed intensively[16]. At the atomic level, STM has provided unambiguous evidence for the coexistence of (4×1) and (8×2) phases well below T_c [234, 257, 278, 298], pointing to a first-order transition (for details about surface heterogeneity see Sec. 4.5). However, a number of theoretical studies argued in favour of a second-order scenario, in which fluctuations between degenerate ground states of the (8×2) structure above $T = 100$ K result in a (4×1) structure on average [239, 276, 296]. However, this is not compatible with Raman measurements [240, 271], which have found distinct, yet similar sets of modes for both phases. A first macroscopic signature of a first-order transition was found by Klasing *et al.* [117], who observed a robust hysteresis of 8.6 K in temperature-dependent LEED measurements. Another argument is provided by the band structure changes described above. Specifically, in the (4 × 1) → (8 × 2) transition the charge transfer between m_1 and $m_{2,3}$ bands and the resulting energy gain due to the formation of the Peierls gap at $\overline{X}_{(8\times2)}$ necessitates the uplifting of states around the $\overline{\Gamma}$ point at the cost of electronic energy.

[16] Naturally, the microscopic mechanism has to be considered in this discussion, since it determines the macroscopic properties of the transition.

This energy can be associated with the characteristic barrier that has to be overcome in a first-order phase transition[17]. For these reasons we can assume that the phase transition is of first order and harness a phenomenological description in terms of an appropriate Landau potential to qualitatively understand its evolution (see also Sec. 2.1.4).

Within this model, the existence of a hysteresis can be explained by the presence of an energy barrier between the energetically degenerate symmetry-broken ground states and the high-symmetry state, which is metastable below the critical temperature T_c (see Fig. 4.12 and Fig. 2.6). Starting in the high-temperature (high-symmetry) (4×1) state, cooling the surface below T_c deforms the one-dimensional PES towards the low-temperature (symmetry-broken) (8×2) state. Due to the non-vanishing energy barrier, the system remains in a supercooled (4×1) state (structural order parameter $q = 0$), for which only thermal fluctuations facilitate a transition over the barrier into the energetically favourable (8×2) state. This lowers the effective transition temperature during cooling by about $\Delta T_{\mathrm{hyst}} \approx -5$ K in experiments [117, 233], depending on the height of the energy barrier ($\Delta E \approx 40$ meV, according to Ref. [9]). In the opposite case, i.e. upon heating the (8×2) structure, the system remains in the local minimum representing the symmetry-broken state ($q \neq 0$) even above T_c .

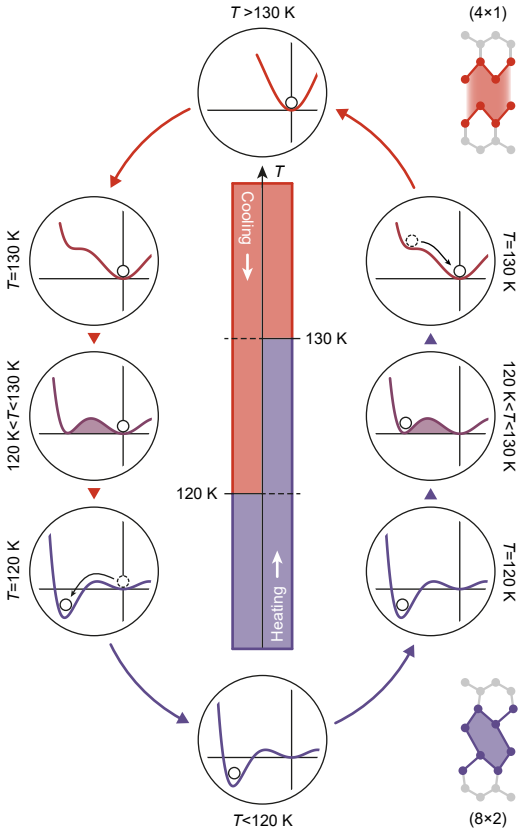

Figure 4.12: Schematic of the adiabatic (4×1) → (8×2) transition. White circles indicate the state of the order parameter throughout the transition.

Finally, we will look into the question of the driving force behind the phase transition. While an answer to this question goes beyond the scope of this work, two

[17] In a real space picture, the Peierls dimerisation of neighbouring (2×) zigzag chains by the corresponding rotation modes requires a mutual shearing, realised by the soft shear mode.

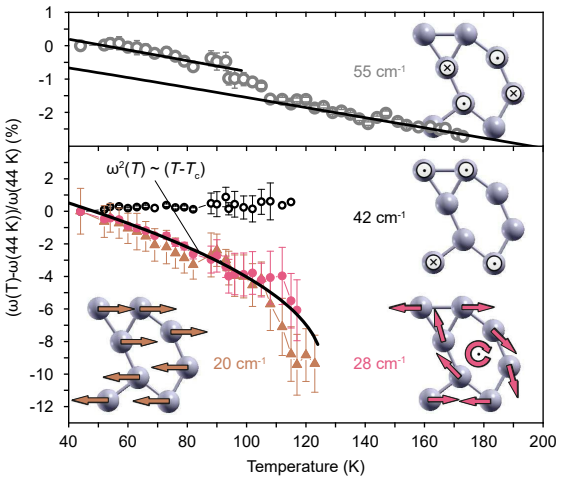

Figure 4.13: Temperature dependence of the normalized frequencies of Raman modes and sketches of the assigned eigenmodes. The shear and rotary modes (golden and pink symbols) are Peierls amplitude modes and exhibit a significant softening, while the mode at 42 cm^{-1} (black symbols) remains at constant frequency and the one at 55 cm^{-1} (gray symbols) shows only a moderate decrease due to the lattice expansion. Adapted with permission from Ref. [237]. © 2016 by the American Physical Society.

current models will be briefly discussed below. First, the interpretation of the transition in terms of a grand canonical triple-Peierls transition [237], assumes that the (8×2) phase is energetically favourable compared to the (4×1) phase due to the formation of electronic band gaps resulting from the phonon-mediated condensation of electron-hole pairs separated by $\Delta k = 2k_F$ in momentum space. In this, the change in energy caused by the lowering of occupied electronic states around $\overline{X}_{(8\times2)}$ compensates the additional Coulomb energy stemming from the formation of a PLD with double periodicity[18]. The shear and rotation phonon modes represent the Peierls or amplitude modes connected to the transition, corroborated by the observed softening of modes in the corresponding frequency regime close to T_c [237] (see Fig. 4.13). Moreover, in a grand canonical ensemble, the substrate can act as a charge reservoir, allowing the high-temperature phase to remain metastable below T_c, in agreement with the first-order character of the transition. Second, the exothermic reaction model [238] attributes the transition to a (×2) periodic lattice distortion induced by the making and breaking of bonds between In atoms. This "surface reaction" also reshapes the electronic band structure, which afterwards exhibits characteristic band gaps, explaining the metal-insulator transition. Furthermore, in contrast to the Peierls model, the formation of the four energetically degenerated basic state configurations of the structure can be understood rather intuitively, according to

[18] In precise terms, it is the balance between electronic energy and vibrational entropy that stabilises the (8×2) phase below T_c [107]. This implies that T_c is not determined by the size of the electronic gap (and the thermal excitation of carriers into the conduction band), but rather by the T-dependent occupation of phonon modes.

Kim and Cho [238]. In summary, while both studies find the same bands and bonds to be relevant for the transition, the two underlying models each represent a more physical or a more chemical interpretation, highlighting either the role of electron-phonon coupling or the drastic bond strength changes [241].

4.4 Ultrafast phase transition dynamics

Up to this point, the phase transition has been discussed for equilibrium conditions, i.e. throughout an adiabatic passage of the hysteresis (see Fig. 4.12). For example, in heating the (8×2) surface above T_c, electrons are thermally excited above the band gap[19] and populate states associated with the excitation of shear and rotation phonons. These modes subsequently transform the hexagon into the zigzag structure. The strong coupling of key vibrational modes to particular electronic states raises the question whether the structural transition can be manipulated optically. The feasibility of this approach has been demonstrated by Terada *et al.* [282] in STM measurements under cw laser illumination at 635 nm wavelength ($\hbar\omega = 1.95$ eV). Here, the generation of electron-hole pairs in the silicon substrate and the subsequent drift of photoholes to the surface were shown to neutralise the excess electrons in the In band, enabling control over the occupation of excited states. This way Terada *et al.* demonstrated deterministic switching of supercooled (4×1) domains back to the (8×2) ground state.

However, direct optical excitation of the (8×2) → (4×1) transition would provide more information about the underlying mechanism involving shear and rotational phonons. In this regard, ultrafast diffraction and spectroscopy promise detailed insights into the transient population of electronic states above the bandgap and the coupling to vibrations of the In monolayer. Indeed, recent time-resolved studies on the (8×2) phase revealed fascinating dynamics in the transition, which are briefly summarized below.

In a pioneering experiment, Wall *et al.* [9] harnessed trRHEED to investigate the (8×2) → (4×1) structural phase transition at $T = 20$ K after femtosecond optical excitation, as well as the subsequent recovery of the ground state. In accordance with DFT [238] and STM [298], long relaxation times of several hundred picoseconds confirmed the metastable nature of the (4×1) state below T_c. Further trRHEED

[19] This naturally leads to the generation of holes in the valence bands.

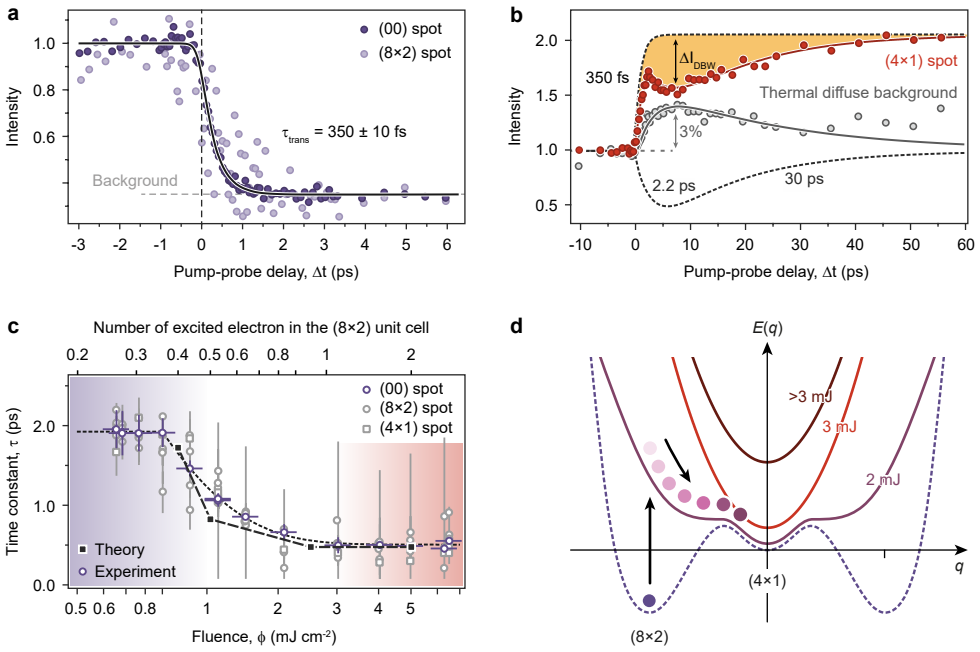

Figure 4.14: Ultrafast structural phase transition studied by trRHEED. **a**, Intensity of (0 0) and (8 × 2) diffraction spots as a function of the pump-probe delay. **b**, Delay-dependent intensity of the (4 × 1) diffraction spot and the thermal diffuse background. **c**, Time-constant of the (8×2) → (4×1) transition as a function of the excitation fluence. **d**, Schematic of the PES for the transition at different excitation fluences between 0 and $> 3\,\mathrm{mJ\,cm^{-2}}$. Coloured circles, order parameter. Figures **a**, **b** and **c** adapted by permission from Springer Nature Customer Service Centre GmbH: Springer Nature, Nature [10], © 2017, Macmillan Publishers Limited, part of Springer Nature (2017). Subfigure **d** adapted from Ref. [116].

measurements at varying adsorbate densities demonstrated the strong influence of surface defects on the lifetime of the metastable state and allowed for an estimation of the (4×1) /(8×2) phase front velocity at $v_{\mathrm{ph}} = 82$ m/s.

In a second trRHEED study with significantly enhanced temporal resolution, Frigge *et al.* [10] found the structural transition to be completed within $\tau_{\mathrm{trans}} = (350 \pm 10)$ fs, monitoring the time-dependent intensities of the (0 0), as well as selected (4×1) and (8×2) diffraction spots (see Fig. 4.14a,b). Interestingly, the transition evolves faster by an order of magnitude compared to most other structural dynamics at surfaces. The high temporal resolution further facilitates the separate observation of transition dynamics solely driven by electronic excitation, and the transient heating of the lattice, which occurs on a six times slower timescale

[10, 56]. The study also reveals that τ_{trans} is a function of the excitation fluence ϕ (Fig. 4.14c)[20]. The results can be interpreted in terms of an instantaneous reshaping of the PES due to electronic excitations, the displacive excitation of shear and rotation modes, and a deterministic or *ballistic* motion of the order parameter along the structural pathway towards the (4×1) state (Fig. 4.14d). Based on this model, the limit value behaviour of τ_{trans} likely originates from the constant gradient of the PES at higher fluences (compare red and dark red potentials in Fig. 4.14d)[21]. Moreover, related DFT calculations provide insights into the connection of electronic excitations to lattice modes facilitating the transition. A transient population of unoccupied states close to the conduction band edge at $\overline{\Gamma}_{(8\times2)}$ weakens the In–In bonds between neighbouring chains and thereby activates the shear mode. On the other hand, occupied states around $\overline{\mathrm{X}}_{(8\times2)}$ correspond to In–In bonds that form upon the dimerisation of the outer In chains, and transient depopulation of these states promotes the rotation mode. Thus, the excitation of shear and rotation modes (either thermally or via direct electronic excitation) results in the melting of the CDW. However, despite their crucial role in the transition, Frigge *et al.* did not report any signature of these modes in trRHEED data, i.e. coherent oscillations of the diffraction spot intensity or pronounced features in the inelastic background. The authors reasoned that the phase transition is completed within about 1/4 of the periods of shear and rotation phonons, meaning that both modes are critically damped.

Whereas trRHEED mainly probes structural dynamics at surfaces, trARPES is sensitive to transient changes in both the occupied and unoccupied states of the electronic band structure. This makes it possible to experimentally check and refine the distributions of excited electrons and photoholes assumed in DFT calculations presented in Frigge *et al.* [10]. However, to observe all relevant features of the transition, the entire first Brillouin zone has to be sampled with high resolution in time and momentum space. Using trARPES at a repetion rate of 500 kHz in combination with 40 fs XUV probe pulses, Nicholson *et al.* [11] achieved a momentum-resolved view of band structure dynamics during the (8×2) → (4×1) transition (see Fig. 4.15).

[20] In a reasonable assumption the ϕ is directly proportional to the electronic excitation in the system.

[21] On the other hand, it may well be that the minimum value for the time constant of the transition observed by Frigge *et al.* is limited by the finite temporal resolution of the experiment.

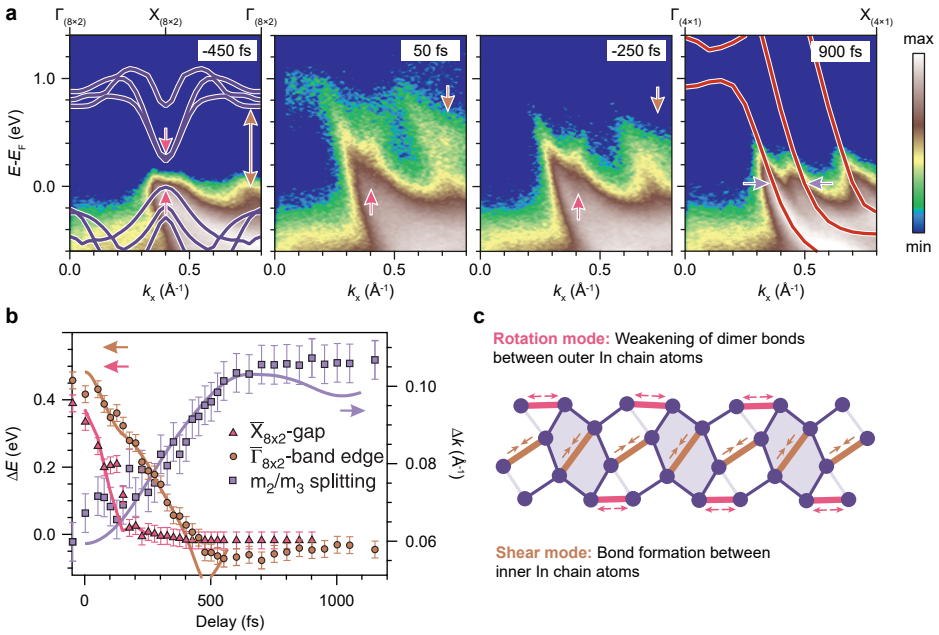

Figure 4.15: Ultrafast $(8\times2) \rightarrow (4\times1)$ phase transition studied by trARPES. **a**, Bandstructure of In/Si(111) along the $\overline{\Gamma} - \overline{\mathrm{X}}$ direction ($k_y = 0.43$ Å^{-1}) for different pump probe delays. Arrows indicate the m_1 band edge (brown) and the m_2/m_3 gap (pink), associated with shear and rotation modes, purple arrows point to the splitting between m_2 and m_3. **b**, Dynamics of the three features highlighted in **a**. **c**, Model of the (8×2) structure and the interatomic bonds associated with shear/rotation modes or the electronic states highlighted in **a**, respectively. Figures **a** and **b** taken from Ref. [11]. Adapted with permission from AAAS.

Following optical excitation, the gap at the $\overline{\mathrm{X}}_{(8\times2)}$ point collapses within 200 fs (see pink features in Fig. 4.15a,b). Next, the m_1 band (brown) at $\overline{\Gamma}_{(8\times2)}$ shifts down and reaches the Fermi level after 500 fs, while the splitting of m_2 and m_3 (violet) occurs within 700 fs, indicating the completion of the structural transition [11]. The time constant of 350 fs for the structural dynamics is in good agreement with Frigge *et al.* [10]. In order to gain insight into the evolution of the atomic structure and bond strengths along the transition pathway (see Fig. 4.15c), the authors performed *ab initio* molecular dynamics simulations based on DFT, constrained by the valence and conduction band populations measured in experiment[22]. The results demonstrate the key role of photo-excited holes located at the $\overline{\mathrm{X}}_{(8\times2)}$ point. Based on their

[22]Further explanations, numerical details and an extended analysis of bond strengths can be found in Refs. [155, 241].

findings, the authors propose a microscopic mechanism for the (8×2) → (4×1) phase transition:

"Upon excitation, holes are created in the bonding states at $\overline{\mathrm{X}}_{(8\times2)}$, which correspond to In–In dimer bonds between the outer In chain atoms. Consequently, the dimer bonds characteristic for the hexagon structure weaken and break. At the same time, a sizable fraction of excited electrons populates the states at $\overline{\Gamma}_{(8\times2)}$ that are formed by a bonding combination of In states from neighboring In chains. Population of these excited states leads to interatomic forces that transform the hexagons into zigzag chains, resulting in bond formation. The electron band related to these bonds (m_1) is lowered in energy as the In atoms contributing to this bond approach each other, further populating those states and strengthening the bond. It finally crosses the Fermi energy [...], resulting in the metallic state of the (4×1) phase." [11].

In a follow-up experiment, Nicholson *et al.* focused on the transfer of energy from the electronic system to the lattice [57], proposing an initial coupling of excited electronic states to high-energy optical modes, and a subsequent, much slower energy relaxation by means of phonon-phonon coupling. This again highlights the key role of shear and rotation modes, which are likely to represent a phonon bottleneck for the energy transfer [57]. Other trARPES studies by Cháves-Cervantes *et al.* [12, 58, 153] demonstrated that the (8×2) → (4×1) transition can be driven by multiphoton absorption across the $\overline{\mathrm{X}}_{(8\times2)}$ band gap and found possible signatures of shear [153] and rotation [12, 66, 153] modes in the excited state populations.

In summary, by decoupling the electronic and lattice degrees of freedom, ultrafast electron diffraction and spectroscopy in combination with DFT and molecular dynamics simulations have contributed to a more comprehensive understanding of the phase transition mechanism. At the same time, central questions concerning, e.g. the impact of possible coherences in shear and rotation motion, and the characteristics of the underlying PES remain open. Specifically, in contrast to Frigge *et al.* [10], the phonon bottleneck for energy relaxation discussed by Nicholson *et al.* [57] suggests that, following ultrafast excitation, optical phonons of the indium layer are out of equilibrium with low-energy surface or substrate modes for several picoseconds. Associating this persistent nonequilibrium population with shear and rotation phonons, and assuming a weak coupling to other vibrational degrees of freedom, it seems possible that coherences in these modes persist for more than a

quarter of the vibrational period. In this context, ULEED offers the capability to resolve subtle changes in surface structure on a 1-ps timescale and is thus perfectly suited to study coherent surface phonons (see Sec. 3.1.3). In view of the objectives of this work, coherences in shear and rotation modes could be harnessed to exert control over the (8×2) → (4×1) transition. Therefore, by combining ULEED with multipulse optical excitation schemes (see Sec. 3.1.1), this work aims at transferring central concepts of femtochemistry to the In/Si(111) surface.

4.5 Phase inhomogeneity

Besides its ultrafast dynamics, the Si(111)(8×2)-In surface has attracted significant attention for a variety of atomic scale phenomena, including phase coexistence [257, 298], dynamical metal-to-CDW junctions [234], defect-induced charge ordering [278] and pinning [283], or chiral solitons [125]. While a direct observation of these effects requires atomic-scale real-space imaging and spectroscopy as provided exclusively by STM and STS, signatures of local surface inhomogeneities may as well influence the results of spatially averaging techniques such as LEED, depending on their density and long-range order.

Due to the first-order nature of the transition, a coexistence of (8×2) and supercooled (4×1) domains is expected for temperatures slightly below T_c. STM topographies of the In/Si(111) surface in this temperature regime reveal the heterogeneity of the surface [298], exhibiting nanometer-sized domains of high- and low-temperature phases (see Fig. 4.16). As a consequence, data from experiments measuring mesoscopic or macroscopic observables typically feature contributions from both phases. This concerns key experimental methods, e.g. ARPES, RHEED, LEED, RAS or Raman spectroscopy. Therefore, understanding phase heterogeneity in this particular system is important, especially with regard to sample preparation and data interpretation. For example, a number of early studies suggested the (8×2) → (4×1) transition to be of second order, based on quasi-continuous changes in observables over a large temperature range, whereas STM measurements later evidenced a "domain-by-domain" conversion at the nanoscale, demonstrating that the transition proceeds in microscopic first order [298]. This contradiction can be resolved by a model of surface areas exhibiting different critical temperatures, that is, barrier heights for the transition on the PES, depending, e.g. on their size [298].

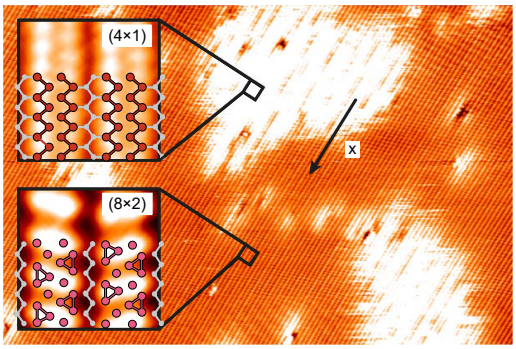

Figure 4.16: Nanoscale coexistence of (4×1) and (8×2) phases below T_c . STM topography of the (4×1) surface recorded at $U_{bias} = -0.7$ V and $I = 100$ pA; $T = 121$ K. Bright areas correspond to (4×1) , darker areas to (8×2) domains. Full image: $150 \times 100\,nm^2$. Insets: High-resolution STM images of the (4×1) (top) and (8×2) (bottom) phases with zigzag and trimer structure models superimposed. Note that the hexagon model had been proposed only recently at the time of publication. Reprinted with permission from Ref. [298]. © 2005 by the American Physical Society.

In probing the surface structure as a function of temperature in ARPES or LEED, the existence of a barrier height distribution on a nanometer to micrometer scale smears out the spatially averaged hysteresis data, thus creating the impression of a second-order transition. Moreover, a significant area fraction of metastable (4×1) domains complicates the interpretation of ARPES spectra, which in this case represent a superposition of signals from metallic and insulating domains [66].

A number of parameters controlling the formation and the coverage of the (4×1) phase below T_c have been identified, such as doping concentration [284], the density of vacancies or substrate defects [233, 284, 298], as well as adatom coverage [233, 261, 283]. Generally, all of these mechanisms influence the carrier density within the In wires and thus deform the "local" PES of the transition. For example, n-type doping of the silicon substrate promotes the formation of supercooled (4×1) domains, while p-type doping leads to a rather pure Si(111)(8×2)-In surface [284]. Similar effects are observed upon alkali-metal absorption, which suppressed the phase transition [283]. Furthermore, a number of different adatoms or adsorbed molecules can either pin the (4×1) phase locally [261], modify the local charge-order [278] or lead to various types of intrachain defects[23] and domain boundaries [125, 275, 299].

[23]The most prominent types of defects being "phase-slip" and "phase-flip" defects, which form upon absorption of additional In atoms [125, 234] and lead to the formation of chiral solitons [125].

Domain boundaries between (4×1) and (8×2) phases represent atomic-scale metal-insulator junctions and have been investigated in a number of combined STM and DFT studies, with regard to their atomic and electronic structure, as well as dynamics and fluctuations [234, 257, 298]. Junctions are formed both along and perpendicular to the indium wires. In the first case, the boundary separates metallic and insulating domains within a single In wire and typically extends over about 7 nm. In the case of an inter-wire junction, however, this characteristic length is significantly reduced to less than 0.5 nm, underlining the quasi-one-dimensional nature of the atomic wire array [234]. A similar reduction of the junction length is found for adatom/defect-induced domain boundaries. Although these phenomenona can also only be directly observed by means of STM, effects on spatially averaging techniques cannot be ruled out. Specifically, it has been shown that within defect-induced junctions, the key phonon modes transforming between the two phases are sterically constrained by the adatom [234]. As a consequence, for a heterogeneous surface exhibiting a high density of $(4\times1)/(8\times2)$ interfaces, the frequencies of shear and rotation modes, as measured by, e.g. Raman spectroscopy, might be redshifted compared to a homogeneous surface.

Chapter 5

Ultrafast structural phase transition in atomic indium wires on Si(111)

This chapter describes the time-resolved structural investigation of quasi-1D atomic indium chains on the Si(111) surface, a prominent Peierls system that has recently attracted interest for its ultrafast dynamics [9–12]. Building on the theoretical basics of CDWs and phase transitions (Sec. 2), as well as the present knowledge on this extensively studied materials system (Sec. 4), ULEED is employed to follow the ultrafast metal-insulator structural phase transition between the symmetry-broken (8×2) and the metastable high-symmetry (4×1) phase. The electronic and lattice structures of both phases have already been characterised in Sec. 4. The following sections, on the other hand, each focus on experimental results regarding specific aspects of the system, i.e. the ultrafast transition, the subsequent relaxation to the ground state and the role of surface heterogeneity. In this, results obtained from measurements with the mm-sized gun are supplemented by the first microgun experiments on a surface-specific structural phase transition. Each section is followed by a brief discussion of the results in view of the current state of the field.

5.1 Single-pulse optical excitation of the (8×2) surface

In a first step, motivated by the pioneering work of Wall *et al.* [9] and Frigge *et al.* [10, 56, 116], we investigate the structural evolution of the (8×2) phase after single-pulse optical excitation in ULEED. Summarising the previous results of trRHEED [9, 10, 56, 116] and trARPES [11, 12, 57, 58, 66, 153] experiments, ultrafast optical excitation of the Si(111)(8×2)-In surface creates both a transient electron population

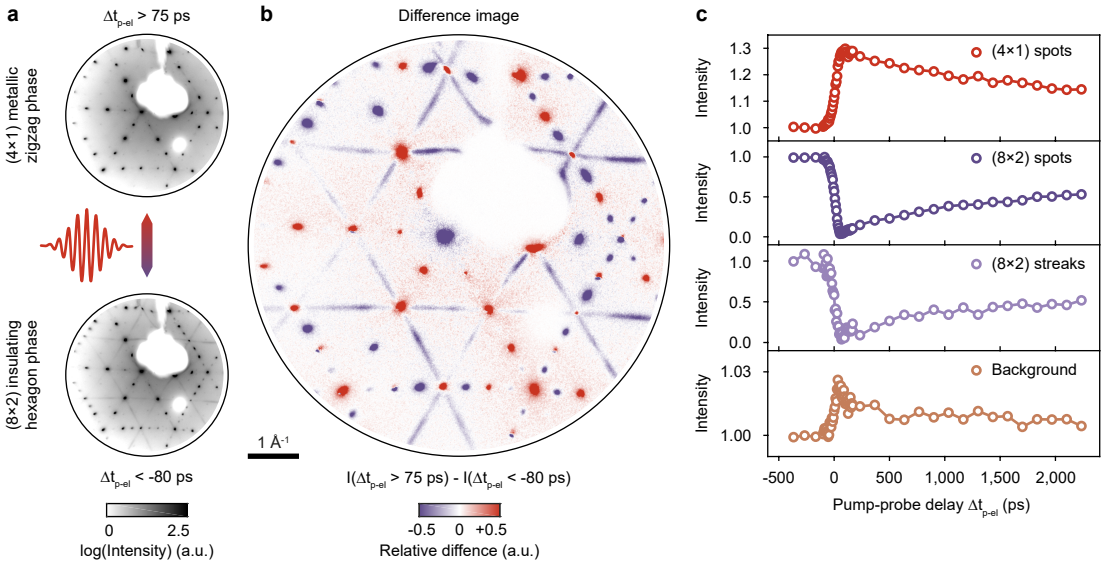

Figure 5.1: Signatures of the ultrafast (8×2) → (4×1) phase transition in ULEED. **a**, Diffraction images of the In/Si(111) surface before (bottom) and after (top) time-zero ($\Delta t_{\text{p-el}} = 0$). **b**, Difference image highlighting the changes in the LEED pattern associated with the phase transition. Red (violet), signal increase (decrease). **c**, Pump-probe traces showing the intensities of (4×1) and (8×2) diffraction spots, as well as (8×2) streaks and the diffuse background as a function of $\Delta t_{\text{p-el}}$ for an excitation fluence of 1.7 mJ cm^{-2}. Intensities normalised to values before $\Delta t_{\text{p-el}} = 0$.

in conduction band states above and localised photoholes below E_{F}. The strong coupling of these states to shear and rotation phonon modes transforming the (8×2) into the (4×1) structure enables to electronically induce the structural transition to the metastable excited state, which is completed within ∼ 1 ps. This is in stark contrast to other prominent CDW systems, where such phase transitions could previously only be initiated by means of a transient temperature increase. In the case of electronically-induced transitions, however, it is possible to drive the structural transformation well below the critical temperature T_{c} [10, 11].

Signatures of the ultrafast phase transition in ULEED

On the basis of the structure models and the static diffraction images of the (4×1) and (8×2) phases recorded above and below T_{c} (see Fig. 4.2 and 4.5 in Sec. 4.2.1 and 4.3.1) we are able to study the signatures of the (8×2) → (4×1) transition in ULEED. For this, a freshly prepared Si(111)(8×2)-In surface is illuminated by fs

light pulses (P_1, $\lambda = 1030$ nm, $\hbar\omega = 1.2\,\mathrm{eV} > \Delta E_g$, $f_{rep} = 100$ kHz; see Sec. 3.1.1 for further details) at base temperature $T_b = 60$ K, while electron pulses from the mm-sized gun probe the state of the surface at a variable delay $\Delta t_{p\text{-}el}$. Figure 5.1a shows ULEED patterns of the surface recorded before (bottom) and after (top) time-zero ($\Delta t_{p\text{-}el} = 0$) for a laser fluence of $1.7\,\mathrm{mJ\,cm^{-2}}$. At this excitation density, the surface is homogeneously switched to the metastable (4×1) state [66, 116]. Subtracting both images allows to highlight and disentangle pump-induced changes to the diffraction pattern (Fig. 5.1b). Specifically, three main features can be identified and linked to the (8×2) → (4×1) transition:

1. The four-fold spots which are present in both the (4×1) and the (8×2) LEED pattern show an increase in intensity[1], and are therefore referred to as (4×1) spots in the following. The higher intensity of these spots in the (4×1) phase is most likely due to changes in the structure factor F, according to Ref. [116].

2. The eight-fold spots and two-fold streaks of the (8×2) structure are suppressed, as they are connected to hexagon/CDW formation and unit cell doubling in the broken-symmetry state. More specifically, the transition into the high-symmetry (4×1) state and the melting of the CDW modify the structure factor F and lattice factor G, which is reflected in the diffraction pattern [204].

3. The diffuse background level increases due to the excitation of phonons of the indium monolayer and the subsequent transfer of energy to low-lying structural modes of the substrate via phonon-phonon coupling. Electron scattering at such modes is incoherent by nature (see Sec. 2.3.3), resulting in a broad intensity distribution and/or localised background features in k-space [300, 301].

Furthermore, ULEED allows to follow the evolution of these features in time with ps resolution. For this purpose, at each delay step, the background-corrected raw data peak intensities are summed up within circular areas of interest (AOI, typical radius $r \sim 0.10\,\mathrm{Å}^{-1}$) around the selected (4×1) and (8×2) spots[2]. To this end, the

[1] There are a few exceptions from this rule, e.g. the $\left(\frac{3}{4}, 0\right)$, $\left(0, -\frac{3}{4}\right)$ or $\left(\frac{3}{4}, \frac{3}{4}\right)$ spots in Fig. 5.1b, which decrease in intensity (for additional information on spot indexing see Fig. B.2 in Appendix B). This opposite trend most likely results from a non-perpendicular incidence of the electron beam and the angular dependence of the structure factor F determining the absolute intensities of individual spots.

[2] To analyse the integrated intensities of the (8×2) streaks, rectangular AOIs are used, and

background in the vicinity of the respective peak is determined within a ring (width $\mathrm{d}r \sim 0.01\,\text{Å}^{-1}$) around the edge of each AOI. Time traces of the main features in the diffraction pattern are depicted in Fig. 5.1c: Here, the integrated intensities of (4×1) and (8×2) peaks, (8×2) streaks and the diffuse background are shown as a function of the pump-probe delay $\Delta t_{\text{p-el}}$, the intensity traces having been normalised to values before time-zero. As main signatures of the ultrafast (8×2) → (4×1) transition, we find a mirror-like suppression/enhancement of the $(8 \times 2)/(4 \times 1)$ diffraction spots within the time-resolution of the experiment (~ 50 ps), and a subsequent relaxation of spot intensities to their initial values on a few-nanosecond time scale, indicating the metastability of the excited state structure (for a more detailed analysis of the relaxation dynamics see Sec. 5.4).

Whereas (8×2) spots and streaks are completely suppressed at this particular excitation density, the integrated (4×1) intensity increases by about 30 %. Assuming a negligibly small Debye-Waller-type contribution to the peak intensity in this fluence regime [56, 116], this "transfer" of intensity primarily relates to the phase transition. The moderate relative changes observed for the (4×1) diffraction spots throughout the transition are consistent with the results of previous LEED and SPA-LEED measurements [117, 233] (see also Fig. 5.3a (top)). As a result, ULEED is more sensitive to changes in (8×2) than in (4×1) peak intensities. By contrast, (tr)RHEED measurements across the phase transition show relative changes of up to 1000 % in the (4×1) signal [116] but typically suffer from a comparably lower signal-to-noise ratio for the significantly weaker (8×2) features.

5.2 Fluence-dependent excitation and relaxation

Next, we address the question of how the level of electronic excitation affects both the transition and the relaxation back to the ground state. Given that electronic excitation scales roughly linear with the incident laser fluence F (for $\hbar\omega > \Delta E_{\text{g}}$), pump-probe measurements as a function of F can provide insights in this regard. As a matter of fact, ULEED traces recorded at fluence values between $F = 0.5 - 1.7\,\text{mJ}\,\text{cm}^{-2}$ reveal increasing/decreasing $(4 \times 1)/(8 \times 2)$ peak intensities at higher excitation flu-

the corresponding background is determined at the edge of the rectangles parallel to the streak direction. The diffuse background intensity is determined within circular AOIs, which are equally distributed over the diffraction pattern (in regions exhibiting neither CDW nor Bragg peaks).

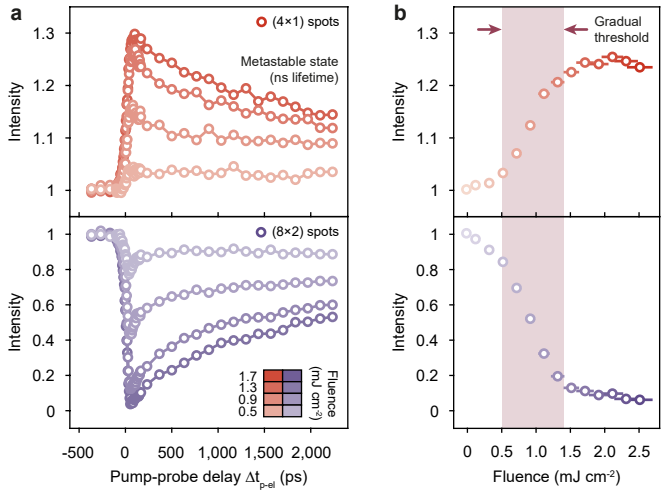

Figure 5.2: Fluence-dependent phase transition. **a**, Integrated intensity of (4×1) and (8×2) spots as a function of the pump-probe delay $\Delta t_{\text{p-el}}$ for four different pump fluences (recorded with the mm-sized gun). **b**, Fluence-dependent enhancement/suppression of (4×1) /(8×2) spot intensities, recorded for a fixed delay $\Delta t_{\text{p-el}} = 75$ ps. Taken from Ref. [53].

ences (see Fig. 5.2a). To determine the fluence threshold for the transition, the integrated peak intensities for a saturated suppression/enhancement ($\Delta t_{\text{p-el}} = 75\,\text{ps}$)[3] are normalized to the value before time-zero and plotted as a function of F in Fig. 5.2b. Interestingly, both (4×1) and (8×2) intensities display a rather gradual threshold in pump fluence compared with the sharper threshold measured under similar conditions for a different CDW transition [18]. This implies that for intermediate excitation densities between $0.5 - 1.4\,\text{mJ}\,\text{cm}^{-2}$, a variable part of the surface is switched to the metastable (4×1) state. The mean threshold fluence of $F_{\text{th}} \approx 1\,\text{mJ}\,\text{cm}^{-2}$ is in quantitative agreement with trRHEED [10, 116] and trARPES [11, 66, 153] studies, as is the critical fluence of $F_{\text{c}} \approx 2\,\text{mJ}\,\text{cm}^{-2}$ for which the entire surface is excited to the (4×1) state. The steepness of the fluence-dependent intensity at the threshold fluence ($F_{\text{th}} \approx 1\,\text{mJ}\,\text{cm}^{-2}$) is given by $F_{\text{th}} \cdot (\text{d}I/\text{d}F)|_{F,\text{th}} \approx 1.7$. Importantly, the observed gradual threshold is not a consequence of a spatially inhomogeneous excitation of the probed surface area[4], but most likely stems from

[3] This delay was chosen to account for the finite electron-pulse duration under the conditions of the experiment ($\Delta\tau_{\text{el}} \approx 50$ ps).

[4] The pump-spot diameter of (321±9) μm is significantly larger than the diameter of the electron spot (about 80 μm).

the microscopic coexistence of (8×2) and supercooled (4×1) domains or several types of atomic-scale defects affecting the local barrier height for the transition [125, 233, 234, 284, 298]. In this respect, the heterogeneity of the Si(111)(8×2)-In surface has been subject to a number of STM [234, 257, 302] and Raman spectroscopy [240] studies. Moreover, the residual intensity of metallic bands observed in trARPES below T_c [66] further supports this interpretation.

Concerning the subsequent relaxation to the ground state, for low and intermediate fluence values, we find a relatively fast recovery of spot intensities within $\sim 100\,\mathrm{ps}$ after excitation (Fig. 5.2). At later delays, however, the relaxation considerably slows down, as evidenced by the persistent suppression/enhancement of diffraction spots even after several nanoseconds. This observation cannot be reasoned in terms of a single exponential decay of the excited state population (see, e.g. Ref. [116]). Likewise, a transient Debye-Waller suppression can be ruled out in this low-fluence regime [116]. This calls for further investigations of the relaxation dynamics with improved time resolution (see Sec. 5.4).

5.3 Temperature calibration

Up to this point, it has been assumed that the ultrafast dynamics underlying the changes in the ULEED pattern are solely driven by means of electronic excitation and subsequent coupling to very few key phonon modes. However, considering the high repetition rate of the experiment, the relatively weak coupling of the indium monolayer to the silicon substrate [66, 256] and the finite thermal conductivity of the sample, a contribution of cumulative heating effects to the observed phase transition cannot be ruled out *a priori*. In other words, further experimental evidence is required to prove that the phase transition is driven neither by a transient nor a constant increase of the surface temperature above T_c. Hence, it is necessary to determine the pump-induced changes to the sample temperature by relating the fluence-dependent spot suppressions in ULEED with the temperature-dependent spot intensities in static LEED measurements (Fig. 5.3, see also Ref. [116]). For this, the integrated intensities of (4×1) and (8×2) diffraction peaks are recorded as a function of the sample temperature T between $T = 60 - 160\,\mathrm{K}$ (Fig. 5.3a; data normalised to the intensities at minimum temperature). In a next step, a Debye-Waller model (see A.11 in Sec. A is fitted to the temperature-dependent intensity

traces for $T < T_c$. This way, assuming identical minimum temperatures of $T_{min} =$

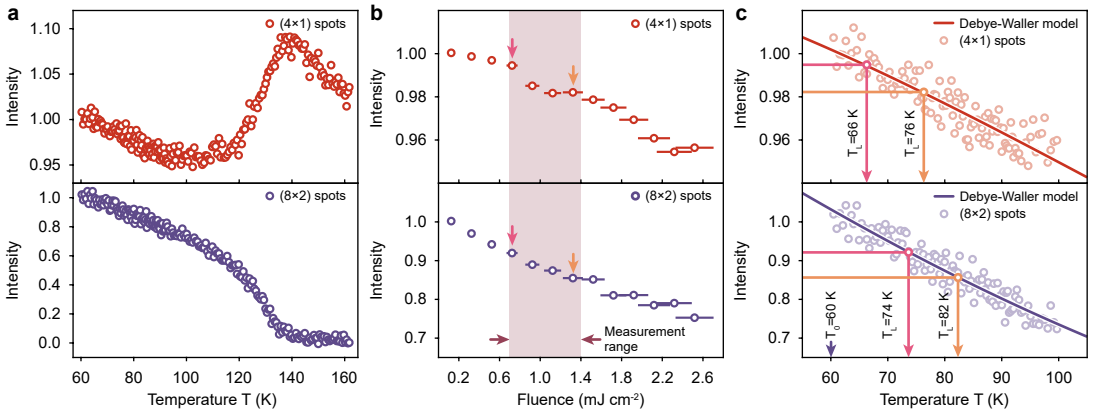

Figure 5.3: Temperature calibration. **a**, Temperature-dependent integrated intensities of (4×1) (top) and (8×2) (bottom) diffraction spots across the phase transition ($T_c \approx 125\,\mathrm{K}$). **b**, Integrated diffraction spot intensities for $\Delta t_{p\text{-}el} < 0$ in Fig. 5.2b as a function of incident fluence. **c**, Temperature calibration: a Debye-Waller model is fitted to the diffraction spot intensities in **a** for temperatures in the range $60\,\mathrm{K} < T < 100\,\mathrm{K}$. Comparing the suppressions in **b** and **c**, we find a maximum temperature increase $\Delta T_b \approx 22\,\mathrm{K}$ for the highest fluence value ($F_{max} \approx 1.35\,\mathrm{mJ\,cm^{-2}}$) within our measurement range. Note that the resulting base temperature $T_b = 82\,\mathrm{K}$ is well below T_c. Taken from Ref. [53].

60 K in both types of experiments, the pump-induced spot suppressions observed for $\Delta t_{p\text{-}el}$ in ULEED can be converted into an increase of the sample base temperature T_b. For the highest fluence in the intermediate fluence regime ($F = 1.35\,\mathrm{mJ\,cm^{-2}}$), we find a moderate temperature increase of $\Delta T_b \approx 22$ K. The resulting absolute base temperature of $T_b = 82\,\mathrm{K}$ is well below T_c. Even when taking into account the additional, transient increase of T following the pump pulse ($\Delta T = 19$ K for $F = 1.3\,\mathrm{mJ\,cm^{-2}}$ in Ref. [10]), the maximum temperature is still well below critical temperature in all relevant measurements.

5.4 Ultrafast transition studied by few-ps electron pulses

The ongoing miniaturisation of electron sources for ULEED recently resulted in the development and application of μm-sized electron guns or "microguns" (see Sec. 3.1.2). As demonstrated in Sec. 3.1.3, this novel type of pulsed electron source enables structural investigations of surface dynamics with few- to 1-ps temporal resolution. Because of the surprisingly small time constant of the $(8 \times 2) \rightarrow (4 \times 1)$

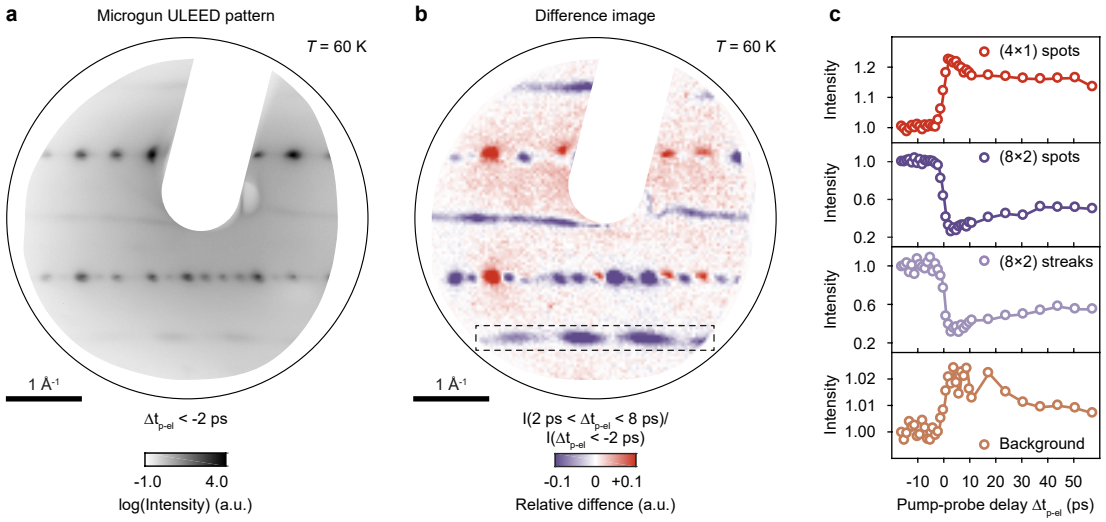

Figure 5.4: The $(8\times2) \rightarrow (4\times1)$ transition monitored by few-ps electron pulses. **a**, Diffraction image of the Si(111)(8×2)-In surface recorded with the microgun at a working distance of $\sim$ 1 mm. Silicon wafers with a miscut of 2° in the $[1\,1\,\bar{2}]$ direction have been used to favour nanowire growth along a single direction. **b**, Difference image highlighting the changes in the LEED pattern associated with the phase transition. Red (violet), signal increase (decrease). Dashed rectangle, pronounced modulation of the streak intensity perpendicular to the chain direction (also visible in **a**). **c**, Pump-probe traces showing the intensities of (4×1) and (8×2) diffraction spots, as well as (8×2) streaks and the diffuse background as a function of $\Delta t_{\text{p-el}}$ for an excitation fluence of 0.85 mJ cm^{-2}. Intensities have been normalised to values before $\Delta t_{\text{p-el}} = 0$.

structural transition ($\Delta\tau \sim 0.35 - 2.0$ ps, depending on excitation density) found by Frigge *et al.* [10], the In/Si(111) system seems ideal to demonstrate the advantages of the microgun concept. Furthermore, while the mm-sized gun is ideally suited for studying the relaxation of the surface at later times ($\Delta t_{\text{p-el}} > 50$ ps), the more than ten times higher temporal resolution of the microgun should in principle allow us to resolve relaxation dynamics and the underlying energy transfer between electrons, key phonons of the indium layer and substrate modes. In the following, we report on very recent microgun experiments on the In/Si(111) system and discuss the first data on the ultrafast phase transition and recovery dynamics.

By analogy with Sec. 5.1 we first analyse the evolution of the main features in the LEED pattern following single-pulse optical excitation. Figure 5.4a shows a microgun ULEED pattern of the Si(111)(8×2)-In surface recorded with $E_{\text{kin}} = 80$ eV

electrons at $T = 60$ K. Note that for this series of experiments, wafers with a miscut angle of $(2\pm0.1)^\circ$ have been used to facilitate the growth of single-domain indium nanowires along the [110] direction. Moreover, the ULEED images have been corrected for distortions arising from the detection with a planar MCP, as well as stray fields from the microgun (for details, see section "Interpolation of correction vector field" in appendix E of Ref. [112]).

Comparing diffraction patterns before ($\Delta t_{\text{p-el}} < -2$ ps) and after ($2\,\text{ps} < \Delta t_{\text{p-el}} < 8\,\text{ps}$) time-zero (see difference image in Fig. 5.4b and time traces in Fig. 5.4c), we find a fast increase/decrease of the (4×1) /(8×2) diffraction spot intensities within the temporal resolution of the experiment ($\sim$ 3 ps; see also Fig. 5.5c). The two-fold streaks vanish and recover just as the diffraction spots of the broken-symmetry phase, suggesting that changes of the interchain correlation occur on a similar time scale as the structural transformations within the wires. Interestingly, we observe a strong periodic modulation of the streak intensity in the direction perpendicular to the chains (see dashed black rectangle in Fig. 5.4b). At this stage, the exact periodicity of this feature remains elusive due to the lack of higher order diffraction spots that could serve as support points for the distortion correction algorithm. Speculating about the origin of the modulation, it seems possible that – just like for diffraction rods – the intensity distribution along streaks is a function of $\boldsymbol{k}$ and energy E (see, e.g. the modulations of the scattering intensity perpendicular to the surface and Ewald construction in Sec. 2.3.2). In this case, the period of the pattern should change as a function of electron energy, which could easily be tested in future energy-dependent ULEED experiments. On the other hand, if the modulation period is energy-independent, it may hint at residual or local order perpendicular to the chains.

As far as the diffuse background is concerned, we find a relative enhancement of 2 % within a few ps and a subsequent cooling of the surface over $\sim$ 50 ps to a persisting level (see also Fig. 5.1c, bottom). This long-lived increase in lattice temperature suggests that the energy transfer between surface layer an substrate is rather inefficient. Similar observations have been made in trARPRES [57, 66] and were discussed as a possible reason for the metastable nature of the photoexcited (4×1) state [66]. In this respect, additional ULEED measurements with improved temporal resolution and a larger delay range are necessary to clearly separate the initial, electronically-driven structural dynamics from the subsequent increase in

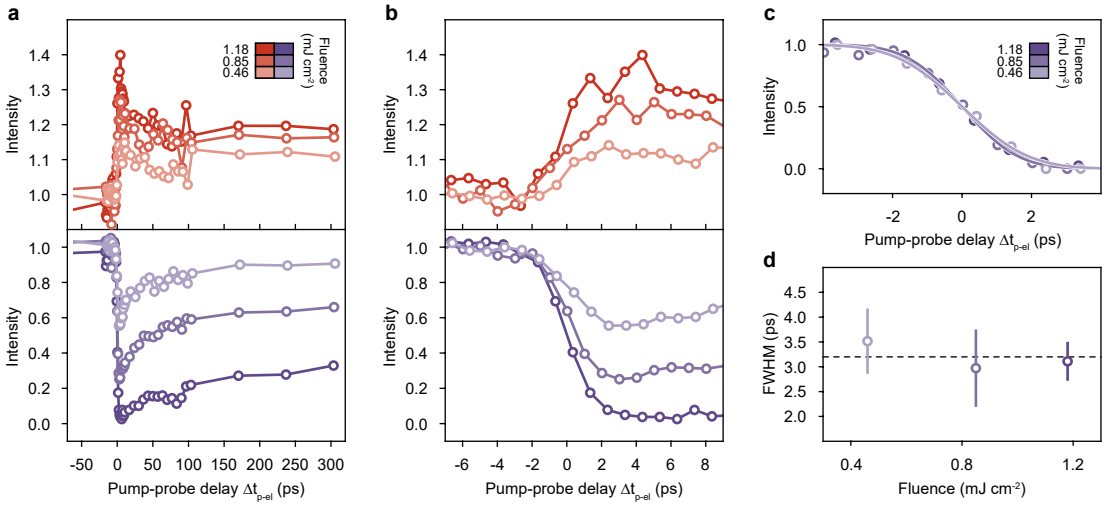

Figure 5.5: Ultrafast $(8\times2)\rightarrow(4\times1)$ phase transition observed on different time scales. **a**, Microgun pump-probe traces showing the intensities of (4×1) (red) and (8×2) (violet) spots as a function of the time delay $\Delta t_{\text{p-el}}$ for three different pump fluences. **b**, Diffraction spot intensities close to $\Delta t_{\text{p-el}} = 0$. **c**, Error function model fitted to the experimental data in the vicinity of time-zero for all three pump fluences. **d**, FWHM of the fit as a function of pump fluence.

lattice temperature (the maximum lattice temperature is reached at $\Delta t_{\text{p-el}} = 6$ ps according to Ref. [10]), and to better understand the role played by the substrate in the relaxation back to the ground state.

In a next step, we perform microgun pump-probe experiments at different fluences between $0.46 - 1.18\,\text{mJ}\,\text{cm}^{-2}$ to investigate how the level of electronic excitation influences both the transition into and the relaxation of the excited state within the first 50 ps after time-zero (Fig. 5.5a,b). Concerning the initial dynamics, the findings of Frigge *et al.* [10] indicate that strong electronic excitation affects the slope of the PES towards the (4×1) state, which in turn leads to an acceleration of atomic motion and a reduced time constant of 350 fs for the transition at high fluences. While the temporal resolution in this first set of ULEED experiments at relatively large gun-sample distances ($\Delta\tau_{\text{e}} \sim 3$ ps as determined from error function fits to the (8×2) spot intensities around $\Delta t_{\text{p-el}} = 0$; see Fig. 5.5c,d) is not sufficient to test this hypothesis, our results underline the fact that the transition occurs extraordinarily fast for a surface-specific structural phase transition. At the same time, all-optical pump-probe measurements (OPP, see Sec. 6.3) carried out as part

of this work, allow us to indirectly follow the structural dynamics of the indium monolayer with tenfold higher resolution in time. These experiments indeed seem to corroborate the picture of accelerated order parameter motion in the high fluence regime. Exploiting the full potential of ULEED [55], future studies should be able to directly track the accelerated motion of the system between the (8×2) and (4×1) states and measure the potential impact of coherent phonons on the structure factor.

As for the recovery of the system after optical excitation, the delay-dependent integrated (8×2) spot intensities recorded at different laser fluences differ considerably (Fig. 5.5a and Fig. 5.6). Specifically, at lower fluences the spot intensity recovers particularly fast within the first $30 - 50$ ps after the transition, followed by a significantly slower relaxation ($\sim$ ns) at later times (see also Fig. 5.2a). While a similar trend is also observed for the highest fluence of $F = 1.18\,\mathrm{mJ\,cm^{-2}}$, the remaining signal suppression after 50 ps is a strong function of F (40/65/85 % at $F = 0.46/0.85/1.18\,\mathrm{mJ\,cm^{-2}}$)[5].

We discuss these observations in the light of a model for the recovery of the Si(111)(8×2)-In surface recently proposed by Hafke *et al.* [303]. Here, the transformation from the (4×1) excited to the (8×2) ground state occurs independently in each atomic wire just like "a falling row of dominoes", i.e. unit cell by unit cell [9, 233, 303]. Assuming that step edges (and adsorbates) function as seeds for the return to the ground state, Hafke *et al.* determined the recovery velocity $v_{\mathrm{rec}} = (100 \pm 40)\,\mathrm{m/s} = (0.1 \pm 0.04)\,\mathrm{nm/ps}$, i.e. the velocity of $(4 \times 1)/(8 \times 2)$ domain boundaries, by recording the distribution of terrace widths Γ on the Si(111) surface in photoemission electron microscopy (PEEM). In this picture, the time it takes for a particular (4×1) domain i to completely transform back to the (8×2) ground state is given by $t_i = \Gamma_i / v_{\mathrm{rec}}$ (see Fig. 5.7a). For a homogeneously switched surface (to the (4×1) state) exhibiting a geometric distribution of barrier heights and a mean value $\langle\Gamma\rangle = 298\,\mathrm{nm}$, the fraction of the surface $p_{(8\times2)}(\Delta t_{\mathrm{p\text{-}el}})$ which has returned to the (8×2) ground state at the arrival time $\Delta t_{\mathrm{p\text{-}el}}$ of the electron pulse is

[5] Note that the fast initial relaxation is unlikely to be caused by a time-dependent DWF for two reasons: First, as demonstrated by Frigge *et al.* [10, 56, 116] and in our experiments, there is no significant DW contribution to the diffraction spot intensities. Second, if there was a DW contribution, it would affect both (4×1) and (8×2) spots in the same manner, which is not the case here.

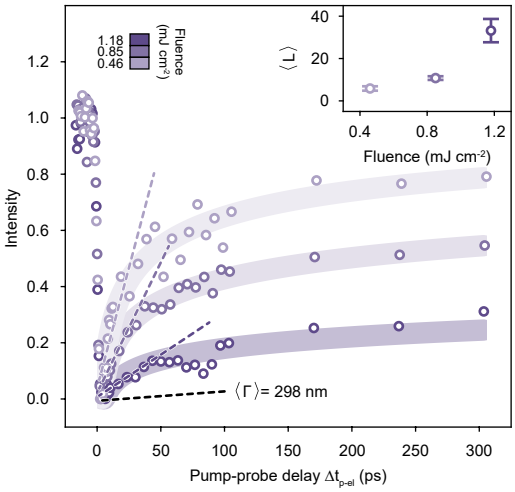

Figure 5.6: Relaxation from the metastable (4×1) state to the (8×2) state. Delay-dependent (8×2) spot intensities for different excitation fluences reveal a partial relaxation of the excited state within ∼ 50 ps and a subsequent slowdown of the recovery dynamics. The data is corrected by the maximum suppression ($\Delta t_{\text{p-el}} \sim 3$ ps) and normalised to values before $\Delta t_{\text{p-el}} = 0$. Shaded traces in background, stretched exponential fits serving as guide to the eye. Dashed coloured lines, linear models fitted to the data for $\Delta t_{\text{p-el}}$ to estimate the initial mean (4×1) domain length. Dashed black line, reference value from Ref. [303]. Inset, calculated mean domain length as a function of excitation fluence.

given by (see Ref. [303])

$$p_{(8\times2)}(\Delta t_{\text{p-el}}) = \int_0^{\Gamma_{\max}} p_\Gamma(\Delta t_{\text{p-el}}) \cdot p(\Gamma) \cdot \Gamma \, \mathrm{d}\Gamma \sim I_{8\times2}(\Delta t_{\text{p-el}}), \tag{5.1}$$

with $\Gamma_{\max}$ being the maximum observed terrace width, $p(\Gamma)$ the distribution of terrace widths, $p_\Gamma(\Delta t_{\text{p-el}} \leq t_i) = t \cdot v_{\text{rec}}/\Gamma_i$, $p_\Gamma(\Delta t_{\text{p-el}} > t_i) = 1$, and $I_{8\times2}(\Delta t_{\text{p-el}})$ the delay-dependent intensity of the (8×2) diffraction spots. This model reproduces the exponential decay of the metastable phase with a time constant of ∼ 3 ns, as observed by trRHEED [116, 303].

Our results now indicate that for fluences below $F_{\text{tot}} \sim 1.7\,\text{mJ}\,\text{cm}^{-2}$, the (8×2) surface is only partially switched to the (4×1) state. In order to estimate the (4×1) surface fraction after the optical pump pulse, we fit an error function model to the fluence-dependent spot suppressions from Fig. 5.2b and obtain a Gaussian distribution of barrier heights with a FWHM of $0.84\,\text{mJ}\,\text{cm}^{-2}$ for the (8×2) → (4×1)

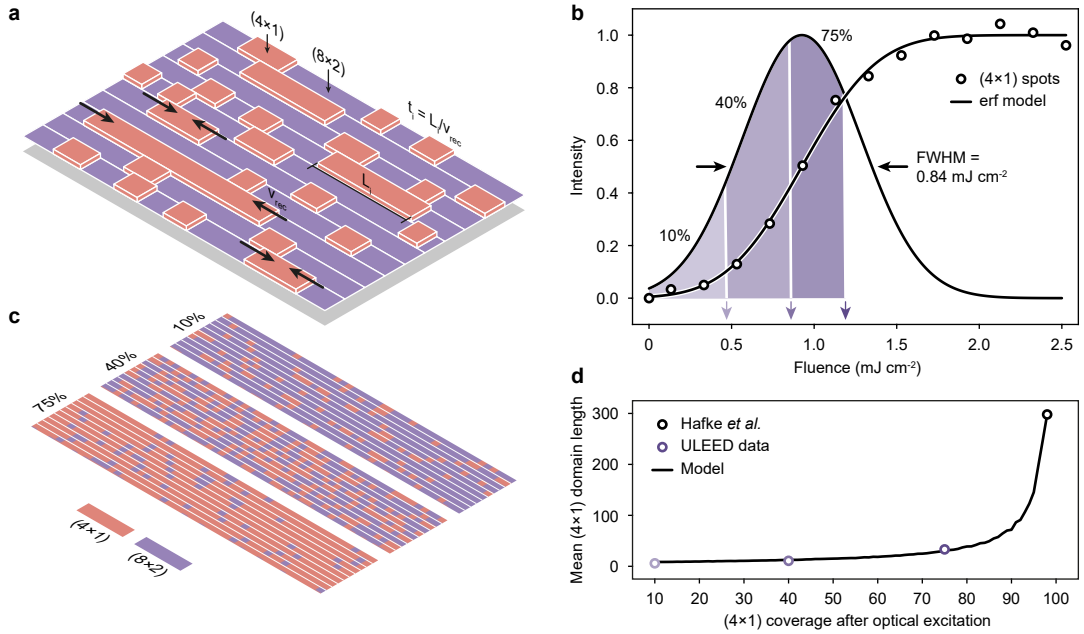

Figure 5.7: Heterogeneity of the surface after moderate optical excitation. **a**, Model of surface heterogeneity after weak optical excitation roughly corresponding to $F = 0.85\,\mathrm{mJ\,cm^{-2}}$ ((4×1) coverage $\sim 40\,\%$). v_{rec}, phase front velocity of the $(4\times1) \rightarrow (8\times2)$ transition; L_i, length of domain i; t_i, lifetime of the respective (4×1) domain. **b**, Gaussian distribution of barrier heights for the $(8\times2) \rightarrow (4\times1)$ transition inferred from the fluence-dependent (4×1) diffraction spot intensity (black dots, see also Fig. 5.2b). Black line, error function model fitted to the experimental data. Shaded areas indicate the fraction of the surface switched for excitation fluences of 0.46, 0.85 and $1.18\,\mathrm{mJ\,cm^{-2}}$ in microgun pump-probe experiments. **c**, Model of the optically excited surface assuming an individual switching efficiency of 10/40/75 % for each unit cell. **d**, Mean (4×1) domain length $\langle L \rangle$ as a function of the (4×1) reconstructed fraction of the surface calculated from the model in (**c**). Dots, domain lengths extracted from trRHEED and ULEED measurements at different fluences. The model curve has been normalized to the value for the mean domain size yielded by Hafke *et al.* [303] in the case of a completely switched surface.

transition (Fig. 5.7b). In this, we assume that surface defects, dopand atoms, as well as boundaries between (8×2) and supercooled (4×1) domains locally alter the effective barrier. Based on this model, we estimate a (4×1) coverage of 10/40/75 % for $F = 0.46/0.85/1.18\,\mathrm{mJ\,mJ^{-2}}$ in microgun experiments. In this context, a comparison of the excited state lifetimes for partially and completely switched surfaces in Ref. [116] points to a spatially heterogeneous distribution of individual (4×1) domains within the illuminated area for $F < F_{\mathrm{tot}}$. Figure 5.7a shows a schematic

representation of such a partially transformed surface for a (4×1) coverage of about 40 %. It is reasonable to assume that the distribution $P(L)$ of domain lengths L is no longer determined by the distribution $P(\Gamma)$ of terrace widths Γ alone. Instead, for a partially switched surface, the mean (4×1) domain size L may be significantly smaller than $\langle\Gamma\rangle$, leading to an overall faster recovery. By comparing the initial recovery rates in our experiments (see linear model fitted to the fluence-dependent (8×2) spot intensities for $\Delta t_{\text{p-el}} < 30$ ps in Fig. 5.6) to the model of Ref. [303] for a homogeneously switched surface (dashed black line), we estimate the mean (4×1) domain size to be (5 ± 1) nm for a (4×1) coverage of ~ 10 % and (33 ± 7) nm for a (4×1) coverage of ~ 75 % (see inset in Fig. 5.6 and Fig. 5.7d). Moreover, a simple numerical model of the surface can be used to further relate these results to Ref. [303]. To this end, we assume an independent switching probability $P_{\text{s}} = A_{(4\times1)}/A_{\text{surface}}$ for each unit cell and calculate the spatial distribution of (4×1) and (8×2) domains on a one-dimensional grid for different values of P_{s} (Fig. 5.7c[6]). From this, we extract the mean (4×1) domain length $\langle L\rangle$ as a function of the (4×1) coverage (Fig. 5.7d). A comparison of the domain lengths inferred from the slope of the delay-dependent (8×2) spot intensities in Fig. 5.6 (coloured dots in Fig. 5.7d) with the predictions of this simple model shows good agreement, suggesting that surface heterogeneity controls the relaxation to the ground state.

Interestingly though, at long delays, the slope of the data Fig. 5.6 decreases significantly and approaches the value found by Hafke *et al.*. This could mean that even after weak optical excitation the surface exhibits a non-negligible fraction of particularly long (4×1) domains. Alternatively, the long-term recovery of the ground state of the indium wires may be influenced by electron dynamics in the substrate. In this scenario, the photo-excitation of carriers in the silicon wafer by the pump pulse could lead to the formation of a space-charge region at the surface and a possible optical doping of the indium monolayer. STM measurements under laser illumination indicate the existence of a related effect and its role in stabilising the (8×2) phase below T_{c} [282]. Furthermore, it is unclear how the decay of the excited state due to thermal fluctuations contributes to the recovery dynamics (see Sec. 2.1.4). While one or more of the above effects may potentially influence the dynamics of the system on a ns time scale, the initial dynamics and relaxation should remain

[6]Note that the one-dimensional array has been reshaped into a two-dimensional surface for better visualisation.

largely unaffected.

In a last step, we explore the potential of time-resolved spot profile analysis (SPA) for the In/Si(111) system. In this context, ULEED has already demonstrated SPA-LEED capabilities, revealing phase-ordering dynamics in the incommensurate phase of $1T$-TaS_2 by measuring the CDW contribution to the FWHM of associated satellite diffraction peaks [18, 120]. Generally, SPA provides access to key properties of surfaces, such as long-range order or domain sizes (see also Sec. 2.3.3). A time-resolved realisation of SPA-LEED thus offers the possibility, e.g. to investigate how long-range order is established after an ultrafast optical quench. For the $(8\times2) \rightarrow (4\times1)$ transition, however, the situation is markedly different, since even for an incomplete transformation of the surface, long-range order is preserved. As a consequence, a significant broadening of diffraction spots is not expected [116]. Nonetheless, as pointed out by Refs. [116, 205], SPA can be used to determine the sizes of (8×2) and (4×1) domains through an analysis of the diffuse background formed due to the coexistence of multiple structural phases[7].

While the microgun design generally allows for time-resolved SPA-LEED measurements [18, 55], for technical reasons, the momentum resolution in the first experiments on the Si(111)(8×2)-In surface is not sufficiently high to extract reliable information. Instead, we discuss delay-dependent changes to the diffraction spot profiles recorded with the mm-sized gun (Fig. 5.8). Figures 5.8a and b show the colour-coded intensity distribution of the of the $(\frac{5}{8}, \frac{3}{8})$ spot before and 700 ps after $\Delta t_{\text{p-el}} = 0$ ($F = 0.9\,\text{mJ}\,\text{cm}^{-2}$). The length of the domains along the chain direction can be inferred from an analysis of the spot profile in the two-fold direction. Specifically, at each delay step the spot profile along $k_\parallel$ (white line in Fig. 5.8a,b) is fitted by a linear combination of the instrumental response function[8] and a Lorentzian background with amplitude A_{bg} and FWHM $= 2\Gamma_{\text{bg}}$. Exemplary fits for $\Delta t_{\text{p-el}} = \pm 700\,\text{ps}$ are shown in Fig. 5.8c and d.

While the amplitude of the Lorentzian is negligibly small before time-zero, we find a significant contribution of the background function for positive delays (red line in Fig. 5.8d; see also Fig. 5.8e). Directly after the transition, however, the (8×2) spots are strongly suppressed, which prevents a meaningful SPA for $\Delta t_{\text{p-el}} < 150\,\text{ps}$. The

[7] Here, the two types of domains are interpreted as terraces of different heights, making up a two-level system at the surface [116].

[8] The instrumental response function is given by the average spot profile recorded for $\Delta t_{\text{p-el}} < 0$.

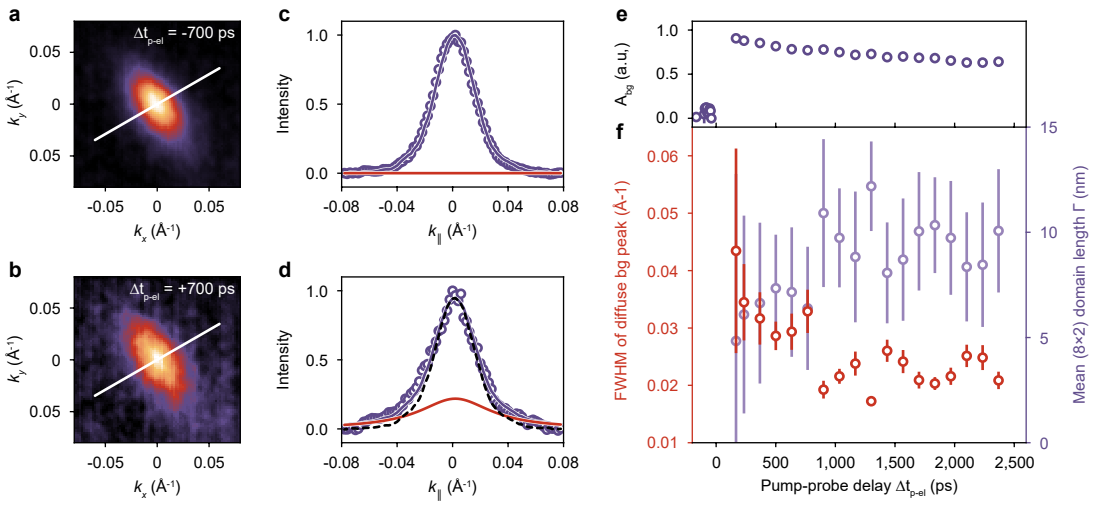

Figure 5.8: Time-resolved spot-profile analysis. **a**,**b**, Selected area from the ULEED pattern of the Si(111)(8×2)-In surface around the $(\frac{5}{8}, \frac{3}{8})$ spot before (**a**) and after (**b**) $\Delta t_{\text{p-el}} = 0$ (data recorded with mm-sized gun). **c**,**d**, Normalized profile of the $(\frac{5}{8}, \frac{3}{8})$ spot along $k_{\|}$ (parallel to chain direction) before (**c**) and after (**d**) $\Delta t_{\text{p-el}} = 0$. Violet dots, experimental data; violet line, linear combination of instrumental response function and Lorentzian background fitted to the data; red line, background contribution to the fit; dashed black line in **d**, instrumental response function or line profile, respectively, from **c**. **e**, Amplitude of the Lorentzian background as a function of the pump-probe delay. **f**, Delay-dependent FWHM of the background signal (red) and corresponding mean domain length Γ (light violet). Note that peaks widths have been analysed only for $\Delta t_{\text{p-el}} > 150$ ps. For shorter delays, the strong initial suppression of the (8×2) spots prevents the reliable determination of γ_{bg}. Error bars, 95 % CI of the fit.

FWHM of the lorentzian background extracted from the fits to the data is shown in Fig. 5.8e and f as a function of the pump-probe delay (red dots and error bars). From this, the mean (8×2) domain length $\langle L \rangle (\Delta t_{\text{p-el}})$ can be calculated using the relation $\langle L \rangle = 4/\text{FWHM}$ given in Ref. [205] (light violet dots). Although we do not observe a significant evolution of the mean domain length after time-zero, the robust background contribution in this delay regime corroborates the notion of a heterogeneous surface with relatively short (8×2) or (4×1) domains, respectively. Essentially, the values for $\langle L \rangle$ obtained from SPA and the determination of the recovery rate (Fig. 5.6) agree with the values yielded by a similar analysis in Ref. [116]. The significance of the SPA is apparently limited by the finite momentum resolution of the ULEED apparatus (see Sec. 3.1.3). In particular, a mean domain length $\langle L \rangle > 100$ nm would be expected for long delays. Considering the maximum transfer

width of 21 nm ($\Delta k = 0.03\,\text{Å}^{-1}$) for the mm-sized gun, this is beyond the current resolution of ULEED. Smaller domains and significant changes of the $(4\times1)/(8\times2)$ fractions are likely to occur closer to time-zero, where the strong spot suppression unfortunately prevents a thorough analysis. Future microgun designs will address these limitations and facilitate ultrafast SPA-LEED studies of the In/Si(111) surface at higher temporal and momentum resolution, as well as improved signal-to-noise ratio.

The first set of microgun experiments of this fascinating surface system underlines the role of nanoscale inhomogeneities on the optically triggered $(8\times2)\rightarrow(4\times1)$ transition, and calls for time-resolved studies with high real-space resolution. It will be interesting to see how ultrafast realisations of surface-sensitive techniques, such as STM, PEEM or LEEM contribute to a better understanding of the microscopic dynamics. Combining ps temporal and nm spatial resolution with high surface sensitivity, these techniques should be able to observe the motion of domain boundaries between (4×1) and (8×2) reconstructed wire segments in real time, considering the characteristic recovery velocity of 0.1 nm/ps. In this, step edges could potentially be utilised as seeds for the structural transformation back to the ground state and thus ensure the necessary reversibility for stroboscopic measurements (see Sec. 7.2.1).

Chapter 6

Coherent control of the surface structural phase transition

6.1 Double-pulse excitation of the (8×2) surface

The previous chapter focused on the ultrafast structural dynamics following single-pulse optical excitation of the Si(111)(8×2)-In surface. While the results of ULEED confirm a number of key observations made by trRHEED [10, 56] and trARPES [11, 12, 57, 58] on the same system, they also shed new light on the role of surface heterogeneity in the transition as well as the subsequent relaxation, stimulating further experiments in this direction. In a next step, we will turn to the main goal of this work and discuss the possibility of exerting coherent control over the $(8\times2) \rightarrow (4\times1)$ transition.

What is particularly interesting in this context is the rather gradual threshold discussed in Sec. 5.2, suggesting a spatial distribution of energy barriers between the (8×2) and (4×1) configurations (see Fig. 5.2b). Bearing in mind the role of electronic excitation in shaping the PES and, consequently, barrier height, it seems likely that the transition is susceptible to weak perturbations within the intermediate fluence regime. Specifically, a large fraction of the remaining (8×2) domains exhibit a sufficiently lowered but not completely vanishing barrier directly after moderate optical excitation. Furthermore, the Peierls-like nature of the transition as well as the key role of displacive excitation in driving the underlying structural changes on a fs time scale [10] suggest that the creation of such an excited (8×2) state is accompanied by the generation of coherent phonons or amplitudons, respectively. However, no observations of coherent phonons of the (8×2) phase have been reported

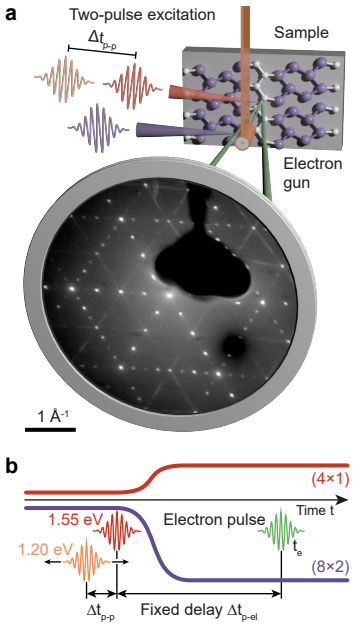

Figure 6.1: Experimental scheme for the coherent control of the phase $(8\times2) \rightarrow (4\times1)$ transition. **a**, ULEED in combination with double (multi-) pulse optical excitation. **b**, Pulse sequence in the time domain. The phase transition efficiency is monitored by the electron pulse (fixed delay $\Delta t_{\text{p-el}}$) as a function of the mutual delay $\Delta t_{\text{p-p}}$ between two optical excitation pulses. Panel **a** taken from Ref. [53].

so far[1]. In this regard, Frigge *et al.* explained the absence of oscillatory signatures in pump-probe experiments by a rapid energy transfer of shear and rotation modes to lower-lying surface and bulk phonons. In contrast, trARPES measurements point to a highly non-thermal distribution of optical phonons after photo-excitation and a bottleneck for the cooling of the electronic system determined by electron-phonon and phonon-phonon coupling [57]. Hence, with respect to the main objective of this work, two main questions arise: (1) Are there long-lived structural coherences connected to the $(8\times2) \rightarrow (4\times1)$ transition? (2) If so, can they be harnessed to exert coherent control over the phase transition?

Answering these questions calls for alternative experimental schemes with high sensitivity to coherent optical phonons and transition efficiency. As described in Sec. 2.2.3, femtochemistry offers a powerful set of experimental and theoretical tools for the investigation and control of electronic or vibrational coherences in molecules. A promising approach is given by time-domain control schemes discussed in Sec. 2.2.3. Here, timed pulse sequences are used to steer the evolution of (vibrational) wave packets on a generally multidimensional PES, e.g. by controlling the vibrational

[1]It should be noted that after discussing first results of this work with Frigge *et al.* [10], the authors reexamined part of their data and found potential signatures of coherent amplitude motion in the dynamics of the (00) spot in trRHEED. The corresponding data sets had been published in Ref. [116]. Moreover, very recently, Refs. [66] and [153] reported the observation of coherent oscillations in excited state populations using trARPES.

amplitude [39, 158, 165, 304]. Motivated by the successful application of this central concept of femtochemistry to molecules [38, 41], we now explore the combination of ULEED and optical pulse sequences for excitation to manipulate the switching efficiency of the (8×2) → (4×1) transition close to its threshold. The basic concept of such "double-pulse" ULEED experiments is visualised in Fig. 6.1: Instead of a single intense optical pulse, we use a pair of weaker pump pulses (P_1, 1030 nm; P_2, 800 nm; see Sec. 3.1.1) with variable delay $\Delta t_{\text{p-p}}$ to drive the transition and probe the resulting structure by ULEED at a later time of $\Delta t_{\text{p-el}} = 75$ ps.[2] This way, ULEED probes the efficiency of the transition, i.e. the fraction of the surface switched to the metastable (4×1) state.

Signatures of coherent control

Figure 6.2a shows exemplary data of a double-pulse ULEED experiment for incident fluences $F_{1,030} = 0.37\,\text{mJ}\,\text{cm}^{-2}$ and $F_{800} = 0.24\,\text{mJ}\,\text{cm}^{-2}$.[3] As a main result, we find that the signature of the metastable state, i.e. the mirror-like suppression/enhancement of the (8×2) /(4×1) diffraction spot intensity discussed in Sec. 5.1, is a strong function of the double-pulse delay $\Delta t_{\text{p-p}}$. Specifically, for combined or total fluences lying within the intermediate regime of $0.5 - 1.4\,\text{mJ}\,\text{cm}^{-2}$ (see Fig. 5.2b in Sec. 5.2), pronounced oscillations with a period of $\sim 1 - 2$ ps are observed on either delay side, with opposing behaviour for the (4×1) and (8×2) spots. The peaked signal around time-zero, on the other hand, is attributed to electronic excitation with a lifetime of ~ 3 ps, which is in agreement with trARPES measurements of excited state populations and transient electronic temperatures in the same fluence regime [12, 57, 66] (see also Fig. 6.4a, bottom). Interestingly though, the maximum suppression/enhancement is not found at $\Delta t_{\text{p-p}} = 0$ but at $\Delta t_{\text{p-p}} \approx \pm 300$ fs, which is about 1/4 of the rotation mode period $T_{\text{rot}} = 1.2$ ps (see Fig. 6.2c).

The observed oscillations clearly demonstrate a coherent response of the signal, the frequency range of the signal modulation (< 1 THz) pointing to a vibrational origin. In particular, coherent atomic motion induced by the first pulse controls the switching efficiency for the second pulse. Based on previous experimental and

[2] This means that, in contrast to Sec. 5, the electron is not scanned across time-zero but fixed at later times to monitor the final state surface structure.

[3] Note that the combined fluence $F_{\text{tot}} = F_{1,030} + F_{800} = 0.61\,\text{mJ}\,\text{cm}^{-2}$ lies within the intermediate fluence regime, where the leverage of optical excitation is largest.

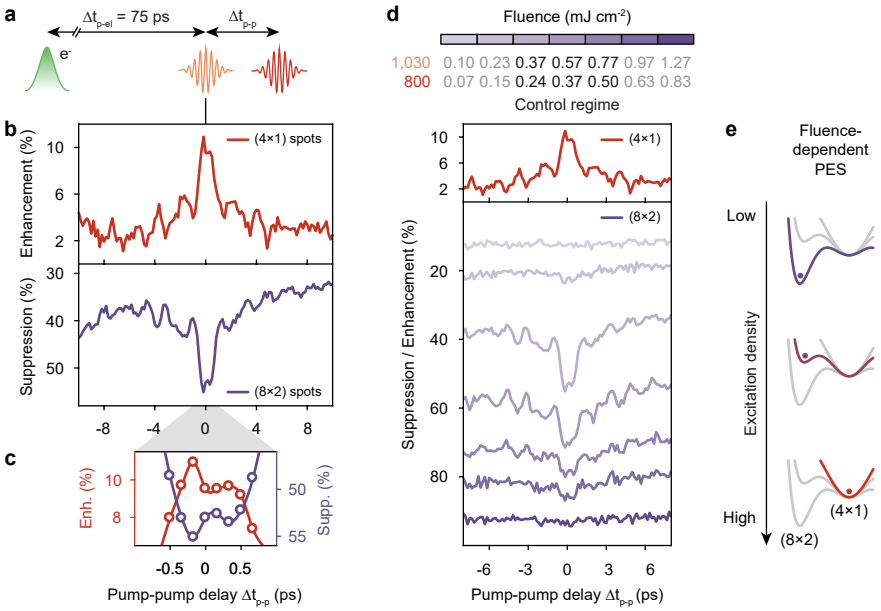

Figure 6.2: Signatures of coherent control. **a**, Pulse sequence in the time domain. Red (orange), 800 (1030) nm optical pump pulses; green, electron pulse. **b**, Suppression or enhancement of the integrated (8×2) and (4×1) diffraction spot intensity as a function of the double-pulse delay $\Delta t_{\text{p-p}}$ for incident fluences $F_{1,030} = 0.37\,\text{mJ}\,\text{cm}^{-2}$ and $F_{800} = 0.24\,\text{mJ}\,\text{cm}^{-2}$. The signal is normalised to values recorded for $F_{1,030} = F_{800} = 0$ and $\Delta t_{\text{p-el}} = 75$ ps. **c**, $(8 \times 2)/(4{\times}1)$ spot suppression/enhancement close to $\Delta t_{\text{p-p}} = 0$. **d**, Double-pulse traces recorded for different pump fluences $F_{1,030}$ and F_{800}. (4×1) trace identical to (**b**). **e**, 1D model of the PES after first optical excitation for low (top), medium (middle) and high (bottom) excitation density or pump fluence, respectively. Coloured dots, position of the order parameter. Taken from Ref. [53].

theoretical studies [10, 155, 241] and considering the resonant excitation conditions ($\hbar\omega > \Delta E_{\text{g}}$), we assume that DECP is the dominant mechanism for the generation of coherent phonons in this system.

Fluence dependence

The prominent signature of long-lived vibrational coherence in double-pulse experiments raises the question of how our results can be reconciled with the findings of Frigge *et al.* [10], who reported a critical damping of modes involved in the transition. To resolve this apparent discrepancy and to determine the maximum leverage of the double-pulse control scheme, we record double-pulse traces for dif-

ferent combined fluences between $0.17 - 2.10\,\mathrm{mJ\,cm^{-2}}$ (Fig. 6.2d)[4]. The data sets are normalized to peak intensities measured at $\Delta t_{\text{p-el}} = 75$ ps and for $F_{1,030} = F_{800} = 0$. Whereas no periodic modulation of the spot intensities is observed below $F_{\text{tot}} = F_{1,030} + F_{800} < 0.4\,\mathrm{mJ\,cm^{-2}}$, coherent oscillations are clearly visible between $0.61\,\mathrm{mJ\,cm^{-2}}$ and $1.27\,\mathrm{mJ\,cm^{-2}}$ ("control regime"). For even higher fluences ($F_{\text{tot}} > 1.5\,\mathrm{mJ\,cm^{-2}}$), the modulation amplitude decreases rapidly. Concerning the leverage in double-pulse experiments, we extract a maximum value of $\sim 4\,\%$ from the fluence-dependent modulation amplitude at $F_{1,030} = 0.37\,\mathrm{mJ\,cm^{-2}}$ and $F_{800} = 0.24\,\mathrm{mJ\,cm^{-2}}$.

These results can be understood within the one-dimensional PES model of the transition [9, 10, 155, 237, 241], assuming a distribution of barrier heights (Fig. 6.2e): At low excitation densities (top), the first pump pulse switches less than 10 % of the surface to the (4×1) phase. This affects only those domains with very small initial barrier height ΔE_{b}. The remaining fraction of the surface remains in a weakly excited (8×2) state exhibiting a distribution of rather large barriers towards the (4×1) state. While the first pulse most probably excites coherent phonons in this state via DECP, vibrational motion does not play a decisive role in promoting or hindering the transition because of the large residual barrier. At high excitation densities (bottom), on the other hand, the first pulse already transforms the majority of (8×2) domains to the metastable state, drastically reducing the switchable fraction of the surface for the second pulse. Only in the control regime (middle), changes in energy due to coherent vibrational motion in the excited (8×2) state are comparable to ΔE_{b} for a sufficiently large fraction of the surface. These observations directly link our work to Ref.[10], which focuses on the initial dynamics of the transition at high excitation densities. For this fluence regime, our measurements explain the absence of coherent amplitude motion and a corresponding contribution to diffraction peak intensities. As discussed in Sec. 3.1.3 and 5.4, future ultrafast electron diffraction experiments with sufficiently high temporal resolution should be able to observe phonon coherences even for single-pulse excitation, provided a high signal-to noise ratio for (8×2) diffraction spots and a measurable impact of coherent atomic motion on the structure factor F.

[4]Note that F_{800} is generally higher than $F_{1,030}$ since the excitation of the transition is driven more efficiently by 800 nm pulses. F_{800} and $F_{1,030}$ are chosen as to achieve equal suppressions of the (8×2) diffraction spots for each of the pulses.

Role of pump-probe delay

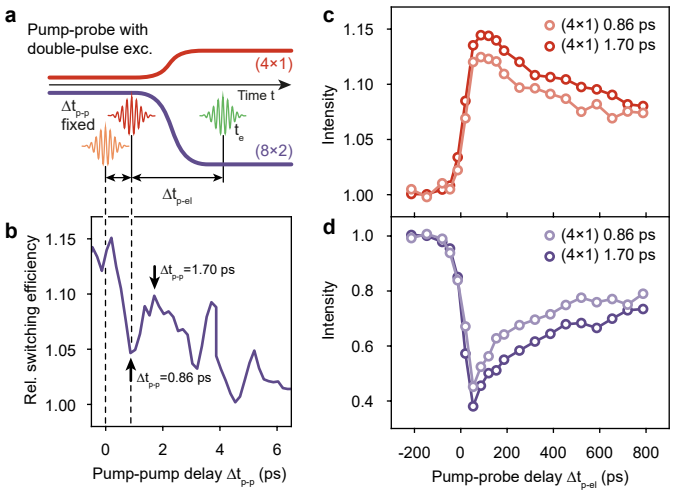

Figure 6.3: Leverage of double-pulse excitation as a function of $\Delta t_{\text{p-el}}$. **a**, Pulse sequence in the time domain. Note that in this set of experiments $\Delta t_{\text{p-p}}$ is fixed while the electron pulse is scanned across time zero. **b**, Relative switching efficiency as a function of the double-pulse delay. Black arrows indicate the two delays between P_1 and P_2 chosen for pump-probe experiments in **c**,**d**. **c**,**d**, Pump-probe traces recorded as a function of $\Delta t_{\text{p-el}}$ for two different double-pulse delays.

The above experiments demonstrate the coherent control over the $(8\times2) \rightarrow (4\times1)$ transition by monitoring diffraction spot intensities at a single pump-probe delay $\Delta t_{\text{p-el}}$. At the same time, the observed recovery dynamics following single-pulse optical excitation (Sec. 5.4) suggest that (4×1) reconstructed surface areas exhibit a distribution of domain lengths, and that individual (4×1) wire segments are sequentially transformed back to the (8×2) ground state at $v_{\text{rec}} \sim 100\,\text{m/s}$. Starting from this model [303], it can be assumed that a large part of the surface relaxes particularly fast through the switching of short (4×1) domains. It therefore seems possible that the leverage of double-pulse excitation is larger close to $\Delta t_{\text{p-el}} = 0$. To investigate this aspect, and to compare the recovery of the surface after single- or double-pulse excitation, respectively, we perform two consecutive experiments: First, the relative switching efficiency

$$E_{\text{s}}(\Delta t_{\text{p-p}}) := 1 - \frac{\left(I_{8\times2}(\Delta t_{\text{p-p}} - \langle I_{8\times2}(\Delta t_{\text{p-p}} > \Delta t^*_{\text{p-p}})\rangle)\right)}{\langle I_{8\times2}(\Delta t_{\text{p-p}} > \Delta t^*_{\text{p-p}})\rangle} \tag{6.1}$$

is determined in pump-pump-probe experiments (Fig. 6.3b)[5]. Based on this data set, we identify two double pulse delays $\Delta t_{\text{p-p,1}} = 0.86$ ps and $\Delta t_{\text{p-p,2}} = 1.70$ ps for which the transition efficiency is either reduced or enhanced. Second, we record the intensities of (4×1) and (8×2) peaks as a function of $\Delta t_{\text{p-el}}$ for double-pulse delays $\Delta t_{\text{p-p}}$ fixed at $\Delta t_{\text{p-p,1}}$ or $\Delta t_{\text{p-p,2}}$ (Fig. 6.3a). The resulting pump-probe traces clearly show the impact of the double-pulse delay on the transition efficiency over hundreds of picoseconds (Fig. 6.3c,d)[6]. On the other hand, the time constant for the decay of the metastable (4×1) state remains largely unaffected by the pump-pump delay. Furthermore, we find no evidence for an increased leverage close to time-zero in experiments with the mm-sized gun. Given the non-trivial decay of the excited state (see the rapid partial recovery of (8×2) spot intensities within < 30 ps in Fig. 5.6), it seems likely that the time-resolution of the experiment (~ 50 ps) is insufficient to resolve potential changes in leverage for small positive delays. Future double-pulse microgun experiments will provide deeper insights in this regard.

6.2 Decisive structural modes

While the periodic modulation of the pump-pump traces evidences the key role played by vibrational coherence in controlling the transition, it remains an open question as to which lattice modes contribute to this effect. In order to identify potential candidates for decisive phonon modes, we perform a Fourier analysis of the relative switching efficiency for a double-pulse experiment with $F_{1,030} = 0.32\,\text{mJ}\,\text{cm}^{-2}$ and $F_{800} = 0.21\,\text{mJ}\,\text{cm}^{-2}$ (Fig. 6.4a, top). The spectral density of the signal exhibits two significant frequency contributions well below 1 THz, peaked at 0.55 THz and 0.83 THz with bandwidths of ~ 0.1 THz (see inset), and an amplitude ratio of about four to one. These frequency bands point to shear and rotational modes of the indium monolayer, two of which are associated with the structural changes during the phase transition [10, 107, 239, 256] (see Fig. 6.4b and Sec. 4.3.3): (1) The antisymmetric shear mode at $f = 0.55$ THz (wave number $18.3\,\text{cm}^{-1}$), corresponding to the shearing of adjacent Peierls chains and coupled to the up/down movement of the m_1 band around the zone center ($\overline{\Gamma}_{(8\times2)}$ point) as well as the charge

[5] $\Delta t^*_{\text{p-p}}$ is significantly larger than the temporal overlap of the two optical pulses given by their cross-correlation, and the damping constant of the coherent phonon oscillations ($\Delta t^*_{\text{p-p}} = 10\,\text{ps}$).

[6] Note that the more suppressed/enhanced trace ($\Delta t_{\text{p-p,1}}$) has been recorded first to account for potential sample aging effects which would lower the transition efficiency.

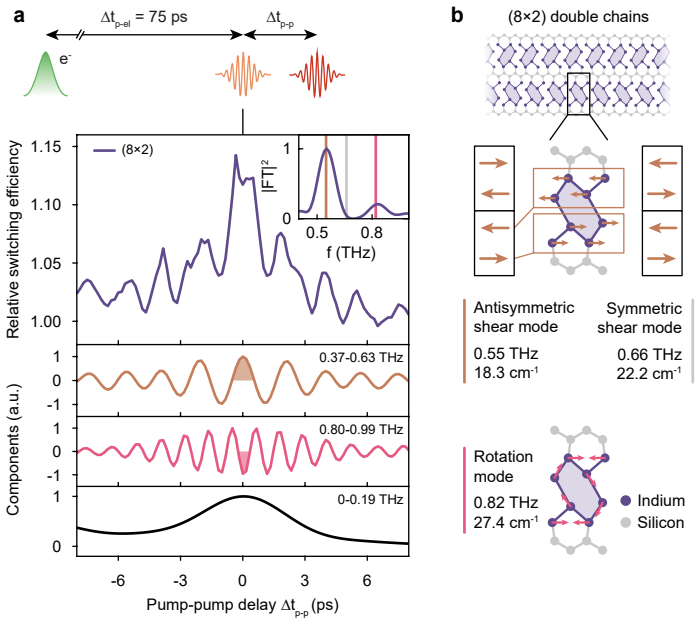

Figure 6.4: Frequency-specific contributions to the switching efficiency. **a**, Top, delay-dependent relative switching efficiency for $F_{1,030} = 0.32\,\mathrm{mJ\,cm^{-2}}$, $F_{800} = 0.21\,\mathrm{mJ\,cm^{-2}}$. Inset, spectral density of switching efficiency; vertical lines represent the frequencies of structural modes given in **b**. FT, Fourier transform. Bottom, Fourier-filtered contributions of different frequency components. Brown and pink shaded regions indicate the distinct initial phases. a.u., arbitrary units. **b**, Prominent low-frequency modes of the (8×2) structure (see also Sec. 4.3.3 and Fig. 6.11 in Sec. 6.4). The symmetric and the antisymmetric shear mode differ with regard to the direction of shear motion in neighbouring (4 × 2) chains. Taken from Ref. [53].

transfer to m_2/m_3. (2) The hexagon rotation mode at $f = 0.82$ THz (wave number $27.4\,\mathrm{cm^{-1}}$), which is associated with the Peierls dimerisation along the chain direction and coupled to the gap at the Brillouin zone boundary ($\overline{\mathrm{X}}_{(8\times2)}$ point). In contrast, the symmetric shear mode at $f = 0.66$ THz (wave number $22.0\,\mathrm{cm^{-1}}$) is not involved in the structural transition but has a prominent signature in Raman measurements [240]. Indeed, the ULEED data presented in Fig. 6.4 suggests that the transition efficiency is modulated by the antisymmetric shear and the hexagon rotation mode.

Fourier-filtered traces of the two observed frequency bands provide further insights into the role of different modes in controlling the transition (Fig. 6.4a, bottom). To extract such frequency-specific contributions to the switching efficiency, we select regions of the Fourier spectrum by multiplying a super-Gaussian window function

of the form

$$F_{\mathrm{filt},f}(f, f_\mathrm{c}) = \exp\left(-\left(\frac{(f-f_\mathrm{c})^2}{2\sigma_f^2}\right)^3\right) \tag{6.2}$$

and afterwards calculate inverse Fourier transform to yield the frequency-filtered signal in the time domain[7]. Interestingly, the two resulting traces exhibit distinct initial phases at $\Delta t_\mathrm{p\text{-}p} = 0$ ($\phi_\mathrm{shear} - \phi_\mathrm{rot} \approx \pi$). In other words, assuming displacive excitation as the main mechanism for excitation of shear and rotation modes, the transition efficiency is increased (decreased) for a maximum initial excitation of the shear (rotation) mode. While this explains the peculiar feature of the phase transition efficiency around $\Delta t_\mathrm{p\text{-}p} = 0$ (see Fig. 6.2c), the reason for the different roles of shear and rotation motion in controlling the transition warrants further investigation (see Sec. 6.3 and 6.4). Apart from the analysis of vibrational coherence, Fourier filtering can also be used to separate and investigate electronic contributions to the transition efficiency (Fig. 6.4a, bottom, 0-0.19 THz). Based on the Landau picture of the transition [9, 10, 116, 237] the increase of $E_\mathrm{s}(\Delta t_\mathrm{p\text{-}p})$ due to electronic excitation can be explained by a transient deformation of the one-dimensional PES, already switching (8×2) domains with relatively small energy barriers towards the (4×1) state. As mentioned before, the extracted lifetime of electronic excitation (~ 3 ps) matches with recent trARPES data [57].

Next, we study how the frequencies of shear and rotational phonons evolve as a function of the double-pulse delay. Such frequency changes are particularly interesting because they allow conclusions to be drawn about the PES of the transition, as well as the role of particular modes, i.e. their orientation relative to the reaction path. For example, as described in Sec. 2.2, modes pointing towards a transition state of the PES typically soften upon electronic excitation or for temperatures approaching T_c (see Sec. 2.2 for details). In this work, delay-dependent frequency shifts are determined from short-time Fourier transforms (STFT) of the data which are presented in in Fig. 6.5. To this end, we calculate the Fourier transform of the delay-dependent relative switching efficiency $E_\mathrm{s}(\Delta t_\mathrm{p\text{-}p})$ within a super-Gaussian window

[7] Central frequency f_c and width σ_f of the Gaussian window function for the shear contribution: $f_\mathrm{c} = 0.50$ THz, $\sigma_f = 0.10$ THz. For the rotation contribution: $f_\mathrm{c} = 0.90$ THz, $\sigma_f = 0.07$ THz. For the DC contribution: $f_\mathrm{c} = 0.0$ THz, $\sigma_f = 0.14$ THz

function

$$F_{\mathrm{filt},t}(\Delta t_{\text{p-p}}, \Delta t_{\mathrm{shift}}) = \exp\left(-\left(\frac{(\Delta t_{\text{p-p}} - \Delta t_{\mathrm{shift}})^2}{2\sigma_t^2}\right)^3\right) \tag{6.3}$$

in the time domain by evaluating the product $F_{\mathrm{filt},t}(\Delta t_{\text{p-p}}, t_{\mathrm{shift}}) \cdot E_{\mathrm{s}}(\Delta t_{\text{p-p}})$ for values $-\Delta t^*_{\text{p-p}} < \Delta t_{\mathrm{shift}} < \Delta t^*_{\text{p-p}}$. Figure 6.5a shows the resulting spectral density as a function of the double-pulse delay $\Delta t_{\text{p-p}}$ and the frequency f. A pronounced softening (hardening) of the shear (rotation) feature is observed towards double-pulse overlap (bottom; see also Fig. 6.5d)[8]. Similar results are obtained in double-pulse experiments with unequal pulse energies (Fig. 6.5b). In this case, a weak pump pulse first excites coherent phonons of the (8×2) structure by means of DECP without transforming a substantial fraction of the surface to the (4×1) state. A stronger second pulse then switches the vibrationally excited ground state depending on $\Delta t_{\text{p-p}}$, resulting in pronounced oscillations at positive double-pulse delays. In contrast, the switching efficiency shows no significant modulation at negative delays, i.e. for a reversed sequence of pulses. This is a consequence of the strong pulse already switching large parts of the surface to the metastable state.

In addition to the softening and hardening of the observed coherent phonons, an analysis of the respective lifetimes τ is interesting with regard to recent trARPES results on momentum-resolved population dynamics [57]. Assuming a linear increase (decrease) in shear (rotation) frequency over time, i.e. $\omega = \omega(\Delta t_{\text{p-p}}) \approx (\Delta\omega/\Delta(\Delta t_{\text{p-p}})) \cdot \Delta t_{\text{p-p}}$, a damped oscillator model can be fitted to the individual frequency contributions from Fig. 6.4a to estimate τ_{shear} and τ_{rot}:

$$\xi(\Delta t_{\text{p-p}}) = \xi_0 \exp\left(-\frac{\Delta t_{\text{p-p}}}{\tau}\right) \cdot \cos(\omega(\Delta t_{\text{p-p}})\Delta t_{\text{p-p}} - \phi). \tag{6.4}$$

From the fits, we extract lifetimes of $\tau_{\mathrm{shear}} = (5.2 \pm 0.5)$ ps for the shear and $\tau_{\mathrm{rot}} = (5.9 \pm 0.6)$ ps for the rotation mode (see also Fig. 6.5c). This indicates that optically-triggered vibrational coherence in shear and rotational phonon modes decays on a similar timescale as the electronic temperature. In this context, Nicholson *et al.* [57] recently proposed a pathway for energy relaxation after ultrafast optical excitation. Based on a thermal model of the electron population dynamics and the observation of a persisting elevated electron temperature well after 1 ps[9], the authors argue

[8] $f_{\mathrm{shear,min}} = 0.50$ THz, $f_{\mathrm{shear,max}} = 0.59$ THz; $f_{\mathrm{rot,min}} = 0.81$ THz, $f_{\mathrm{rot,max}} = 0.87$ THz.
[9] Similar results were reported by Cháves-Cervantes *et al.* [12].

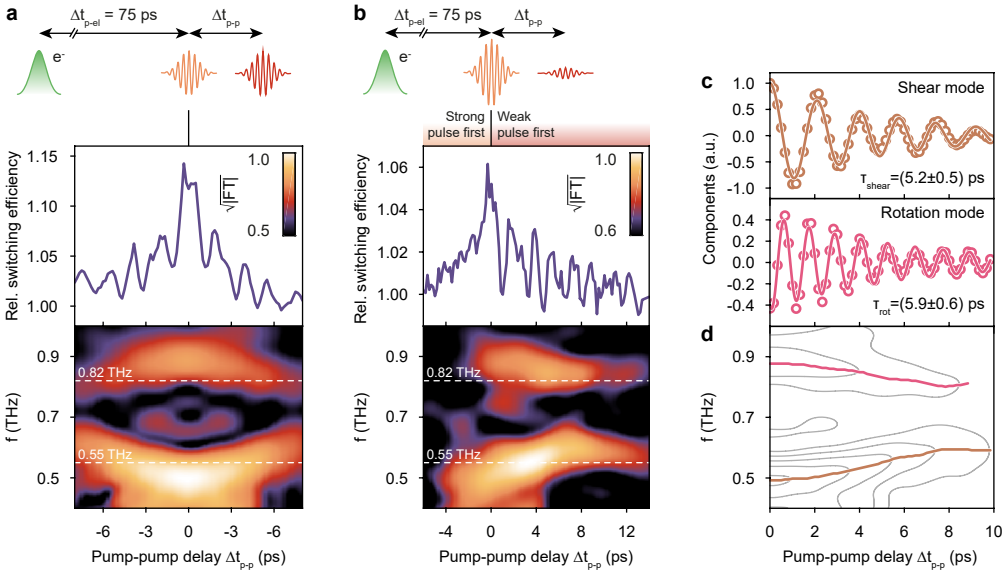

Figure 6.5: Phonon softening, hardening and lifetimes. **a**, Relative switching efficiency as a function of the double-pulse delay $\Delta t_{\text{p-p}}$ (top) and short-time Fourier transform (bottom) for equal pump pulses ($F_{1,030} = 0.32\,\text{mJ}\,\text{cm}^{-2}$; $F_{800} = 0.21\,\text{mJ}\,\text{cm}^{-2}$), revealing a pronounced softening/hardening of the shear/rotation component close to $\Delta t_{\text{p-p}} = 0$. **b**, Relative switching efficiency and short-time Fourier transform for unequal pump pulses ($F_{1,030} = 0.48\,\text{mJ}\,\text{cm}^{-2}$; $F_{800} = 0.15\,\text{mJ}\,\text{cm}^{-2}$). **c**, Shear (top) and rotation (bottom) frequency components of the relative switching efficiency trace in (**a**) (dots), and damped oscillator models (lines) fitted to the data. **d**, Delay-dependent dominant frequency of shear (gold) and rotation (pink) modes as a function of $\Delta t_{\text{p-p}}$ (dataset **a**). Grey contour lines, STFT from **a**. Panels **a** and **b** taken from Ref. [53].

that high-energy optical phonons act as a bottleneck for the cooling of electrons. In this scenario, electronic energy is transferred preferentially into high-energy optical phonons, which are strongly coupled to the electronic system, but rather weakly coupled to lower-energy acoustic phonons (see Fig. 6.6). From this, Nicholson *et al.* predict a highly nonthermal distribution of these phonons, decaying on a few-ps time scale determined by phonon-phonon coupling to lower-lying modes. In this regard, the observation of coherent optical shear and rotation phonons in ULEED confirms this hypothesis. Furthermore, the corresponding lifetimes τ_{shear} and τ_{rot} extracted from the Fourier-filtered contributions to the switching efficiency suggest that the energy stored in shear and rotation motion is transferred to the underlying lattice within $\sim$ 6 ps, where trRHEED finds the maximum lattice temperature[10]

[10] Frigge *et al.* [10, 56] determine the maximum lattice temperature from delay-dependent Debye-

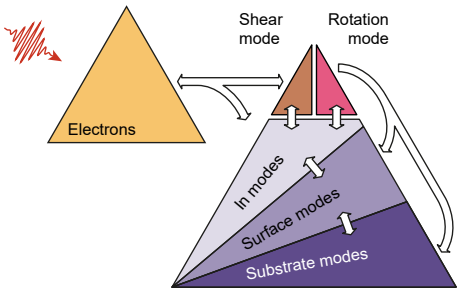

Figure 6.6: Couplings and energy flow between the electronic system and different types of lattice modes in the (8×2) state. Based on trAPRES [57, 153] and ULEED [53] results, it seems likely that the electronic system predominantly couples to shear and rotation modes. These in turn couple only weakly to other lattice modes, resulting in a phonon bottleneck.

[10, 56].

In summary, the above double-pulse ULEED experiments demonstrate coherent control over the efficiency of the metal-insulator structural phase transition in atomic indium wires at the Si(111) surface. In this, the existence of long-lived vibrational coherence in shear and rotational phonon modes of the (8×2) structure is crucial. Furthermore, the distinct initial phases and the delay-dependent softening or hardening of the frequency-specific contributions to the switching efficiency suggest different roles of shear and rotation motion in the transition. In a certain sense, our results also form the link between electronic excitation and band structure dynamics measured by trARPES [11, 12, 57] and the structural response observed in trRHEED [56], providing insights into energy relaxation in a strongly-coupled, quasi-one-dimensional system. At the same time, a number of important questions remains unanswered, including those about the underlying control mechanisms, the shape of the PES, and the precise origin of the shear feature. This motivates the ultrafast optical pump-probe measurements discussed below. Moreover, future double-pulse ULEED experiments with significantly shorter pump-pulse durations could reveal possible signatures of higher-frequency structural modes involved the phase transition, e.g. normal displacement modes around 1.5 THz (50 cm^{-1}) [240, 256].

Waller-type spot suppressions in trRHEED. While optical phonons have an effect on the DWF, Nicholson *et al.* argue that their contribution is rather small compared that of acoustic modes, mainly because of a smaller vibrational amplitude [57].

6.3 Optical pump-probe measurements

As reported in Sec. 6.1, the combination of ULEED with double-pulse optical excitation schemes enables us to study specific coherent surface phonons by monitoring their impact on the transition efficiency. Optical pump-probe spectroscopy (OPP), on the other hand, allows for direct detection of coherent phonons by means of their impact on reflectivity, absorption and transmission (see also Sec. 2.3.4). Whereas OPP typically lacks surface sensitivity due to the large penetration depth of the IR pulses used for probing, particularly strong changes in the optical properties of the surface layer may still be observable, provided a sufficiently high signal to noise ratio and a negligible contribution of the bulk substrate. Motivated by the signatures or shear and rotation modes in ULEED and the in-depth characterisation of the Si(111)(4×1)-In and Si(111)(8×2)-In surfaces with respect to vibrational Raman modes [240], we study the ultrafast (8×2) → (4×1) transition in OPP experiments (for details of the setup, see Sec. 3.2). Specifically, we record the pump-induced changes to the sample reflectivity as a function of the pump-probe delay $\Delta t_{\text{p-pr}}$ for different excitation densities.

The results are summarised in Figure 6.7: A fast initial decrease in reflectivity is observed within ∼ 500 fs after optical excitation (maximum relative change $\Delta R/R = -2.3 \cdot 10^{-3}$ for highest fluence value) followed by a slower recovery of the signal to a persisting level over ∼ 3 ps (Fig. 6.7a). These two features are mainly attributed to electronic excitation and the subsequent transfer of energy to the lattice modes via electron-phonon coupling. Moreover, the long-lasting suppression of the signal at later times likely originates from the distinct optical properties of the metastable (4×1) phase. In this context, Fleischer *et al.* [269] find a lower total reflectivity of the (4×1) surface compared with the (8×2) surface and speculate that this change in R may be caused by an increased density of states close to E_{F} in the symmetry-broken state. On this basis, we interpret the reduction of R observed for $\Delta t_{\text{p-pr}} > 5$ ps by OPP as a signature of the metastable state or the structural transition, respectively. Tracking this feature as a function of laser fluence reveals a gradual threshold (orange line and dots in Fig. 6.7c), in line with pump-probe ULEED results (Fig.5.2b).

Importantly, the delay-dependent reflectivity $\Delta R/R(\Delta t_{\text{p-pr}})$ is periodically modulated at two frequencies $f_1 \approx 0.65$ THz and $f_2 \approx 0.84$ THz, again pointing to shear and rotation modes of the (8×2) structure (Fig. 6.7b). However, while the rotation

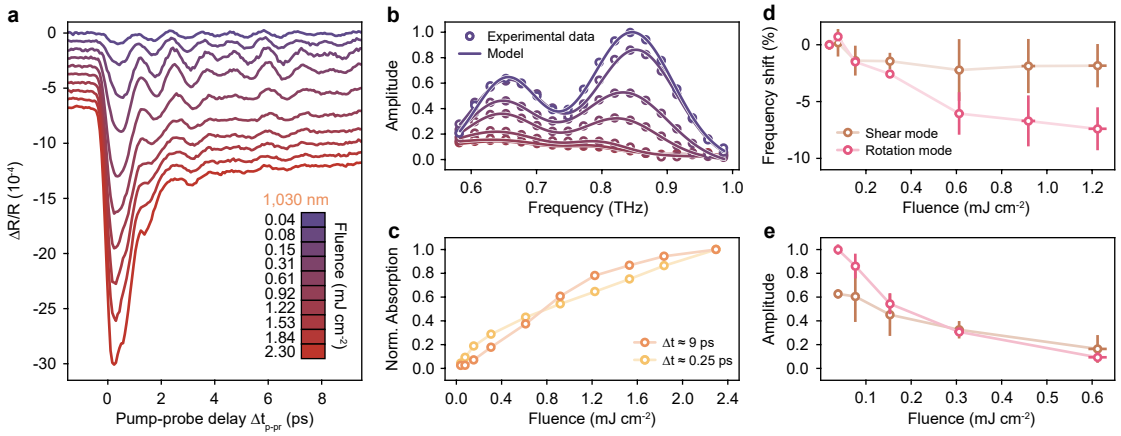

Figure 6.7: Ultrafast reflectivity measurements. **a**, Reflectivity change $\Delta R/R$ of the In-/Si(111) surface as a function of the time-delay $\Delta t_{\text{p-pr}}$ between pump (1,030 nm) and probe pulses (800 nm; $F_{800} = 0.14\,\text{mJ}\,\text{cm}^{-2}$). Offsets are added to the datasets for clarity. **b**, Fourier spectra of $\Delta R/R(t_{\text{p-pr}})$ for $F = 0.04 - 1.22\,\text{mJ}\,\text{cm}^{-2}$, revealing two main coherent contributions ($f_1 = 0.65\,\text{THz}$, $f_2 = 0.84\,\text{THz}$ for $F = 0.04\,\text{mJ}\,\text{cm}^{-2}$) to the signals in **a**. **c**, Transient ($\Delta t_{\text{p-pr}} \approx 0.25$ ps) and long-lived ($\Delta t_{\text{p-pr}} \approx 9$ ps) contributions to $\Delta R/R$ as a function of pump fluence. The data are normalized to $\Delta R/R(\Delta t_{\text{p-pr}})$ and the respective values for $F = 2.30\,\text{mJ}\,\text{cm}^{-2}$. **d**, Fluence-dependent frequency shifts of the two modes. The rotation mode softens significantly for higher fluences (error bars, 95% CI of the fit). **e**, Fourier amplitudes of shear and rotation modes normalised to the Fourier component at $f = 0$ as a function of fluence. Taken from Ref. [53].

mode frequencies in ULEED and OPP are almost identical, the shear mode frequencies differ significantly in both types of experiments[11]. Judging from OPP alone, the shear feature modulating the reflectivity seems to be associated with the higher-frequency symmetric shear mode (for a detailed discussion of this discrepancy between OPP and ULEED, see Sec. 6.4). To extract the fluence-dependent frequencies and amplitudes of shear and rotation contributions to the transient reflectivity data in Fig. 5.2a, two Gaussian model functions are fitted to the corresponding Fourier spectra, assuming a linear background (see coloured lines in Fig. 5.2b). Interestingly – and in contrast to the shear feature – the rotation mode softens considerably with increasing fluence ($\sim 10\,\%$ for $F = 1.22\,\text{mJ}\,\text{cm}^{-2}$ in Fig. 6.7d), which is expected for an amplitude mode connected to a Peierls transition [70]. A similarly strong softening of the this mode was observed in Raman measurements just below T_c [237] (see Fig. 4.13). Furthermore, the amplitudes of shear and rotation oscillations are sup-

[11] $f_{\text{shear}}^{\text{ULEED}} \approx 0.55$ THz, $f_{\text{shear}}^{\text{OPP}} \approx 0.64$ THz; $f_{\text{rot}}^{\text{ULEED}} \approx 0.82$ THz, $f_{\text{rot}}^{\text{OPP}} \approx 0.83$ THz.

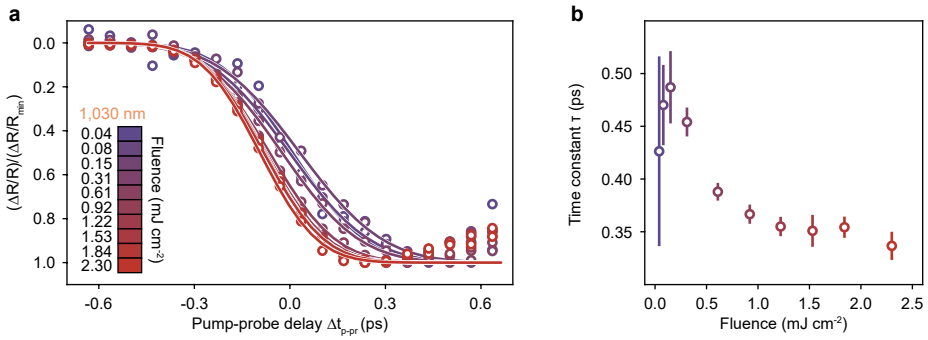

Figure 6.8: Initial dynamics after optical excitation studied by OPP. **a**, Fluence-dependent reflectivity traces $\Delta R/R(\Delta t_{\text{p-pr}})$ normalised to the minimum value $\Delta R/R_{\text{min}}$ reached after $250 - 300$ fs (points). Coloured lines, error function models fitted to the data. **b**, Time constant τ (FWHM) of the initial reflectivity change from the fits in **a** as a function of excitation fluence F. Note that due to the finite resolution of the experiment, given values represent an upper limit for τ. Error bars, 95% CI of the fit.

pressed at higher excitation densities (Fig. 6.7e), suggesting that the corresponding modes are related to the (8×2) structure.

In addition, the high temporal resolution of OPP allows to investigate the initial dynamics of the phase transition. To this end, the prominent drop in reflectivity around $\Delta t_{\text{p-pr}} = 0$ is analysed in more detail (Fig. 6.8). Specifically, an error function model is fitted to the normalised reflectivity in order to determine the time constant τ of the initial change in $\Delta R/R$ as a function of fluence (Fig. 6.8a). At low fluence values ($F < 0.31\,\text{mJ}\,\text{cm}^{-2}$), $\Delta R/R$ decreases within $\tau \sim 450$ fs (FWHM). However, a significantly smaller time constant is observed at higher fluences ($\tau = (336 \pm 16)$ fs at $F = 2.30\,\text{mJ}\,\text{cm}^{-2}$). In this context, Frigge *et al.* [10, 116] reported an acceleration of the structural transition above $F = 0.9\,\text{mJ}\,\text{cm}^{-2}$ in trRHEED to a limit value of $\tau = (350 \pm 10)$ fs. Although the transient reflectivity data certainly show a similar trend, caution should be exercised when comparing the results. In particular, in the case of the OPP, it is unclear whether the initial dip in reflectivity originates from electronic excitation, Raman scattering or a combination of both effects. In the first case, the OPP data should rather be compared with trARPES measurements, which suggest a fluence-dependent time constant for electronic dynamics at the zone boundary ($\overline{\text{X}}_{(8\times2)}$) [66]. In the second case, our results would support the interpretation of Frigge *et al.* in terms of accelerated, ballistic motion of the indium atoms, and it would be interesting to analyse the initial frequencies and phases of

shear and rotation contributions. However, it seems likely that $\Delta R/R$ is influenced by both electronic excitation and Raman scattering from very early on. In any case, it is reasonable to assume that stronger electronic excitation further enhances the charge density variations within the unit cell. The resulting higher net forces on the nuclei accelerate their motion towards the high-symmetry configuration and thus reduce the time constant for the transition. In this respect, future OPP experiments with improved temporal resolution or different pump wavelengths could help to separate electronic and lattice contributions to the transient reflectivity and further improve our understanding of the interplay between electrons and phonons in the transition. While OPP has been as a supplementary technique in this work, these first results stimulate further experiments in this direction, including wavelength-dependent measurements or all-optical multipulse experiments in analogy to two-dimensional infrared spectroscopy (2D-IR).

6.4 Control mechanisms and PES model of the transition

Both ULEED and OPP prove the existence of long-lived vibrational coherence after optical excitation of the (8×2) surface. At this point, the question arises as to how this coherent atomic motion enables control over the (8×2) → (4×1) transition efficiency in double-pulse experiments (see Sec.6.1). Accordingly, the following section will introduce two control mechanisms linked to generation and utilisation of coherent phonons. Based on the experimental results obtained in ULEED and OPP both mechanisms will be discussed with regard to their possible impact on the phase transition. Irrespective of the specific mechanism, the different characteristics of shear and rotation modes observed in ULEED call for an extended model of the PES of the system. A possible approach to this is presented below.

The optical excitation of structural phase transitions generally involves the conversion of light energy into kinetic energy stored in the motion of lattice atoms. For example, in the (8×2) → (4×1) transition, by absorbing photons of the pump pulse, electrons are promoted to unoccupied states above E_F in the band structure via interband transitions. Following the subsequent thermalisation, the electrons transfer their energy to shear and rotation modes transforming the broken-symmetry into the high-symmetry structure (see also Fig. 2.13 in Sec. 2.2.2).

Absorption control

In a first step, we will discuss how coherent phonons can control the structural transition by modulating the absorption of light, i.e. the initial energy flow into the system ("absorption control", see Fig. 6.9a). As discussed in Sec. 2.3.4, distortions of the crystal lattice affect the optical properties of a solid, i.e. its complex dielectric function $\epsilon(\omega, \boldsymbol{k})$ and related quantities. In particular, coherent Raman-active phonons were found to modulate the optical absorption A of a surface [42, 50] on picosecond time scales, enabling ultrafast vibrational spectroscopy of solids via pump-probe experiments. In double-pulse experiments, however, the same mechanism can be harnessed to control the transition efficiency. Specifically, after the first pump pulse, coherent Raman-active modes of the indium monolayer periodically change the optical constants (reflectivity R, absorption A and transmission T) of the surface. Consequently, A becomes a function of the vibrational phase of the system at the arrival of the second pump pulse. At the same time, the absorption of photons or energy, respectively, directly impacts the level of electronic excitation, which in turn determines the final-state PES of the system.

As an example, we consider DECP of a single Raman-active phonon by the first pump pulse and assume that displacements $\delta\boldsymbol{q}$ of this particular mode reduce the absorption of the surface. For a second pump pulse arriving at ($\Delta t_{\text{p-p}} = (n + 1/2) \cdot T_{\text{phon}}$), that is, at the point of maximum displacement, the absorption of the surface is minimal. Accordingly, the level of electronic excitation is reduced to a minimum and the final PES resembles the ground state PES (violet surface in Fig. 6.9a). This way, the order parameter is trapped in the symmetry-broken phase and the overall transition efficiency is reduced[12]. In contrast, for $\Delta t_{\text{p-p}} = n \cdot T_{\text{phon}}$, $\delta\boldsymbol{q} = 0$ and the absorption of the surface is maximal, leading to a higher level of electronic excitation and – depending on the barrier height after the first pump pulse – a final state PES that facilitates the transition into the high-symmetry state (red surface).

This absorption control scheme applies to all Raman-active modes $\boldsymbol{q}$, and might be used in a variety of phase-change materials. However, amplitude modes of symmetry-broken states are expected to play a major role in this mechanism, given their direct link to structural transformations and their susceptibility to strong displacive excitation. Moreover, it is important to note that $\Delta t_{\text{p-p}}$ not only affects the

[12] Recall the distribution of barrier heights, which further complicates the picture.

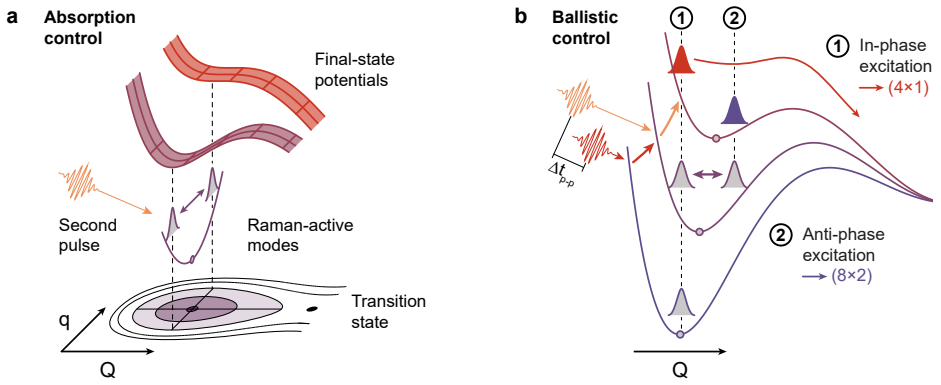

Figure 6.9: Coherent control mechanisms. **a**, Absorption control scheme: Raman-active modes of the (8×2) structure excited by a first optical excitation periodically modulate the (energy) absorption of the indium monolayer and thus control the final state PES. This mechanism is active both along q and Q. **b**, Ballistic control scheme: A first optical excitation induces coherent vibrational motion in the excited (8×2) potential via DECP (middle). A second optical excitation delayed by $\Delta t_{\text{p-p}}$ either increases or decreases the vibrational amplitude, depending on the momentary vibrational phase. For a non-vanishing barrier after the second excitation, kinetic energy contributes to overcoming the barrier into the (4×1) state (top). This mechanism is feasible for modes along the reaction coordinate Q. Taken from Ref. [53].

absorption of the second pump pulse, but also controls the vibrational amplitude. In multi-pulse experiments, this might be used to selectively (de-)excite specific phonons and increase the leverage of absorption control.

Ballistic control

The second control mechanism harnesses the energy stored in the coherent motion of lattice atoms: The ballistic nature of the (8×2) → (4×1) transition [10] and the influence of DECP suggest that kinetic energy contributes to overcoming a sufficiently lowered but not completely vanishing barrier ("ballistic control", see Fig. 6.9b). For the vibrational motion along a reaction coordinate $\boldsymbol{Q}$, in-phase excitation with a second pulse maximizes the effect of DECP, increases the vibrational amplitude and allows barrier-crossing to the (4×1) state (1). Anti-phase excitation, on the other hand, vibrationally de-excites the system, which then has insufficient kinetic energy and remains in the (8×2) state (2). In a corresponding real-space picture, by weakening or strengthening different indium-indium bonds [11] and thus shifting the equilibrium atomic positions, the second pulse either adds further mechanical stress

to the system (1) or removes it (2) (see also Fig. 2.13b,e). Whereas the absorption modulation described above may apply to all Raman-active modes $\boldsymbol{q}$, this ballistic contribution is only feasible for modes along the reaction coordinate $\boldsymbol{Q}$.

Comparison of ULEED and OPP results

In order to identify the possible contributions of absorption and ballistic control mechanisms to the modulations of the transition efficiency, we compare double-pulse ULEED and OPP traces recorded at identical pump fluence $F = 0.15\,\mathrm{mJ\,cm^{-2}}$ (Fig. 6.10). Beforehand, we note that OPP probes changes in optical reflectivity, which are proportional to absorption changes for a monolayer on a substrate with real refractive index (see Sec. 2.3.4 and Ref. [207]). Therefore, OPP directly measures the contribution of absorption modulation. In contrast, ULEED is sensitive to the relative transition efficiency and should thus be able to observe potential signatures of the ballistic mechanism as well. While both ULEED and OPP signals are clearly modulated by shear and rotational phonons, there certainly is no one-to-one correspondence between the two data sets. Therefore, a trivial connection between energy absorption and transition efficiency seems rather unlikely at this point. A more detailed comparison of shear and rotation contributions yields further insights in this regard.

Rotation contribution Concerning the rotation feature, ULEED and OPP measure very similar frequencies (ULEED: $f_{\mathrm{rot}}^{\mathrm{ULEED}} = 0.83$ THz; OPP: $f_{\mathrm{rot}}^{\mathrm{OPP}} = 0.82\,\mathrm{THz}$). Furthermore, recalling the connection between monolayer reflectivity and absorption (see Eqs. 2.66, 2.68 and 6.5), the OPP data indicates that the absorption of the surface layer is increased if the indium atoms are displaced according to the rotation mode eigenvectors. This is consistent with the reduced switching efficiency at $\Delta t_{\mathrm{p\text{-}p}} = 0$ found in ULEED (see Fig. 6.4a) and the maximum rotation mode contribution at $\Delta t_{\mathrm{p\text{-}p}} \approx T_{\mathrm{rot}}/4 = 300$ fs. However, these observations are incompatible with a significant contribution of the ballistic mechanism for this mode, since in this case, in-phase excitation is expected to increase the vibrational amplitude and enhance the switching efficiency for $\Delta t_{\mathrm{p\text{-}p}} = 0$ (see Fig. 6.9b). Taken together, these points rule out the ballistic mechanism for the rotation mode. We therefore attribute its signature in the ULEED signal to absorption modulation. This assignment is further corroborated by the rotation-induced modulation am-

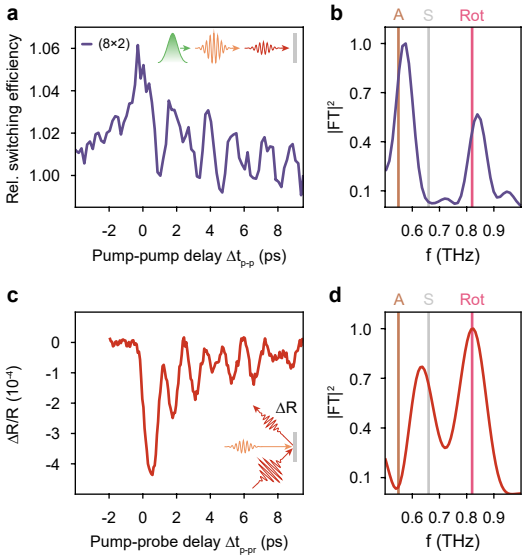

Figure 6.10: Comparison between ULEED and OPP. **a**, Relative switching efficiency recorded for unequal pump pulses in ULEED ($F_{1,030} = 0.48\,\mathrm{mJ\,cm^{-2}}$, $F_{800} = 0.15\,\mathrm{mJ\,cm^{-2}}$). **b**, Corresponding spectral density with reference frequencies (see also Fig. 6.4). A, S and Rot indicate the frequencies of antisymmetric, symmetric and rotation modes, respectively. **c**, Delay-dependent reflectivity changes $\Delta R/R$ of the surface measured in optical pump-probe experiments ($F_{\mathrm{pump}} = 0.15\,\mathrm{mJ\,cm^{-2}}$). **d**, Corresponding spectral density. $\Delta t_{\mathrm{p\text{-}pr}}$, delay between optical pump and optical probe pulses. Taken from Ref. [53].

plitudes in ULEED and OPP, which are linked through the total absorption A of the monolayer. Based on the optical properties of an ultrathin layer on top of a dielectric substrate derived in Sec. 2.3.4, A can be estimated in the following way: First, we notice that the presence of the monolayer results in a ratio of reflectance change ΔR to layer absorption A given by

$$\frac{\Delta R}{A} = -\frac{(1-n_{\mathrm{s}})}{(1+n_{\mathrm{s}})} = -0.57. \tag{6.5}$$

Here, ΔR and A refer to Eqs. 2.66 and 2.68, and $n_{\mathrm{s}} = 3.67 + 0.005\mathrm{i}$ is the refractive index of the silicon substrate at a pump wavelength of $\lambda = 800$ nm. To calculate the absorption A of the indium monolayer, we harness that pump-induced variations of the sheet conductivity σ^{s} due to coherent oscillations of the rotation mode will induce variations in reflectance (δR) and absorption (δA) following the same ratio $\delta R/\delta A = \Delta R/A$. This relation, however, can be expressed in terms of experimen-

tally accessible quantities:

$$\begin{aligned} \delta A = \delta R \cdot \left(\frac{\Delta R}{A}\right)^{-1}; \\ \iff A \cdot \left(\frac{\delta A}{A}\right) = R \cdot \left(\frac{\delta R}{R}\right) \cdot \left(\frac{\Delta R}{A}\right)^{-1}; \\ \iff A = R \cdot \left(\frac{\delta R}{R}\right) \cdot \left(\frac{\delta A}{A}\right)^{-1} \cdot \left(\frac{\Delta R}{A}\right)^{-1}. \end{aligned} \tag{6.6}$$

Specifically, the relative changes in absorption $(\delta A/A)_{\mathrm{rot}}$ (OPP) and diffraction signal $(\delta I/I)_{\mathrm{rot}}$ (ULEED) due to the rotation mode are related by the steepness of the fluence-dependent diffraction spot intensity at the threshold fluence F_{th} via

$$\left(\frac{\delta A}{A}\right)_{\mathrm{rot}} = \left(F_{\mathrm{th}} \cdot \left(\frac{\mathrm{d}I}{\mathrm{d}F}\right)\Big|_{F_{\mathrm{th}}}\right)^{-1} \cdot \left(\frac{\delta I}{I}\right)_{\mathrm{rot}}. \tag{6.7}$$

In other words, modulations of the monolayer absorption also modulate the transition efficiency by controlling the energy received by the surface (per unit area), i.e. the absorbed fluence. In this context, the parameter $F_{\mathrm{th}} \cdot (\mathrm{d}I/\mathrm{d}F)|_{F,\mathrm{th}}$ measures how the diffraction signal – and consequently E_{s} – reacts to changes in the absorbed energy. With a value of $F_{\mathrm{th}} \cdot (\mathrm{d}I/\mathrm{d}F)|_{F,\mathrm{th}} \approx 1.7$ as determined in Sec. 5.2 and a relative modulation amplitude of $(\delta I/I)_{\mathrm{rot}} = 0.8\,\%$ in ULEED[13], we have $(\delta A/A)_{\mathrm{rot}} = 0.47\,\%$. Finally, for a relative modulation amplitude in OPP ($(\delta R/R)_{\mathrm{rot}} = -8 \cdot 10^{-5}$) and a measured total reflectivity of $R = 33\,\%$, we obtain

$$A \approx R \cdot \left(\frac{\delta R}{R}\right)_{\mathrm{rot}} \cdot \left(\frac{\delta A}{A}\right)^{-1}_{\mathrm{rot}} \cdot \left(\frac{\Delta R}{A}\right)^{-1} \approx 1\,\%. \tag{6.8}$$

This value for the total absorption of the monolayer is in good agreement with a recent estimate of Frigge *et al.* ($A = (1-R)\alpha_{\mathrm{abs}} = 0.5\,\%$) [10, 116] based on measurements of the surface Debye temperature and the corresponding specific heat c_{v} of the indium wires.

Shear contribution As for the lower-frequency shear component, the picture is

[13] All parameters have been extracted from the two data sets shown in Fig. 6.10. To determine the relative modulation ampiltudes in both types of experiments, the rotation mode contribution was isolated via Fourier filtering and its amplitude normalised to the total signal level (before time-zero).

apparently more complex. Specifically, distinct frequencies are found for this feature in ULEED ($f_{\mathrm{shear}}^{\mathrm{ULEED}} = 0.57$ THz) and OPP ($f_{\mathrm{shear}}^{\mathrm{OPP}} = 0.64$ THz). In addition, comparing the shear amplitudes in both types of experiments[14], we find that this dominant feature in ULEED modulates the switching efficiency to a disproportionately higher degree than expected from the overall transient reflectivity ($A_{\mathrm{shear}}^{\mathrm{ULEED}}/A_{\mathrm{rot}}^{\mathrm{ULEED}} \approx 1.6$, $A_{\mathrm{shear}}^{\mathrm{OPP}}/A_{\mathrm{rot}}^{\mathrm{OPP}} \approx 0.75$; see Fig. 6.10b,d). In the following, we discuss two possible explanations for these observations.

In a first scenario, the differences in frequency and amplitude could result from OPP and ULEED probing the same mode in different areas of the surface. This argument is based on the assumption of a heterogeneous surface and a spatial distribution of barrier heights for the transition after the first excitation (see Sec. 5.4). From the general properties of potential energy surfaces discussed in Sec. 2.2.1, it follows that variations in the local barrier height also affect the frequencies of vibrational modes. Specifically, for regions with a strongly reduced barrier, we expect mode softening, i.e. a shift to lower phonon frequencies. As discussed above, OPP is sensitive to changes in the sample reflectivity caused by Raman-active modes and thus measures the coherent vibrational response of all (8×2) (and possibly (4 × 1)) domains. Therefore, the frequencies observed in OPP represent an average over the entire barrier height (frequency) distribution. ULEED, on the other hand, measures the transition efficiency, and is therefore only sensitive to surface regions close to the threshold. This subset of surface domains, however, likely exhibits shallower potential landscapes, larger vibrational amplitudes, as well as lower barriers and phonon frequencies on average.

In a second scenario, the different shear frequencies and amplitudes in ULEED and OPP can be interpreted as signatures of two distinct modes. In fact, DFT [107, 256] and Raman spectroscopy [237, 240] predict two separate shear phonons in the relevant frequency range, i.e. the symmetric and the antisymmetric shear mode, which have already been referenced above (see Fig. 6.4b and Fig. 6.11 for further details). Both are $\overline{\Gamma}$ point modes of the (8×2) structure and considered Raman-active. The symmetric shear mode ($f_{\mathrm{S}} = 0.66$ THz as predicted by DFT [240, 256], Fig. 6.11b) is closely related to a $\overline{\Gamma}$ point shear mode of the (4×1) structure, but is red-shifted in the (8×2) phase because of the weaker indium-indium bonds between

[14] Relative to the rotation amplitude, which was associated with absorption modulation in both ULEED and OPP.

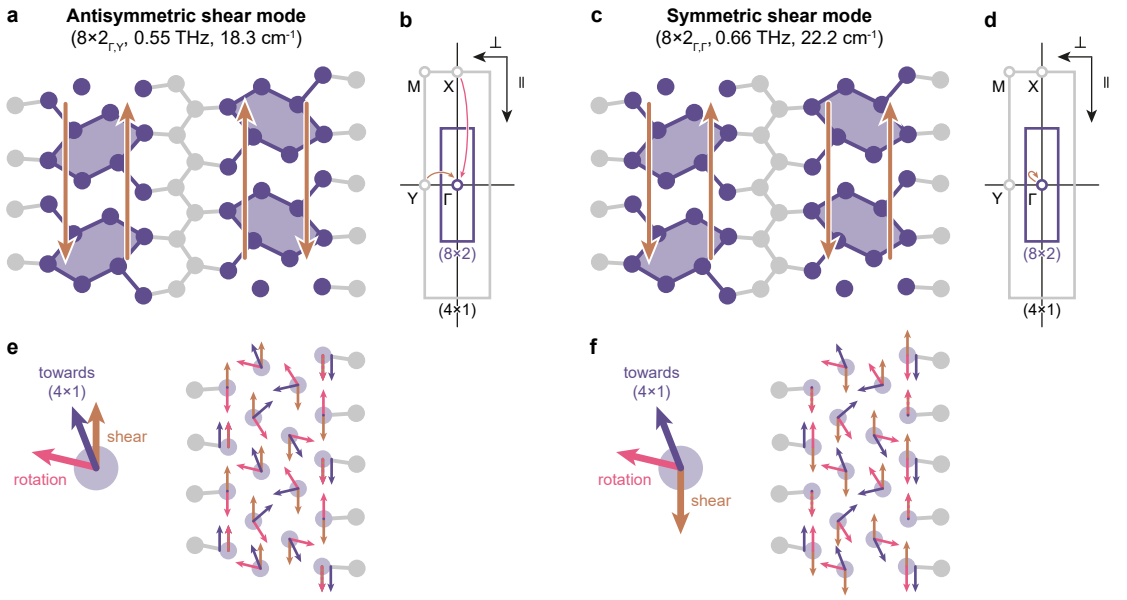

Figure 6.11: Antisymmetric and symmetric shear modes of the (8×2) structure. **a**, Simplified atomic displacement pattern of the antisymmetric shear mode (golden arrows). Grey, silicon atoms; violet, indium atoms. **b**, SBZs of the (4×1) (grey) and (8×2) (violet). The antisymmetric shear (hexagon rotation) mode originates from the backfolding of a $\overline{\mathrm{Y}}_{(4\times1)}$ ($\overline{\mathrm{X}}_{(4\times1)}$) point mode, as indicated by the golden (pink) arrow. **c**, Displacement pattern of the symmetric shear mode. Note that for the antisymmetric (symmetric) mode, atoms of neighboring (4×) chains oscillate out of phase (in phase). **d**, Location of the symmetric shear mode in the SBZ (golden dot). Note that this mode is the counterpart of a $\overline{\Gamma}$ point mode of the (4×1) structure. **e**,**f**, Atomic displacements in the right 4× chain due to antisymmetric (**e**) and symmetric (**f**) shear modes and the rotation mode compared to the normalized displacement vectors pointing towards the ideal (4×1) structure.

adjacent zigzag chains [240]. This mode strongly contributes to Raman spectra recorded by Speiser *et al.* [240] below T_c. On the other hand, the antisymmetric shear mode (DFT: $f_{AS} = 0.55$ THz [240, 256], Fig. 6.11a) originates from the backfolding of a $\overline{\mathrm{Y}}$ point shear mode of the (4×1) phase, caused by the unit cell doubling perpendicular to the atomic chain direction. Signatures of this mode in Raman spectroscopy seem to be significantly weaker than for its symmetric counterpart and have been reported only once so far [237]. Moreover, it is worth noting that the antisymmetric shear mode is not identified by Speiser *et al.* [240].

Importantly, whereas the antisymmetric shear mode plays a key role in transforming the (8×2) into the (4×1) structure, the symmetric shear mode has no relevance

for the transition at all. This can be understood by considering the anti-phase arrangement between hexagons of neighboring (4×) chains in the true (8×2) ground state (see hexagon orientation in Fig. 6.11 and displacement patterns in Fig. 6.11e and f). Taking into account the distinct roles of the two modes in the transition as well as the different relative amplitudes and frequencies of shear and rotation contributions in both types of experiments, it is reasonable to assume that each of OPP and ULEED mainly probes a different one of these modes, namely the higher-frequency symmetric and the lower-frequency antisymmetric shear oscillation, respectively.

To summarise, based on these considerations and the control mechanisms discussed above, two potential roles of shear motion can be identified. First, if the transition is indeed driven by a shear mode separate from that seen in OPP, we must invoke the ballistic mechanism (Fig. 6.9b) to explain the ULEED data, directly linking this mode to the reaction coordinate. Alternatively, to identify the shear contributions in ULEED and OPP with the same mode and absorption modulation (Fig. 6.9a), the observed frequency difference requires further explanation. In particular, this would necessitate a greatly softened and larger-amplitude shear mode oscillation only in surface regions that can be switched by the second pulse, with an unaltered rotation frequency. Based on the experimental observations presented so far, there is no unambiguous evidence for either of the two scenarios. An analysis of the Raman tensor with regard to the possibly different contributions of symmetric and antisymmetric shear modes to the transient absorption of the monolayer could provide clarity.

The above results raise a number of interesting questions that may be tackled in future experiments. Concerning the potential signature of the symmetric shear mode, it remains an open question as to how this mode would be excited in ULEED and OPP experiments. Specifically, it is not clear how symmetric shear motion in two coupled (4×2) chains can be driven by means of displacive excitation, as DECP typically forces the structure towards the high-symmetry state. For the symmetric mode, however, atoms in one of the (4×2) chains would have to move in the exact opposite direction. In this regard, ULEED experiments with sub-bandgap excitation ($\hbar\omega < \Delta E_g$) [58] could investigate the potential role of ISRS for the excitation the symmetric shear mode. While these and other key questions remain unanswered, the combination of ULEED and OPP has contributed to a better understanding of the material system, especially with regard to vibrational coherence.

Two-dimensional PES model of the transition

The comparison of ULEED and OPP traces provide further experimental evidence for the decisive role of shear and rotation phonon modes for the transition, predicted by DFT or frozen phonon calculations, respectively [107, 239, 256, 296]. In addition, DFT can be used to model the evolution of the order parameter in the nonequilibrium (8×2) → (4×1) transition after ultrafast optical excitation. To this end, the excited state PES is calculated by manually placing electrons (holes) in conduction (valence) band (valence band) states associated with shear and rotation modes or the weakening and strengthening of specific indium-indium bonds [10, 11, 241]. Recently, combined trARPES/DFT studies of the (8×2) → (4×1) transition showcased how experimental input can advance such model calculations, highlighting the roles of localised photoholes and a broad momentum distribution of excited electrons [11, 57]. This raises the question of what information about the PES and possible transition pathways can be inferred from ULEED.

Perhaps most importantly, our results shed new light on the dimensionality of the PES and the minimum-energy pathway for the phase transition. Previous studies on the ultrafast (8×2) → (4×1) transition reasoned their findings on the basis of a one-dimensional, i.e. straight pathway of the order parameter between (8×2) and (4×1) states on the PES [10, 11, 241]. This implies that the transition state T^* lies on a direct line between initial and final state, and is therefore reached by means of a simultaneous and equally strong excitation of shear and rotation modes. However, whereas both of these modes indeed leave their signature in the switching efficiency measured by ULEED, the pronounced softening (hardening) of the shear (rotation) feature around $\Delta t_{\text{p-p}} = 0$, as well as the considerably larger shear amplitude in ULEED compared with OPP are difficult to reconcile with this one-dimensional model. Instead, we propose a description of the transition in terms of a two-dimensional PES spanned by the rotation and shear deformations of the (4×1) structure (Fig. 6.12a). In this scenario, the system initially resides in the (8×2) minimum (top left) which is separated from the (4×1) state by a finite energy barrier[15]. To understand the generation and the role of coherent atomic motion along shear and rotation coordinates, we consider the effect of ultrafast electronic

[15]Note that the model presented in Fig. 6.12 takes into account only one of four energetically degenerate (8×2) ground states.

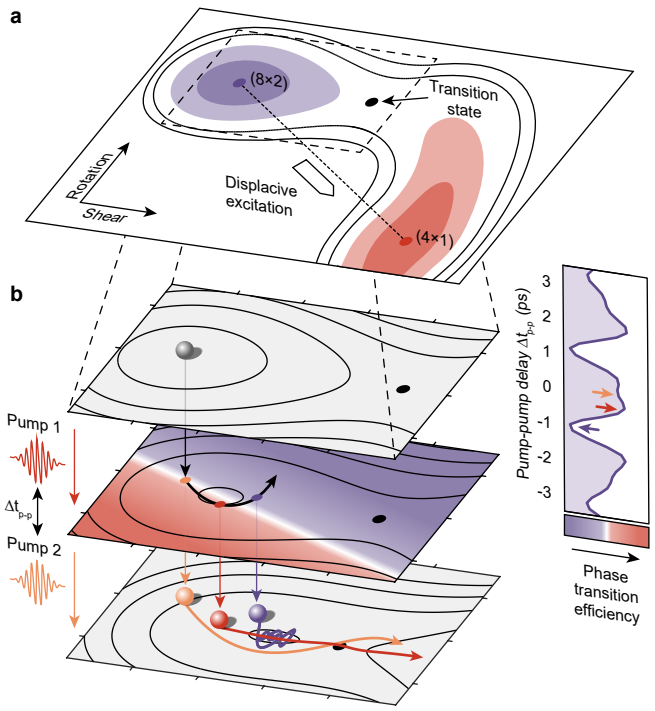

Figure 6.12: Two-dimensional picture of the phase transition dynamics. **a**, Proposed two-dimensional model of the potential energy surface for the (8×2) → (4×1) transition in shear/rotation configuration space, exhibiting a transition state along the shear axis from the (8×2) state. **b**, Sketch of exemplary system trajectories close to the (8×2) state before (top), in between (middle) and after (bottom) two subsequent displacive excitations (yellow, $\Delta t_{\text{p-p}} = 0$; red, $\Delta t_{\text{p-p}} \approx T_{\text{rot}}/2$; violet, $\Delta t_{\text{p-p}} \approx T_{\text{shear}}/2$). T_{shear} and T_{rot}, oscillation period of the shear and rotation mode, respectively. The phase transition efficiency (colour-coded) is a strong function of the vibrational coordinates at the time of the second pulse (middle and right panel). Highest efficiency is achieved for a maximum sheared/minimum rotated structure (see middle panel). Taken from ref. [53].

excitation on the PES. DFT calculations [10, 241] suggest that the (8×2) minimum of the excited PES is shifted quasi-instantaneously towards the high-symmetry state following optical excitation by the first pump pulse (see black line in Fig. 6.12a). This in turn leads to a displacive excitation of coherent shear and rotation phonons inside the local (8×2) potential (Fig 6.12b)[16]. In this respect, the ULEED measurements

[16]To illustrate the evolution of the order parameter in double-pulse ULEED experiments (Fig. 6.12), we neglect a possible coupling between shear and rotation modes and numerically solve the equations of shear and rotation motion inside the separable, model potential $F(x_{\text{s}}, x_{\text{r}}) = \frac{1}{2}(\omega_{\text{s}}^2 x_{\text{s}}^2 + \omega_{\text{r}}^2 x_{\text{r}}^2) - a x_{\text{s}}^3 + \frac{1}{2} b(\Delta t_{\text{p-p}}) \omega_{(4\times1)}^2 [(x_{\text{s}} - x_{\text{s},0})^2 + (x_{\text{r}} - x_{\text{r},0})^2]$. In this, the first term defines the local (8×2) potential, whereas the second term creates a transition state T^* along the shear axis. The last term models the electronic excitation towards the (4×1) state. Note that the ultrashort

evidence that the switching efficiency for the second pulse becomes a strong function of the momentary vibrational state in this intermediate potential (see Fig 6.12b, middle and right panel).

The combined observations – that is, the differences in frequency and relative amplitudes between ULEED and OPP, as well as the phases of both modes in the double-pulse traces (Fig. 6.4a, bottom) – now suggest an "off-diagonal" transition state in configuration space with a strongly reduced shear but a largely unaltered rotation (compared with the (8×2) state, see Fig. 6.12a). This interpretation is further supported by the transient softening and hardening of the shear and rotation mode, respectively, near $\Delta t_{\text{p-p}} = 0$ (Fig. 6.5a,b; recall Sec. 2.2.1). In this picture, the "direct" pathway proposed in Refs. [10] and [11] does not represent the lowest energy pathway for the transition, since it crosses the barrier at a distance from the transition state for which the activation energy is minimised. Speculating about potential consequences of an off-diagonal transition state, a series of two or more properly-timed pump pulses could potentially reach transition efficiencies unattainable by a single excitation. Moreover, depending on the actual location of T^* relative to the direct pathway between (8×2) and (4×1) states, the shear displacement may even be referred to as the primary reaction coordinate, whereas the rotation completing the transition is of a secondary nature. In this case, overcoming an "early" barrier [43], the indium chains would be first "un-sheared" and subsequently transformed into the zigzag structure by a rotation.

Recent calculations of the multi-dimensional ground state PES by S. Wippermann indeed show an off-diagonal transition state in the two-dimensional subspace spanned by shear and rotational displacements, strongly supporting our interpretation of ULEED and OPP data. At the same time, the exact location of T^* in these calculations does not support the picture of an early-barrier transition. It is important to note that the same calculations, performed at the DFT-LDA[17] level of theory, show that the trimer model is not a local minimum on the potential energy surface. The optimum transition path does not traverse the trimer structure and is instead avoiding it, thus eliminating the possibility of a stable intermediate configuration between (8×2) and (4×1) structures. Future calculations of the excited-state PES will help to better understand the transient softening and hardening of shear

optical excitation is represented by two delay-dependent step-like increases of $b(\Delta t_{\text{p-p}})$.

[17] LDA, local density approximation.

and rotational modes. In particular, the hardening of the rotation mode close to $\Delta t_{\text{p-p}} = 0$ in ULEED is hard to reconcile with the temperature-dependent softening of the same mode in temperature-dependent Raman studies[18]. This suggests that the ultrafast optical excitation of specific electronic states results in a PES different from the one that is relevant for the temperature-driven transition.

Finally, considering the connection of shear and rotational motion to k-dependent band structure dynamics and the making and breaking of electronic bonds in real space, it would be interesting to further investigate the implications of the off-diagonal transition state on the PES for the microscopic picture and the possible sequential nature of the ultrafast $(8\times2) \rightarrow (4\times1)$ transition.

6.5 Mode-selective excitation and two-dimensional spectroscopy

The combination of ULEED and double-pulse optical excitation allows conclusions to be drawn about particular features of the PES for the $(8\times2) \rightarrow (4\times1)$ transition. At the same time, the question arises whether it is possible to achieve an even higher degree of control over the trajectory of the system as it evolves on the excited PES. Furthermore, more detailed knowledge about shear and rotation modes and their possible mutual coupling is highly desirable. In this context, two-dimensional nuclear magnetic resonance spectroscopy (2D-NMR) [305] and two-dimensional infrared spectroscopy (2D-IR) [306–308] have proven to be excellent tools for the investigation of molecular vibrations. The applicability of these concepts to solids and their surfaces has been demonstrated by combining the high energy-resolution and surface-sensitivity of PEEM with excitation schemes of 2D-IR ("coherent two-dimensional nanoscopy", [211]). Thus, to answer the above questions, the existing ULEED double-pulse excitation scheme has to be further developed in this direction. Accordingly, this section presents the results of recent multi-pulse ULEED measurements carried out by Hannes Böckmann-Clemens building on the experiments described in Sec. 6.1-6.4.

In a first step, we explore the possibility to selectively excite shear and rotation modes by a sequence of three optical pulses (Fig. 6.13a). Specifically, a first, weak

[18] The softening of the shear mode is discussed in Ref. [237]. This mode, however, is believed to be only weakly Raman-active due to its symmetry. A subsequent Raman study was indeed unable to detect it [240] (recall Fig. 4.13 in Sec. 4.3.3).

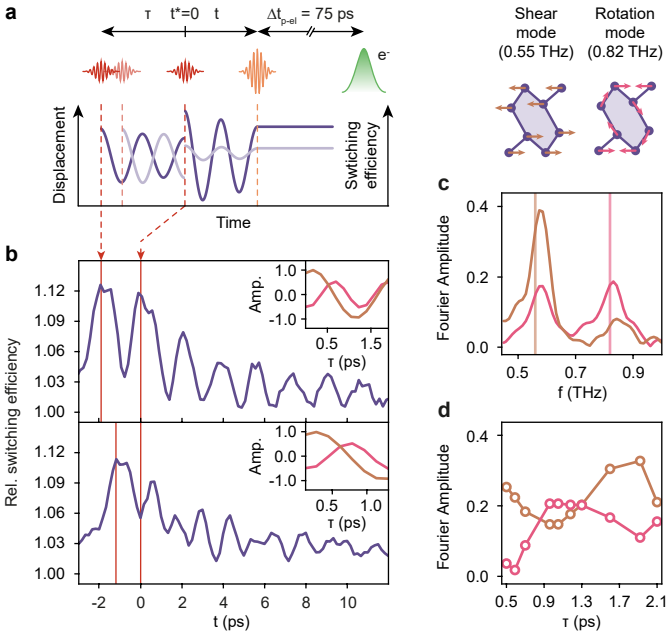

Figure 6.13: Selective excitation of shear and rotation modes. **a**, Pulse sequence in mode-selective ULEED experiments. (Light) red, weak excitation pulses (800 nm); orange, strong "detection" pulse (1030 nm); green, electron pulse. **b**, Relative switching efficiency E_s as a function of the detection time t for τ_{shear} (top) and τ_{rot} (bottom). Inset, Fourier-filtered contributions of shear and rotation modes to E_s as a function of τ. Values on the right edge correspond to the amplitudes at the arrival of the second weak excitation pulse. **c**, Fourier transforms of the traces shown in **b**. Gold (pink), in-phase excitation of the shear (rotation) mode. **d**, Fourier amplitudes of shear (gold) and rotation (pink) contributions as a function of the delay τ between the weak pump pulses.

pump pulse (λ_c = 800 nm) triggers coherent vibrational motion along shear and rotation coordinates. The associated wave packet is allowed to evolve on the PES over a time interval τ (excitation time), until a second weak pump pulse launches another wave packet. The coherent superposition of the two wave packets is then translated into an observable of ULEED by a stronger third pulse (λ_c = 1030 nm) at delay t (detection time), switching the surface depending on the vibrational state of the system (see control mechanisms in Sec. 6.4). This way, the momentary vibrational state at t is – to some extent – encoded in the t-dependent switching efficiency[19]. Recording $E_s(t)$ for different delays between the first two excitations

[19]In principle, this is also the case for double-pulse experiments. In three-pulse experiments, however, the manipulation of the coherent phonon amplitudes can be better separated from the phase transition itself.

allows to detect resonances, i.e. coherent phonons of the surface structure influencing the transition. As far as the (8×2) → (4×1) transition is concerned, the effects of resonant excitation at shear (rotation) mode frequencies on the delay-dependent switching efficiency can be investigated.

Figure 6.13b displays triple-pulse traces $E_s(t)$ recorded for in-phase excitation of shear ($\tau \approx T_{shear} = 1.81$ ps, top) and rotation ($\tau \approx T_{rot} = 1.21$ ps, bottom) motion. The two data sets show striking differences in terms of the oscillatory contribution to the switching efficiency. Comparing the Fourier amplitudes at shear and rotation frequencies in both cases (Fig. 6.13c), we find a ratio of $A_{shear}/A_{rot} \approx 5$ for $\tau \approx T_{shear}$, and $A_{shear}/A_{rot} \approx 1$ for $\tau \approx T_{rot}$. A series of triple-pulse experiments with varying excitation times further reveals that the individual amplitudes are strong functions of τ (Fig. 6.13d). These results evidence all-optical control over the individual amplitudes of shear and rotation phonons and, consequently, coherent control over the transition by actively steering the trajectory of the system on the PES (recall Fig. 6.12b). The selectivity of this sequential excitation scheme is mainly limited by the integer frequency ratio $f_{rot}/f_{shear} = 0.82/0.55 \approx 3/2$ of shear and rotation modes (see, e.g. insets in Fig. 6.13b): since two periods of the shear mode correspond to three periods of the rotational mode, repeated stimulation of the shear mode amplitude also excites the rotation mode. Future experiments could possibly circumvent this complication by tuning the excitation wavelength to the electronic excitations associated with shear and rotation motion.

In principle, such mode-selective approaches could be harnessed to drive transitions "purely vibrationally", i.e. without raising the electronic temperature, given a sufficiently small damping close to the transition state and vibrational coherence in Raman-active key modes outlasting electronic excitation (see Sec. 7.2.1) [158, 165, 304]. With respect to direct resonant excitation of optically-active modes [4, 139, 309, 310], such schemes could provide a complementary path towards the control of phase transitions far from equilibrium.

Next, multi-pulse excitation of the Si(111)(8×2)-In surface can be used to perform ULEED experiments in some analogy to two-dimensional spectroscopy. More specifically, we utilise a very basic concept commonly referred to as correlation spectroscopy. To this end, the switching efficiency $E_s = E_s(t)|_{\tau=\text{const.}}$ is recorded for a range of excitation times τ, resulting in a two-dimensional map of $E_s(t, \tau)$ (Fig. 6.14a). Due to the exponentially decaying amplitudes of shear and rotation

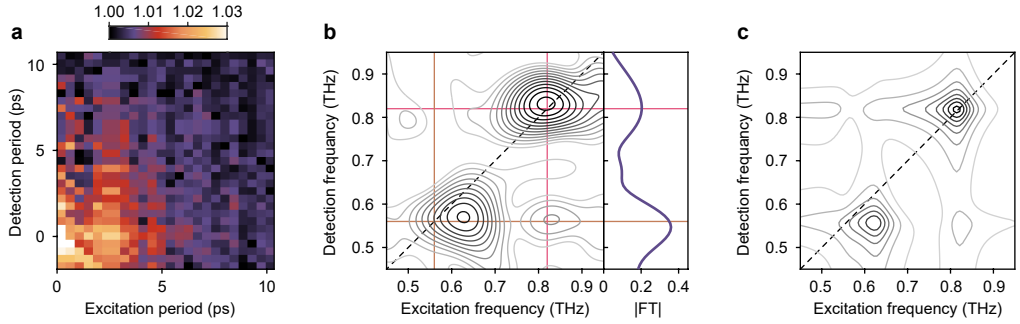

Figure 6.14: Combining ULEED and two-dimensional spectroscopy. **a**, Relative switching efficiency E_s as a function of the excitation period (excitation time) τ and the detection period t. **b**, (Left) 2D spectrum of the system as a function of excitation and detection frequency. Dashed line, diagonal; golden lines, antisymmetric shear frequency ($f_\mathrm{shear} = 0.55$ THz); pink line, rotation frequency ($f_\mathrm{rot} = 0.82$ THz). (Right) 1D spectrum integrated along the τ-axis. **c**, 2D spectrum calculated for a model system of three harmonic oscillators with $f_1 = f_\mathrm{rot}$, $f_2 = f_\mathrm{s}$ (active only between first and second excitation) and $f_3 = f_\mathrm{as}$ (active only after second excitation).

modes, the highest efficiencies are found for small tuples (t, τ) (lower left corner in Fig. 6.14a). The 2D spectrum of the system follows from a two-dimensional Fourier transform of the data set and is depicted in Fig. 6.14b.

What can be learned from the 2D spectrum? First, we note that while the 2D data is taken in a single measurement, signals along excitation and detection axes can each be associated with two different kinds of experiments. Specifically, the excitation axis refers to the delay between two weak excitations of the PES close to its ground state. Here, we expect that the signal reflects the accumulated vibrational amplitude, which is mainly influenced by the timing of displacive excitation and absorption modulation – just like in OPP. For the detection axis, on the other hand, the main observable is given by the transition efficiency, since the strong detection pulse significantly reshapes the PES and thus facilitates the transition depending on t. Along this axis, modes that potentially influence the switching efficiency via the ballistic mechanism are also relevant[20].

As for the results, the resonance frequencies observed along excitation and detection axes are in line with the double-pulse ULEED and OPP measurements discussed in Sec. 6.1-6.4. In particular, the shear component exhibits a significantly higher frequency along the τ-axis (∼OPP) than along the t-axis (∼ULEED). Again,

[20] In this respect, our experiments differ significantly from typical 2D-IR schemes.

this could be explained either by a pronounced softening of the symmetric shear mode in (8×2) regions close to the threshold, or an additional contribution of the antisymmetric shear mode to the switching efficiency via the ballistic mechanism (see Sec. 6.4). Furthermore, the spectrum shows a weak off-diagonal peak in the lower right quadrant, which is, however, not connected to the possible coupling of shear and rotation modes[21]. Rather, due to the particular frequency ratio $f_{\mathrm{rot}}/f_{\mathrm{shear}}$, a resonant excitation of the rotation mode by the first two pulses and the resulting absorption modulation positively influences the switching probability for a third pulse at $t = T_{\mathrm{shear}}$. A similar argument explains the absence of the maximum in the upper left quadrant. Central features of the 2D spectrum can be reproduced by a DECP model featuring three harmonic oscillators with frequencies $f_1 = f_{\mathrm{rot}}$, $f_2 = f_{\mathrm{s}}$ and $f_3 = f_{\mathrm{as}}$, assuming that the (anti-) symmetric shear mode is only active before (after) the second weak pump pulse[22] (Fig. 6.14c).

To summarise, these first triple-pulse measurements serve as a starting point for future experiments aiming at a higher level of control over coherent atomic motion and, consequently, phase transitions. As for the perspectives of 2D ULEED spectroscopy, the totally different observables compared to 2D-NMR or 2D-IR have to be considered. This could be a challenge for future studies, but also offer the possibility of observing effects that are not detectable with standard two-dimensional spectroscopy techniques. In particular, the new technique provides insights into how ultrafast excitations and the resulting transient changes of the PES affect the amplitudes and frequencies of modes involved in structural transitions. Moreover, it would be interesting to perform similar experiments on systems susceptible to ISRS, for which coherent phonons can be excited without changing the PES[23].

[21] In 2D-IR spectroscopy, off-diagonal elements typically indicate a coupling of different modes. In our case, such peaks rather contain information about how one mode influences the amplitude of another - not necessarily through direct coupling, but through absorption modulation, for example. Moreover, it may be expected that the switching process itself, i.e. the transition of the system into the (4×1) state initiated by the strong switching pulse, represents a nonlinearity, which could as well lead to the occurrence of off-diagonal peaks in the 2D spectrum, even in absence of direct couplings.

[22] This would correspond to a scenario in which the transition efficiency is dominated by the (ballistic) contribution of the antisymmetric shear mode.

[23] Considering that the shear and rotation modes are Raman-active, it might be even be possible to realise to perform such experiment on the Si(111)(8×2)-In surface using sub-bandgap excitation.

Chapter 7

Conclusions and perspectives

7.1 Conclusions

The work performed in the framework of this thesis comprises the first investigation of a surface-specific structural phase transition by ultrafast low-energy electron diffraction (ULEED), as well as the demonstration of coherent control over the Peierls-like transition in atomic indium wires on the (111) surface of silicon. To this end, ULEED is combined with multipulse optical excitation and ultrafast optical pump-probe spectroscopy (OPP).

In the first part of this thesis, ULEED with few-ps electron pulses and OPP were employed to study the ultrafast $(8\times2)\rightarrow(4\times1)$ transition and the subsequent recovery of the ground state after single-pulse optical excitation. The main findings are:

- The $(8\times2)\rightarrow(4\times1)$ transition can be driven well below critical temperature T_c by means of photo-excitation of carriers into electronic states connected to shear and rotational phonon modes of the (8×2) structure. The nonequilibrium nature of the transition is evidenced by the time constant of (336 ± 16) fs observed at high fluences by OPP (Sec. 6.3), and a determination of the maximum pump-induced temperature increase of the surface in ULEED (Sec. 5.3).

- OPP data on the initial dynamics of the transition further corroborates the hypotheses of a fluence-dependent initial time constant formulated by Frigge *et al.* [10], which suggests an acceleration of ballistic order parameter motion due to a transient deformation of the potential energy surface (Sec. 6.3).

- The gradual fluence-threshold of the (8×2) → (4×1) transition (FWHM = $(0.84 \pm 0.09)\,\mathrm{mJ\,cm^{-2}}$) indicates a spatially heterogeneous distribution of barrier heights, likely originating from $(8 \times 2)/(4 \times 1)$ interfaces or surface defects, such as dopand atoms, step edges, and adsorbates (Sec. 5.2).

- A fluence-dependent analysis of the recovery dynamics based on Ref. [303] suggests that for a partially switched surface, the relaxation to the ground state via successive back-transformation of (4×1) domains is not determined by the average terrace width of the Si(111) substrate, but rather by the mean (4×1) domain length, which is found to be a strong function of excitation density (Sec. 5.4).

In the second part of this work, we demonstrated coherent vibrational control over the (8×2) → (4×1) transition by combining ULEED with control tactics of femtochemistry, i.e. double pulse excitation, resulting in the following observations:

- Vibrational coherence in key structural modes can be harnessed to affect the efficiency of the structural phase transition in atomic indium wires on Si(111) (Sec. 6.1).

- Due to the distribution of barriers on the surface, the leverage of the double-pulse coherent control scheme is maximised at intermediate fluences between $0.5 - 1.4\,\mathrm{mJ\,cm^{-2}}$, for which a significant amount of the surface domains exhibits particularly low barriers and is susceptible to weak perturbations (Sec. 6.1).

- Coherent control over the transition is facilitated by vibrational coherence in shear and rotational phonon modes, two of which are connected to the transition (Sec. 6.2). The lifetimes of $\tau_{\mathrm{shear}} = (5.2 \pm 0.5)$ ps for the shear and $\tau_{\mathrm{rot}} = (5.9 \pm 0.6)$ ps for the rotation mode are in good agreement with the long-lived elevated electron temperature observed by trARPES and the maximum lattice temperature found at ~ 6 ps by trRHEED. In this context, the observation of vibrational coherence in ULEED represents the missing piece in understanding the pathway for energy relaxation in this model system, and supports the phonon bottleneck hypothesis put forward by Ref. [57].

- Based on our results, we have identified two possible control mechanisms and linked them to shear and rotation contributions to the switching efficiency (Sec. 6.4). Absorption control denotes the modulation of energy absorption from the second pump pulse due to coherent Raman-active phonons, and can clearly be associated with the rotation mode by quantitative considerations. Ballistic control, on the other hand, refers to the possible contribution of kinetic energy or ballistic order parameter motion in overcoming a sufficiently reduced but not completely vanishing barrier. While there is no unambiguous evidence for a ballistic contribution along the shear coordinate at this point, our results are likely to stimulate future works on this subject.

- The transient softening (hardening) of shear (rotation) modes observed in double- and multipulse ULEED experiments and the different relative signal amplitudes in ULEED and OPP suggest a description of the transition in terms of a two-dimensional PES with an off-diagonal transition state. This 2d-model reinforces the role of shear motion and is corroborated by recent DFT calculations (Sec. 6.4).

In summary, this work demonstrates the capability of ULEED to study surface-specific dynamics with high temporal and angular resolution, as well as ultimate surface sensitivity. Enabled by ULEED, the demonstration of coherent control over a surface-structural phase transition opens new routes to switching chemical and physical functionalities through metastable and nonequilibrium states.

7.2 Perspectives

The results of this thesis represent a promising starting point for future investigations of low-dimensional systems, and motivate the development of novel experimental schemes targeting ultrafast structural dynamics at surfaces. Accordingly, the following sections present a number of future experiments that could broaden our understanding of the $(8\times2) \rightarrow (4\times1)$ transition and other nonequilibrium phenomena at surfaces, followed by a discussion of the prospects and possible directions of ULEED and related techniques.

7.2.1 Further investigations of the In/Si(111) sample system

Excitation and control mechanisms

The experimental evidence of long-lived vibrational coherence in shear and rotation modes of the indium layer and their decisive role in the transition again highlights the role of the In/Si(111) surface as a model system for the investigation of electron-phonon coupling and the interactions of light and matter on ultrafast timescales. However, with regard to these points, some essential questions remain open. First, direct evidence for the sequential nature of the phase transition in terms of shear and rotation motion has yet to be found. In this context, ULEED experiments and recent calculations of the excited-state PES by S. Wippermann indicate a stronger initial excitation of the shear mode compared with the rotation mode. Moreover, trARPES clearly observes distinct time scales for electronic excitations and band structure dynamics at different points in k-space [11]. However, it remains to be shown that this is reflected in the initial displacements of atoms along the eigenvectors of shear and rotation modes. In other words: Is there a clear sequence of shear and rotational distortions or do both types of motion occur more or less simultaneously? An answer to this question could be given by observing the direct impact of vibrational motion on the structure factor [140], i.e. the diffraction spot intensity. However, this would require both sub-ps temporal resolution and a high signal-to-noise ratio, as coherent atomic motion is expected to affect only diffraction spots related to the (8×2) phase – possibly with a maximum amplitude of only a few percent. Considering the progress made in development of miniaturised electron guns and pulse compression schemes for ULEED or trRHEED, such experiments could be feasible in the medium term.

Further questions concern the mechanisms underlying the optical excitation of shear and rotation modes. For instance, the possible signature of the symmetric shear mode in ULEED double-pulse traces and/or OPP is difficult to reconcile with the scenario of DECP as the sole excitation or switching mechanism. In particular, for every second (4×) double chain, the corresponding displacement vectors for the individual indium atoms point away from the equilibrium coordinates of the (4×1) structure. By contrast, DECP typically forces initial motion of atoms towards the high-symmetry phase. Alternatively, a potential excitation of this mode could be explained in terms of impulsive stimulated Raman scattering (ISRS). This hypotheses could be tested by OPP experiments with sub-bandgap excitation [58], provided

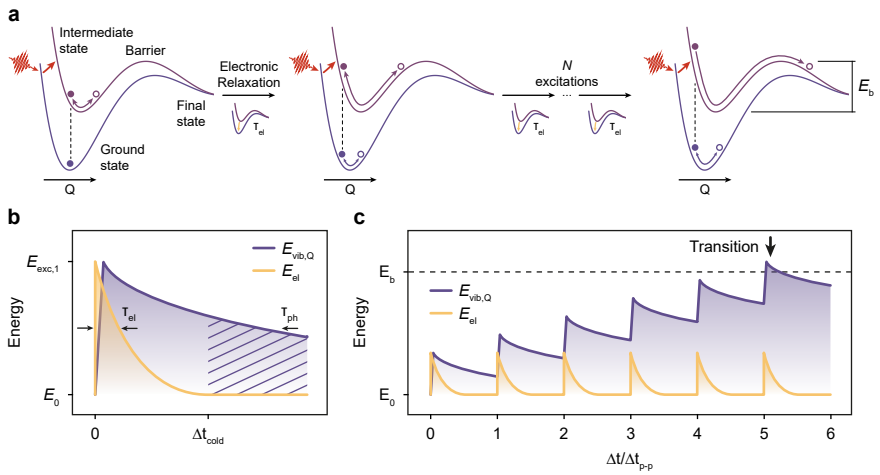

Figure 7.1: Cold driving scheme for phase transitions, assuming DECP as the dominant excitation mechanism. **a**, PES of the transition after one, two and N optical excitations. Note that the excited ground state always relaxes back between successive excitations and that the cold driving scheme only applies to modes pointing towards the transition state (along structural coordinate Q, but not along arbitrary q). E_b, barrier height. **b**, Sketch of electronic energy E_el and the energy $E_\mathrm{vib,Q}$ stored in coherent lattice motion as a function of the time after excitation. The hatched area indicates vibrational coherence outlasting electronic excitation. **c**, Sketch of $E_\mathrm{el}(\Delta t/\Delta t_\mathrm{p\text{-}p})$ and $E_\mathrm{vib,Q}(\Delta t/\Delta t_\mathrm{p\text{-}p})$. The transition occurs for $E_\mathrm{vib,Q}(\Delta t/\Delta t_\mathrm{p\text{-}p}) > E_\mathrm{b}$.

a sufficiently large bandwidth or short duration, respectively, of the pump pulses.

Last, we discuss the possibility of a purely vibrational excitation of the transition (Fig. 7.1), i.e. by repeatedly amplifying the coherent vibrational amplitude without increasing the overall level of electronic excitation [165]. Assuming DECP as the main excitation mechanism in this system, the feasibility of this "cold" driving scheme requires long-lived vibrational coherence, with $\tau_\mathrm{ph} > \tau_\mathrm{el}$ (Fig. 7.1b). In this case, repeated in-phase excitation of atomic oscillations for $\Delta t_\mathrm{p\text{-}p} > \Delta t_\mathrm{cold}$ could increase the vibrational energy of the system, and thus facilitate a ballistic transition across the barrier (Fig. 7.1a,c). As discussed in Sec. 6.2 the vibrational coherence in shear and rotation modes indeed outlasts the electronic excitations. At the same time, recent ULEED experiments with up to five pump pulses and $\Delta t_\mathrm{p\text{-}p} > \Delta t_\mathrm{cold}$ did not show a significant enhancement of the vibrational amplitude. It would be interesting to perform similar experiments in combination with OPP, which directly observes the vibrational amplitude of Raman-active modes. Moreover, if shear and rotation modes are susceptible to ISRS, the vibrational amplitude could be enhanced after a single oscillation period without a significant increase in electronic tempera-

ture. Irrespective of the applicability of the "cold" driving scheme to this particular surface system, the underlying concept is simply fascinating and should be pursued in future ULEED studies.

Atomic-scale heterogeneity

As exemplified by the findings of this work and recent results of PEEM, trRHEED, STM and DFT [116, 234, 303], the role of surface heterogeneity for the transition deserves further consideration. In particular, the progression of the $(4\times1) \rightarrow (8\times2)$ on a microscopic level in the form of moving interfaces between (4×1) and (8×2) wire segments ("falling row of dominoes" [9, 233]) makes the sample system a playground for ultrafast nano- and mesoscale surface science. Promising future directions include the role of atomic-scale defects, local doping and the dynamic nature of (8×2) /(4×1) interfaces.

Although signatures of the heterogeneous nature of the surface after weak optical excitation can in principle be investigated by diffraction [53, 116], ultrafast spatially-resolved studies of the surface would significantly broaden the range of accessible phenomena. In this context, recent advances in the integration of scanning tunneling microscopy and ultrafast optical excitation enable the observation and control of atomic-scale dynamics at surfaces on a nm length an fs-ps time scale [311–316]. A similar approach is currently being pursued by the group of Martin Wenderoth here in Göttingen. Such techniques could address question of how atomic-scale defects and interfaces locally influence the phase transition and the phonon modes involved. While there are countless aspects worthy of investigation for the In/Si(111) surface alone[1], only one STM-related proposal will be discussed here.

Specifically, synchronisation of the readout process in STM with optical excitation of the Si(111)(8×2)-In surface could be used to determine not only the recovery velocity v_{rec}, i.e. the velocity of the propagating (4×1) /(8×2) phase front, but also the influence of atomic scale defects, such as dopand atoms, on the latter. To this end, the STM tip would be placed in a distance L from a step on the Si(111) substrate (see Fig. 7.2d), which functions as a seed for the recovery of the (8×2) ground state in the case of a completely switched surface [303]. By measuring the delay between

[1] The evolution of interwire correlations following optical stimulus or the microscopic dynamics underlying the changes in the switching efficiency reported in this work [53], to name just two.

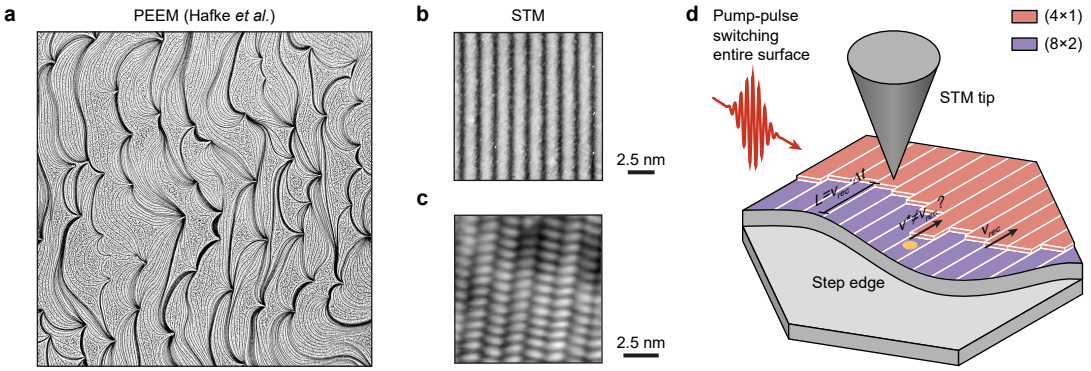

Figure 7.2: Perspectives for time-resolved investigations of surface heterogeneity. **a**, PEEM image of an Ag-decorated Si(111) surface with a field of view of $50 \times 50\,\mu\mathrm{m}^2$. Steps are represented as dark lines. Reprinted from Ref. [303]; used in accordance with the Creative Commons Attribution (CC BY) license. **b**,**c**, First STM topographies of (4×1) (**b**) and (8×2) (**c**) reconstructed surfaces recorded by Georg Träger. Bias voltage and current: -0.7 V, 50 pA (4×1) ; -0.3 V, 100 pA (8×2) . **d**, Proposal for an ultrafast STM experiment to investigate domain wall motion triggered by optical excitation and the subsequent back-transformation of the (4×1) structure at recovery velocity v_{rec}.

excitation of the surface and the arrival of the propagating $(4 \times 1)/(8 \times 2)$ interface at the position of the tip, v_{rec} could be estimated. Furthermore, by comparing the progression of the transition along wires with and without defects, fascinating insights into the dynamic interaction of CDWs with nanoscale inhomogeneities could be gained. We note that L would have to be chosen large enough to clearly separate the optical excitation from the readout process. For example, placing the tip in a distance of 100 nm from the next step edge (corresponding to half of the mean terrace width on the Si(111) surface [303], see also Fig. 7.2a) and assuming $v_{\mathrm{rec}} \approx 100\,\mathrm{m/s} = 0.1\,\mathrm{nm/ps}$ as reported by Ref. [303], the arrival of the phase front at the should be delayed by ~ 1 ns, which is within the resolution of state-of-the-art STM electronics. Encouragingly, first steps towards time-resolved STM studies of the In/Si(111) surface have already been taken in cooperation with Georg Träger (Wenderoth group), including preparation of Si(111)(4×1)-In and Si(111)(8×2)-In surfaces and real-space characterisation by STM (see Fig. 7.2b,c).

As far as ULEED is concerned, future experiments could investigate the effect of doping on the threshold for the optically-induced transition and the frequencies of the modes involved. In this context, the crucial role of the substrate carrier density in stabilising the (8×2) phase slightly below T_{c} and the possibility to switch supercooled

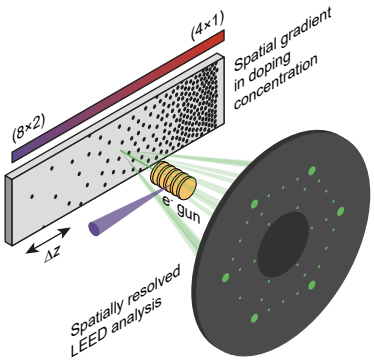

Figure 7.3: ULEED studies on Si(111) wafers with spatially varying doping concentration. To investigate the influence of doping on the ultrafast (8×2) → (4×1) transition, the microgun could be harnessed to record pump-probe traces at different positions of the wafer. Comparison of (8×2) and (4×1) intensities static diffraction pattern should provide information on the corresponding surface fractions.

(4×1) domains by depleting the space charge region at the interface between substrate and monolayer has been demonstrated in STM [282]. Time-resolved studies of these effects in ULEED could be facilitated by ion beam implantation of dopand atoms, which would allow for the preparation of Si wafers with spatially varying doping concentrations [317] (see Fig. 7.3). This concept has already been harnessed for the doping of graphene [318]. Moreover, future generations of miniaturised, pulsed electron guns could provide a sufficiently enhanced momentum resolution to resolve the recovery of the ground state shortly following photo-excitation.

7.2.2 Perspectives for ULEED

Time-resolved structure determination by ULEED

Since the first realisation of ULEED the technique has successfully demonstrated its capabilities with regard to time-resolved analysis of spot intensities and profiles [17, 18, 53, 55]. However, one key achievement of conventional LEED still has to be transferred to the time domain. If there was an ultimate experiment for ULEED, it would involve surface structure determination, commonly referred to as surface crystallography or I(V)-LEED. Here, recording the diffraction pattern of the sample surface for a wide range of electron energies allows to track characteristic oscillations in the intensities of individual spots. A comparison of the resulting experimental data sets with structure models via calculations of the dynamic scattering factor [111, 180] can be used to determine the atomic positions at the surface with sub-angstrom resolution and element specificity.

Consequently, a time-resolved realisation of I(V)-LEED holds the potential to resolve the crystal structure of metastable, or other light-induced nonequilibrium

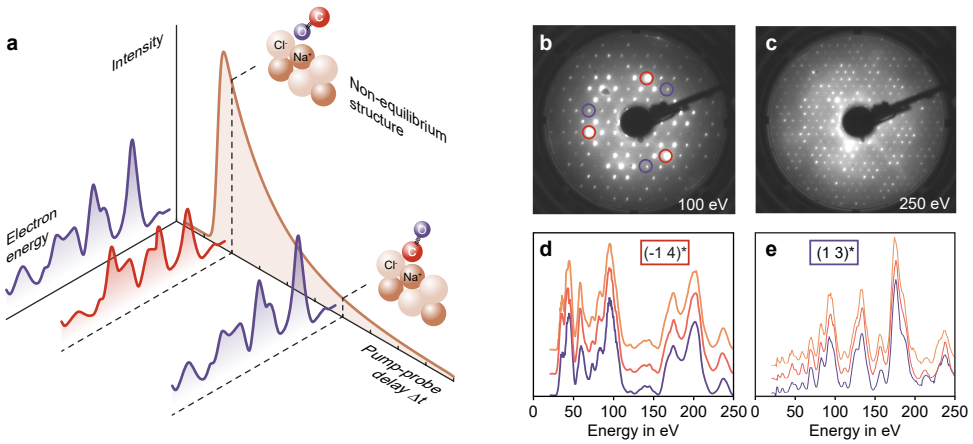

Figure 7.4: Concept of time-resolved surface structure determination by ULEED. **a**, Schematic drawing of a tr-I(V)-LEED experiment. Energy-dependent spot intensities ("LEED spectra") are recorded for different pump-probe delays to identify structural changes and reconstruct the time-dependent positions of surface atoms or adsorbates. **b**,**c**, LEED patterns of the commensurate CDW phase of 1T-TaS_2 taken at electron energies of 100 eV (**b**) and 250 eV (**c**). **d**,**e**, LEED spectra recorded between 20 and 250 eV for two triplets of symmetry-equivalent spots indicated in **b** (red and violet circles). Figures **b**-**e** adapted with permission from Ref. [319]. © 2019 by the American Physical Society.

states at surfaces, which are not accessible by standard techniques for structure determination. The experimental scheme of tr-I(V)-LEED is presented in Fig. 7.4a. Optical excitation is used to steer the surface into a nonequilibrium state with finite lifetime, while energy-dependent spot intensities are recorded by ULEED for a fixed pump-delay $\Delta t_{\text{p-el}}$. Repeating this procedure for different delays with respect to the excitation of the transient structure, the evolution of the structure can be monitored throughout the relaxation process. By delivering precise atomic coordinates, ultrafast LEED crystallography would strongly influence and support the theoretical modelling of states and structures far from equilibrium. Beyond that, given ideal experimental conditions[2] and sufficiently high computing capacity, tr-I(V)-LEED could be used to record true molecular movies of surfaces undergoing structural transitions.

The road map towards time-resolved surface crystallography features a number of challenges that need to be overcome. First, depending on the desired accu-

[2]That is, long-term stability of the laser system and the electron source, as well as a negligible influence of sample degradation.

racy and overall validity of the structural analysis, LEED spectra would have to be recorded over a wide energy range. At the same time, the current microgun design allows for energies between 30 and 120 eV. Assuming a single digit number of non-symmetry equivalent spots, the maximum size of the data set for analysis is limited to ~ 1000 eV[3], which is small compared to conventional I(V)-LEED studies. While this motivates further development of the miniaturised electron sources for ULEED, first tr-I(V)-LEED experiments will readily provide valuable insights into ultrafast structural changes even for a reduced energy range. Second, the complexity of dynamic structure factor calculations poses a significant challenge for the interpretation of results and thus ideally requires expertise in this field. In this regard, in a recent cooperation with Lutz Hammer and Tilman Kisslinger from the University of Erlangen-Nürnberg, such calculations have successfully been performed for the commensurate CDW phase of $1T$-TaS_2 by a Master's student from our group, namely Gevin von Witte [319] (the associated experimental data shown in Fig. 7.4b was recorded together with Tilman Kisslinger over the course of this thesis). This will serve as a starting point for the future implementation of time-resolved surface crystallography. A further technical challenge is posed by the synchronisation of optical pump pulses with electron pulses of different energies. For tr-I(V)-LEED experiments with a gun-sample distance of 500 μm and an electron energy range between 30 and 120 eV, the maximum difference in time-of-flight is $\Delta t_{\mathrm{max}} \approx 80$ ps. To maintain the high temporal resolution of ULEED in ultrafast surface crystallography, this energy-dependent additional delay has to be compensated at every energy step of the measurement by adapting the optical path length for the pump pulse ($\Delta s_{\mathrm{max}} \approx 24$ mm).

Despite these challenges, tr-I(V)-LEED remains a highly desirable extension of ULEED capabilities and thus represents the next milestone in the further development of the experiment. Importantly, possible sample systems for proof-of-principle experiments are already at hand. This includes the photo-excited (4×1) phase of indium on Si(111) investigated in this work, or the upside-down isomer of CO on the NaCl(110) surface produced by infrared laser excitation [320]. Regarding indium on silicon, time-resolved surface crystallography would be the ideal tool to identify potential differences between the metastable and the equilibrium (4×1) structure.

[3] In I(V)-LEED, the size of the data set is typically given by the total width of energy intervals over which LEED oscillations of individual spots are observed.

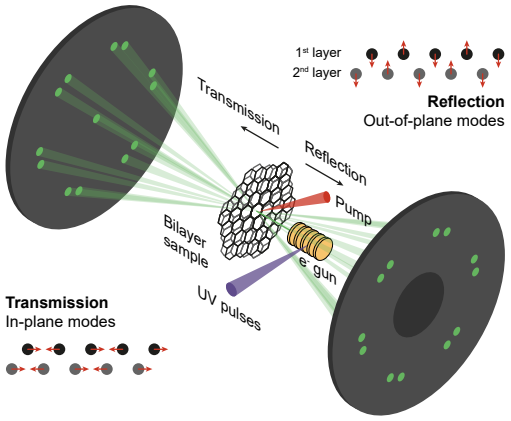

Figure 7.5: Experimental scheme of stereo-ULEED. Low-energy electron pulses from a μm-sized gun are scattered by a mono- or bilayer structure. The diffraction patterns formed by forward- and back-scattered electrons are recorded by MCPs as a function of the pump-probe delay. Comparison of reflection and transmission data yields insights into, e.g. the roles and/or couplings of in-plane (for transmission) and out-of-plain (for reflection) modes of the sample.

Ultrafast Stereo-LEED in transmission and reflection

ULEED with ps temporal resolution was first demonstrated in a transmission geometry, revealing ultrafast polymer dynamics on graphene after optical excitation [17, 217]. While this approach was without alternative at the time due to the relatively large electron source, today the combination of this concept with the functionalities of miniaturised electron guns opens up new perspectives for ULEED, as will be discussed below.

The physical properties of two-dimensional (quantum) materials often depends on the number of layers, their relative orientation and inter-layer coupling. In recent years, this ever-expanding class of materials attracted significant interest, aided by the observation of novel electronic phases in magic-angle twisted bi- or multilayers of graphene [28] or the investigations of phase transitions in transition metal dichalcogenide (TMDC) heterostructures [29, 30]. Whereas studies in this field typically employ transport measurements or ARPES to investigate the electronic subsystem, information about the potential role played by structural degrees of freedom remains relatively scarce. In particular, the influence of in- and out-of-plane modes on the properties of atomically thin layers is still an open subject.

Here, the concept of stereo-ULEED could make a significant contribution to the understanding of such systems in terms of interlayer coupling or energy relaxation channels. In stereo-LEED, diffraction patterns of transmitted and reflected low-energy electron pulses would be recorded simultaneously as a function of the pump-probe delay (see Fig. 7.5). This way, by harnessing the sensitivity of LEED in transmission (reflection) to in-plane (out-of-plane) modes and comparing the two

LEED patterns, contributions of both types of lattice vibrations, e.g. to phase transitions, could be disentangled.

A major challenge in realising stereo-ULEED is given by the preparation of large and clean mono- or bilayer samples. However, the μm spot size of the microgun should prove advantageous in this respect. Moreover, pump-probe experiments on thin films and at high repetition rates demand a sufficiently good thermal contact between sample and holder to prevent cumulative heating. Fortunately, similar challenges have been overcome in the context of ultrafast TEM experiments in our group [224]. Building on this expertise, we are optimistic about this point. Lastly, it is unclear, if the relatively low maximum electron energy available in ULEED ($\sim 100 - 150$ eV) and the small resulting mean free path allows for transmission experiments on bi-layer samples. However, given the ongoing development of the miniaturised electron guns, an extension of the energy range to 200 eV seems possible.

Combined ULEED and OPP studies

The outcome of this thesis has benefited significantly from the combination of ULEED and optical pump-probe spectroscopy. For this reason, the next step is to develop this concept even further. As a motivation, many CDW materials exhibit prominent amplitude modes with oscillation periods currently lying beyond the temporal resolution of ULEED. In this respect, OPP could – to some extend – supplement ULEED in terms of temporal resolution. Moreover, the complementary observables in both types of experiments would allow for the investigation of ultrafast surface and monolayer (bilayer) dynamics from an electronic and a lattice perspective. From a practical point of view, OPP experiments can often be carried out significantly faster than electron diffraction experiments. Therefore, future candidates for materials to be studied by ULEED could be examined first by OPP under identical conditions. For example, measurements of ultrafast changes in the absorption spectrum of molecules adsorbed on the surface could be used to fine-tune optical excitation in ULEED, in which resonances can only be observed indirectly by means of the resulting changes to the lattice structure. Finally, depending on the chosen wavelength and the resulting finite penetration depth of the pump light, transient reflectivity rather probes the bulk response of materials and thus provides

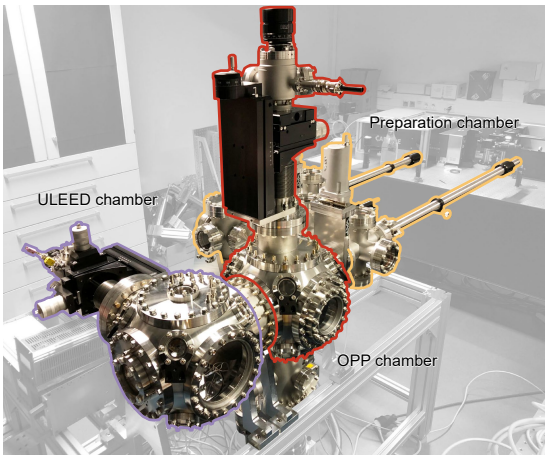

Figure 7.6: New experimental chamber for combined ULEED and OPP studies of structural and electronic dynamics at surfaces. The new UHV setup features two separate chambers for ULEED (violet) and OPP (red) measurements. Optical viewports mounted at the cube corners allow for excitation and at probing and long wavelengths. Yellow, load lock, preparation chamber and sample storage.

complementary information about the coupling between surface layer and substrate, or energy relaxation, respectively.

Recognising the potential of combined ULEED and OPP studies, an entirely new ULEED setup has been designed within the last months of this work, and is currently under construction (see Fig. 7.6). In particular, the new experiment features two UHV cubes (one for ULEED and one for OPP experiments), facilitating optical access to the sample and the mounting of different optical viewports optimised for specific pump wavelengths. Each of the cubes is equipped with a cryo-manipulator to enable ULEED and OPP measurements under identical conditions. In the first construction stage, the preparation capabilities include cleaving of samples, electron beam heating and the evaporation of molecules. The associated laser system can be operated at repetition rates of up to 400 kHz, which will prove advantageous with respect to future OPP studies. In summary, combining two complementary techniques for the study ultrafast surface dynamics will yield exciting insights into couplings and correlations between electronic and lattice degrees of freedom.

ULEED with multipulse or resonant optical excitation

The use of pulse sequences for the coherent control of the (8×2) transition and mode-selective excitation of shear and rotation modes of the (8×2) structure in this work motivates the application of this methodology to phase transitions in other materials systems.

A promising first target is given by the transition between the commensurate CDW phase of $1T$-TaS_2 and the recently discovered hidden state of this material, for which electronic excitation is believed to play a key role [36]. In this context, essential questions concern the lifetime of electrons in the corresponding electronic states and the possible role of coherences for the switching process. Here, ULEED in combination with double-pulse optical excitation ($F_1 = F_2 < F_{\mathrm{th}}$ and $F_1 + F_2 > F_{\mathrm{th}}$) could show that the transition can be driven by means of accumulated electronic excitation, and determine the time constant for the decay of excitations connected to the switching dynamics. Moreover, it would be interesting to see if the absorption control scheme harnessed in this work can be applied to other materials with prominent Raman-active modes.

In an alternative approach, future ULEED experiments could use intense MIR and THz pulses to resonantly excite key structural modes. In this respect, the seminal works of A. Cavalleri and co-workers demonstrate the potential of this ansatz for the control of electronic [139, 309], superconducting [3] or ferroelectric [310] phases. Since many of these experiments require base temperatures well below 10 K, future ULEED measurements in this field can only be realised for a new cryostat design. At slightly higher temperatures, the switching between the two isomers of CO molecules adsorbed on NaCl(100) via resonant pumping at MIR wavelength [320] could pose a rewarding challenge for ULEED.

7.2.3 Ultrafast low-energy electron microscopy

The role of microscopic inhomogeneities on dynamical processes at surfaces goes far beyond the case of indium on silicon – in fact, it represents a central aspect of the physics of low-dimensional systems or surface catalysis. While electronic structure dynamics at surfaces can readily be examined by a variety of techniques, including ultrafast optical spectroscopy, trARPES, THz-STM [311, 316] or trPEEM [321], methods directly accessing the lattice structure remain relatively scarce. To mention another aspect, in many cases, a comprehensive understanding of surface processes cannot be achieved by studies of the micro-scale correlations of electrons, phonons or spins alone (see Fig. 7.7a). Rather, the macroscopic properties of surfaces and their potential for technical applications are determined by dynamics occurring on a mesoscale, such as domain wall or motion or the interaction of light with nanos-

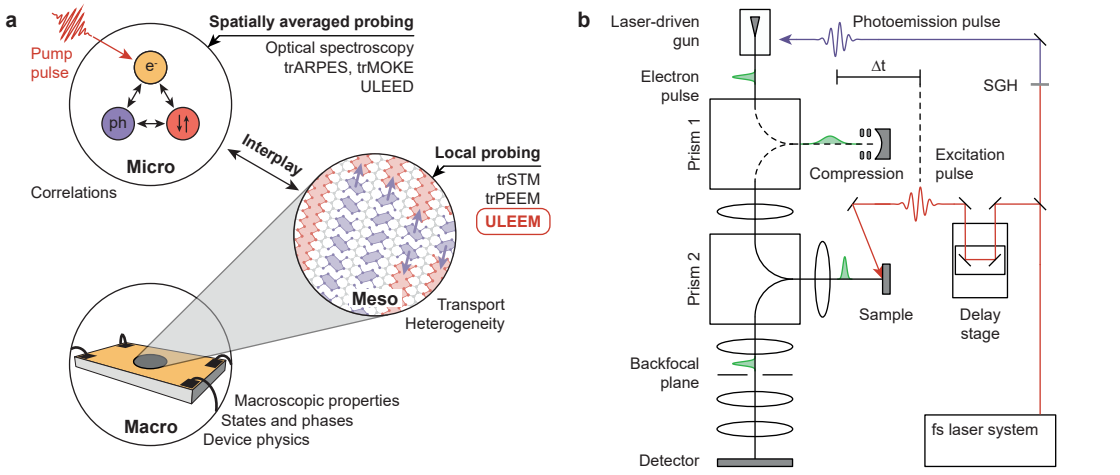

Figure 7.7: Motivation and concept for ULEEM. **a**, Hierarchies of couplings and correlations leading to macroscopic materials properties and functionalities. Short-pulsed excitation of a sub-system (here, optical excitation of the charges) may be used to probe microscopic equilibration of structural, electronic and spin degrees of freedom, typically in a spatially averaged way. However, these processes are strongly affected by mesoscale structural heterogeneity, governing, for example, the spatiotemporal redistribution of excitations, their ballistic and diffusive transport, and the nucleation of domains. The ULEEM project aims at the direct observation of spatiotemporal nonequilibrium phenomena on the nanoscale. **b**, Experimental scheme of ULEEM. Ultrashort electron pulses from a laser-driven field emitter are accelerated to keV energies and pass the lens system as well as the electrostatic prism array for beam shaping and compression (optional). The electrons are subsequently decelerated and focused onto the optically excited sample. Reflected electrons re-enter prism 2 and are deflected towards the detector.

tructured materials. These phenomena can only be studied indirectly by spatially-averaging techniques, which motivates the search for local probes of electron and specifically lattice dynamics. However, as of today, there is no existing ultrafast microscopy scheme with direct sensitivity to the atomic-scale surface structure.

Recognising the potential of such an approach, and considering the experience gained in the development and application of ULEED and ultrafast transmission electron microscopy (UTEM), a technical realisation of ultrafast low-energy electron microscopy (ULEEM) for the time-resolved observation of structural dynamics at surfaces on a nm-fs scale seems a promising and realistic objective. LEEM is a versatile and powerful technique, which employs low-energy electron scattering off surfaces to obtain both real-space and diffraction information on surface structures with resolutions down to 2 nm [322]. As is typical for electron microscopies in general, it

encompasses not just one, but a variety of contrast mechanisms, with different methods tailored to specific structural and electronic observables. By combining LEEM with stroboscopic imaging in an optical pump-probe scheme (see Fig. 7.7b) this range of functionalities can be employed for time-resolved investigations. Major challenges in the realisation of ULEEM include the control over the energy bandwidth and duration of ultrashort keV electron pulses[4], and the realisation of reversible dynamics, e.g. by structured illumination [224]. In meeting these challenges, the transfer of knowledge from UTEM and ULEED will prove extremely helpful.

As far as potential applications of ULEEM are concerned, recent dark field schemes developed in UTEM [224] could be adapted for ULEEM to observe the order parameter motion in surface-specific structural phase transitions. Moreover, the combination of high temporal resolution and energy-resolved operation modes, such as PEEM [321], low-energy electron potentiometry (LEEP) [323] or angle-resolved reflected-electron spectroscopy (ARRES) [324] would enable two-dimensional spectroscopy studies on the nanoscale [211]. Finally, the local switching of CDW materials or catalytic surfaces on fs-ps timescales via the sub-wavelength confinement of light at nanostructures is another fascinating objective. Such experiments would represent an important step for the functionalisation of phase change materials, e.g. in terms of ultrafast switches or logic gates, and the active optical control over the transient domain structure of surfaces.

[4]Note that in LEEM, electrons are first accelerated to $\sim$ 15 keV ($U_{\mathrm{cathode}} = -15$ kV) to be decelerated just before the sample surface ($U_{\mathrm{sample}} = U_{\mathrm{cathode}} - \Delta U$, with $\mathrm{e}\Delta U = E_{\mathrm{kin,surf}}$)

Appendix A

Debye-Waller effect and diffuse scattering

Bragg reflexes in the LEED pattern originate from the coherent elastic back-scattering of electrons from atomic cores or inner shell electrons of a solid. Herein, the atomic positions within the unit cell determine the spot intensities (see Sec. 2.3.2). However, in deriving the structure factor F (see Sec. 2.3.2), we have ignored that at finite temperature the crystal is no longer static, and atoms move around their equilibrium coordinates ρ_j[1]. This thermal motion influences the diffraction pattern in different ways. Most strikingly, Bragg spot intensities decrease with increasing temperature, as first described by Debye [202] and Waller [203]. This *Debye-Waller suppression* occurs not only in LEED, but also in other diffraction techniques, and is often used to infer temperature changes of a sample. The associated *Debye-Waller factor* (DWF) is often interpreted as a measure of the (lattice) coherence in elastic scattering [179]. In kinematic scattering theory, the DWF appears as first-order contribution of thermal motion to the diffraction pattern. Furthermore, the second-order contribution to I, commonly referred to as *thermal diffusive scattering* (TDS), contains complementary information about collective excitations of the atomic lattice (e.g. phonons or plasmons) and is accessible via the inelastic background analysis. Both Debye-Waller suppressions and TDS have recently been investigated by means of time-resolved diffraction, providing insights into nonequilibrium heat transfer and single-phonon populations.

Debye-Waller effect In order to quantitatively understand the influence of temperature on the LEED pattern, we recall the structure factor F, (second factor in

[1] To be precise, even at $T = 0$, the uncertainty principle dictates small deviations from equilibrium positions (zero-point motion) [186].

Eq. 2.41)[2]. Specifically, we follow Ref. [186] and calculate $I(\Delta\boldsymbol{k}) = |F|^2$ for identical scatterers ($f_i = f_j = f$) located at positions ρ_i and ρ_j:

$$I(\Delta\boldsymbol{k}) = f^2 \sum_{i,j} \exp(-\mathrm{i}\Delta\boldsymbol{k} \cdot (\boldsymbol{\rho_i} - \boldsymbol{\rho_j})). \tag{A.1}$$

For $\Delta\boldsymbol{k} = \boldsymbol{G}_{hk}$ this gives all elastic (Bragg) reflexes of the LEED pattern. However, as previously indicated, Eq. 2.41 and Eq. A.1 neglect both zero-point vibrations ($T = 0$ K) and thermal occupation of phonon modes ($T > 0$ K) causing atoms to fluctuate around their equilibrium positions. This results in diffraction from a distorted lattice, since interactions between electrons and atoms take place on timescales significantly shorter than phonon oscillation periods [111]. To take into account this thermal motion, the atomic coordinates $\boldsymbol{\rho}_i$ in Eq. A.1 are split into time-dependent and independent terms, so that $\boldsymbol{\rho}_i = \boldsymbol{\rho}_i(t) = \boldsymbol{\rho}_{i,0} + \boldsymbol{u}_i(t)$. In this case, the time-averaged intensity is given by

$$\langle I(t)\rangle = I_0 \sum_{i,j} \langle \exp(-\mathrm{i}\Delta k[u_i(t) - u_j(t)])\rangle, \tag{A.2}$$

where $I_0 = f^2 \sum_{i,j} \exp(-\mathrm{i}\Delta\boldsymbol{k} \cdot [\boldsymbol{\rho}_{i,0} - \boldsymbol{\rho}_{j,0}])$ is the intensity calculated from the structure factor of the ideal (frozen) lattice and $u_i(t) = \Delta\boldsymbol{k} \cdot \boldsymbol{u}_i(t)$ the component of thermal atomic motion in the direction of the scattering vector. For small mean oscillation amplitudes the time-dependent factor in Eq.A.2 can be expanded to second order in powers of $\Delta k[u_i(t) - u_j(t)] = \Delta k \Delta u_{ij}(t)$, yielding

$$\langle \exp(-\mathrm{i}\Delta k \Delta u_{ij}(t))\rangle \approx 1 - \frac{1}{2}\langle (\Delta k \Delta u_{ij}(t))^2\rangle + ... \tag{A.3}$$

Here, we have used that term linear in $\Delta k \Delta u_{ij}(t)$, that is, the first moment (mean value) of the spatial probability density distribution vanishes, because the time-dependent displacements occur statistically in all directions. Equation A.3 can therefore be further approximated by

$$(1 - \langle (\Delta k \Delta u_{ij}(t))^2\rangle/2 + ...) \approx \exp\left(-\Delta k^2 \langle \Delta u_{ij}(t)\rangle^2/2\right). \tag{A.4}$$

[2]Here we neglect the possibility of a thermally induced structural phase transition, which would also influence the lattice factor G.

Inserting this expression into Eq. A.2 gives

$$\begin{aligned}\langle I(t)\rangle &\approx I_0 \sum_{i,j} \exp\left(-(\Delta k u_i)^2/2\right) \exp\left(-(\Delta k u_j)^2/2\right) \exp\left(-\Delta k^2 \langle u_i(t) u_j(t)\rangle\right) \\ &\approx I_0 \sum_{i,j} \exp\left(-(\Delta k u_i)^2/2\right) \exp\left(-(\Delta k u_j)^2/2\right) [1 - \Delta k^2 \langle u_i(t) u_j(t)\rangle + ...].\end{aligned} \tag{A.5}$$

In the first line, we have used that $\langle \Delta u_{ij}(t)\rangle^2 = \langle u_i(t) - u_j(t)\rangle^2 = u_i^2 + u_i^2 - 2\langle u_i(t) u_j(t)\rangle$. Finally, Eq. A.5 is obtained by expanding the last exponential factor for small amplitudes vibrational amplitudes $u_i(t)$. Consequently, the first-order contribution to the intensity of the diffraction pattern is

$$I_1 = I_0 \exp(-\Delta k^2 \langle u^2\rangle) = I_0 \exp(-2M), \tag{A.6}$$

with the Debye-Waller factor DWF $= \exp(-2M)$. Since I_0 is solely determined by the Laue condition, Eq.A.6 describes the temperature-induced suppression of reflex intensities. We further note that thermal atomic motion has no effect on the width of diffraction spots. Moreover, the DWF is larger for higher-order spots due to its Δk^2-dependence.

DWF in the Debye model Notwithstanding these insights, the mean quadratic displacement $\langle u^2\rangle$ is hardly accessible experimentally. Hence, for practical reasons, a description of intensity suppression as a function of temperature T is desirable. The connection between $\langle u^2\rangle$ and T has been worked out by Refs. [186] and [10]. Here, based on a harmonic approximation, the mean quadratic displacement $\langle u^2\rangle_\omega$ of all phonon modes is related to the energy $E_{\mathrm{osc}}(\omega, T) = \hbar\omega(n(\omega, T) + 1/2)$ of the oscillator via

$$\langle u^2\rangle_\omega = \int_0^{\omega_\mathrm{D}} \mathrm{d}\omega \, \frac{E_{\mathrm{osc}}(\omega, T)}{m\omega^2} \, D(\omega), \tag{A.7}$$

with ω_D being the Debye frequency, $n(\omega, T) = \hbar\omega/[\exp(\hbar\omega/k_\mathrm{B}T) - 1]$ the Boltzmann distribution and $D_\mathrm{D}(\omega)$ the dispersion relation in the Debye model. Further evaluating Eq. A.7 yields [186]

$$\langle u^2(t)\rangle = \frac{9\hbar^2}{m_\mathrm{a} k_\mathrm{B} \theta_\mathrm{D}} \left[\frac{1}{4} + \frac{T}{\theta_\mathrm{D}^2} \int_0^{\theta_\mathrm{D}/T} \frac{\xi}{\exp(\xi) - 1} \, \mathrm{d}\xi\right], \tag{A.8}$$

where m_a is the atomic mass, k_b the Boltzmann constant, $\theta_\mathrm{D} = \hbar\omega_\mathrm{D}$ the Debye temperature, and $\xi = \hbar\omega/k_\mathrm{B}T$. The temperature θ_D is defined such that for $T > \theta_\mathrm{D}$ all phonon modes are thermally excited, whereas for $T < \theta_\mathrm{D}$ certain modes freeze out depending on their energy. Moreover, we note that the occurring integral cannot be solved analytically. For $T > \theta_\mathrm{D}$, however, $\xi/[\exp(\xi) - 1)] \to 0$, and Eq. A.8 can be drastically simplified:

$$\langle u^2 \rangle \approx \frac{9\hbar^2 T}{m_\mathrm{a} k_\mathrm{B} \theta_\mathrm{D}^2}. \tag{A.9}$$

Thus, in the high-temperature limit, the Deybe-Waller-type suppression of the spot intensities in LEED ($\Delta k = G_{hk}$) is described by

$$I_1 = I_0 \exp\left(\frac{3\hbar^2 G_{hk}^2}{m_\mathrm{a} k_\mathrm{B}} \frac{T}{\theta}\right). \tag{A.10}$$

Here, we have used that $\langle \Delta\boldsymbol{k} \cdot \boldsymbol{u}_i(t)^2 \rangle = |\Delta\boldsymbol{k}|^2 \langle \boldsymbol{u}_i(t)^2 \rangle \langle \cos^2(\varphi) \rangle$ and $\langle \cos^2(\varphi) \rangle = 1/3$. Importantly, for temperatures $T < \theta_\mathrm{D}$, Eq. A.9 deviates from the numerical solution of Eq. A.8. For this low-temperature case, Hardy *et al.* [325] have proposed an exponential approximation of the integral in Eq. A.8, leading to

$$\langle u^2(t) \rangle \approx \frac{9\hbar^2}{m_\mathrm{a} k_\mathrm{B}} \left[\frac{1}{4} + \frac{\pi^2}{6}\left(\frac{T}{\theta_\mathrm{D}}\right)^2 \left(1 - \exp\left(-\left(\frac{\pi^2}{6} - 1\right)\frac{\theta_\mathrm{D}}{T}\right)\right)\right]. \tag{A.11}$$

As the majority of experiments carried out as part of this work were performed at cryostatic temperatures either close to or below θ_D, Eq. A.11 will be used most of the time in analysing temperature-induced spot suppression.

Thermal diffuse scattering We now examine the second order contribution in Eq. A.5 associated with thermal diffuse scattering (TDS), following the arguments of Ref. [186]. For this, we note that the time-dependent thermal motion of atoms can be decomposed into the phonon eigenmodes of the crystal:

$$\boldsymbol{u}(t) = \sum_{\boldsymbol{q},m} A_{\boldsymbol{q},m}\, \hat{\boldsymbol{e}}_m \cos(\omega_m(\boldsymbol{q})t - \boldsymbol{q} \cdot \boldsymbol{\rho}_m + \phi_m(\boldsymbol{q})). \tag{A.12}$$

Here, we sum over the wave vectors $\boldsymbol{q}$ of all $3N$ modes m, N being the number of atoms in the unit cell. $A_{\boldsymbol{q},m}$ is the phonon amplitude with polarisation $\hat{\boldsymbol{e}}_m$, $\omega_m(\boldsymbol{q})$ the phonon frequency and $\phi_m(\boldsymbol{q})$ the initial phase. By using this ansatz to calculate

$\langle u_i(t)u_j(t)\rangle$, the second order contribution in Eq. A.5 becomes [186]

$$I_2 = I_0 \exp(-2M)\,\frac{N}{2}\sum_{\boldsymbol{q},m}\frac{(n_{\boldsymbol{q},m}+1/2)}{\omega(\boldsymbol{q})}|F_m(\Delta\boldsymbol{k},\boldsymbol{G}_{hk})|^2\cdot\ldots$$
$$[\delta(\Delta\boldsymbol{k}+\boldsymbol{q}-\boldsymbol{G}_{hk})+\delta(\Delta\boldsymbol{k}-\boldsymbol{q}-\boldsymbol{G}_{hk})], \tag{A.13}$$

where $n_{\boldsymbol{q},m}$ is the mode the mode-specific population due to the Bose-Einstein distribution, δ the dirac delta function and $F_m(\Delta\boldsymbol{k})$ the single-phonon structure factor

$$|F_m(\Delta\boldsymbol{k})|^2 = \sum_i \frac{f_i}{\sqrt{m_{\mathrm{a},i}}}\exp(-M_i)(\Delta\boldsymbol{k}\cdot\hat{e}_{m,i,\Delta\boldsymbol{k}}), \tag{A.14}$$

with the atomic mass $m_{\mathrm{a},i}$, the single-phonon DWF $\exp(-M_i)$ and the phonon polarisation denoted by $\hat{e}_{m,i,\Delta\boldsymbol{k}}$. According to Eq. A.13, TDS arises from correlated atomic motion or phonons, respectively [186]. Since the intensity of TDS directly depends on $\omega(\boldsymbol{q})$, Eq. A.13 can be used to reconstruct the phonon dispersion relation. In the diffraction pattern, for each phonon, TDS produces satellite peaks around Bragg spots at positions $\boldsymbol{G}\pm\boldsymbol{q}$ with intensities depending on (1) the relative orientation of the scattering vector $\Delta\boldsymbol{k}$ and direction of the lattice vibration $\hat{e}_{m,i,\Delta\boldsymbol{k}}$, as well as (2) the phonon amplitude related to $(n_{\boldsymbol{q},m}+1/2)$. For large crystals the TDS signal is a continuous function of $\Delta\boldsymbol{k}$ since all occupied structural modes with wave vectors $\boldsymbol{q}$ contribute to the signal[3]. As a alternative to neutron scattering, TDS has been employed to investigate phonon band structures [326]. Lately, ultrafast measurements of the thermal diffuse background in XRD [327] and high-energy electron diffraction [301, 328, 329] allowed to follow energy relaxation due to electron-phonon and phonon-phonon coupling by extracting the time-dependent populations of individual phonon modes. Furthermore, a recent work from our group [55, 112] demonstrates that an analysis of the thermal diffuse background in ULEED provides access to the occupation of zone center acoustic modes on a few-picosecond timescale, while maintaining high surface sensitivity.

[3] In many cases, i.e. for a subset of phonons fulfilling both condition (1) and (2) particularly well, the thermal diffuse background features pronounced streaks between Bragg spots.

Appendix B

Additional information

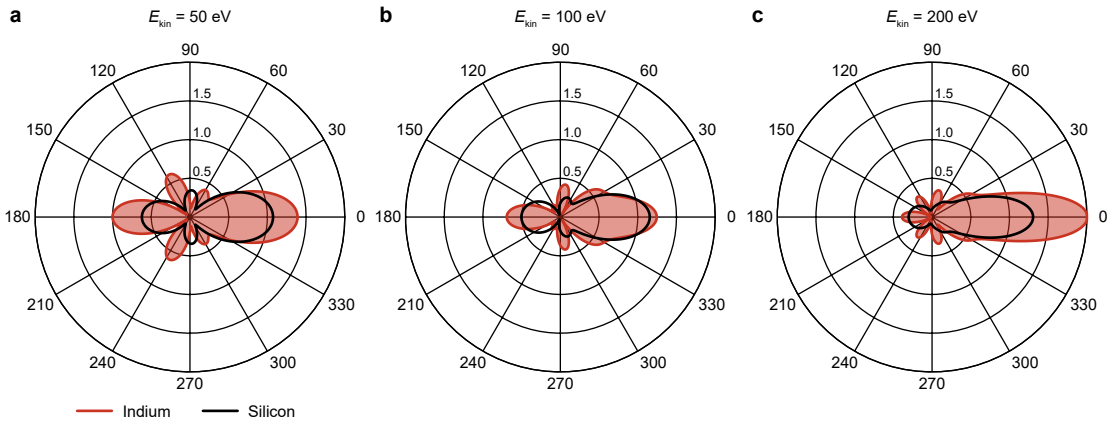

Figure B.1: Scattering amplitudes of indium and silicon as a function of the scattering angle for electron kinetic energies of 50 eV (**a**), 100 eV (**b**) and 200 eV (**c**). Note that the scattering amplitudes have been calculated for bulk structures (indium: tetragonal phase). For low electron energies ($E_{\mathrm{kin}} \sim 100$ eV) the LEED signal is dominated by back-scattering ($\varphi = 180°$) from the heavier indium atoms. The underlying calculations have been carried out by Tilman Kisslinger (University of Erlangen-Nürnberg).

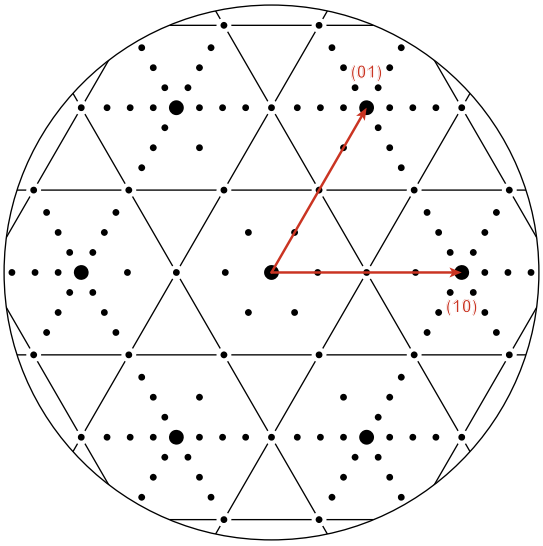

Figure B.2: Scheme of the (8×2) diffraction pattern used as a reference for spot indexing in the main text.

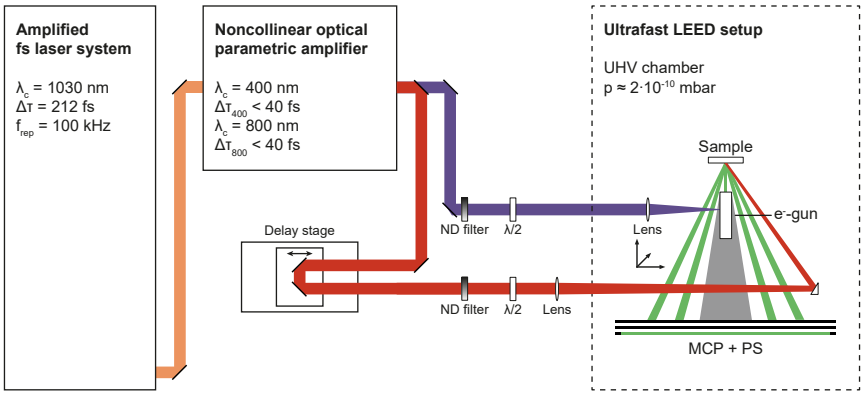

Figure B.3: Optical setup for microgun experiments. An Yb:YAG laser amplifier systsm (Light conversion "Pharos", central wavelength $\lambda_c = 1030$ nm, $\hbar\omega = 1.20$ eV, pulse duration $\Delta\tau = 212$ fs, output power $P_{\text{out}} = 15$ W, repetition rate $f_{\text{rep}} = 100$ kHz, pulse energy $E_p = 150\,\mu J$) pumps a non-collinear optical parametric amplifier (NOPA, Light conversion "Orpheus-N-2H"), generating fs light pulses at central wavelengths of $\lambda_c = 800$ nm ("signal"; $\hbar\omega = 1.55$ eV) $\lambda_c = 400$ nm ("second harmonic"). The second harmonic beam is attenuated and focused onto a tungsten needle emitter inside the micrometer-sized electron gun to generate photoelectron pulses by means of two-photon photoemission. The signal beam, on the other hand, passes an optical delay stage and pumps the sample at an adjustable time delay with respect to the electron pulses probing the state of the surface. ND, neutral density; $\lambda/2$, half-wave plate; MCP, micro-channel plate; PS, phosphor screen; 1030 nm beam, orange; 800 nm beam, red; 400 nm beam, violet.

Bibliography

[1] Cavalleri, A., Tóth, C., Siders, C. W., Squier, J. A., Ráksi, F., Forget, P., and Kieffer, J. C. Femtosecond structural dynamics in VO_2 during an ultrafast solid-solid phase transition. *Physical Review Letters*, 87(23):237401, 2001. Cited on p. 1, 30, 87

[2] Morrison, V. R., Chatelain, R. P., Tiwari, K. L., Hendaoui, A., Bruhács, A., Chaker, M., and Siwick, B. J. A photoinduced metal-like phase of monoclinic VO_2 revealed by ultrafast electron diffraction. *Science*, 346(6208):445–448, 2014. Cited on p. 1, 87

[3] Fausti, D., Tobey, R. I., Dean, N., Kaiser, S., Dienst, A., Hoffmann, M. C., Pyon, S., Takayama, T., Takagi, H., and Cavalleri, A. Light-induced superconductivity in a stripe-ordered cuprate. *Science*, 331(6014):189–191, 2011. Cited on p. 1, 30, 42, 43, 62, 186

[4] Mitrano, M., Cantaluppi, A., Nicoletti, D., Kaiser, S., Perucchi, A., Lupi, S., Di Pietro, P., Pontiroli, D., Riccò, M., Clark, S. R., Jaksch, D., and Cavalleri, A. Possible light-induced superconductivity in K_3C_{60} at high temperature. *Nature*, 530(7591):461–464, 2016. Cited on p. 170

[5] Budden, M., Gebert, T., Buzzi, M., Jotzu, G., Wang, E., Matsuyama, T., Meier, G., Laplace, Y., Pontiroli, D., Riccò, M., Schlawin, F., Jaksch, D., and Cavalleri, A. Evidence for metastable photo-induced superconductivity in K_3C_{60}. *Nature Physics*, pages 1–8, 2021. Cited on p. 1, 43

[6] Hellmann, S., Rohwer, T., Kalläne, M., Hanff, K., Sohrt, C., Stange, A., Carr, A., Murnane, M. M., Kapteyn, H. C., Kipp, L., Bauer, M., and Rossnagel, K. Time-domain classification of charge-density-wave insulators. *Nature Communications*, 3(1):1069, 2012. Cited on p. 1, 82, 87

[7] Eichberger, M., Schäfer, H., Krumova, M., Beyer, M., Demsar, J., Berger, H., Moriena, G., Sciaini, G., and Miller, R. J. D. Snapshots of cooperative atomic motions in the optical suppression of charge density waves. *Nature*, 468(7325): 799–802, 2010. Cited on p. 3, 20, 26, 30

[8] Haupt, K., Eichberger, M., Erasmus, N., Rohwer, A., Demsar, J., Rossnagel, K., and Schwoerer, H. Ultrafast metamorphosis of a complex charge-density wave. *Physical Review Letters*, 116(1):016402, 2016. Cited on p. 20, 82, 84, 87

[9] Wall, S., Krenzer, B., Wippermann, S., Sanna, S., Klasing, F., Hanisch-Blicharski, A., Kammler, M., Schmidt, W. G., and Horn-von Hoegen, M. Atomistic picture of charge density wave formation at surfaces. *Physical Review Letters*, 109(18):186101, 2012. Cited on p. 2, 3, 21, 29, 44, 60, 77, 79, 90, 104, 113, 115, 123, 133, 145, 149, 178

[10] Frigge, T., Hafke, B., Witte, T., Krenzer, B., Streubühr, C., Samad Syed, A., Mikšić Trontl, V., Avigo, I., Zhou, P., Ligges, M., von der Linde, D., Bovensiepen, U., Horn-von Hoegen, M., Wippermann, S., Lücke, A., Sanna, S., Gerstmann, U., and Schmidt, W. G. Optically excited structural transition in atomic wires on surfaces at the quantum limit. *Nature*, 544(7649):207–211, 2017. Cited on p. 10, 26, 39, 41, 60, 74, 75, 77, 79, 94, 97, 104, 110, 116, 117, 118, 119, 123, 124, 127, 129, 130, 132, 133, 141, 142, 144, 145, 147, 149, 151, 152, 155, 158, 161, 165, 166, 167, 173, 191

[11] Nicholson, C. W., Lücke, A., Schmidt, W. G., Puppin, M., Rettig, L., Ernstorfer, R., and Wolf, M. Beyond the molecular movie: Dynamics of bands and bonds during a photoinduced phase transition. *Science*, 362(6416):821–825, 2018. Cited on p. 38, 94, 97, 98, 110, 117, 118, 119, 123, 124, 127, 141, 152, 158, 165, 167, 176

[12] Chávez-Cervantes, M., Krause, R., Aeschlimann, S., and Gierz, I. Band structure dynamics in indium wires. *Physical Review B*, 97(20):201401, 2018. Cited on p. 1, 3, 97, 119, 123, 141, 143, 150, 152

[13] Bovensiepen, U. and Kirchmann, P. S. Elementary relaxation processes investigated by femtosecond photoelectron spectroscopy of two-dimensional materials. *Laser & Photonics Reviews*, 6(5):589–606, 2012. Cited on p. 1, 30

[14] Puppin, M., Deng, Y., Nicholson, C. W., Feldl, J., Schröter, N. B. M., Vita, H., Kirchmann, P. S., Monney, C., Rettig, L., Wolf, M., and Ernstorfer, R. Time- and angle-resolved photoemission spectroscopy of solids in the extreme ultraviolet at 500 kHz repetition rate. *Review of Scientific Instruments*, 90(2): 023104, 2019. Cited on p.

[15] Keunecke, M., Möller, C., Schmitt, D., Nolte, H., Jansen, G. S. M., Reutzel, M., Gutberlet, M., Halasi, G., Steil, D., Steil, S., and Mathias, S. Time-resolved momentum microscopy with a 1 MHz high-harmonic extreme ultraviolet beamline. *Review of Scientific Instruments*, 91(6):063905, 2020. Cited on p. 1

[16] Hanisch-Blicharski, A., Janzen, A., Krenzer, B., Wall, S., Klasing, F., Kalus, A., Frigge, T., Kammler, M., and Horn-von Hoegen, M. Ultra-fast electron diffraction at surfaces: From nanoscale heat transport to driven phase transitions. *Ultramicroscopy*, 127:2–8, 2013. Cited on p. 1, 75, 79

[17] Gulde, M., Schweda, S., Storeck, G., Maiti, M., Yu, H. K., Wodtke, A. M., Schäfer, S., and Ropers, C. Ultrafast low-energy electron diffraction in transmission resolves polymer/graphene superstructure dynamics. *Science*, 345 (6193):200–204, 2014. Cited on p. 3, 44, 45, 60, 69, 70, 75, 78, 180, 183

[18] Vogelgesang, S., Storeck, G., Horstmann, J. G., Diekmann, T., Sivis, M., Schramm, S., Rossnagel, K., Schäfer, S., and Ropers, C. Phase ordering of charge density waves traced by ultrafast low-energy electron diffraction. *Nature Physics*, 14(2):184–190, 2018. Cited on p. 3, 20, 24, 44, 45, 60, 69, 70, 75, 78, 82, 83, 84, 87, 127, 137, 180

[19] Janzen, A., Krenzer, B., Heinz, O., Zhou, P., Thien, D., Hanisch, A., Meyer zu Heringdorf, F.-J., von der Linde, D., and Horn von Hoegen, M. A pulsed electron gun for ultrafast electron diffraction at surfaces. *Review of Scientific Instruments*, 78(1):013906, 2007. Cited on p. 75

[20] Siwick, B. J., Dwyer, J. R., Jordan, R. E., and Miller, R. J. D. An Atomic-Level View of Melting Using Femtosecond Electron Diffraction. *Science*, 302 (5649):1382–1385, 2003. Cited on p. 75, 79

[21] Chatelain, R. P., Morrison, V. R., Godbout, C., and Siwick, B. J. Ultrafast electron diffraction with radio-frequency compressed electron pulses. *Applied Physics Letters*, 101(8):081901, 2012. Cited on p. 79

[22] Zewail, A. *4D Electron Microscopy: Imaging in Space and Time*. Imperial College Press, London, 2010. Cited on p. 2, 30, 44, 75

[23] Feist, A., Bach, N., Rubiano da Silva, N., Danz, T., Möller, M., Priebe, K. E., Domröse, T., Gatzmann, J. G., Rost, S., Schauss, J., Strauch, S., Bormann, R., Sivis, M., Schäfer, S., and Ropers, C. Ultrafast transmission electron microscopy using a laser-driven field emitter: Femtosecond resolution with a high coherence electron beam. *Ultramicroscopy*, 176:63–73, 2017. Cited on p. 1, 79

[24] Beaurepaire, E., Merle, J.-C., Daunois, A., and Bigot, J.-Y. Ultrafast Spin Dynamics in Ferromagnetic Nickel. *Physical Review Letters*, 76(22):4250–4253, 1996. Cited on p. 1

[25] Möller, C., Probst, H., Otto, J., Stroh, K., Mahn, C., Steil, S., Moshnyaga, V., Jansen, G. S. M., Steil, D., and Mathias, S. Ultrafast element-resolved magneto-optics using a fiber-laser-driven extreme ultraviolet light source. *arXiv:2103.12367*, 2021. Cited on p. 1

[26] Stanev, V., Oses, C., Kusne, A. G., Rodriguez, E., Paglione, J., Curtarolo, S., and Takeuchi, I. Machine learning modeling of superconducting critical temperature. *npj Computational Materials*, 4(1):1–14, 2018. Cited on p. 1

[27] Nørskov, J. K., Bligaard, T., Rossmeisl, J., and Christensen, C. H. Towards the computational design of solid catalysts. *Nature Chemistry*, 1(1):37–46, 2009. Cited on p. 1

[28] Cao, Y., Fatemi, V., Fang, S., Watanabe, K., Taniguchi, T., Kaxiras, E., and Jarillo-Herrero, P. Unconventional superconductivity in magic-angle graphene superlattices. *Nature*, 556(7699):43–50, 2018. Cited on p. 1, 183

[29] Geim, A. K. and Grigorieva, I. V. Van der Waals heterostructures. *Nature*, 499(7459):419–425, 2013. Cited on p. 2, 183

[30] Jin, C., Ma, E. Y., Karni, O., Regan, E. C., Wang, F., and Heinz, T. F. Ultrafast dynamics in van der Waals heterostructures. *Nature Nanotechnology*, 13(11):994–1003, 2018. Cited on p. 2, 183

[31] Ruf, J. P., Paik, H., Schreiber, N. J., Nair, H. P., Miao, L., Kawasaki, J. K., Nelson, J. N., Faeth, B. D., Lee, Y., Goodge, B. H., Pamuk, B., Fennie, C. J., Kourkoutis, L. F., Schlom, D. G., and Shen, K. M. Strain-stabilized superconductivity. *Nature Communications*, 12(1):59, 2021. Cited on p. 2

[32] Wang, Y. H., Steinberg, H., Jarillo-Herrero, P., and Gedik, N. Observation of Floquet-Bloch states on the surface of a topological insulator. *Science*, 342 (6157):453–457, 2013. Cited on p. 2, 30

[33] Stekolnikov, A. A., Seino, K., Bechstedt, F., Wippermann, S., Schmidt, W. G., Calzolari, A., and Nardelli, M. B. Hexagon versus Trimer Formation in In Nanowires on Si(111): Energetics and Quantum Conductance. *Physical Review Letters*, 98(2):026105, 2007. Cited on p. 2, 104

[34] Kimel, A. V., Kirilyuk, A., Usachev, P. A., Pisarev, R. V., Balbashov, A. M., and Rasing, T. Ultrafast non-thermal control of magnetization by instantaneous photomagnetic pulses. *Nature*, 435(7042):655–657, 2005. Cited on p. 2

[35] Schlauderer, S., Lange, C., Baierl, S., Ebnet, T., Schmid, C. P., Valovcin, D. C., Zvezdin, A. K., Kimel, A. V., Mikhaylovskiy, R. V., and Huber, R. Temporal and spectral fingerprints of ultrafast all-coherent spin switching. *Nature*, 569(7756):383, 2019. Cited on p. 2

[36] Stojchevska, L., Vaskivskyi, I., Mertelj, T., Kusar, P., Svetin, D., Brazovskii, S., and Mihailovic, D. Ultrafast switching to a stable hidden quantum state in an electronic crystal. *Science*, 344(6180):177–180, 2014. Cited on p. 2, 29, 30, 186

[37] Sie, E. J., Nyby, C. M., Pemmaraju, C. D., Park, S. J., Shen, X., Yang, J., Hoffmann, M. C., Ofori-Okai, B. K., Li, R., Reid, A. H., Weathersby, S., Mannebach, E., Finney, N., Rhodes, D., Chenet, D., Antony, A., Balicas, L., Hone, J., Devereaux, T. P., Heinz, T. F., Wang, X., and Lindenberg, A. M. An

ultrafast symmetry switch in a Weyl semimetal. *Nature*, 565(7737):61, 2019. Cited on p. 2, 29, 30, 77

[38] Zewail, A. H. Femtochemistry: Atomic-scale dynamics of the chemical bond using ultrafast lasers (Nobel lecture). *Angewandte Chemie International Edition*, 39(15):2586–2631, 2000. Cited on p. 2, 29, 39, 42, 93, 143

[39] Potter, E. D., Herek, J. L., Pedersen, S., Liu, Q., and Zewail, A. H. Femtosecond laser control of a chemical reaction. *Nature*, 355(6355):66, 1992. Cited on p. 2, 3, 43, 93, 143

[40] Dantus, M. and Lozovoy, V. V. Experimental Coherent Laser Control of Physicochemical Processes. *Chemical Reviews*, 104(4):1813–1860, 2004. Cited on p. 2, 42

[41] Nuernberger, P., Vogt, G., Brixner, T., and Gerber, G. Femtosecond quantum control of molecular dynamics in the condensed phase. *Physical Chemistry Chemical Physics*, 9(20):2470–2497, 2007. Cited on p. 2, 29, 42, 93, 143

[42] Zeiger, H. J., Vidal, J., Cheng, T. K., Ippen, E. P., Dresselhaus, G., and Dresselhaus, M. S. Theory for displacive excitation of coherent phonons. *Physical Review B*, 45(2):768–778, 1992. Cited on p. 2, 39, 41, 157

[43] Polanyi, J. C. and Wong, W. H. Location of energy barriers. I. Effect on the dynamics of reactions A + BC. *The Journal of Chemical Physics*, 51(4): 1439–1450, 1969. Cited on p. 2, 32, 33, 34, 35, 167

[44] Polanyi, J. C. Concepts in reaction dynamics. *Accounts of Chemical Research*, 5(5):161–168, 1972. Cited on p. 34

[45] Polanyi, J. C. and Zewail, A. H. Direct observation of the transition state. *Accounts of Chemical Research*, 28(3):119–132, 1995. Cited on p. 2, 33

[46] Shapiro, M. and Brumer, P. Coherent Control of Atomic, Molecular, and Electronic Processes. In Bederson, B. and Walther, H., editors, *Advances In Atomic, Molecular, and Optical Physics*, pages 287–345. Academic Press, 2000. Cited on p. 2, 29, 42, 43

[47] Tannor, D. J., Kosloff, R., and Rice, S. A. Coherent pulse sequence induced control of selectivity of reactions: Exact quantum mechanical calculations. *The Journal of Chemical Physics*, 85(10):5805–5820, 1986. Cited on p. 2, 42

[48] Tannor, D. J. and Rice, S. A. Control of selectivity of chemical reaction via control of wave packet evolution. *The Journal of Chemical Physics*, 83(10): 5013–5018, 1985. Cited on p. 2, 42

[49] Nibbering, E. T., Fidder, H., and Pines, E. Ultrafast Chemistry: Using time-resolved vibrational spectroscopy for interrogation of structural dynamics. *Annual Review of Physical Chemistry*, 56(1):337–367, 2005. Cited on p. 3

[50] Wall, S., Wegkamp, D., Foglia, L., Appavoo, K., Nag, J., Haglund Jr, R. F., Stähler, J., and Wolf, M. Ultrafast changes in lattice symmetry probed by coherent phonons. *Nature Communications*, 3:721, 2012. Cited on p. 3, 87, 157

[51] Neugebauer, M. J., Huber, T., Savoini, M., Abreu, E., Esposito, V., Kubli, M., Rettig, L., Bothschafter, E., Grübel, S., Kubacka, T., Rittmann, J., Ingold, G., Beaud, P., Dominko, D., Demsar, J., and Johnson, S. L. Optical control of vibrational coherence triggered by an ultrafast phase transition. *Physical Review B*, 99(22):220302, 2019. Cited on p. 26, 43

[52] Rettig, L., Chu, J.-H., Fisher, I. R., Bovensiepen, U., and Wolf, M. Coherent dynamics of the charge density wave gap in tritellurides. *Faraday Discussions*, 171(0):299–310, 2014. Cited on p. 3, 26, 43

[53] Horstmann, J. G., Böckmann, H., Wit, B., Kurtz, F., Storeck, G., and Ropers, C. Coherent control of a surface structural phase transition. *Nature*, 583(7815): 232–236, 2020. Cited on p. 3, 75, 82, 127, 129, 142, 144, 148, 151, 152, 154, 158, 160, 166, 178, 180

[54] Storeck, G., Vogelgesang, S., Sivis, M., Schäfer, S., and Ropers, C. Nanotip-based photoelectron microgun for ultrafast LEED. *Structural Dynamics*, 4(4): 044024, 2017. Cited on p. 69, 70, 80, 81, 82

[55] Storeck, G., Horstmann, J. G., Diekmann, T., Vogelgesang, S., von Witte, G., Yalunin, S. V., Rossnagel, K., and Ropers, C. Structural dynamics of

incommensurate charge-density waves tracked by ultrafast low-energy electron diffraction. *Structural Dynamics*, 7(3):034304, 2020. Cited on p. 3, 29, 53, 60, 69, 75, 78, 82, 87, 133, 137, 180, 193

[56] Frigge, T., Hafke, B., Witte, T., Krenzer, B., and Horn-von Hoegen, M. Non-equilibrium lattice dynamics of one-dimensional In chains on Si(111) upon ultrafast optical excitation. *Structural Dynamics*, 5(2):025101, 2018. Cited on p. 3, 74, 75, 97, 117, 123, 126, 133, 141, 151, 152

[57] Nicholson, C. W., Puppin, M., Lücke, A., Gerstmann, U., Krenz, M., Schmidt, W. G., Rettig, L., Ernstorfer, R., and Wolf, M. Excited-state band mapping and momentum-resolved ultrafast population dynamics in In/Si(111) nanowires investigated with XUV-based time- and angle-resolved photoemission spectroscopy. *Physical Review B*, 99(15):155107, 2019. Cited on p. 94, 97, 100, 110, 119, 123, 131, 141, 142, 143, 149, 150, 152, 165, 174

[58] Chávez-Cervantes, M., Topp, G. E., Aeschlimann, S., Krause, R., Sato, S. A., Sentef, M. A., and Gierz, I. Charge Density Wave Melting in One-Dimensional Wires with Femtosecond Subgap Excitation. *Physical Review Letters*, 123(3): 036405, 2019. Cited on p. 3, 37, 97, 119, 123, 141, 164, 176

[59] Hase, M., Kitajima, M., Nakashima, S.-i., and Mizoguchi, K. Forcibly driven coherent soft phonons in GeTe with intense THz-rate pump fields. *Applied Physics Letters*, 83(24):4921–4923, 2003. Cited on p. 3, 72, 73

[60] Weiner, A. M., Leaird, D. E., Wiederrecht, G. P., and Nelson, K. A. Femtosecond multiple-pulse impulsive stimulated Raman scattering spectroscopy. *JOSA B*, 8(6):1264–1275, 1991. Cited on p.

[61] Feurer, T., Vaughan, J. C., and Nelson, K. A. Spatiotemporal coherent control of lattice vibrational waves. *Science*, 299(5605):374–377, 2003. Cited on p. 3, 43

[62] Feynman, R., Leighton, R., and Sands, M. *The Feynman Lectures on Physics*. Addison-Wesley Pub. Co., Reading, Mass, 1963. Cited on p. 7

[63] Peierls, R. E. *Quantum Theory of Solids*. Clarendon Press, Oxford, 1955. Cited on p. 7, 10

[64] Gross, R. and Marx, A. *Festkörperphysik*. Walter de Gruyter GmbH, Berlin/ Boston, 2014. Cited on p. 7, 39, 49, 50, 52

[65] Anderson, P. W. More Is Different. *Science*, 177(4047):393–396, 1972. Cited on p. 8

[66] Nicholson, C. W. *Electronic Structure and Dynamics of Quasi-One Dimensional Materials*. PhD thesis, Freie Universität Berlin, 2018. Cited on p. 8, 12, 28, 31, 94, 99, 119, 121, 123, 125, 127, 128, 131, 142, 143, 155

[67] Bardeen, J., Cooper, L. N., and Schrieffer, J. R. Theory of Superconductivity. *Physical Review*, 108(5):1175–1204, 1957. Cited on p. 8

[68] Onnes, H. The Resistance of Pure Mercury at Helium Temperatures. *Commun. Phys. Lab. Univ. Leiden*, (12), 1911. Cited on p. 8

[69] Grüner, G. The dynamics of charge-density waves. *Reviews of Modern Physics*, 60(4):1129–1181, 1988. Cited on p. 8, 10, 11, 15

[70] Grüner, G. *Density Waves In Solids*. CRC Press, Boca Raton, 1994. Cited on p. 8, 9, 10, 11, 12, 13, 14, 15, 16, 17, 18, 21, 22, 23, 25, 26, 27, 28, 29, 94, 154

[71] Grüner, G. The dynamics of spin-density waves. *Reviews of Modern Physics*, 66(1):1–24, 1994. Cited on p. 8, 9

[72] The rise of quantum materials. *Nature Physics*, 12(2):105–105, 2016. Cited on p. 8, 9

[73] Landau, L. Oscillations in a Fermi Liquid. *Journal of Experimental and Theoretical Physics*, 5(1):101, 1957. Cited on p. 9

[74] Landau, L. The Theory of a Fermi Liquid. *Journal of Experimental and Theoretical Physics*, 3(6):920, 1957. Cited on p.

[75] Landau, L. On the Theory of the Fermi Liquid. *Journal of Experimental and Theoretical Physics*, 35(8):70, 1959. Cited on p. 9

[76] Deshpande, V. V., Bockrath, M., Glazman, L. I., and Yacoby, A. Electron liquids and solids in one dimension. *Nature*, 464(7286):209–216, 2010. Cited on p. 9

[77] Giamarchi, T. *Quantum Physics in One Dimension*. Clarendon Press, Oxford, 2004. Cited on p. 9, 12

[78] Auslaender, O. M., Steinberg, H., Yacoby, A., Tserkovnyak, Y., Halperin, B. I., Baldwin, K. W., Pfeiffer, L. N., and West, K. W. Spin-Charge Separation and Localization in One Dimension. *Science*, 308(5718):88–92, 2005. Cited on p. 9

[79] Haldane, F. D. M. 'Luttinger liquid theory' of one-dimensional quantum fluids. I. Properties of the Luttinger model and their extension to the general 1D interacting spinless Fermi gas. *Journal of Physics C: Solid State Physics*, 14 (19):2585–2609, 1981. Cited on p. 9

[80] Blumenstein, C., Schäfer, J., Mietke, S., Meyer, S., Dollinger, A., Lochner, M., Cui, X. Y., Patthey, L., Matzdorf, R., and Claessen, R. Atomically controlled quantum chains hosting a Tomonaga–Luttinger liquid. *Nature Physics*, 7(10): 776–780, 2011. Cited on p. 94

[81] Watson, M. D., Feng, Y., Nicholson, C. W., Monney, C., Riley, J. M., Iwasawa, H., Refson, K., Sacksteder, V., Adroja, D. T., Zhao, J., and Hoesch, M. Multiband One-Dimensional Electronic Structure and Spectroscopic Signature of Tomonaga-Luttinger Liquid Behavior in $K_2Cr_3As_3$. *Physical Review Letters*, 118(9):097002, 2017. Cited on p. 9, 94

[82] Bednorz, J. G. and Müller, K. A. Possible high T_c superconductivity in the Ba-La-Cu-O system. *Zeitschrift für Physik B Condensed Matter*, 64(2):189–193, 1986. Cited on p. 9

[83] Damascelli, A., Hussain, Z., and Shen, Z.-X. Angle-resolved photoemission studies of the cuprate superconductors. *Reviews of Modern Physics*, 75(2): 473–541, 2003. Cited on p.

[84] Paglione, J. and Greene, R. L. High-temperature superconductivity in iron-based materials. *Nature Physics*, 6(9):645–658, 2010. Cited on p.

[85] Lee, P. A., Nagaosa, N., and Wen, X.-G. Doping a Mott insulator: Physics of high-temperature superconductivity. *Reviews of Modern Physics*, 78(1):17–85, 2006. Cited on p. 9

[86] Fawcett, E. Spin-density-wave antiferromagnetism in chromium. *Reviews of Modern Physics*, 60(1):209–283, 1988. Cited on p. 9, 94

[87] Chen, C.-W., Choe, J., and Morosan, E. Charge density waves in strongly correlated electron systems. *Reports on Progress in Physics*, 79(8):084505, 2016. Cited on p. 9, 19

[88] Mott, N. *Metal-Insulator Transitions*. Taylor & Trancis Ltd., London New York Philadelphia, 1990. Cited on p. 9, 10

[89] Stormer, H. L., Tsui, D. C., and Gossard, A. C. The fractional quantum Hall effect. *Reviews of Modern Physics*, 71(2):S298–S305, 1999. Cited on p. 9

[90] Fröhlich, H. On the theory of superconductivity: The one-dimensional case. *Proceedings of the Royal Society of London. Series A. Mathematical and Physical Sciences*, 223(1154):296–305, 1954. Cited on p. 10

[91] Jérome, D. Organic Conductors: From Charge Density Wave TTF-TCNQ to Superconducting (TMTSF)2PF6. *Chemical Reviews*, 104(11):5565–5592, 2004. Cited on p. 10, 14

[92] Little, W. A. Possibility of Synthesizing an Organic Superconductor. *Physical Review*, 134(6A):A1416–A1424, 1964. Cited on p. 10

[93] Overhauser, A. *Anomalous Effects in Simple Metals*. Wiley VCH Verlag GmbH & Co. KGaA, Weinheim, 2010. Cited on p. 10

[94] Rossnagel, K. On the origin of charge-density waves in select layered transition-metal dichalcogenides. *Journal of Physics: Condensed Matter*, 23 (21):213001, 2011. Cited on p. 10, 19, 20, 82, 87

[95] Wilson, J. A., Di Salvo, F. J., and Mahajan, S. Charge-Density Waves in Metallic, Layered, Transition-Metal Dichalcogenides. *Physical Review Letters*, 32(16):882–885, 1974. Cited on p. 10

[96] Ravy, S., Requardt, H., Le Bolloc'h, D., Foury-Leylekian, P., Pouget, J.-P., Currat, R., Monceau, P., and Krisch, M. Inelastic x-ray scattering study of charge-density-wave dynamics in the $Rb_{0.3}MoO_3$ blue bronze. *Physical Review B*, 69(11):115113, 2004. Cited on p. 10, 14

[97] Pouget, J. P., Hennion, B., Escribe-Filippini, C., and Sato, M. Neutron-scattering investigations of the Kohn anomaly and of the phase and amplitude charge-density-wave excitations of the blue bronze $K_{0.3}MoO_3$. *Physical Review B*, 43(10):8421–8430, 1991. Cited on p. 10, 14

[98] Gweon, G.-H., Denlinger, J. D., Clack, J. A., Allen, J. W., Olson, C. G., DiMasi, E., Aronson, M. C., Foran, B., and Lee, S. Direct Observation of Complete Fermi Surface, Imperfect Nesting, and Gap Anisotropy in the High-Temperature Incommensurate Charge-Density-Wave Compound $SmTe_3$. *Physical Review Letters*, 81(4):886–889, 1998. Cited on p. 10

[99] Laverock, J., Dugdale, S. B., Major, Z., Alam, M. A., Ru, N., Fisher, I. R., Santi, G., and Bruno, E. Fermi surface nesting and charge-density wave formation in rare-earth tritellurides. *Physical Review B*, 71(8):085114, 2005. Cited on p.

[100] Brouet, V., Yang, W. L., Zhou, X. J., Hussain, Z., Moore, R. G., He, R., Lu, D. H., Shen, Z. X., Laverock, J., Dugdale, S. B., Ru, N., and Fisher, I. R. Angle-resolved photoemission study of the evolution of band structure and charge density wave properties in RTe_3 (R=Y, La, Ce, Sm, Gd, Tb, and Dy). *Physical Review B*, 77(23):235104, 2008. Cited on p. 10

[101] Snijders, P. C. and Weitering, H. H. Colloquium: Electronic instabilities in self-assembled atom wires. *Reviews of Modern Physics*, 82(1):307–329, 2010. Cited on p. 10, 14, 44, 45, 56, 96, 101

[102] Yeom, H. W., Takeda, S., Rotenberg, E., Matsuda, I., Horikoshi, K., Schaefer, J., Lee, C. M., Kevan, S. D., Ohta, T., Nagao, T., and Hasegawa, S. Instability and charge density wave of metallic quantum chains on a silicon surface. *Physical Review Letters*, 82(24):4898–4901, 1999. Cited on p. 10, 14, 20, 89, 94, 96, 97, 99, 100, 101, 104, 105, 107

[103] Kuper, C. G. and Fröhlich, H. The thermal decomposition of ammonium perchlorate II. The kinetics of the decomposition, the effect of particle size, and discussion of results. *Proceedings of the Royal Society of London. Series A. Mathematical and Physical Sciences*, 227(1169):214–228, 1955. Cited on p. 11

[104] Solyom, J. *Fundamentals of the Physics of Solids, Volume 3 - Normal, Broken-Symmetry and Correlated Systems.* Springer-Verlag, Berlin Heidelberg New York, 2010. Cited on p. 12

[105] Yang, X., Xian, J.-J., Li, G., Nagaosa, N., Zhang, W.-H., Qin, L., Zhang, Z.-M., Lü, J.-T., and Fu, Y.-S. Possible Phason-Polaron Effect on Purely One-Dimensional Charge Order of Mo_6Se_6 Nanowires. *Physical Review X*, 10 (3):031061, 2020. Cited on p. 14

[106] Johannes, M. D. and Mazin, I. I. Fermi surface nesting and the origin of charge density waves in metals. *Physical Review B*, 77(16):165135, 2008. Cited on p. 14, 19

[107] Wippermann, S. and Schmidt, W. G. Entropy explains metal-insulator transition of the Si(111)-In nanowire array. *Physical Review Letters*, 105(12):126102, 2010. Cited on p. 19, 94, 97, 107, 108, 109, 110, 112, 114, 147, 162, 165

[108] Hofmann, P., Ugeda, M. M., Tamtögl, A., Ruckhofer, A., Ernst, W. E., Benedek, G., Martínez-Galera, A. J., Stróżecka, A., Gómez-Rodríguez, J. M., Rienks, E., Jensen, M. F., Pascual, J. I., and Wells, J. W. Strong-coupling charge density wave in a one-dimensional topological metal. *Physical Review B*, 99(3):035438, 2019. Cited on p. 19

[109] Zhu, X., Guo, J., Zhang, J., and Plummer, E. W. Misconceptions associated with the origin of charge density waves. *Advances in Physics: X*, 2(3):622–640, 2017. Cited on p. 19

[110] Pynn, R. Incommensurable structures. *Nature*, 281(5731):433–437, 1979. Cited on p. 20

[111] Fauster, T., Hammer, L., Heinz, K., and Schneider, M. *Oberflächenphysik. Grundlagen Und Methoden.* Oldenbourg Verlag, München, 2013. Cited on p. 20, 44, 46, 47, 48, 49, 50, 52, 53, 54, 55, 180, 190

[112] Storeck, G. *Non-Equilibrium Structural Dynamics of Incommensurate Charge-Density Waves: Diffractive Probing with a Micron-Scale Ultrafast Electron Gun.* PhD thesis, Georg-August-Universität Göttingen, 2020. Cited on p. 20, 29, 45, 53, 69, 70, 75, 79, 80, 83, 131, 193

[113] Landau, L. On the Theory of Phase Transitions. *Zh. Eksp. Teor. Fiz.*, 7: 19–32, 1937. Cited on p. 21, 23

[114] Landau, L. and Lifshitz, E. *Lehrbuch Der Theoretischen Physik V: Statistische Physik I.* Akademischer Verlag, Berlin, 1987. Cited on p. 21, 23

[115] McMillan, W. L. Landau theory of charge-density waves in transition-metal dichalcogenides. *Physical Review B*, 12(4):1187–1196, 1975. Cited on p. 21, 24, 26

[116] Frigge, T. *Ultraschnelle strukturelle Nichtgleichgewichtsdynamik des optisch angeregten Si(111)(*8×2*)->(*4×1*)-In Phasenübergangs.* PhD thesis, Universität Duisburg-Essen, 2016. Cited on p. 21, 22, 60, 74, 79, 90, 97, 104, 105, 116, 123, 125, 126, 127, 128, 133, 134, 135, 137, 138, 142, 149, 155, 161, 178

[117] Klasing, F., Frigge, T., Hafke, B., Krenzer, B., Wall, S., Hanisch-Blicharski, A., and Horn-von Hoegen, M. Hysteresis proves that the In/Si(111) (8×2) to (4×1) phase transition is first-order. *Physical Review B*, 89(12):121107, 2014. Cited on p. 22, 23, 90, 97, 104, 105, 112, 113, 126

[118] Hanggi, P. Escape from a metastable state. *Journal of Statistical Physics*, 42 (1):105–148, 1986. Cited on p. 24

[119] Ginzburg, V. and Landau, L. *Zh. Eksp. Teor. Fiz.*, 20:1064, 1950. Cited on p. 24

[120] Vogelgesang, S. *Ultrafast Low-Energy Electron Diffraction at Surfaces.* PhD thesis, Georg-August-Universität Göttingen, 2019. Cited on p. 24, 60, 69, 70, 75, 79, 80, 84, 137

[121] Lee, P. A., Rice, T. M., and Anderson, P. W. Conductivity from charge or spin density waves. *Solid State Communications*, 14(8):703–709, 1974. Cited on p. 26

[122] Neugebauer, M. J. *Ultrafast Nonlinear Excitation and Optical Control of Vibrational Coherence in Solids.* PhD thesis, ETH Zürich, 2020. Cited on p. 26

[123] Torchinsky, D. H., Mahmood, F., Bollinger, A. T., Božović, I., and Gedik, N. Fluctuating charge-density waves in a cuprate superconductor. *Nature Materials*, 12(5):387–391, 2013. Cited on p. 26

[124] Liu, H. Y., Gierz, I., Petersen, J. C., Kaiser, S., Simoncig, A., Cavalieri, A. L., Cacho, C., Turcu, I. C. E., Springate, E., Frassetto, F., Poletto, L., Dhesi, S. S., Xu, Z.-A., Cuk, T., Merlin, R., and Cavalleri, A. Possible observation of parametrically amplified coherent phasons in $K_{0.3}MoO_3$ using time-resolved extreme-ultraviolet angle-resolved photoemission spectroscopy. *Physical Review B*, 88(4):045104, 2013. Cited on p. 26

[125] Cheon, S., Kim, T.-H., Lee, S.-H., and Yeom, H. W. Chiral solitons in a coupled double Peierls chain. *Science*, 350(6257):182–185, 2015. Cited on p. 27, 97, 120, 121, 128

[126] Mermin, N. D. and Wagner, H. Absence of Ferromagnetism or Antiferromagnetism in One- or Two-Dimensional Isotropic Heisenberg Models. *Physical Review Letters*, 17(22):1133–1136, 1966. Cited on p. 27

[127] Hohenberg, P. C. Existence of Long-Range Order in One and Two Dimensions. *Physical Review*, 158(2):383–386, 1967. Cited on p.

[128] Coleman, S. There are no Goldstone bosons in two dimensions. *Communications in Mathematical Physics*, 31(4):259–264, 1973. Cited on p. 27

[129] Hafke, B., Brand, C., Witte, T., Sothmann, B., Horn-von Hoegen, M., and Erwin, S. C. Thermally Induced Crossover from 2D to 1D Behavior in an Array of Atomic Wires: Silicon Dangling-Bond Solitons in Si(553)-Au. *Physical Review Letters*, 124(1):016102, 2020. Cited on p. 28, 94, 96

[130] Nicholson, C. W., Berthod, C., Puppin, M., Berger, H., Wolf, M., Hoesch, M., and Monney, C. Dimensional Crossover in a Charge Density Wave Material Probed by Angle-Resolved Photoemission Spectroscopy. *Physical Review Letters*, 118(20):206401, 2017. Cited on p. 28

[131] Nova, T. F. *Nonequilibrium control of broken-symmetry phases in quantum materials*. PhD thesis, Universität Hamburg, 2020. Cited on p. 29, 30, 42, 43, 62

[132] De Schryver, C., De Feyter, S., and Schweitzer, G. *Femtochemistry*. Wiley VCH Verlag GmbH & Co. KGaA, Weinheim, 2001. Cited on p. 29, 42

[133] Warren, W. S., Rabitz, H., and Dahleh, M. Coherent Control of Quantum Dynamics: The Dream Is Alive. *Science*, 259(5101):1581–1589, 1993. Cited on p. 29, 42, 43

[134] Weiner, A. *Ultrafast Optics*. John Wiley & Sons, Inc., Hobocken, NJ, 2008. Cited on p. 30, 44

[135] Schultz, T. and Vrakking, M. *Attosecond and XUV Physics: Ultrafast Dynamics and Spectroscopy*. Wiley VCH Verlag GmbH & Co. KGaA, Weinheim, 2014. Cited on p. 30

[136] Schmitt, F., Kirchmann, P. S., Bovensiepen, U., Moore, R. G., Rettig, L., Krenz, M., Chu, J.-H., Ru, N., Perfetti, L., Lu, D. H., Wolf, M., Fisher, I. R., and Shen, Z.-X. Transient Electronic Structure and Melting of a Charge Density Wave in $TbTe_3$. *Science*, 321(5896):1649–1652, 2008. Cited on p. 30

[137] De Silvestri, S., Cerullo, G., and Lanzani, G. *Coherent Vibrational Dynamics*. CRC Press, Boca Raton, 2008. Cited on p. 42

[138] Gerber, S., Yang, S.-L., Zhu, D., Soifer, H., Sobota, J. A., Rebec, S., Lee, J. J., Jia, T., Moritz, B., Jia, C., Gauthier, A., Li, Y., Leuenberger, D., Zhang, Y., Chaix, L., Li, W., Jang, H., Lee, J.-S., Yi, M., Dakovski, G. L., Song, S., Glownia, J. M., Nelson, S., Kim, K. W., Chuang, Y.-D., Hussain, Z., Moore, R. G., Devereaux, T. P., Lee, W.-S., Kirchmann, P. S., and Shen, Z.-X. Femtosecond electron-phonon lock-in by photoemission and x-ray free-electron laser. *Science*, 357(6346):71–75, 2017. Cited on p.

[139] Rini, M., Tobey, R., Dean, N., Itatani, J., Tomioka, Y., Tokura, Y., Schoenlein, R. W., and Cavalleri, A. Control of the electronic phase of a manganite by mode-selective vibrational excitation. *Nature*, 449(7158):72–74, 2007. Cited on p. 42, 43, 170, 186

[140] Sokolowski-Tinten, K., Blome, C., Blums, J., Cavalleri, A., Dietrich, C., Tarasevitch, A., Uschmann, I., Förster, E., Kammler, M., Horn-von-Hoegen, M.,

and von der Linde, D. Femtosecond X-ray measurement of coherent lattice vibrations near the Lindemann stability limit. *Nature*, 422(6929):287–289, 2003. Cited on p. 30, 41, 59, 176

[141] Laughlin, R. B. and Pines, D. The Theory of Everything. *Proceedings of the National Academy of Sciences*, 97(1):28–31, 2000. Cited on p. 31

[142] Born, M. and Oppenheimer, R. Zur Quantentheorie der Molekeln. *Annalen der Physik*, 389(20):457–484, 1927. Cited on p. 31

[143] Lewars, E. *Computational Chemistry*. Springer Science+Business Media, Basel, 2016. Cited on p. 31, 32, 33, 34

[144] Marcelin, R. Potential energy surface. *Annales de Physique*, 3(152), 1915. Cited on p. 31

[145] Mok, M. H. and Polanyi, J. C. Location of Energy Barriers. II. Correlation with Barrier Height. *The Journal of Chemical Physics*, 51(4):1451–1469, 1969. Cited on p. 32, 33, 34

[146] Polanyi, J. C. Some Concepts in Reaction Dynamics (Nobel Lecture). *Angewandte Chemie International Edition in English*, 26(10):952–971, 1987. Cited on p. 32, 33, 34

[147] Chung, H. S., Piana-Agostinetti, S., Shaw, D. E., and Eaton, W. A. Structural origin of slow diffusion in protein folding. *Science*, 349(6255):1504–1510, 2015. Cited on p. 32

[148] Eyring, H. The Activated Complex in Chemical Reactions. *The Journal of Chemical Physics*, 3(2):107–115, 1935. Cited on p. 33

[149] Eyring, H. and Polanyi, M. *Zeitschrift für Physikalische Chemie*, 12(1):279, 1931. Cited on p. 33

[150] Huber, A. *Ultrafast Probing of Coherent Structural Dynamics in Solids*. PhD thesis, ETH Zürich, 2015. Cited on p. 36, 39

[151] Cardona, M. and Güntherodt, G. *Light Scattering in Solids II: Basic Concepts and Instrumentation*. Springer, Berlin, 1982. Cited on p. 36

[152] Schrader, B. *Infrared and Raman Spectroscopy: Methods and Applications*. Wiley VCH Verlag GmbH & Co. KGaA, Weinheim, 1995. Cited on p. 36

[153] Chávez-Cervantes, M. *Photo-Carrier Dynamics and Photo-Induced Melting of Charge Density Waves In Indium Wires*. PhD thesis, Universität Hamburg, 2020. Cited on p. 37, 97, 99, 119, 123, 127, 142, 152

[154] Puschnig, P., Berkebile, S., Fleming, A. J., Koller, G., Emtsev, K., Seyller, T., Riley, J. D., Ambrosch-Draxl, C., Netzer, F. P., and Ramsey, M. G. Reconstruction of Molecular Orbital Densities from Photoemission Data. *Science*, 326(5953):702–706, 2009. Cited on p. 38

[155] Lücke, A. *Coupling of Electron and Ion Dynamics in 1D, 2D and 3D Materials*. PhD thesis, University of Paderborn, 2017. Cited on p. 39, 110, 118, 144, 145

[156] Hunklinger, S. *Festkörperphysik*. Oldenbourg Verlag, München, 2011. Cited on p. 39, 46, 49, 50, 52, 53

[157] Yan, Y.-X., Gamble, E. B., and Nelson, K. A. Impulsive stimulated scattering: General importance in femtosecond laser pulse interactions with matter, and spectroscopic applications. *The Journal of Chemical Physics*, 83(11):5391–5399, 1985. Cited on p. 39, 40

[158] Weiner, A. M., Leaird, D. E., Wiederrecht, G. P., and Nelson, K. A. Femtosecond multiple-pulse impulsive stimulated Raman scattering spectroscopy. *JOSA B*, 8(6):1264–1275, 1991. Cited on p. 40, 143, 170

[159] Ishioka, K. and Misochko, O. Coherent Lattice oscillations in Solids and Their Optical Control, Part I. Fundamentals and Optical Detection Techniques. In *Progress in Ultrafast Intense Laser Science V*. Springer, Berlin Heidelberg. Cited on p. 40

[160] Zhu, L., Kleiman, V., Li, X., Lu, S. P., Trentelman, K., and Gordon, R. J. Coherent Laser Control of the Product Distribution Obtained in the Photoexcitation of HI. *Science*, 270(5233):77–80, 1995. Cited on p. 42

[161] Kosloff, R., Rice, S. A., Gaspard, P., Tersigni, S., and Tannor, D. J. Wavepacket dancing: Achieving chemical selectivity by shaping light pulses. *Chemical Physics*, 139(1):201–220, 1989. Cited on p. 42

[162] Pimentel, G. and Coonrod, J. *Opportunities in Chemistry: Today and Tomorrow*. The National Academic Press, Washington, DC, 2001. Cited on p. 42

[163] Först, M., Mankowsky, R., and Cavalleri, A. Mode-Selective Control of the Crystal Lattice. *Accounts of Chemical Research*, 48(2):380–387, 2015. Cited on p. 42, 43

[164] Cheng, Y.-H., Gao, F. Y., Teitelbaum, S. W., and Nelson, K. A. Coherent control of optical phonons in bismuth. *Physical Review B*, 96(13):134302, 2017. Cited on p. 43

[165] Nelson, K. A. The prospects for impulsively driven, mode-selective chemistry in condensed phases. In Jortner, J., Levine, R. D., and Pullman, B., editors, *Mode Selective Chemistry*, The Jerusalem Symposia on Quantum Chemistry and Biochemistry, pages 527–533. Springer Netherlands, 1991. Cited on p. 43, 143, 170, 177

[166] Rosenthal, D. Functional surfaces in heterogeneous catalysis: A short review. *physica status solidi (a)*, 208(6):1217–1222, 2011. Cited on p. 44, 56

[167] Hasan, M. Z. and Kane, C. L. Colloquium: Topological insulators. *Reviews of Modern Physics*, 82(4):3045–3067, 2010. Cited on p. 44

[168] Chen, C. *Introduction to Scanning Tunneling Microscopy*. Oxford University Press, New York, 1993. Cited on p. 44

[169] Haugstad, G. *Atomic Force Microscopy: Understanding Basic Modes and Advanced Applications*. John Wiley & Sons, Inc., Hobocken, NJ, 2012. Cited on p. 44

[170] Hüfner, S. *Photoelectron Spectroscopy: Principles and Applications*. Springer, Berlin Heidelberg New York, 2003. Cited on p. 44, 76

[171] Giannetti, C., Capone, M., Fausti, D., Fabrizio, M., Parmigiani, F., and Mihailovic, D. Ultrafast optical spectroscopy of strongly correlated materials and high-temperature superconductors: A non-equilibrium approach. *Advances in Physics*, 65(2):58–238, 2016. Cited on p. 44

[172] Kuzmany, H. *Solid-State Spectroscopy: An Introduction*. Springer-Verlag, Berlin Heidelberg, 2009. Cited on p.

[173] Demtröder, W. *Laser Spectroscopy: Basic Concepts and Instrumentation*. Springer-Verlag, Berlin Heidelberg, 2003. Cited on p. 44

[174] Siders, C. W., Cavalleri, A., Sokolowski-Tinten, K., Tóth, C., Guo, T., Kammler, M., von Hoegen, M. H., Wilson, K. R., von der Linde, D., and Barty, C. P. J. Detection of Nonthermal Melting by Ultrafast X-ray Diffraction. *Science*, 286(5443):1340–1342, 1999. Cited on p. 44

[175] Ruan, C.-Y., Vigliotti, F., Lobastov, V. A., Chen, S., and Zewail, A. H. Ultrafast electron crystallography: Transient structures of molecules, surfaces, and phase transitions. *Proceedings of the National Academy of Sciences*, 101 (5):1123–1128, 2004. Cited on p. 44

[176] Bordo, V. and Rubahn, H.-G. *Optics and Spectroscopy at Surfaces and Interfaces*. Wiley VCH Verlag GmbH & Co. KGaA, Weinheim, 2005. Cited on p. 44

[177] Lander, J. J. and Morrison, J. Surface Reactions of Silicon (111) with Aluminum and Indium. *Journal of Applied Physics*, 36(5):1706–1713, 1965. Cited on p. 45, 94, 95, 96, 97

[178] Chapman, H. N., Fromme, P., Barty, A., White, T. A., Kirian, R. A., Aquila, A., Hunter, M. S., Schulz, J., DePonte, D. P., Weierstall, U., Doak, R. B., Maia, F. R. N. C., Martin, A. V., Schlichting, I., Lomb, L., Coppola, N., Shoeman, R. L., Epp, S. W., Hartmann, R., Rolles, D., Rudenko, A., Foucar, L., Kimmel, N., Weidenspointner, G., Holl, P., Liang, M., Barthelmess, M., Caleman, C., Boutet, S., Bogan, M. J., Krzywinski, J., Bostedt, C., Bajt, S., Gumprecht, L., Rudek, B., Erk, B., Schmidt, C., Hömke, A., Reich, C., Pietschner, D., Strüder, L., Hauser, G., Gorke, H., Ullrich, J., Herrmann, S., Schaller, G., Schopper, F., Soltau, H., Kühnel, K.-U., Messerschmidt, M., Bozek, J. D., Hau-Riege, S. P., Frank, M., Hampton, C. Y., Sierra, R. G., Starodub, D., Williams, G. J., Hajdu, J., Timneanu, N., Seibert, M. M., Andreasson, J., Rocker, A., Jönsson, O., Svenda, M., Stern, S., Nass, K.,

Andritschke, R., Schröter, C.-D., Krasniqi, F., Bott, M., Schmidt, K. E., Wang, X., Grotjohann, I., Holton, J. M., Barends, T. R. M., Neutze, R., Marchesini, S., Fromme, R., Schorb, S., Rupp, D., Adolph, M., Gorkhover, T., Andersson, I., Hirsemann, H., Potdevin, G., Graafsma, H., Nilsson, B., and Spence, J. C. H. Femtosecond X-ray protein nanocrystallography. *Nature*, 470 (7332):73–77, 2011. Cited on p. 46

[179] Van Hove, M. A., Weinberg, W. H., and Chan, C.-M. *Low-Energy Electron Diffraction: Experiment, Theory and Surface Structure Determination*. Springer Series in Surface Sciences. Springer-Verlag, Berlin Heidelberg, 1986. Cited on p. 46, 48, 51, 56, 58, 189

[180] Van Hove, M. A. and Tong, S. *Surface Crystallography by LEED*. Springer-Verlag, Berlin Heidelberg New York, 1979. Cited on p. 46, 48, 49, 54, 180

[181] Warren, B. *X-Ray Diffraction*. Dover Publications, Mineola, N.Y., 1990. Cited on p. 46, 49

[182] Bragg, W. H. and Bragg, W. L. The Structure of the Diamond. *Nature*, 91 (2283):557–557, 1913. Cited on p. 46

[183] Ertl, G. and Küppers, J. *Low Energy Electronc and Surface Chemistry*. Wiley VCH Verlag GmbH & Co. KGaA, Weinheim, 1987. Cited on p. 46, 48, 56

[184] Henzler, M. and Göpel, W. *Oberflächenphysik Des Festkörpers*. B.G. Teubner, Stuttgart, 1994. Cited on p. 48, 55

[185] Oura, K., Lifshits, V., Saranin, A., Zotov, A., and Katayama, M. *Surface Science: An Introduction*. Springer-Verlag, Berlin Heidelberg, 2003. Cited on p. 46, 55

[186] Zuo, J. and Spence, J. C. H. *Advanced Transmission Electron Microscopy*. Springer Science+Business Media, New York, 2017. Cited on p. 46, 189, 190, 191, 192, 193

[187] Furrer, A., Mesot, J., and Strässle, T. *Neutron Scattering in Condensed Matter Physics*. World Scientific Publishing Co. Pte. Ltd., Singapore, 2009. Cited on p. 46

[188] Kaufmann, S., Schwarzer, D., Reichardt, C., Wodtke, A. M., and Bünermann, O. Generation of ultra-short hydrogen atom pulses by bunch-compression photolysis. *Nature Communications*, 5(1):5373, 2014. Cited on p. 46

[189] Jardine, A. P., Hedgeland, H., Alexandrowicz, G., Allison, W., and Ellis, J. Helium-3 spin-echo: Principles and application to dynamics at surfaces. *Progress in Surface Science*, 84(11):323–379, 2009. Cited on p. 46

[190] Chidsey, C. E. D., Liu, G.-Y., Rowntree, P., and Scoles, G. Molecular order at the surface of an organic monolayer studied by low energy helium diffraction. *The Journal of Chemical Physics*, 91(7):4421–4423, 1989. Cited on p.

[191] Graham, A. P. The low energy dynamics of adsorbates on metal surfaces investigated with helium atom scattering. *Surface Science Reports*, 49(4): 115–168, 2003. Cited on p. 46

[192] Farias, D. and Rieder, K.-H. Atomic beam diffraction from solid surfaces. *Reports on Progress in Physics*, 61(12):1575–1664, 1998. Cited on p. 46

[193] Clarke, L. *Surface Crystallography: An Introduction to Low Energy Electron Diffraction*. John Wiley & Sons, Chichester New York Brisbane Toronto Singapore, 1985. Cited on p. 47

[194] Altland, A. Advanced quantum mechanics. 2013. Cited on p. 48, 49

[195] Mizuno, S., Mizuno, Y. O., and Tochihara, H. Structural determination of indium-induced Si(111) reconstructed surfaces by LEED analysis: $(\sqrt{3} \times \sqrt{3})R30^\circ$ and (4×1). *Physical Review B*, 67(19):195410, 2003. Cited on p. 53, 97

[196] Bovensiepen, U., Wolf, M., and Petek, H. *Dynamics at Solid State Surfaces and Interfaces, Volume 1: Current Developments*. Wiley VCH Verlag GmbH & Co. KGaA, Weinheim, 2010. Cited on p. 55

[197] Bovensiepen, U., Petek, H., and Wolf, M. *Dynamics at Solid State Surfaces and Interfaces, Volume 2: Fundamentals*. Wiley VCH Verlag GmbH & Co. KGaA, Weinheim, 2012. Cited on p.

[198] Groß, A. *Theoretical Surface Science: A Microscopic Perspective*. Springer-Verlag, Berlin Heidelberg, 2003. Cited on p. 55

[199] Jiang, W., Liu, Z., Zhou, M., Ni, X., and Liu, F. Pi conjugation in the epitaxial Si(111)-($\sqrt{3} \times \sqrt{3}$) surface: Unconventional "bamboo hat" bonding geometry for Si. *Physical Review B*, 95(24):241405, 2017. Cited on p. 56

[200] Park, R. L. and Madden, H. H. Annealing changes on the (100) surface of palladium and their effect on CO adsorption. *Surface Science*, 11(2):188–202, 1968. Cited on p. 56

[201] Wood, E. A. Vocabulary of Surface Crystallography. *Journal of Applied Physics*, 35(4):1306–1312, 1964. Cited on p. 56

[202] Debye, P. Interferenz von Röntgenstrahlen und Wärmebewegung. *Annalen der Physik*, 348(1):49–92, 1913. Cited on p. 59, 189

[203] Waller, I. Zur Frage der Einwirkung der Wärmebewegung auf die Interferenz von Röntgenstrahlen. *Zeitschrift für Physik*, 17(1):398–408, 1923. Cited on p. 59, 189

[204] Overhauser, A. W. Observability of Charge-Density Waves by Neutron Diffraction. *Physical Review B*, 3(10):3173–3182, 1971. Cited on p. 60, 125

[205] Horn von Hoegen, M. Growth of semiconductor layers studied by spot profile analysing low energy electron diffraction – Part I1. *Zeitschrift für Kristallographie - Crystalline Materials*, 214(10):591–629, 1999. Cited on p. 60, 137, 138

[206] Dresselhaus, M. Solid State Physics - Part II: Optical Properties of Solids. Cited on p. 61, 62, 63, 64

[207] Li, Y. and Heinz, T. F. Optical models for thin layers. *arXiv:1801.00402*, 2018. Cited on p. 61, 64, 65, 159

[208] Brorson, S. D., Fujimoto, J. G., and Ippen, E. P. Femtosecond electronic heat-transport dynamics in thin gold films. *Physical Review Letters*, 59(17): 1962–1965, 1987. Cited on p. 66

[209] Hommelhoff, P., Sortais, Y., Aghajani-Talesh, A., and Kasevich, M. A. Field Emission Tip as a Nanometer Source of Free Electron Femtosecond Pulses. *Physical Review Letters*, 96(7):077401, 2006. Cited on p. 70, 77

[210] Ropers, C., Solli, D. R., Schulz, C. P., Lienau, C., and Elsaesser, T. Localized Multiphoton Emission of Femtosecond Electron Pulses from Metal Nanotips. *Physical Review Letters*, 98(4):043907, 2007. Cited on p. 70, 77, 78

[211] Aeschlimann, M., Brixner, T., Fischer, A., Kramer, C., Melchior, P., Pfeiffer, W., Schneider, C., Strüber, C., Tuchscherer, P., and Voronine, D. V. Coherent Two-Dimensional Nanoscopy. *Science*, 333(6050):1723–1726, 2011. Cited on p. 73, 168, 188

[212] Siwick, B. J., Dwyer, J. R., Jordan, R. E., and Miller, R. J. D. Ultrafast electron optics: Propagation dynamics of femtosecond electron packets. *Journal of Applied Physics*, 92(3):1643–1648, 2002. Cited on p. 75, 76

[213] Weathersby, S. P., Brown, G., Centurion, M., Chase, T. F., Coffee, R., Corbett, J., Eichner, J. P., Frisch, J. C., Fry, A. R., Gühr, M., Hartmann, N., Hast, C., Hettel, R., Jobe, R. K., Jongewaard, E. N., Lewandowski, J. R., Li, R. K., Lindenberg, A. M., Makasyuk, I., May, J. E., McCormick, D., Nguyen, M. N., Reid, A. H., Shen, X., Sokolowski-Tinten, K., Vecchione, T., Vetter, S. L., Wu, J., Yang, J., Dürr, H. A., and Wang, X. J. Mega-electron-volt ultrafast electron diffraction at SLAC National Accelerator Laboratory. *Review of Scientific Instruments*, 86(7):073702, 2015. Cited on p. 79

[214] Mo, M. Z., Chen, Z., Li, R. K., Dunning, M., Witte, B. B. L., Baldwin, J. K., Fletcher, L. B., Kim, J. B., Ng, A., Redmer, R., Reid, A. H., Shekhar, P., Shen, X. Z., Shen, M., Sokolowski-Tinten, K., Tsui, Y. Y., Wang, Y. Q., Zheng, Q., Wang, X. J., and Glenzer, S. H. Heterogeneous to homogeneous melting transition visualized with ultrafast electron diffraction. *Science*, 360 (6396):1451–1455, 2018. Cited on p. 75, 77

[215] Yang, D.-S., Gedik, N., and Zewail, A. H. Ultrafast Electron Crystallography. 1. Nonequilibrium Dynamics of Nanometer-Scale Structures. *The Journal of Physical Chemistry C*, 111(13):4889–4919, 2007. Cited on p. 77

[216] Neacsu, C. C., Reider, G. A., and Raschke, M. B. Second-harmonic generation from nanoscopic metal tips: Symmetry selection rules for single asymmetric nanostructures. *Physical Review B*, 71(20):201402, 2005. Cited on p. 77

[217] Gulde, M. *Development of an Ultrafast Low-Energy Electron Diffraction Setup*. PhD thesis, Georg-August-Universität Göttingen, 2014. Cited on p. 77, 78, 82, 183

[218] Schweda, S. *Entwicklung Eines Experiments Zur Zeitaufgelösten Beugung Niederenergetischer Elektronen*. Master's thesis, Georg-August-Universität Göttingen, 2013. Cited on p. 78

[219] Wit, B., Bunjes, O., Wenderoth, M., and Ropers, C. Structure and Nonequilibrium Heat-Transfer of a Physisorbed Molecular Layer on Graphene. *Advanced Materials Interfaces*, 7(13):2000473, 2020. Cited on p. 78, 82

[220] Müller, M., Paarmann, A., and Ernstorfer, R. Femtosecond electrons probing currents and atomic structure in nanomaterials. *Nature Communications*, 5 (1):5292, 2014. Cited on p. 79

[221] Müller, M., Kravtsov, V., Paarmann, A., Raschke, M. B., and Ernstorfer, R. Nanofocused Plasmon-Driven Sub-10 fs Electron Point Source. *ACS Photonics*, 3(4):611–619, 2016. Cited on p.

[222] Vogelsang, J., Hergert, G., Wang, D., Groß, P., and Lienau, C. Observing charge separation in nanoantennas via ultrafast point-projection electron microscopy. *Light: Science & Applications*, 7(1):55, 2018. Cited on p. 79

[223] Feist, A., Echternkamp, K. E., Schauss, J., Yalunin, S. V., Schäfer, S., and Ropers, C. Quantum coherent optical phase modulation in an ultrafast transmission electron microscope. *Nature*, 521(7551):200–203, 2015. Cited on p. 79

[224] Danz, T., Domröse, T., and Ropers, C. Ultrafast nanoimaging of the order parameter in a structural phase transition. *Science*, 371(6527):371–374, 2021. Cited on p. 79, 184, 188

[225] Breuer, J. and Hommelhoff, P. Laser-Based Acceleration of Nonrelativistic Electrons at a Dielectric Structure. *Physical Review Letters*, 111(13):134803, 2013. Cited on p. 79

[226] Bormann, R. *Development and Characterization of an Electron Gun for Ultrafast Electron Microscopy*. PhD thesis, Georg-August-Universität Göttingen, 2015. Cited on p. 79

[227] Bryant, P. J., Kim, H. S., Zheng, Y. C., and Yang, R. Technique for shaping scanning tunneling microscope tips. *Review of Scientific Instruments*, 58(6): 1115–1115, 1987. Cited on p. 79

[228] Schröder, B., Weber, T., Yalunin, S. V., Kiel, T., Matyssek, C., Sivis, M., Schäfer, S., von Cube, F., Irsen, S., Busch, K., Ropers, C., and Linden, S. Real-space imaging of nanotip plasmons using electron energy loss spectroscopy. *Physical Review B*, 92(8):085411, 2015. Cited on p. 79

[229] van Oudheusden, T., Pasmans, P. L. E. M., van der Geer, S. B., de Loos, M. J., van der Wiel, M. J., and Luiten, O. J. Compression of Subrelativistic Space-Charge-Dominated Electron Bunches for Single-Shot Femtosecond Electron Diffraction. *Physical Review Letters*, 105(26):264801, 2010. Cited on p. 79

[230] Kealhofer, C., Schneider, W., Ehberger, D., Ryabov, A., Krausz, F., and Baum, P. All-optical control and metrology of electron pulses. *Science*, 352 (6284):429–433, 2016. Cited on p. 79

[231] Buchsteiner, P., Sohn, F., Horstmann, J. G., Voigt, J., Ciomaga Hatnean, M., Balakrishnan, G., Ropers, C., Blöchl, P. E., and Wenderoth, M. Surface resonance of the (2×1) reconstructed lanthanum hexaboride (001)-cleavage plane: A combined STM and DFT study. *Physical Review B*, 100(20):205407, 2019. Cited on p. 82, 85, 86

[232] Park, R. L., Houston, J. E., and Schreiner, D. G. The LEED Instrument Response Function. *Review of Scientific Instruments*, 42(1):60–65, 1971. Cited on p. 84

[233] Klasing, F. *Indium on Si(111) - Low-Energy Electron Diffraction Experiments and Simulations on the Striped (8×2) Surface Reconstruction and on the (4×1)<->(8×2) Phase-Transition*. PhD thesis, Universität Duisburg-Essen, 2014. Cited on p. 90, 91, 104, 113, 121, 126, 128, 133, 178

[234] Song, S. K., Samad, A., Wippermann, S., and Yeom, H. W. Dynamical Metal to Charge-Density-Wave Junctions in an Atomic Wire Array. *Nano Letters*, 19(8):5769–5773, 2019. Cited on p. 90, 97, 112, 120, 121, 122, 128, 178

[235] Denoyer, F., Comès, R., Garito, A. F., and Heeger, A. J. X-Ray-Diffuse-Scattering Evidence for a Phase Transition in Tetrathiafulvalene Tetracyanoquinodimethane (TTF-TCNQ). *Physical Review Letters*, 35(7):445–448, 1975. Cited on p. 94

[236] Comès, R., Shapiro, S. M., Shirane, G., Garito, A. F., and Heeger, A. J. Neutron-Scattering Study of the 38- and 54-K Phase Transitions in Deuterated Tetrathiafulvalene- Tetracyanoquinodimethane (TTF-TCNQ). *Physical Review Letters*, 35(22):1518–1521, 1975. Cited on p. 94

[237] Jeckelmann, E., Sanna, S., Schmidt, W. G., Speiser, E., and Esser, N. Grand canonical Peierls transition in In/Si(111). *Physical Review B*, 93(24):241407, 2016. Cited on p. 94, 97, 98, 114, 145, 149, 154, 162, 163, 168

[238] Kim, S.-W. and Cho, J.-H. Origin of the metal-insulator transition of indium atom wires on Si(111). *Physical Review B*, 93(24):241408, 2016. Cited on p. 94, 109, 110, 111, 114, 115

[239] González, C., Ortega, J., and Flores, F. Metal–insulator transition in one-dimensional In-chains on Si(111): Combination of a soft shear distortion and a double-band Peierls instability. *New Journal of Physics*, 7:100–107, 2005. Cited on p. 94, 103, 104, 108, 109, 112, 147, 165

[240] Speiser, E., Esser, N., Wippermann, S., and Schmidt, W. G. Surface vibrational Raman modes of In:Si(111) (4×1) and (8×2) nanowires. *Physical Review B*, 94(7):075417, 2016. Cited on p. 94, 97, 99, 105, 107, 111, 112, 128, 148, 152, 153, 162, 163, 168

[241] Lücke, A., Gerstmann, U., Kühne, T. D., and Schmidt, W. G. Efficient PAW-based bond strength analysis for understanding the In/Si(111)(8×2) – (4×1) phase transition. *Journal of Computational Chemistry*, 38(26):2276–2282, 2017. Cited on p. 94, 98, 110, 115, 118, 144, 145, 165, 166

[242] Binnig, G., Rohrer, H., Gerber, C., and Weibel, E. 7×7 Reconstruction on Si(111) Resolved in Real Space. *Physical Review Letters*, 50(2):120–123, 1983. Cited on p. 95

[243] Ganz, E., Ing-Shouh, H., Fulin, X., Theiss, S. K., and Golovchenko, J. Growth and morphology of Pb on Si(111). *Surface Science*, 257(1):259–273, 1991. Cited on p. 95

[244] Le Lay, G. The Au/Si(111) interface: Growth mode, energetics, structural and electronic properties. *Journal of Crystal Growth*, 54(3):551–557, 1981. Cited on p. 95, 96

[245] Baski, A. A., Nogami, J., and Quate, C. F. Si(111)-5×1-Au reconstruction as studied by scanning tunneling microscopy. *Physical Review B*, 41(14):10247–10249, 1990. Cited on p. 95, 96

[246] Tegenkamp, C., Ohta, T., McChesney, J. L., Dil, H., Rotenberg, E., Pfnür, H., and Horn, K. Coupled Pb Chains on Si(557): Origin of One-Dimensional Conductance. *Physical Review Letters*, 100(7):076802, 2008. Cited on p. 96

[247] Lipton-Duffin, J. A., Mark, A. G., MacLeod, J. M., and McLean, A. B. Si(557)-Ag: A metallic quasi-one-dimensional system. *Physical Review B*, 77(12): 125419, 2008. Cited on p. 96

[248] Hafke, B., Frigge, T., Witte, T., Krenzer, B., Aulbach, J., Schäfer, J., Claessen, R., Erwin, S. C., and Horn-von Hoegen, M. Two-dimensional interaction of spin chains in the Si(553)-Au nanowire system. *Physical Review B*, 94(16): 161403, 2016. Cited on p. 96

[249] Carpinelli, J. M., Weitering, H. H., Plummer, E. W., and Stumpf, R. Direct observation of a surface charge density wave. *Nature*, 381(6581):398–400, 1996. Cited on p. 96

[250] Abukawa, T., Sasaki, M., Hisamatsu, F., Goto, T., Kinoshita, T., Kakizaki, A., and Kono, S. Surface electronic structure of a single-domain Si(111)4×1-In surface: A synchrotron radiation photoemission study. *Surface Science*, 325 (1):33–44, 1995. Cited on p. 96, 97, 99, 105

[251] Rotenberg, E., Koh, H., Rossnagel, K., Yeom, H. W., Schäfer, J., Krenzer, B., Rocha, M. P., and Kevan, S. D. Indium $\sqrt{7} \times \sqrt{3}$ on Si(111): A Nearly Free Electron Metal in Two Dimensions. *Physical Review Letters*, 91(24):246404, 2003. Cited on p. 96

[252] Jäger, M., Pfnür, H., Fanciulli, M., Weber, A. P., Dil, J. H., and Tegenkamp, C. Formation of Sn-Induced Nanowires on Si(557). *physica status solidi (b)*, 256(10):1970037, 2019. Cited on p. 96

[253] Kawaji, M., Baba, S., and Kinbara, A. Superstructures of submonolayer indium films on silicon (111)7 surfaces. *Applied Physics Letters*, 34(11):748–749, 1979. Cited on p. 96, 97

[254] Baba, S., Hirayama, H., Zhou, J. M., and Kinbara, A. Adatoms of indium on Si(111) surfaces: Application of reflection high energy electron diffraction to desorption experiments. *Thin Solid Films*, 90(1):57–61, 1982. Cited on p. 96

[255] Kraft, J., Ramsey, M. G., and Netzer, F. P. Surface reconstructions of In on Si(111). *Physical Review B*, 55(8):5384–5393, 1997. Cited on p. 96, 97, 99

[256] Wippermann, S. *Understanding Substrate-Supported Atomic-Scale Nanowires from Ab Initio Theory*. PhD thesis, University of Paderborn, 2010. Cited on p. 97, 98, 101, 102, 104, 107, 108, 112, 128, 147, 152, 162, 163, 165

[257] Lee, G., Guo, J., and Plummer, E. W. Real-Space Observation of Nanoscale Inhomogeneities and Fluctuations in a Phase Transition of a Surface Quasi-One-Dimensional System: In/Si(111). *Physical Review Letters*, 95(11):116103, 2005. Cited on p. 97, 112, 120, 122, 128

[258] Hatta, S., Ohtsubo, Y., Aruga, T., Miyamoto, S., Okuyama, H., Tajiri, H., and Sakata, O. Dynamical fluctuations in In nanowires on Si(111). *Physical Review B*, 84(24):245321, 2011. Cited on p. 97

[259] Shim, H., Jeon, Y., Yeo, J., and Lee, G. Homogeneous and heterogeneous nucleations in the surface phase transition: Si(111)4 × 1-In. *New Journal of Physics*, 17(6):063026, 2015. Cited on p. 97

[260] Nakamura, N., Anno, K., and Kono, S. Structure analysis of the single-domain Si(111)4 × 1-In surface by μ-probe Auger electron diffraction and μ-probe reflection high energy electron diffraction. *Surface Science*, 256(1):129–134, 1991. Cited on p. 97

[261] Ryjkov, S. V., Nagao, T., Lifshits, V. G., and Hasegawa, S. Phase transition and stability of Si(111)–8x‘2’-In surface phase at low temperatures. *Surface Science*, 488(1):15–22, 2001. Cited on p. 97, 104, 121

[262] Fukaya, Y., Hashimoto, M., Kawasuso, A., and Ichimiya, A. Surface structure of Si(111)-(8×2)–In determined by reflection high-energy positron diffraction. *Surface Science*, 602(14):2448–2452, 2008. Cited on p. 97, 104

[263] Bunk, O., Falkenberg, G., Zeysing, J. H., Lottermoser, L., Johnson, R. L., Nielsen, M., Berg-Rasmussen, F., Baker, J., and Feidenhans'l, R. Structure determination of the indium-induced Si(111)-(4×1) reconstruction by surface x-ray diffraction. *Physical Review B*, 59(19):12228–12231, 1999. Cited on p. 97, 104

[264] Ahn, J. R., Byun, J. H., Kim, J. K., and Yeom, H. W. Absence of dynamic fluctuation in metallic In chains on Si(111): Core-level and valence-band photoemission study. *Physical Review B*, 75(3):033313, 2007. Cited on p. 97

[265] Öfner, H., Surnev, S. L., Shapira, Y., and Netzer, F. P. In overlayers on Si(111)7×7: Growth and evolution of the electronic structure. *Physical Review B*, 48(15):10940–10949, 1993. Cited on p. 97

[266] Liu, C., Inaoka, T., Yaginuma, S., Nakayama, T., Aono, M., and Nagao, T. Disappearance of the quasi-one-dimensional plasmon at the metal-insulator phase transition of indium atomic wires. *Physical Review B*, 77(20):205415, 2008. Cited on p. 97

[267] Pedreschi, F., O'Mahony, J. D., Weightman, P., and Power, J. R. Evidence of electron confinement in the single-domain (4×1)-In superstructure on vicinal Si(111). *Applied Physics Letters*, 73(15):2152–2154, 1998. Cited on p. 97, 99

[268] Fleischer, K., Chandola, S., Esser, N., Richter, W., and McGilp, J. F. Reflectance Anisotropy Spectroscopy of Si(111)-(4 × 1)-In. *physica status solidi (a)*, 188(4):1411–1416, 2001. Cited on p.

[269] Fleischer, K., Chandola, S., Esser, N., Richter, W., and McGilp, J. F. Phonon and polarized reflectance spectra from Si(111)-(4 × 1): Evidence for a charge-density-wave driven phase transition. *Physical Review B*, 67(23):235318, 2003. Cited on p. 97, 153

[270] Fleischer, K., Chandola, S., Esser, N., Richter, W., McGilp, J. F., Schmidt, W. G., Wang, S., Lu, W., and Bernholc, J. Atomic indium nanowires on Si(111): The (4×1)–(8×2) phase transition studied with reflectance anisotropy spectroscopy. *Applied Surface Science*, 234(1):302–306, 2004. Cited on p. 97, 104

[271] Fleischer, K., Chandola, S., Esser, N., Richter, W., and McGilp, J. F. Surface phonons of the Si(111):In-(4 × 1) and (8 × 2) phases. *Physical Review B*, 76 (20):205406, 2007. Cited on p. 97, 107, 111, 112

[272] Tanikawa, T., Matsuda, I., Kanagawa, T., and Hasegawa, S. Surface-State Electrical Conductivity at a Metal-Insulator Transition On Silicon. *Physical Review Letters*, 93(1):016801, 2004. Cited on p. 97, 103

[273] Stevens, J. L., Worthington, M. S., and Tsong, I. S. T. 4 × 1 reconstruction of indium deposited on vicinal Si(111) surfaces. *Physical Review B*, 47(3): 1453–1459, 1993. Cited on p. 97, 99

[274] Uchihashi, T. and Ramsperger, U. Electron conduction through quasi-one-dimensional indium wires on silicon. *Applied Physics Letters*, 80(22):4169–4171, 2002. Cited on p.

[275] Kim, T.-H. and Yeom, H. W. Topological Solitons versus Nonsolitonic Phase Defects in a Quasi-One-Dimensional Charge-Density Wave. *Physical Review Letters*, 109(24):246802, 2012. Cited on p. 97, 121

[276] Cho, J.-H., Oh, D.-H., Kim, K. S., and Kleinman, L. Weakly correlated one-dimensional indium chains on Si(111). *Physical Review B*, 64(23):235302, 2001. Cited on p. 97, 99, 102, 104, 112

[277] Bechstedt, F., Krivosheeva, A., Furthmüller, J., and Stekolnikov, A. A. Vibrational properties of the quasi-one-dimensional Si(111)-(4×1) system. *Physical Review B*, 68(19):193406, 2003. Cited on p. 97

[278] Park, S. J., Yeom, H. W., Min, S. H., Park, D. H., and Lyo, I. W. Direct Evidence of the Charge Ordered Phase Transition of Indium Nanowires on Si(111). *Physical Review Letters*, 93(10):106402, 2004. Cited on p. 98, 99, 103, 105, 112, 120, 121

[279] Cornelison, D. M., Worthington, M. S., and Tsong, I. S. T. Si(111)-(4×1)In surface reconstruction studied by impact-collision ion-scattering spectrometry. *Physical Review B*, 43(5):4051–4056, 1991. Cited on p. 97

[280] Saranin, A. A., Khramtsova, E. A., Ignatovich, K. V., Lifshits, V. G., Numata, T., Kubo, O., Katayama, M., Katayama, I., and Oura, K. Indium-induced Si(111)4×1 silicon substrate atom reconstruction. *Physical Review B*, 55(8): 5353–5359, 1997. Cited on p. 97

[281] Saranin, A. A., Zotov, A., Ignatovich, K. V., Lifshits, V. G., Numata, T., Kubo, O., Tani, H., Katayama, M., and Oura, K. Structural model for the Si(111)-4×1-In reconstruction. *Physical Review B*, 56(3):1017–1020, 1997. Cited on p. 97

[282] Terada, Y., Yoshida, S., Okubo, A., Kanazawa, K., Xu, M., Takeuchi, O., and Shigekawa, H. Optical doping: Active control of metal-insulator transition in nanowire. *Nano Letters*, 8(11):3577–3581, 2008. Cited on p. 98, 115, 136, 180

[283] Morikawa, H., Hwang, C. C., and Yeom, H. W. Controlled electron doping into metallic atomic wires: Si(111)4×1-In. *Physical Review B*, 81(7):075401, 2010. Cited on p. 120, 121

[284] Zhang, H., Ming, F., Kim, H.-J., Zhu, H., Zhang, Q., Weitering, H. H., Xiao, X., Zeng, C., Cho, J.-H., and Zhang, Z. Stabilization and Manipulation of Electronically Phase-Separated Ground States in Defective Indium Atom Wires on Silicon. *Physical Review Letters*, 113(19):196802, 2014. Cited on p. 98, 121, 128

[285] Gallus, O., Pillo, T., Hengsberger, M., Segovia, P., and Baer, Y. A system with a complex phase transition: Indium chains on Si(111). *The European Physical Journal B - Condensed Matter and Complex Systems*, 20(3):313–319, 2001. Cited on p. 99, 103, 104, 105, 107

[286] Yeom, H. W., Horikoshi, K., Zhang, H. M., Ono, K., and Uhrberg, R. I. G. Nature of the broken-symmetry phase of the one-dimensional metallic In/Si(111) surface. *Physical Review B*, 65(24):241307, 2002. Cited on p.

[287] Ahn, J. R., Byun, J. H., Koh, H., Rotenberg, E., Kevan, S. D., and Yeom, H. W. Mechanism of Gap Opening in a Triple-Band Peierls System: In Atomic Wires on Si. *Physical Review Letters*, 93(10):106401, 2004. Cited on p. 99, 100, 104, 105, 106, 107

[288] Sun, Y. J., Agario, S., Souma, S., Sugawara, K., Tago, Y., Sato, T., and Takahashi, T. Cooperative structural and Peierls transition of indium chains on Si(111). *Physical Review B*, 77(12):125115, 2008. Cited on p. 99, 100, 103, 104, 105, 106, 107, 109, 110

[289] Kanagawa, T., Hobara, R., Matsuda, I., Tanikawa, T., Natori, A., and Hasegawa, S. Anisotropy in Conductance of a Quasi-One-Dimensional Metallic Surface State Measured by a Square Micro-Four-Point Probe Method. *Physical Review Letters*, 91(3):036805, 2003. Cited on p. 99, 100

[290] Schmidt, W. G., Wippermann, S., Sanna, S., Babilon, M., Vollmers, N. J., and Gerstmann, U. In-Si(111)$(4 \times 1)/(8 \times 2)$ nanowires: Electron transport, entropy, and metal-insulator transition. *physica status solidi (b)*, 249(2):343–359, 2012. Cited on p. 101

[291] Kumpf, C., Bunk, O., Zeysing, J. H., Su, Y., Nielsen, M., Johnson, R. L., Feidenhans'l, R., and Bechgaard, K. Low-Temperature Structure of Indium Quantum Chains on Silicon. *Physical Review Letters*, 85(23):4916–4919, 2000. Cited on p. 102, 104, 105, 107, 108

[292] Sankey, O. F. and Niklewski, D. J. Ab initio multicenter tight-binding model for molecular-dynamics simulations and other applications in covalent systems. *Physical Review B*, 40(6):3979–3995, 1989. Cited on p. 103

[293] Chandola, S., Hinrichs, K., Gensch, M., Esser, N., Wippermann, S., Schmidt, W. G., Bechstedt, F., Fleischer, K., and McGilp, J. F. Structure of Si(111)-In Nanowires Determined from the Midinfrared Optical Response. *Physical Review Letters*, 102(22):226805, 2009. Cited on p. 104

[294] Wippermann, S., Schmidt, W. G., Bechstedt, F., Chandola, S., Hinrichs, K., Gensch, M., Esser, N., Fleischer, K., and McGilp, J. F. Optical anisotropy of Si(111)-$(4 \times 1)/(8 \times 2)$-In nanowires calculated from first-principles. *physica status solidi c*, 7(2):133–136, 2010. Cited on p. 104

[295] Lipson, H. and Singer, K. E. Disorder in a film of gold deposited on silicon: Investigation by low-energy electron diffraction. *Journal of Physics C: Solid State Physics*, 7(1):12, 1974. Cited on p. 104

[296] González, C., Flores, F., and Ortega, J. Soft Phonon, Dynamical Fluctuations, and a Reversible Phase Transition: Indium Chains on Silicon. *Physical Review Letters*, 96(13):136101, 2006. Cited on p. 108, 109, 112, 165

[297] González, C., Guo, J., Ortega, J., Flores, F., and Weitering, H. H. Mechanism of the Band Gap Opening across the Order-Disorder Transition of Si(111)(4×1)-In. *Physical Review Letters*, 102(11):115501, 2009. Cited on p. 108, 109, 110

[298] Park, S. J., Yeom, H. W., Ahn, J. R., and Lyo, I.-W. Atomic-scale phase coexistence and fluctuation at the quasi-one-dimensional metal-insulator transition. *Physical Review Letters*, 95(12):126102, 2005. Cited on p. 112, 115, 120, 121, 122, 128

[299] Zhang, H., Choi, J.-H., Xu, Y., Wang, X., Zhai, X., Wang, B., Zeng, C., Cho, J.-H., Zhang, Z., and Hou, J. G. Atomic Structure, Energetics, and Dynamics of Topological Solitons in Indium Chains on Si(111) Surfaces. *Physical Review Letters*, 106(2):026801, 2011. Cited on p. 121

[300] Waldecker, L., Bertoni, R., Hübener, H., Brumme, T., Vasileiadis, T., Zahn, D., Rubio, A., and Ernstorfer, R. Momentum-Resolved View of Electron-Phonon Coupling in Multilayer ${\mathrm{WSe}}_{2}$. *Physical Review Letters*, 119(3):036803, 2017. Cited on p. 125

[301] Stern, M. J., René de Cotret, L. P., Otto, M. R., Chatelain, R. P., Boisvert, J.-P., Sutton, M., and Siwick, B. J. Mapping momentum-dependent electron-phonon coupling and nonequilibrium phonon dynamics with ultrafast electron diffuse scattering. *Physical Review B*, 97(16):165416, 2018. Cited on p. 125, 193

[302] Guo, J., Lee, G., and Plummer, E. W. Intertwined Electronic and Structural Phase Transitions in the In/Si(111) Interface. *Physical Review Letters*, 95(4): 046102, 2005. Cited on p. 128

[303] Hafke, B., Witte, T., Janoschka, D., Dreher, P., Meyer zu Heringdorf, F.-J., and Horn-von Hoegen, M. Condensation of ground state from a supercooled phase in the Si(111)-$(4 \times 1) \rightarrow (8 \times 2)$-indium atomic wire system. *Structural Dynamics*, 6(4):045101, 2019. Cited on p. 133, 134, 135, 136, 146, 174, 178, 179

[304] Weiner, A. M., Leaird, D. E., Wiederrecht, G. P., and Nelson, K. A. Femtosecond pulse sequences used for optical manipulation of molecular motion. *Science*, 247(4948):1317–1319, 1990. Cited on p. 143, 170

[305] Hamm, P. and Zanni, M. *Concepts and Methods of 2D Infrared Spectroscopy*. Cambridge University Press, New York, 2011. Cited on p. 168

[306] Zanni, M. T. and Hochstrasser, R. M. Two-dimensional infrared spectroscopy: A promising new method for the time resolution of structures. *Current Opinion in Structural Biology*, 11(5):516–522, 2001. Cited on p. 168

[307] Cho, M. Coherent Two-Dimensional Optical Spectroscopy. *Chemical Reviews*, 108(4):1331–1418, 2008. Cited on p.

[308] Cahoon, J. F., Sawyer, K. R., Schlegel, J. P., and Harris, C. B. Determining Transition-State Geometries in Liquids Using 2D-IR. *Science*, 319(5871):1820–1823, 2008. Cited on p. 168

[309] Tobey, R. I., Prabhakaran, D., Boothroyd, A. T., and Cavalleri, A. Ultrafast electronic phase transition in $La_{1/2}Sr_{3/2}MnO_4$ by coherent vibrational excitation: Evidence for nonthermal melting of orbital order. *Physical Review Letters*, 101(19):197404, 2008. Cited on p. 170, 186

[310] Nova, T. F., Disa, A. S., Fechner, M., and Cavalleri, A. Metastable ferroelectricity in optically strained $SrTiO_3$. *Science*, 364(6445):1075–1079, 2019. Cited on p. 170, 186

[311] Cocker, T. L., Peller, D., Yu, P., Repp, J., and Huber, R. Tracking the ultrafast motion of a single molecule by femtosecond orbital imaging. *Nature*, 539(7628):263–267, 2016. Cited on p. 178, 186

[312] Peller, D., Kastner, L. Z., Buchner, T., Roelcke, C., Albrecht, F., Moll, N., Huber, R., and Repp, J. Sub-cycle atomic-scale forces coherently control a single-molecule switch. *Nature*, 585(7823):58–62, 2020. Cited on p.

[313] Böckmann, H., Liu, S., Mielke, J., Gawinkowski, S., Waluk, J., Grill, L., Wolf, M., and Kumagai, T. Direct Observation of Photoinduced Tautomerization in Single Molecules at a Metal Surface. *Nano Letters*, 16(2):1034–1041, 2016. Cited on p.

[314] Schröder, B., Bunjes, O., Wimmer, L., Kaiser, K., Traeger, G. A., Kotzott, T., Ropers, C., and Wenderoth, M. Controlling photocurrent channels in scanning tunneling microscopy. *New Journal of Physics*, 22(3):033047, 2020. Cited on p.

[315] Kloth, P., Thias, T., Bunjes, O., von der Haar, J., and Wenderoth, M. A versatile implementation of pulsed optical excitation in scanning tunneling microscopy. *Review of Scientific Instruments*, 87(12):123702, 2016. Cited on p.

[316] Müller, M., Martín Sabanés, N., Kampfrath, T., and Wolf, M. Phase-Resolved Detection of Ultrabroadband THz Pulses inside a Scanning Tunneling Microscope Junction. *ACS Photonics*, 7(8):2046–2055, 2020. Cited on p. 178, 186

[317] Bangert, U., Pierce, W., Kepaptsoglou, D. M., Ramasse, Q., Zan, R., Gass, M. H., Van den Berg, J. A., Boothroyd, C. B., Amani, J., and Hofsäss, H. Ion Implantation of Graphene—Toward IC Compatible Technologies. *Nano Letters*, 13(10):4902–4907, 2013. Cited on p. 180

[318] Willke, P., Amani, J. A., Sinterhauf, A., Thakur, S., Kotzott, T., Druga, T., Weikert, S., Maiti, K., Hofsäss, H., and Wenderoth, M. Doping of Graphene

by Low-Energy Ion Beam Implantation: Structural, Electronic, and Transport Properties. *Nano Letters*, 15(8):5110–5115, 2015. Cited on p. 180

[319] von Witte, G., Kißlinger, T., Horstmann, J. G., Rossnagel, K., Schneider, M. A., Ropers, C., and Hammer, L. Surface structure and stacking of the commensurate $(\sqrt{13} \times \sqrt{13})$R13.9° charge density wave phase of $1T$-TaS_2(0001). *Physical Review B*, 100(15):155407, 2019. Cited on p. 181, 182

[320] Lau, J. A., Choudhury, A., Chen, L., Schwarzer, D., Verma, V. B., and Wodtke, A. M. Observation of an isomerizing double-well quantum system in the condensed phase. *Science*, 367(6474):175–178, 2020. Cited on p. 182, 186

[321] Davis, T. J., Janoschka, D., Dreher, P., Frank, B., zu Heringdorf, F.-J. M., and Giessen, H. Ultrafast vector imaging of plasmonic skyrmion dynamics with deep subwavelength resolution. *Science*, 368(6489), 2020. Cited on p. 186, 188

[322] Tromp, R. M., Hannon, J. B., Ellis, A. W., Wan, W., Berghaus, A., and Schaff, O. A new aberration-corrected, energy-filtered LEEM/PEEM instrument. I. Principles and design. *Ultramicroscopy*, 110(7):852–861, 2010. Cited on p. 187

[323] Kautz, J., Jobst, J., Sorger, C., Tromp, R. M., Weber, H. B., and van der Molen, S. J. Low-Energy Electron Potentiometry: Contactless Imaging of Charge Transport on the Nanoscale. *Scientific Reports*, 5(1):13604, 2015. Cited on p. 188

[324] Jobst, J., van der Torren, A. J. H., Krasovskii, E. E., Balgley, J., Dean, C. R., Tromp, R. M., and van der Molen, S. J. Quantifying electronic band interactions in van der Waals materials using angle-resolved reflected-electron spectroscopy. *Nature Communications*, 7(1):13621, 2016. Cited on p. 188

[325] Hardy, K., Parker, F., and Walker, J. A better approximation to the Debye-Waller factor. *Nuclear Instruments and Methods*, 86(1):171–172, 1970. Cited on p. 192

[326] Xu, R. and Chiang, T. C. Determination of phonon dispersion relations by X-ray thermal diffuse scattering. *Zeitschrift für Kristallographie - Crystalline Materials*, 220(12):1009–1016, 2005. Cited on p. 193

[327] Trigo, M., Chen, J., Vishwanath, V. H., Sheu, Y. M., Graber, T., Henning, R., and Reis, D. A. Imaging nonequilibrium atomic vibrations with x-ray diffuse scattering. *Physical Review B*, 82(23):235205, 2010. Cited on p. 193

[328] Maldonado, P., Chase, T., Reid, A. H., Shen, X., Li, R. K., Carva, K., Payer, T., Horn von Hoegen, M., Sokolowski-Tinten, K., Wang, X. J., Oppeneer, P. M., and Dürr, H. A. Tracking the ultrafast nonequilibrium energy flow between electronic and lattice degrees of freedom in crystalline nickel. *Physical Review B*, 101(10):100302, 2020. Cited on p. 193

[329] Waldecker, L. *Electron-Lattice Interactions and Ultrafast Structural Dynamics of Solids*. PhD thesis, Freie Universität Berlin, 2016. Cited on p. 193

Publications and Conference Talks

Publications

The following articles originated over the course of this work:

(1) **J. G. Horstmann**, H. Böckmann, B. Wit, F. Kurtz, G. Storeck, and C. Ropers, *Coherent Control of a surface structural phase transition*, Nature **583**, 232-236 (2020).

(2) H. Böckmann-Clemens, **J. G. Horstmann**, A. S. Razzaq, S. Wippermann, and C. Ropers, in preparation (2021).

(3) S. Vogelgesang, G. Storeck, **J. G. Horstmann**, T. Diekmann, M. Sivis, S. Schramm, K. Rossnagel, S. Schäfer, and C. Ropers, *Phase ordering of charge density waves traced by ultrafast low-energy electron diffraction*, Nat. Phys. **14**, 184-190 (2018).

(4) G. von Witte, T. Kisslinger, **J. G. Horstmann**, K. Rossnagel, M. A. Schneider, C. Ropers, and L. Hammer, *Surface structure and stacking of the commensurate* $(\sqrt{13}\times\sqrt{13})R13.9°$ *charge density wave phase of* $1T-TaS_2(0001)$, Phys. Rev. B **100**, 155407 (2019).

(5) P. Buchsteiner, F. Sohn, **J. G. Horstmann**, J. Voigt, M. Ciomaga Hatnean, G. Balakrishnan, C. Ropers, P. E. Blöchl, and Martin Wenderoth, textitSurface resonance of the (2×1) *reconstructed lanthanum hexaboride* (001)*-cleavage plane: A combined STM and DFT study*, Phys. Rev. B **100**, 205407 (2019).

(6) G. Storeck, **J.G. Horstmann**, T. Diekmann, S. Vogelgesang, G. von Witte, S. V. Yalunin, K. Rossnagel, and C. Ropers, *Structural dynamic of incommensurate charge-density waves tracked by ultrafast low-energy electron diffraction*, Struct. Dyn. **7**, 034304 (2020).

Conference Talks

- *Ultrafast LEED: Exploring surface dynamics on a picosecond timescale with short electron pulses*, ECSCD, 2017, San Sebastian, Spain
- *Phase-ordering kinetics of charge density waves mapped by ultrafast LEED*, DPG Spring Meeting, 2018, Berlin, Germany
- *Tracing structural phase transitions and phase ordering at surfaces with ultrafast LEED*, ECOSS-34, 2018, Aarhus, Denmark
- *Structural phase transitions and phase ordering at surfaces probed by ultrafast LEED*, Ultrafast Phenomena XXI, 2018, Hamburg, Germany
- *Time-resolved spot-profile analysis and coherent control of low-dimensional solid-state systems*, 9^{th} international workshop on low energy electron diffraction and related techniques, 2018, Remagen, Germany
- *Coherent control of the structural phase transition in In-nanowires on Si(111)*, DPG Spring Meeting, 2019, Regensburg, Germany
- *Coherent control of a surface-specific structural phase transition examined by ultrafast LEED*, FEIS-4, 2019, Lincoln (NE), USA
- *Coherent control of the Peierls transition in quasi-one-dimensional atomic wires*, IWCE, 2019, Göttingen, Germany
- *Ultrafast LEED: Observing and controlling structural phase transitions at surfaces*, Annual symposium of the Royal Society of Chemistry (solid surfaces group), 2020, London, UK, **Invited**
- *Exerting coherent control over a surface structural phase transition via amplitude modes*, Ultrafast Phenomena XXII, 2020, Shanghai, China (online)
- *Ultrafast LEED - observing and controlling surface structural phase transitions*, 9^{th} International Symposium on Surface Science (ISSS-9), 2020 (postponed to 2021), Takamatsu, Japan, **Invited**

Awards

- ECOSS Prize for best oral presentation at ECOSS-34, 2018, Aarhus, Denmark
- Born-Franck dissertation award of the Faculty of Physics of the University of Göttingen, 2021

Acknowledgements

Science is *always* a collective effort. Over the years I have been very fortunate to work with many outstanding scientists and/or human beings without whom this work would not have been possible. Therefore, I would like to use the following lines to thank *all of you*. In the event that I have forgotten someone - whether consciously or unconsciously - or have not sufficiently appreciated individual contributions, I ask for either prompt clarification or years of offended silence.

First of all, I would like to thank Claus Ropers for being an excellent supervisor, a generous advocate and supporter, as well as an incorrigible optimist. For never holding a grudge, for caring for his people in good times and bad, and for always giving the authentic impression that he would love to be in the lab with you right now.

I thank Stefan Mathias for being the second reviewer of this thesis. I still have a score to settle with trARPES, and it was exciting to follow the work in your lab and to see that it actually works. Furthermore, I thank all members of the examination committee for the smooth communication leading up to the defense.

I would also like to take this opportunity to acknowledge the many scientific collaborators that had an influence on this work. Before meeting Lutz Hammer and Tilman Kisslinger, I thought I knew about LEED. It turned out I was just touching the surface. Thank you for giving me an idea of what lies beneath. I thank Stefan Wippermann for the detailed theoretical insights into the materials system. It was exciting to see how theory and experiment can benefit from each other. Furthermore, I would like to thank Kai Rossnagel and Kerstin Hanff for the beautiful 1T-TaS_2 samples which allowed us to prepare surfaces with reproducible quality from the very beginning. Moreover, I am grateful to Chris W. Nicholson, Ralph Ernstorfer and Martin Wolf, Michael Horn-von Hoegen, Heinrich Schwoerer, Alec M. Wodtke, Martin Wenderoth and Salvatore Manmana for numerous insightful discussions.

Moreover, I am grateful to those who carefullly proofread my thesis: Benjamin

Schröder, Jan-Wilke Henke, Felix Kurtz, and finally Olé Bunjes (he really wanted to, but I messed it up).

And here is to you, my fellow ULEEDers: It was a blast. It is impossible to remember your passion and dedication, all the fun and struggle we had, or all these countless little moments of desperation and enthusiasm in just a few lines. Perhaps an unnamed member of the ULEED team put it best after spending a few weeks with us: "How the hell can this group be so successful?" Although it is always difficult to single out individuals, special thanks goes to Gero Storeck, Felix Kurtz, Dennis Epp, Simon Vogelgesang and Murat Sivis, who developed and fabricated the miniaturised electron guns. Without your effort, this work would not have been possible. I would also like to say a special thank you to Hannes Böckmann-Clemens, who joined me in the nanowire business. It was a pleasure to work with and learn from you. I still don't understand your LabView code though.

Another big thank you goes to the entire working group – including the UTEM team. All these years I was allowed to be part of this remarkable bunch of people who engaged in countless group activities, awkward birthday celebrations and daily fights over optomechanical components. I had the privilege of watching your children grow up and your hair turn grey (or fall out). There were days of joy and of grief. But at any time, even in the midst of a global pandemic, you made sure that no one had to feel alone.

I would also like to say thank you to Karin Ahlborn and Bernhard Spicher, Rasit Kösker and Jörg Malindretos for their (technical) support throughout this work. To Antje Spliethoff-Laiser, who took care of administrative matters which go far beyond my imagination. And to the team of the central workshop, especially to Christof Schmidt and Alexander Gehrt, who managed to turn even the weirdest CAD drawings into reality.

To my friends: Thank you for the countless road bike tours, runs, walks, and hikes, the half-empty wine bottles, every word of encouragement, and for all the things I cannot talk about here for legal reasons.

During all these years, I was lucky to have a family around me who supported and grounded me at all times. I feel this is a great privilege and would like to thank you all for your support.

And finally, I thank you, Mónica. I have written countless versions of this paragraph - most of which were either far too cheesy or overly complicated. I have

thought about writing something in Spanish, but was afraid of making some embarrassing mistake that people would laugh about years later. In the end, I decided to do what I obviously failed to do in the past 242 pages: keep it short. I simply want to thank you for all your love and for all the things you have taught me.